Factors Affecting Charge Collection and Photo-Stability of Organic Solar Cells

by

Graeme Williams

A thesis

presented to the University of Waterloo

in fulfilment of the

thesis requirement for the degree of

Doctor of Philosophy

in

Electrical and Computer Engineering

Waterloo, Ontario, Canada, 2015.

Author's Declaration

I hereby declare that I am the sole author of this thesis. This is a true copy of the thesis, including any required final revisions, as accepted by my examiners.

I understand that my thesis may be made electronically available to the public.

Abstract

Organic photovoltaics employ small molecules or polymers as their primary light absorbing materials and thus differ strongly from traditional silicon-based photovoltaics. Their primary technological benefit is a significant reduction in materials and module fabrication costs. While research on organic solar cells (OSCs) has increased dramatically in the past decade, both OSC efficiencies and device lifetimes must be improved before they can compete with existing second generation photovoltaic technologies. Many of the gains in OSC efficiency to date can be attributed to the vast and concurrent trial-and-error experiments on new donor materials and processing techniques to form traditional bulk heterojunction structures. The field is consequently lacking in predictive power, and many stipulations regarding ideal device architectures and optimal interfacial layers remain ambiguous. Furthermore, OSC lifetime is much less studied in literature compared to OSC efficiency, and fundamental studies identifying the primary mode of degradation observed in OSCs under standard operation are lacking. It is thus beneficial to systematically study charge transport and charge extraction in modern OSCs, especially as these phenomena vary over the lifetime of the OSC.

This thesis comprehensively examines charge collection in OSCs as a function of OSC device architecture. To maintain a coherent test platform, vacuum-deposited OSCs are fabricated with various metal phthalocyanine donor materials and a fullerene acceptor. This is in contrast to the solution-processed OSCs that have been the focus of most OSC research since 2005. By removing complications in solution coating (especially film formation and phase separation considerations), it is significantly more straightforward to study photo-physics and charge collection behaviour. In this regard, the role of interfacial layers in charge extraction is investigated, the optimal combination/proportion of neat or mixed donor and acceptor layers in terms of the photo-active materials' properties is studied, and the impact of adding a third component to the mixed layer (i.e. ternary OSCs) is elucidated. The culmination of this work illuminates limitations in charge collection, especially in terms of the distribution of donor and acceptor material in the OSC (both in the bulk mixed layers and with regard to vertical distribution), as well as with variations made at the organic/electrode interface. The results provide guidelines to overcome device performance limitations that are pertinent for future research in both vacuum-deposited and solution-coated OSCs.

Having established a strong understanding of device performance in terms of device architecture, the variations in OSC performance and associated charge collection processes are studied as they change with time and under various stress conditions (e.g. light, heat, electrical). To this end, the most critical avenues toward hindered charge collection during the operation (light exposure) of OSCs are identified. To widen the impact and applicability of this research, a systematic study on degradation phenomena for both solution-coated polymer OSCs as well as vacuum-deposited small molecule OSCs is performed. Photo-degradation phenomena in terms of the OSC device architecture are also examined. It is shown that photo-induced degradation of the organic-electrode interface is the dominant degradation mechanism in all OSCs regardless of fabrication methodology, and that the prudent selection of interfacial layers can minimize these effects. A stronger understanding of charge collection processes in as-made and photo-degraded OSCs ultimately allows for intelligent device design to grant stable and highly efficient OSCs.

Acknowledgements

I wish to express deep gratitude to my supervisor, Professor Hany Aziz for his guidance, his sharp observations and, most critically, his kind words that served to motivate me through difficult experiments. His tireless assistance and insights were key driving forces that made this research possible. Hany, thank you for making my PhD such a productive, exciting and enjoyable experience.

I am grateful to all of my group members for their thoughts and wisdom throughout my PhD, especially Qi Wang, Afshin Zamani, Baolin Tian, Uyxing Vongsaysy, Sibi Sutty, Thomas Borel, Bin Sun and Mike Zhang. I am also incredibly thankful to Richard Barber, who helped me troubleshoot, upgrade and repair countless pieces of equipment throughout my PhD.

I would like to thank Dr. Richard Klenkler and Dr. Matthew Heuft from the Xerox Research Centre of Canada (XRCC) for helpful discussions regarding the research herein. Furthermore, most of the metal phthalocyanines used in this research were generously provided by XRCC, which allowed for many of the experiments to be possible.

Financial support to this work from the Natural Sciences and Engineering Research Council of Canada (NSERC) is gratefully acknowledged. I further acknowledge financial support through the NSERC Alexander Graham Bell Canada Graduate Scholarship, Ontario Graduate Scholarship, and WIN Nanofellowship.

Finally, the research in this thesis would not have been possible without the constant support, kindness and love of my wife, Kati Kalmar. Her infectious optimism, delicious home-cooked meals and sage advice were all the support that I needed to continue running my late night experiments, even in the face of finicky and complex device fabrication processes.

Contents

List of Figures

List of Tables

List of Abbreviations

AFM:	Atomic Force Microscopy / Atomic Force Microscope
BHJ:	Bulk Heterojunction
CTE:	Charge Transfer Exciton
EEL:	Electron Extraction Layer
EQE:	External Quantum Efficiency
FF:	Fill Factor
HEL:	Hole Extraction Layer
HOMO:	Highest Occupied Molecular Orbital
ICP:	Inductively Coupled Plasma
IPCE:	Incident-Photon-to-Carrier-Efficiency
IQE:	Internal Quantum Efficiency
IV:	Current-Voltage (e.g. characteristics)
I_{sc}:	Short Circuit Current
J_{sc}:	Short Circuit Current Density
JV:	Current Density-Voltage (e.g. characteristics)
LUMO:	Lowest Unoccupied Molecular Orbital
OLED:	Organic Light Emitting Diode
OPD:	Organic Photodetector
OPV:	Organic Photovoltaics
OSC:	Organic Solar Cell
PCE:	Power Conversion Efficiency
PHJ:	Planar Heterojunction
PL:	Photoluminescence
PM-HJ:	Planar-Mixed Molecular Heterojunction
PT-:	CF_4 Plasma Treated
R_s:	Series Resistance
R_{sh}:	Shunt Resistance
SM-OSC:	Small Molecule Organic Solar Cell
P-OSC:	Polymer Organic Solar Cell or Polymer Solar Cell
V_{oc}:	Open Circuit Voltage

XPS:	X-ray Photoelectron Spectroscopy

Chemical Names

Alq_3:	Tris(8-hydroxyquinolinato)aluminium
BAlq:	Bis(2-methyl-8-quinolinolate)-4-(phenylphenolato)aluminium
BCP:	bathocuproine
BPhen:	4,7-diphenyl-1,10-phenanthroline
DCV5T:	α,α'-Bis(2,2-dicyanovinyl)-quinquethiophene
FIrPic:	Bis(3,5-difluoro-2-(2-pyridyl)phenyl-(2-carboxypyridyl)iridium(III)
$Ir(mppy)_3$:	Tris[2-(p-tolyl)pyridine]iridium(III)
$Ir(piq)_3$:	Tris(1-phenylisoquinoline)iridium(III)
$Ir(ppy)_3$:	Tris(2-phenylpyridine)iridium(III)
Liacac:	lithium acetylacetonate
ITO:	indium tin oxide
NPB:	N,N'-bis(naphthalen-1-yl)-N,N'-bis(phenyl)-benzidine
P3HT:	poly(3-hexylthiophene-2,5-diyl)
Pc:	phthalocyanine
m-Pc:	metal phthalocyanine, metallophthalocyanine
	Also note: CuPc = copper phthalocyanine, ZnPc = Zinc Phthalocyanine, etc.
PCBM:	[6,6]-phenyl-C61-butyric acid methyl ester
PEDOT:PSS:	poly(3,4-ethylenedioxythiophene) poly(styrenesulfonate)
PEG:	poly(ethylene glycol)
PTCBI:	3,4,9,10 perylenetetracarboxylic bisbenzimidazole
PtOEP:	Pt(II) octaethylporphine
TAPC:	Di-[4-(N,N-ditolyl-amino)-phenyl]cyclohexane
TPBi:	1,3,5-tris(N-phenylbenzimiazole-2-yl)benzene
TPD:	N,N'-bis(3-methylphenyl)-N,N'-bis(phenyl)-benzidine

Chapter One:

Introduction

1.1. Background

Organic solar cells (OSCs) fall under the realm of second generation photovoltaics, which aim to surpass first generation silicon solar cell technology on the basis of reduced fabrication costs. The most significant cost reduction for OSCs is the use of aromatic hydrocarbon semiconductor materials that can be produced cheaply through batch reactor syntheses. Additional benefits for OSCs include: the potential for fully solution-processable devices, which may substantially reduce device fabrication costs; high material absorptivity, allowing for thinner films and reduced materials costs; and device flexibility, allowing for form-fitting solar cells. These benefits have resulted in extensive, widespread research on OSCs and, more recently, several companies focusing on the commercialization of OSCs. To this end, Heliatek, Mitsubishi and Solarmer have each announced OSCs with power conversion efficiencies (PCEs) greater than 10%.[1-3] These successes have relied heavily on the clever engineering of new organic molecules and polymers with enhanced spectral match to the sun's emission and with improved electrical properties.

In spite of their many successes, there remain a number of critical roadblocks to the effective commercialization of OSCs. These roadblocks relate to the inherently limited charge collection of OSCs

and their inadequate level of stability. OSCs generally employ a donor-acceptor configuration, where a donor material absorbs light and transfers a photo-excited electron to the acceptor material at a donor-acceptor interface. Correspondingly, donors are hole transport materials (easily oxidized) and acceptors are electron transport materials (easily reduced). The traditional approach to achieve good output properties in OSCs is the formation of a mixed donor-acceptor "bulk heterojunction" (BHJ) layer. With this structure, many donor-acceptor interfaces exist throughout the OSC for efficient charge separation, and the active layer can be made thicker than with a simple planar heterojunction (PHJ) structure, allowing for enhanced light absorption. A further description of this technology is provided in Section 1.2.2. Once free carriers have been generated, they drift to their relevant contacts where they are collected. Charge collection is largely hindered by the poor free carrier mobilities within the BHJ, but may also be limited by recombination of free carriers or by weak drift due to unoptimized contacts. Furthermore, charge collection within an OSC is shown to deteriorate with aging by ambient moisture/oxygen,[4-8] by light,[9-13] and by heat,[14, 15] which exacerbates the need for improved device architectures and stable solar cell materials.

This thesis focuses on gaining a better understanding of the limiting factors involved in charge collection for OSCs, especially in consideration of how these factors vary with time. This is accomplished by first bolstering the knowledgebase of the role of the standard OSC device architectures in charge collection/extraction. Having established the basic output performance of more traditional OSC structures, alternative (previously unstudied or poorly understood) device architectures are examined for their enhanced OSC properties. Finally, charge collection variations (and, as a consequence, variations in OSC output parameters) with device aging under several controlled experimental regimes are elucidated: light-stress, heat-stress, electrical stress and dark, all in inert N_2 atmosphere. A more complete overview of the organization of this thesis is provided in Chapter 2.

1.2. Organic Solar Cell Structures and Operation

1.2.1. Basic Device Operation

Since the early OSC research by Tang in 1986,[16] OSCs have largely comprised a donor and an acceptor to aid in the separation of photo-induced excitons into their constituent electrons and holes. The donor's lowest unoccupied molecular orbital (LUMO) is offset from the acceptor's LUMO such that transfer of electron from the donor to the acceptor is energetically favourable. The generation of electrical current in an OSC can be described in the following manner (illustrated in Figure 1-1.B, with a diagram of a simple OSC structure in Figure 1-1.A):

i. a photon enters the cell through its transparent contact
ii. the photon generates an exciton in either the donor or the acceptor
iii. the exciton diffuses to a donor-acceptor interface
iv. the electron is transferred to the LUMO of the acceptor (or the hole is transferred to the highest occupied molecular orbital (HOMO) of the donor if the exciton exists on the acceptor) to form a charge transfer exciton (CTE)
v. the CTE is further broken into a free electron within the acceptor material and a free hole within the donor material
vi. the free electron and free hole are collected at the cathode and anode respectively

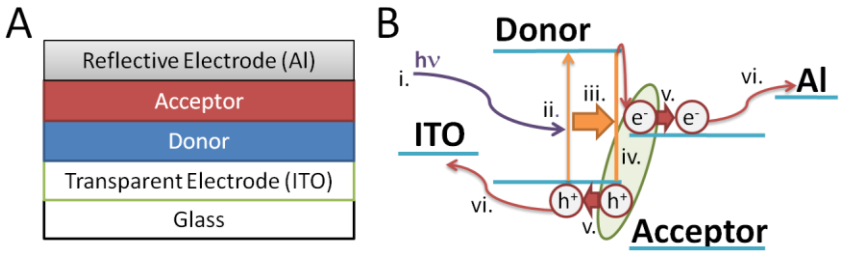

Figure 1-1 - A) Illustration of the device structure for a standard PHJ OSC B) Energy level diagram of the same and illustration of the charge collection process as detailed above.

In Tang's early work, copper phthalocyanine (CuPc) acted as the donor species to donate its electron to the 3,4,9,10 perylenetetracarboxylic bisbenzimidazole (PTCBI) acceptor in a PHJ configuration (thin layers of CuPc and PTCBI deposited sequentially). Aluminum was used as the cathode, and indium tin oxide (ITO) was used as the anode. While ITO and aluminum are still commonly used for OSC contacts, most OSC research has shifted toward fullerene derivatives for the acceptor species. Further, while some research still continues on CuPc, substantial research efforts have been dedicated to the synthesis of new donor species.[17-22] For polymeric OSCs, the most studied donor-acceptor system comprises a poly(3-hexylthiophene-2,5-diyl) (P3HT) donor and a [6,6]-phenyl-C61-butyric acid methyl ester (PCBM) acceptor.[23]

The efficiency limitations of OSCs are discussed further in Section 1.4; however, from the brief description of the OSC device operation above, researchers face a clear optimization problem:

> *In order to improve the absorption efficiency, one must increase the device thickness; however, increasing the device thickness hinders exciton diffusion and charge collection processes*.

Examining a PHJ OSC specifically, increasing the thickness of either the donor or acceptor layers serves to increase light absorption. However, it is unlikely that light absorbed deep in either the donor or acceptor material will generate an exciton that will successfully diffuse to the donor-acceptor interface to form free carriers. Instead, these excitons will largely undergo non-radiative recombination and the absorbed energy will be lost as heat. For example, one may use a 100 nm CuPc absorbing layer, but only excitons formed within 10 nm of a CuPc-PTCBI junction will yield photocurrent.[24]

1.2.2. Organic Solar Cell Device Architectures

Two common device architectures have been established to address the optimization problem discussed above: the tandem OSC and the BHJ OSC. In the case of the tandem OSC, multiple cells of

either the same or varied donor-acceptor material may be stacked on top of each other and separated by a 'recombination contact' or a tunneling junction. The goal of the tandem cell is to have a summative large device thickness for efficient absorption of light, while maintaining thin individual donor/acceptor layers for efficient diffusion/dissociation of excitons. Since a tandem cell is nearly the equivalent of multiple OSCs connected electrically in series, the output current is equal to that of the lowest current device, and the output voltage is the sum of the voltages of the individual cells. This effect is clear from the representative energy level diagram for a tandem device shown in Figure 1-2.A. Peumans and coworkers were among the first to study the multiple junction OSCs, and wrote an exhaustive review on the topic.[24]

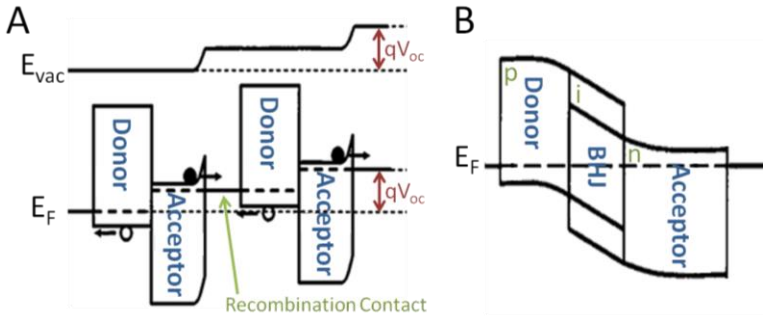

Figure 1-2 - Energy level diagram of A) the tandem device structure with PHJ sub-cells B) the 'p-i-n' device structure with a pure donor 'p' layer, a BHJ 'i' layer and a pure acceptor 'n' layer. Figures adapted from [24] and [26] with permission.

For the BHJ OSC, the donor and acceptor species are mixed together, such that many donor-acceptor interfaces exist throughout the light absorbing layer. The ideal BHJ active layer consists of phase-separated domains of pure donor and pure acceptor material, with domain sizes equal to the materials' respective exciton diffusion lengths. The BHJ may be made thick to increase the amount of light absorbed while allowing excitons to separate at the innumerable donor-acceptor interfaces. Unfortunately, the BHJ also introduces a number of morphological complications that have remained the basis of much of the OSC research for the past decade. Specifically, it is very difficult to form, in a controlled and reproducible manner, phase-separated donor and acceptor layers with the ideal domain size. It is further difficult to form an interpenetrating network of donor and acceptor phases, such that

there are no 'dead ends' – free carriers must be able to traverse the thickness of the film to be collected at the relevant electrodes. Finally, since the mobility of free carriers within the BHJ is reduced compared to the pure materials, it is more difficult to achieve OSCs with low R_s values.

For vacuum-deposited OSCs, the BHJ concept can be further extended to a 'p-i-n' architecture (analogous to the 'p-i-n' architectures used in amorphous silicon solar cells) with a BHJ 'intrinsic' layer. Maennig and coworkers implemented this idea with hole- and electron-doped 'p' and 'n' organic layers.[25] In contrast, Xue and coworkers employed 'p' and 'n' layers of pure donor and acceptor materials respectively (as illustrated in Figure 1-2.B), which they named the 'hybrid planar-mixed molecular heterojunction' (PM-HJ).[26]

The highest efficiency solar cells developed by Solarmer and Heliatek rely on a combination of these two common device architectures.[1, 3, 27] To this end, the researchers fabricate two BHJs with different donor/acceptor combinations to absorb light strongly over the entire visible spectrum. They then stack these BHJs in tandem configuration, separating them with either a thin metallic nanoparticle layer or a heavily doped organic recombination contact. While this approach allows for efficiencies above 10%, device fabrication is also incredibly complex and will inevitably hinder future large-scale manufacturing efforts. It is thus important to gain a better understanding of device physics of current device structures to isolate performance limiting factors and to ultimately develop simple-fabrication, high-efficiency OSCs. It is further important to study new device architectures, such as the ternary mixture OSC and the cascade OSC, which can potentially achieve similar efficiencies with much simpler device structures.

1.2.3. Interfacial Extraction Layers

In addition to optimizing the structure of the bulk of the OSC, substantial efforts have been made to optimize the contacts of OSCs for enhanced carrier extraction. This task is frequently

accomplished through the use of interfacial extraction layers, which are deposited between the active organic layers and the relevant electrodes. Depending on their location in the device, these interfacial layers can be classified according to their functionality as (i) hole extraction layers (HELs), and (ii) electron extraction layers (EELs)). An ideal extraction layer serves three purposes:

- to better align the work function of the contact to either the HOMO or the LUMO of the organic material of interest
- to offer hole- or electron-specific carrier selectivity and reduce the interfacial trap density, thereby reducing the probability of free carrier recombination and enhancing the charge extraction capabilities of the contacts
- to provide improved photo-stability, thermal stability and ambient (oxygen/moisture) stability

Commonly used HEL and EEL materials include poly(3,4-ethylenedioxythiophene) poly(styrenesulfonate) (PEDOT:PSS)[28-30] and MoO_3[11, 31] for HELs, and LiF,[8, 32] Cs_2CO_3,[33, 34] TiO_x[31, 35, 36] and ZnO[37, 38] for EELs – the latter two materials are usually used in inverted solar cells, where the top electrode serves as the hole-extracting electrode.

It is also worth noting an additional organic-cathode interfacial layer for vacuum-deposited small molecule OSCs (SM-OSCs), which is commonly used to satisfy two alternative roles:

- to block both excitons and free holes from diffusing toward and recombining at the cathode
- to prevent damage to the organic layers during deposition of the metal cathode

The most common interfacial layer employed for this purpose is bathocuproine (BCP),[39, 40] although researchers have recently investigated 1,3,5-tris(N-phenylbenzimiazole-2-yl)benzene (TPBI),[41] and 4,7-diphenyl-1,10-phenanthroline (BPhen).[42]

1.3. Solar Cell Output Characteristics and Circuit Model

A solar cell under light exposure may be modeled as a current source. Due to the nature of exciton dissociation and carrier collection, an efficient solar cell is also a rectifying device. Furthermore, some resistances, R_{series} (R_s) and R_{shunt} (R_{sh}), must also be considered due to non-idealities in the device structure and operation. R_s occurs due to the contact resistances between the electrodes and the organic semiconductor, as well as the resistance throughout the bulk of the active layers and the resistances of the electrodes themselves. R_{sh} is generally included due to leakage current and recombination current within the device. The corresponding solar cell has the following current-voltage characteristic, with an equivalent circuit model shown below in Figure 1-3:

$$I = -I_{ph} + I_0\left(\exp\left[\frac{V+IR_s}{nV_{th}}\right] - 1\right) + G_{sh}(V + IR_s) \qquad \textbf{(1.1)}$$

Since this is a transcendental equation, solutions can be obtained and solar cell parameter extraction can be performed through numerical methods. Many different approaches to solar cell parameter extraction have been established, several of which have been reproduced in MATLAB for the purpose of this thesis work (discussed in **Appendix 2.2**).

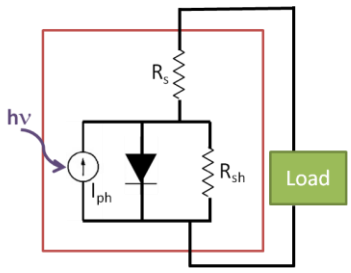

Figure 1-3 - Equivalent circuit model for an OSC.

Comparisons among solar cells are generally made in terms of their power conversion efficiencies (PCE or η_{PCE}), which refer to the amount of useful electrical energy produced as a function of input optical power. Other notable solar cell parameters include:

- I_{sc}/J_{sc}: short circuit current/short circuit current density – the measured current of the illuminated OSC when the voltage across the OSC is zero
- V_{oc}: open circuit voltage – the voltage across the illuminated OSC when the measured current is zero
- FF: fill factor – the ratio of the 'actual' maximum output power to the 'possible' maximum power (where there are no losses due to R_s and R_{sh}, and the OSC is a perfect rectifier). The FF is thus a measure of the OSC's closeness to an ideal solar cell, and is defined as:

$$FF = \frac{V_m I_m}{V_{OC} I_{SC}} \ , \qquad \textbf{(1)}$$

where V_m and I_m are the voltage and current values at the maximum power point

- η_{EQE}: external quantum efficiency (EQE) – the number of carriers collected per number of photons impingent on the solar cell at a given wavelength of interest. This quantity may also be referred to as the incident-photon-to-carrier efficiency (IPCE), and is defined as:

$$IPCE = EQE = \eta_{EQE} = \frac{hc \cdot I_{sc}(\lambda)}{e\lambda \cdot P(\lambda)} \ , \qquad \textbf{(2)}$$

where h is Planck's constant, c is the speed of light, I_{sc} is the wavelength-dependent short circuit current, e is the charge of an electron, λ is the wavelength of light and P is the wavelength-dependent light intensity.

- η_{IQE}: internal quantum efficiency (IQE) – the number of carriers collected per number of photons absorbed by the active organic semiconductor. This factor excludes optical losses due to reflection: $\eta_{EQE} = (1 - R)\eta_{IQE}$, where R is the reflectivity of the substrate-air interface.

In terms of the above quantities, the PCE may be found as: $PCE = \frac{FFV_{OC}I_{SC}}{Input\ Optical\ Power\ (W)}$ **(3)**.

1.4. Efficiency Limitations and Sources of Energy Loss in Organic Solar Cells

Before addressing the advanced device architectures to be studied in this thesis work, it is worthwhile to examine the efficiency limitations with the common device structures detailed in Section 1.2. IQE is typically defined in terms of four efficiencies:[43]

$$\eta_{IQE} = \eta_A \eta_{ED} \eta_{CT} \eta_{CC} \,, \qquad (4)$$

with η_A = efficiency of absorption of light,

η_{ED} = efficiency of exciton diffusion to a donor-acceptor interface,

η_{CT} = efficiency of charge transfer – dissociation of an exciton into electron/hole,

η_{CC} = efficiency of charge collection at the relevant electrodes

1.4.1. Absorption Efficiency Limitations

η_A is associated with the material absorptivity (both the strength and specific spectral region of absorbance), as well as the thicknesses of the individual layers of the OSC. As noted previously, increasing the thicknesses of the donor and acceptor layers can result in stronger absorption of light, thus increasing η_A. Further, the thickness can be increased without sacrificing η_{ED} through the use of tandem devices and BHJ active layers. Also noted previously, numerous researchers have sought new active layer materials with wider absorption bands,[17-22] especially to achieve absorption in the near-infrared regions.

It should be noted that OSCs with multiple layers, especially tandem devices, offer additional complications to light absorption due to the partial reflections of light and its constructive/

deconstructive interference. To this end, when incorporating a larger active layer thickness into a given OSC, the peak optical field may be shifted to regions that do not contribute to photocurrent (e.g. within the transparent conductor or an interfacial layer). In order to take these factors into effect, several groups have applied transfer matrix formalism to find the light intensity distribution throughout stacked thin films and full OSC structures.[44, 45] Such methodologies have been reproduced in MATLAB to aid in understanding the work completed in this thesis and are provided in the Supplemental Information (**Appendix 2.3**).

1.4.2. Exciton Diffusion Efficiency Limitations

Due to the low level of order in organic films, exciton diffusion is essentially a 'random walk' process dictated by Fick's laws of diffusion. The movement of the exciton is accomplished by energy transfer mechanisms, of which two processes dominate: Förster resonance energy transfer (FRET) and Dexter energy transfer. Förster energy transfer typically occurs over a longer distance (1-10 nm, with efficiency decreasing as r^{-6}) due to dipole-dipole interactions. Further, for efficient Förster energy transfer, there must be substantial overlap of the emission/absorption spectra of the involved species. In contrast, Dexter energy transfer involves the direct exchange of electrons and occurs over a very short distance (<1 nm). While this process does not require overlap of emission/absorption spectra, it does require strong overlap of the molecular orbital wavefunctions of the involved species.

As noted in Section 1.2, exciton diffusion is strongly associated with the device structure. In general, one strives for a donor-acceptor interface spaced one to two exciton diffusion lengths apart. This allows for dissociation of the exciton into a free hole and a free electron before it recombines. Traditionally, this has been accomplished with tandem structures and the BHJ active layer.

1.4.3. Exciton Dissociation Limitations

In early OSC research, Van Hal and coworkers observed ultra-fast exciton energy transfer from thiophene donors to fullerene acceptors to occur on a timeframe of ~95 fs, with subsequent dissociation into a CTE (Figure 1-1.B, step iv) over ~10 ps.[46] In order to generate free electrons and holes, it is necessary to further break apart the CTE. By modelling the CTE with a single electron Hamiltonian for a hydrogenic atom, Muntwiler and coworkers have shown that several CTE states may be present and only 'hot' CTE states can be easily separated into free electrons and holes.[47] In spite of this, dissociation of CTEs into free carriers has generally been observed to occur with much higher probability than predicted. Researchers have suggested that the separation of excitons is field assisted,[48, 49] and that a dipole layer present at the donor-acceptor interface may further aid dissociation of the CTE.[50] Using transient photocurrent measurements, some researchers have held that CTE recombination is not of substantial concern when carriers are being transported across the cell[51] – i.e. when the cell is carrying current.[52] While this rule generally holds true it should be noted that, in certain material combinations, relaxation of the CTE to the lowest triplet excited state has been observed and can contribute to substantial recombination current.[53, 54] Furthermore, for new low bandgap polymers, low CTE lifetimes (and thus low CTE dissociation probability) due to unfavourable morphologies of donor and acceptor are believed to be a limiting factor toward the FF and PCE.[55]

CTEs further play a critical role in an OSC's output parameters: the V_{oc} is dictated by the effective bandgap of the CTE. qV_{oc} may be approximated as E_g(CTE) - ~0.4 eV, where the 0.4 eV loss is attributed to Coulombic exciton binding energy, energy level pinning at the organic-electrode contacts and spread in energy levels due to general disorder in the organic films.[54] Several researchers have also observed absorption, photoluminescence (PL) and electroluminescence corresponding to the binding energy of the CTE.[56, 57] It has since been suggested that ideal OSCs may obtain maximum V_{oc} when

charge generation due to light absorption is balanced with radiative recombination of the CTE. As such, in order to approach the thermodynamic limit for V_{oc}, one must reduce all other forms of leakage/recombination current. In terms of macroscopic parameters, one must minimize the reverse saturation current density (J_0) by improving charge collection,[58] as discussed below in Section 1.4.4.

1.4.4. Charge Collection Limitations

When considering simple PHJs, η_{CC} is typically close to unity.[43] It is logical that, given an electric field maximum of $V_{built\text{-}in}/t_{organics}$ (on the order of ~MV/m), any free carriers will quickly and efficiently drift toward the contacts. However, this simplistic approach is not valid for BHJ active layers, which may have unoptimized morphology and dead ends in either the donor or acceptor material resulting in eventual carrier recombination. As noted in Section 1.2, it is necessary to obtain interpenetrating networks of donor and acceptor phases in a BHJ. Furthermore, as OSCs draw nearer to commercialization, thicker active layers will necessarily be used to improve yields during scale-up. As device thicknesses increase, charge collection will rapidly become a limiting factor in OSC efficiency.

There are several key limitations toward charge collection in OSCs, including:

- high contact resistance, high resistivity of the electrode or poorly matched electrode work function, which can all result in charge accumulation at the electrodes
    - This limitation is usually obvious from the OSC current-voltage (IV) characteristic, which shows double-diode 'S-shape' behavior.[59, 60]
- bimolecular recombination
    - Linear scaling of photocurrent with light intensity has historically been quoted as a disproof for bimolecular recombination in BHJ OSCs; however, this is not always a valid stipulation. Due to the phase separated domains of donor and acceptor, bimolecular recombination is dictated only by the slowest carrier.[61] For standard

OSCs with thick active layers, illumination through ITO results in a shorter average distance for holes to travel and a longer average distance for electrons to travel (for thinner films, optical interference effects can play a large role in peak optical field intensity). Depending on the slowest carrier in the OSC, this can either reduce or exacerbate bimolecular recombination. In the case of P3HT:PCBM, bimolecular recombination is more with illumination from the opposite electrode, especially with thicker films.[62] Further, recent studies have suggested that bimolecular recombination can occur even with an observed linear scaling of photocurrent with light intensity,[63] and models employing bimolecular recombination as the principle recombination mechanism have shown tremendous predictive power.[64, 65]

- traps within the bulk of the active OSC layer
    - This limitation can lead to an accumulation of trapped charges, which can distort the electric field within the OSC active layers to hinder charge collection.[66] Trap-assisted recombination of free carriers through sequential trapping of holes or electrons has been suggested as a significant source of recombination current. To this end, trap-assisted recombination occurs when devices show linear scaling of photocurrent with light intensity, and models employing the Hecht expression (which described charges collected versus charges trapped in terms of the carrier mobility-lifetime product) have been used to fit output characteristics for BHJ OSCs over a wide range of light intensities.[48]

From this discussion it is clear that, given the current device architectures, charge collection is one of the most significant limiting factors toward high efficiency OSCs. By minimizing charge recombination, it is possible to strongly improve the FF of OSCs.[67] Further, with enhanced charge transport properties, the active layers can be made thicker to absorb more light and to improve J_{sc}. It is

the goal of this thesis to offer insights toward improving upon the charge collection limitations in both fresh OSCs and OSCs that have been exposed to some external stress (e.g. photo-aged OSCs).

1.5. The Role of Device Structure for Enhanced Charge Collection

Since 2005, the vast majority of OSC research has focused on binary (donor-acceptor) BHJ structures in both polymer OSCs (P-OSCs) and SM-OSCs. As described in Section 1.4, the BHJ structure suffers from a number of efficiency limitations and trade-offs. Furthermore, very high efficiency OSCs have largely focused on tandem device structures, which involve tremendous device complexity. To this end, optimization of both sub-cells to achieve matched photocurrents generally requires optical spacers and a high level of process control. If one sub-cell provides less photocurrent at any point throughout the lifetime of the tandem OSC, any gains to efficiency will be lost and the device will inevitably suffer from charge accumulation effects to negatively impact device stability. As discussed below, alternative approaches may exist to provide enhanced charge collection while obtaining the same principal goals as the tandem structures and/or with substantially simplified device structures.

1.5.1. Fullerene-based Schottky Organic Solar Cells

While a large portion of OSC research has been geared toward more complicated device architectures, such as the tandem approach, a simple variant of the basic BHJ structure has recently garnered interest in the organic photovoltaic (OPV) community for its high performance and unique photovoltaic properties. The fullerene-based Schottky OSC has been responsible for the best performing vacuum-deposited (single cell) OSCs to date,[68-70] with efficiency values on the order of 8% – on par with the highest performing solution-coated (single cell) OSCs. This device structure is an offshoot of the simple BHJ, with two minor addenda:

- the mixed layer contains high fullerene content (e.g. at least 1:3 donor:acceptor content)
- the anode has a very deep work function

To achieve the latter goal, it is common to employ an ITO/MoO_3 contact, which has been demonstrated to have a work function as deep as 6.8 eV.[71] The formation of the MoO_3/C_{60} interface results in extensive band bending in the C_{60} layer, as shown in Figure 1-4.A, such that a simple MoO_3/C_{60} (single layer) OSC can generate a few mA/cm^2 of current and a V_{oc} of 1.3 V, albeit with a very poor FF.

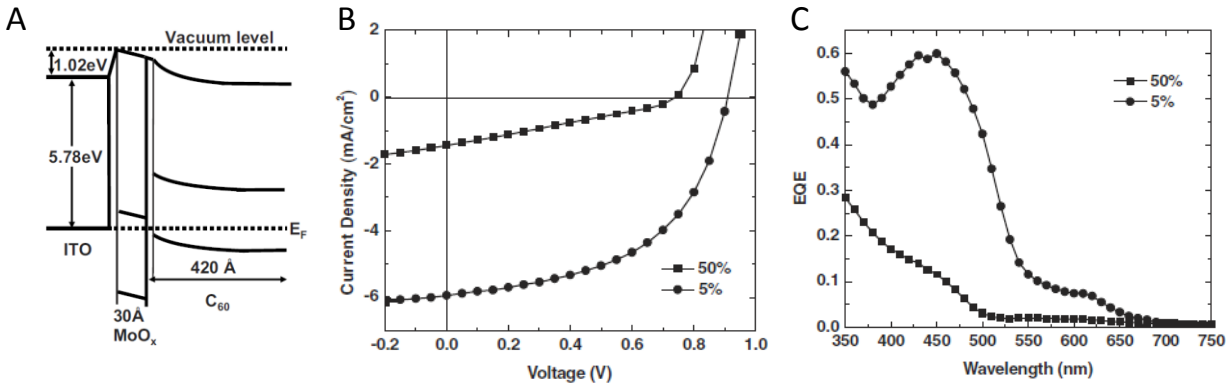

Figure 1-4 - A) Energy level diagram of an ITO/MoO_3/C_{60} interface. B) JV characteristics of TAPC:C_{60} Schottky (5% TAPC) and simple BHJ (50% TAPC) OSCs. C) EQE spectra of the devices from B. Figures re-used from [42] and [71] with permission.

Adding a small amount of donor to the C_{60} layer (analogous to depositing a BHJ with low donor content) generates OSCs with significantly improved J_{sc} and FF values, while still retaining high V_{oc} values.[42, 72, 73] In fact, depending on the chosen donor material, the improvement in performance can allow for OSCs with substantially improved performance over the standard 1:1 donor:acceptor BHJ, as shown in Figure 1-4.B. The J_{sc} improvement has been attributed to the photocurrent contributions from the donor, and more significantly due to photocurrent from strongly bound intermolecular CTEs present in C_{60} aggregates, shown at 450 nm in Figure 1-4.C.[42, 72] The improvement in FF is due to reduced charge accumulation and space charge effects with the presence of the donor. The V_{oc} typically remains at some intermediate value between 1.3 V (defined by band bending effects), and the V_{oc} value of the simple BHJ (defined by the donor-acceptor CTE bandgap). Compared to the simple BHJ, the fullerene-based Schottky OSC thus provides improved J_{sc} values, due to fullerene (especially with C_{70}) contributing

strongly to photocurrent, comparable FF values and strongly improved V_{oc} values. More critically, these improvements are achieved with virtually no added device complexity since MoO_3 is a common HEL and the mixed BHJ layer only needs to be adjusted slightly in donor:acceptor mixing ratio. Since the fullerene-based Schottky OSC structure is a relatively new development in the OPV community, there are a number of details regarding its operation that must still be elucidated, especially in consideration of its charge transport characteristics and how they vary with time.

1.5.2. Ternary Organic Solar Cells

Ternary mixtures in the BHJ may be a feasible and simpler alternative to tandem cells to enhance the spectral coverage of OSCs. In a ternary OSC, an additional component is added to the traditional BHJ mixture of donor and acceptor to improve the range of light absorption. Due to thermalization losses of photogenerated carriers, this device structure may not achieve the same levels of efficiency as optimized tandem devices; however, proper materials selection can allow for gains over traditional binary OSCs. The ternary mixture BHJ has gained some interest in the past few years with solution-coated P-OSCs, including both systems with additional donors,[74-84] and with additional acceptors. [85-88] It is worth noting that this is a virtually unstudied field in vacuum-deposited SM-OSCs. While the results from literature have been generally positive, allowing for enhancement of the EQE and J_{sc}, there are some notable limitations to the ternary BHJ. The most significant limitation relates to the morphology of the ternary mixture, where a third component can adversely affect the phase separation of the original two components and thus degrade device performance. For this reason, the vast majority of research uses small percentages of the third component, on the order of 1 to 10 weight percent. The second limitation concerns the energy alignment of the third component, which should have a HOMO and LUMO positioned between that of the original donor and acceptor materials to avoid deterioration of the V_{oc}. It should be noted, however, that violation of this rule does not necessarily

imply that the OSC will provide the lowest V_{oc} set by the HOMO/LUMO values of the constituent species – Khlyabich and coworkers have shown that the V_{oc} can be tunable between the two values set by the pairs of donor/acceptor.[87, 89] In spite of the recent successes with ternary OSCs in literature, it is difficult to disentangle the variations in performance due to changes in morphology (especially changes in phase separation of donor and acceptor) versus changes owed to the optoelectronic properties of the third component. It is necessary to better establish the origin of enhanced output properties in the ternary OSC, such that materials can be chosen appropriately to ensure efficient charge transport in the energetically muddled three-component mixed layer.

1.5.3. Cascade Organic Solar Cells

Building off of the concept of multiple donors or acceptors for enhanced light absorption, several groups have investigated energy cascade OSCs.[90-93] In principle, this technology aims to achieve the same goal as ternary cells: add additional species to grant efficient absorption over a wider range of wavelengths. The difference in this approach is that excitons are transferred across multiple neat donor or acceptor layers to the donor-acceptor interface by energy transfer mechanisms (i.e. Dexter and Förster energy transfer). An example cascade donor structure is shown in Figure 1-5.

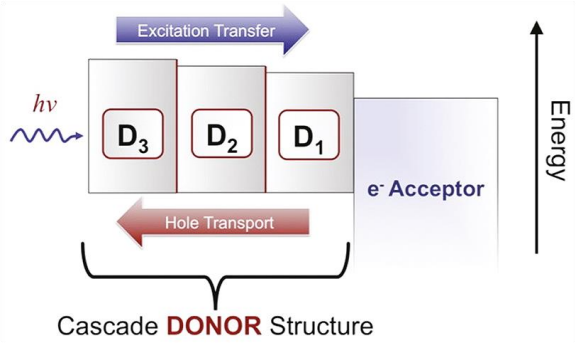

Figure 1-5 - Illustration of the cascade OSC concept with three complementary donors. Figure re-used from [91] with permission.

Since cascade OSCs can employ much simpler PHJ structures while potentially absorbing light strongly over a wide range of wavelengths, many of the efficiency limitations associated with charge

collection, as discussed throughout Section 1.4, can be avoided. The primary limitations to this technology are then the strict energy level requirement for the comprising materials and, correspondingly, the few qualified small molecules available that can be implemented without materials deposition or processing difficulties. In the early demonstrations of this structure, the secondary donor was used primarily as an inter-layer at the donor-acceptor interface with a thickness of ~10 nm.[90, 92, 93] Schlenker and coworkers expanded upon the cascade OSC concept to have multiple, thick donor layers, but achieved only meagre efficiencies due to the relatively ineffective donor materials.[91] More recently, Griffith and Forrest developed an optimized cascade OSC, with the donor materials chosen very carefully to have perfectly aligned energy levels, which was demonstrated to be capable of 7.1% PCE.[94] Cnops et al. further expanded upon the cascade structure, using multiple acceptors (subphthalocyanine (SubPc) and subnaphthalocyanine (SubNc)) instead of multiple donors, to achieve impressive efficiencies up to 8.4%.[95] The cascade architecture, with its simplistic device structure without the need for mixed donor:acceptor layers, is thus exceptionally promising for cheap and high efficiency OSCs. To this end, the cascade OSC merits further study, especially with materials that are both cost-effective and simple to deposit, such as metal phthalocyanines (m-Pcs) that have been the cornerstone of much of the initial OSC research efforts.

1.6. Charge Collection Variations with Device Aging

OSCs have improved in efficiency immensely in the past decade, offering competitive PCE values and, accordingly, drawing a more recent focus on their potential commercial applications. In line with this focus, there have been increasing research efforts toward their stability, especially since OSCs must compete with entrenched silicon photovoltaic technologies that are known to have lifetimes in excess of 25 years.[96] To this end, there are now numerous studies on the ambient stability of OSCs that have shown moisture and oxygen to have deleterious effects on both the photo-active layers and the contact

electrodes,[5, 7, 97-100] including several reviews on this topic,[4, 96, 101, 102] and an extensive inter-laboratory OSC stability research effort.[103-106] The motivation for such studies arose naturally since most OSCs are required to be tested in a dry, inert atmosphere (or otherwise encapsulated) in order to make good, reproducible electrical measurements. While a great deal of knowledge has been gleaned regarding the potential avenues toward ambient-induced degradation of OSCs, there yet remain many unknowns regarding OSC degradation mechanisms in inert environment, with generally fewer systematic studies completed in inert atmosphere.[11-13, 15, 107-109] Studying the intrinsic photo-stability and thermal stability of OSCs individually (i.e. in the absence of species that serve to chemically alter the photo-active layers) is of particular interest, as it provides a more rigorous understanding of the physical processes involved in the decrease in PCE values under regular OSC operation. If specific materials or device configurations are found to be photo-unstable in an inert environment, it follows that they would degrade at least as fast or potentially faster under ambient test conditions. Furthermore, it is interesting to examine what aspect of light irradiation under regular operation is a dominant factor in altering the charge extraction properties of OSCs (e.g. light-induced heating vs. photo-chemical effects vs. electrical current effects). With a better understanding of how a particular OSC degrades, one may devise strategies that specifically target inadequacies, whether they are related to bolstering the stability of the constituent materials or employing alternative device architectures.

From the discussions in Section 1.4 and 1.5, charge transport and charge collection within the bulk/photo-active layer of the OSC can be considered a major limiting factor toward high efficiency devices. In contrast, when considering how charge transport varies with time, the organic-electrode interface has been established as a weak point and a common point of failure for organic electronic devices in general.[110, 111] In an extensive ambient stability study, the ISOS-3 inter-laboratory collaboration examined seven sets of OSCs from research labs around the world, finding that that degradation at the organic-electrode interface is the primary cause for immediate, significant reductions

in efficiency.[103-106] Earlier work by Jorgensen and coworkers supports this claim, noting strong chemical degradation of the metal electrode and further degradation associated with the commonly used PEDOT:PSS HEL.[7] It is thus logical that research has begun toward the implementation of specialized extraction layers to improve OSC stability in addition to satisfying the remaining criteria established in Section 1.2.3. Krebs and coworkers observed a reduction in ambient O_2/H_2O degradation with the use of a C_{60} EEL.[112] Hayakawa and coworkers employed a TiO_x EEL as a barrier to physical damage and chemical degradation.[36] Kawano and coworkers used a stacked C_{60}/LiF EEL to enhance device lifetime, attributing improvements to better alignment of the electrode work function with the LUMO of their active organic species.[10] Kanai and coworkers made use of a MoO_3 HEL to substantially improve device photo-stability, primarily due to added stability in the V_{oc} of the OSC.[9] Voroshazi and coworkers even noted the potential for inter-electrode degradation due to the likely release of moisture from a PEDOT:PSS HEL and subsequent chemical interaction with the low work function cathode.[11] Furthermore, researchers have recently focused on inverted OSCs,[113] which typically exhibit improved stability by eliminating the need for a low work function/reactive metal and replacing it with a low work function transport layer (EEL) such as ZnO and TiO_x.[114, 115] With the development of countless new interfacial extraction layers for use in OSCs,[116-119] there are many uncertainties regarding their effect on stability and device lifetime, especially in consideration of the many other experimental variables in the OSC, such as the device structure (e.g. BHJ vs. Schottky), the comprising materials or even the method of fabrication (e.g. solution-coated vs. vacuum-deposited OSCs). For OSCs to become market-ready, a more thorough and coherent understanding of degradation mechanisms must be established, especially in consideration of the OSC device structure and the interfacial extraction layers that may be employed.

Chapter Two:

Thesis Overview

2.1. Research Objectives

This thesis examines charge transport and charge collection limitations in OSCs, especially as they vary over time and under light exposure. In consideration of this research focus, the objectives are detailed below alongside principal questions to be addressed in the corresponding research. The major findings of this work, and thus the answers to these questions, are provided in the conclusions in **Chapter 11**.

- to obtain a more robust understanding of charge collection limitations in modern OSCs
    - in consideration of structural components, especially the interfacial layers
        - What defines a good interfacial extraction layer, and how does its selection impact charge collection? What materials are specifically interesting for efficient, stable OSCs?
    - in consideration of standard device architectures
        - What are the limiting factors in charge collection and thus the performance of PHJ, BHJ and PM-HJ OSCs? Which device structures suffer from charge

accumulation or recombination effects, and how can these effects be addressed? Which device structure offers optimal charge collection properties?

    - in consideration of advanced device architectures
        - Can the ternary or cascade architectures be used to enhance the performance and charge collection properties of OSCs? What are the major limitations, in terms of charge transport, toward the successful use of these device structures?

- to obtain a comprehensive understanding of OSC performance variations with time in inert atmosphere (intrinsic stability)
    - tested under dark, heat, light and electrical stress conditions
        - What is the major contributor to changes in OSC performance? Are photo-induced changes in OSC performance related to associated heat or electrical stresses, or are they primarily due to photo-chemical changes?
    - considering both P-OSCs and SM-OSCs
        - Do vacuum-deposited and solution-coated OSCs show significant similarities or differences in major degradation pathways? How are charge collection processes affected in both systems as they are exposed to light or heat?
    - considering both interfacial and bulk degradation effects
        - Is the interface or the bulk organic material more strongly affected under regular operation of an OSC (i.e. exposed to 1-sun intensity light)? Does the device architecture affect possible degradation pathways? What approaches can be employed to help minimize degradation phenomena?

This thesis is therefore structured in such a manner that the reader first obtains a rigorous understanding of the device physics and performance limitations of modern OSCs. Using this knowledge, the reader can then appreciate the variations in OSC performance over time.

2.2. Organization of Content

Experimental details for the work completed in this thesis are provided in **Chapter 3**. To make relevant and impacting conclusions, two materials systems are studied, with the rationale for this materials selection provided in **Chapter 4**:

- Solution-coated P-OSCs, based on the ubiquitous P3HT:PCBM materials system
- Vacuum-deposited SM-OSCs, based on m-Pc/fullerene materials systems (especially chloroindium phthalocyanine (ClInPc), chlorogallium phthalocyanine (ClGaPc) and SubPc)

By maintaining a consistent materials system throughout this thesis, a systematic understanding of the limitations in charge collection in modern OSCs is obtained. As a point of terminological clarification, in chapters or sections where only one fabrication methodology is employed (only vacuum deposition or solution coating), the general term 'OSC' is used. For chapters where cross comparisons are made among the device fabrication methodologies, the devices are explicitly denoted as SM-OSCs or P-OSCs. **Chapter 4** also provides a working understanding of the Schottky device architecture as it compares to the standard BHJ structure.

Having established the materials system of interest, a rigorous study of charge transport and charge collection in OSCs at time zero is conducted. To aid in this understanding, both the interfacial extraction layers (between the electrodes and the organic layers) as well as the overall device structure (the bulk of the device) are considered. As described in **Chapter 1**, the interfacial extraction layers are critically important in achieving high efficiency OSCs, as they help to align the work functions of the contacts with the energy levels of the active materials. This point is further emphasized in **Chapter 5**, where the subtleties regarding the use of various EELs and HELs are elaborated. Naturally, the overall device structure is also decisive in the performance of OSCs, with the bulk layers dictating charge transport and, as a consequence, playing a major role in charge accumulation or charge trapping effects.

This topic is discussed at depth in **Chapter 6**, where all relevant combinations of neat donor, neat acceptor and mixed donor-acceptor layers are implemented into OSCs and studied. This chapter allows for the identification of an ideal device structure for high efficiency OSCs in consideration of charge transport and charge extraction limitations. With a more robust understanding of the basic operational behavior of the standard OSC structures, more advanced device architectures are studied in **Chapter 7**. This chapter focuses primarily on the ternary mixture OSC and offers some additional insights regarding the cascade OSC.

With the time-zero device behavior well established, charge transport and charge extraction variations with time are examined, specifically for OSCs exposed to 1-sun intensity irradiation or heat (corresponding to the temperatures that OSCs reach during regular operation). As with the time-zero studies, this work focuses on two major aspects of the OSC structure. Specifically, light-induced variations at the organic-electrode interfaces are considered, as well light-induced changes in the bulk (organic photo-active layers) of the device. **Chapter 8** and **Chapter 9** address light-induced interfacial variations, which are found to be a dominant degradation mechanism accounting for most of the loss in OSC performance with time. **Chapter 10** examines bulk effects that are more visible once the interfacial degradation effects are minimized, especially photo-induced changes in OSCs that employ high C_{60} content. This chapter specifically examines the photo-stability of the newly discovered fullerene-based Schottky OSC as it compares to the standard BHJ device structure.

Chapter Three:

Experimental Procedures

3.1. Overview of Device Geometry

Two device geometries are employed for OSC fabrication, as shown in Figure 3-1 below. The two geometries are classified as 'large' and 'small' for the 10-device substrates and 3-device substrates respectively.

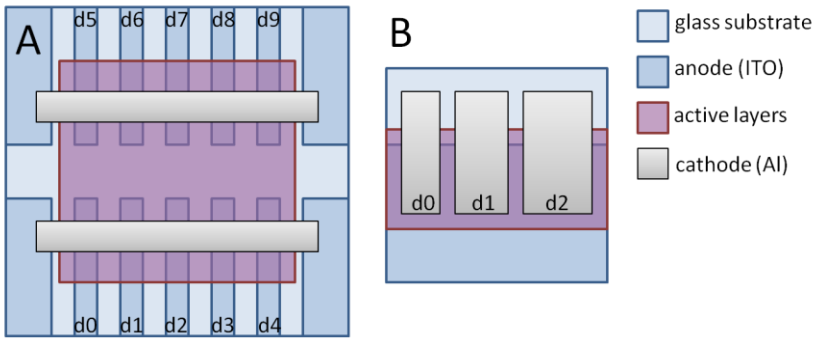

Figure 3-1 - Illustration of device geometry for A) large substrates (5 cm X 5 cm) and B) small substrates (1.4 cm X 1.4 cm)

For the large substrates, all individual devices are 4 mm by 5 mm in size. This is the primary device geometry that is used throughout this research. A cathode strip extends over the active organic layers and contacts side ITO pads. This eliminates issues associated with scratching the metal since devices can be repeatedly tested by contacting only ITO pads. In the studies detailed throughout this thesis, comparisons are generally made among devices made on the same large substrate and in the

same deposition run. For example, donor:acceptor OSCs with varying mixing ratios (3:1, 1:1, 1:3 and 1:7) can easily be fabricated in duplicate with the same extraction layers/cathode on the same substrate. This approach greatly reduces substrate-to-substrate variation, simplifies comparisons among devices and allows for easy identification of variations in charge transport or charge extraction, which is critically important to the present research (especially for observing variations with time).

The smaller substrates have devices of varying dimensions, with d0=5 mm by 2 mm, d1=5 mm by 2.5 mm and d2=5 mm by 3.5 mm. As such, the smaller substrates are particularly well suited to testing variations in device performance with device area. Their smaller size also makes them well suited for rapid and efficient OSC fabrication by solution coating, since many different spincoating recipes can be completed with a small amount of solid material.

3.2. Materials

Unless stated otherwise, materials are purchased from Sigma Aldrich and used as received. Patterned ITO slides are purchased from Luminescence Technology Corp. With the exception of SubPc, all m-Pcs are obtained from the Xerox Research Centre of Canada, where they are also purified by train sublimation. Sublimed SubPc and BCP (>99% pure) are obtained from Luminescence Technology Corp. Electronic grade regioregular P3HT is obtained from Sigma Aldrich. Purified $PC_{60}BM$ is obtained from 1-material. C_{60} (>99.9% pure) is obtained from M.E.R. Corporation. Pure metals (Al, Ag) as well as MoO_3 are obtained from American Elements. Since materials selection is a topic of particular interest for the research in this thesis, it is addressed comprehensively in **Chapter 4**.

3.3. Substrate Cleaning

Patterned ITO slides are cleaned by successive sonication in acetone, Micro-90 surfactant and isopropyl alcohol. The slides are scrubbed with a cotton swab after each of the acetone and Micro-90

sonication steps. The slides are then placed in an oven at 100 ^{o}C for at least one hour but no longer than one day before use. Prior to deposition of interfacial or active layers, the slides are exposed to O_2 plasma for 3 minutes using a Trion Phantom II RIE system equipped with an inductively coupled plasma (ICP) source.

3.4. Application of Hole Extraction Interfacial Layer

PEDOT:PSS layers are applied by spincoating Clevios P VP Al4083 PEDOT:PSS at 2300 RPM, followed by annealing at 180 ^{o}C for 10 minutes, to produce 30 nm-thick films. CF_4:O_2 plasma treatments are completed using the Trion Phantom II RIE system's ICP with an optimized CF_4:O_2 (3:1) gas mixture in lieu of the O_2 cleaning procedure detailed in Section 3.3. Plasma conditions of the CF_4:O_2 treatment are: gas pressure - 20 Pa; RF power - 100 W; treatment time - 2 minutes. Thin, 2-10 nm films of MoO_3 are formed by vacuum thermal evaporation by depositing MoO_3 at 0.5 Å/s at a chamber pressure less than 5 microtorr.

3.5. Fabrication of Polymer Solar Cell Active Layer

Preparation of the 1:1 ratio of P3HT:PCBM chlorobenzene solutions at 20 mg/mL solids is as follows: 20 mg/mL PCBM is first prepared in chlorobenzene and placed on a hotplate at 62 ^{o}C (measured solution temperature) and stirred at 650 RPM for 2 hours. 20 mg/mL P3HT is then prepared in chlorobenzene in a separate vial and placed on the hotplate, with the solution temperature reduced to 57 ^{o}C while stirred at 650 RPM for 3 hours. The PCBM solution is then mixed into the P3HT solution, and the P3HT:PCBM solution is stirred at 57 ^{o}C/650 RPM for at least 1 hour. The solution is removed from the hot plate and allowed to cool for approximately 15 to 30 minutes prior to use. Solutions are always used within the day of being prepared. After application of an HEL, the 70 nm P3HT:PCBM layer is formed by spincoating at a spin speed of 1100 RPM for 60 seconds. This active layer film is then annealed at 110 ^{o}C for 10 minutes prior to the deposition of the top interfacial extraction layer and the

top electrode. For the post-annealed devices, this annealing step is completed after deposition of the top electrode.

3.6. Fabrication of Small Molecule Solar Cell Active Layer

For SM-OSCs, the active layers are deposited by vacuum thermal evaporation at rates of 1-3 Å/s at a chamber pressure less than 5 microtorr. The thicknesses of the deposited layers are monitored by quartz crystal microbalances in the deposition chamber that are calibrated with a Veeco Dektak 8 Stylus Profiler. After application of an HEL, the active organic layers are sequentially deposited. Several variants of device structures are detailed below:

- PHJ: a donor material (e.g. 10-20 nm ClInPc) is evaporated, followed by an acceptor material (e.g. 20-30 nm C_{60})
- BHJ: both the donor material and the acceptor are evaporated together (e.g. ClInPc:C_{60} @ 1:3 ratio @ 10-30 nm, with a total summative rate of 1-3 Å/s)
    - a neat C_{60} layer can be deposited after the BHJ (e.g. 20-30 nm C_{60})
    - a neat donor layer can be deposited prior to the BHJ (e.g. 10-20 nm ClInPc)
    - if both neat layers are present, the device is defined as a PM-HJ OSC

3.7. Application of the Electron Extraction Layer and Top Electrode

All regular orientation (i.e. not inverted) OSCs employ vacuum-deposited EELs deposited at rates of 1-3 Å/s at a chamber pressure less than 5 microtorr. In this research, BCP, BPhen, 1,3,5-tris(N-phenylbenzimiazole-2-yl)benzene (TPBi), LiF, lithium acetylacetonate (Liacac) and Cs_2CO_3 EELs are employed. The organic EEL (BCP, Bphen, TPBi) thicknesses are optimized at specific values generally between 5 to 15 nm (see **Chapter 5** for more information). The inorganic EELs (LiF, Liacac, Cs_2CO_3) are

much thinner, generally between 0.5 to 2 nm. It is worth noting that not all EELs are suitable for both SM-OSCs and P-OSCs, as discussed in **Chapter 9**. To complete the devices, the aluminum top electrode is deposited to a film thickness of 100 nm at a rate of 3 Å/s.

3.8. Considerations for Single Carrier and Inverted Organic Solar Cells

For electron-only devices and inverted devices, the HEL adjacent ITO is replaced with a suitable EEL to make the bottom contact extract electrons. To this end, ultra-thin (~0.5 nm) Cs_2CO_3 is applied by spincoating a dilute, 0.1 wt-% solution of Cs_2CO_3 in 2-ethoxyethanol at 4000 RPM and subsequently annealed at 150 ^{o}C for 20 minutes. For hole-only devices and inverted devices, the EEL adjacent the top electrode can be replaced with a suitable HEL, typically a thick layer of MoO_3 (5 to 25 nm).

3.9. Device Characterization

3.9.1. Electrical Characterization

All tests and stability experiments are conducted in a dry N_2 environment unless stated otherwise. The basic output parameters and OSC performances are measured via light and dark IV characteristics, where light measurements are taken under standard 1-sun (100 mW/cm^2), air mass 1.5 (AM1.5) exposure produced by an ABET Sun 3000 Class AAA Solar Simulator (ASTM E 927-10, IEC 60904-9 ED 2.0 and JIS C 8912 compliant), as calibrated with a NREL-certified mono-crystalline silicon (KG-5 window) reference cell. This spectrum is analogous to light impingent on the earth after it has traveled through the earth's atmosphere a distance of 1.5 atmosphere thicknesses. It is effectively an 'average' spectrum of outdoor light impingent on a solar cell in a practical setting. IV sweeps are performed with

an Agilent HP4155C Semiconductor Parameter Analyzer (with ICS Metrics control software) or a Keithley 2400 SourceMeter (with ABET Solar Simulator software).

3.9.2. Optical Characterization

All tests and stability experiments are conducted in a dry N_2 environment unless stated otherwise. EQE measurements are made with the PV Measurements QEX10 Quantum Efficiency Measurement System, or with a custom EQE set-up using a Stanford Research Systems SR810 Lock-In Amplifier and a Newport Cornerstone 1/4 m Monochromator (as controlled by custom LabView software). For PL measurements, a xenon arc lamp in series with an Oriel 1/4 m Monochromator is used to excite the organic film, and the PL signal is routed to an Ocean Optics spectrometer. Transient photocurrent measurements are made with LEDs pulsed by a Stanford Research Systems DG535 pulse generator (pulsed for 5 μs at 100 Hz) and a Tektronix TDS5054 oscilloscope. A custom MATLAB program is used to extract the transient photocurrent decay (falling) data, and to calculate single or bi-exponential fits. Absorption and transmittance measurements are made in air with a Shimadzu UV-2501PC on thin films deposited on glass.

3.9.3. Morphological Characterization

Atomic force microscopy (AFM) is performed in air with the Veeco-Digital Instruments Dimension 3100 Scanning Probe Microscope in tapping mode with an etched silicon tip. Roughness measurements are made over 10 to 20 μm scan sizes, while finer features are measured over 1 to 5 μm. Further morphological characterization is made for P3HT:PCBM films using an OSC-organic light emitting diode (OLED) composite structures. These structures employ a bilayer N,N'-bis(naphthalen-1-yl)-N,N'-bis(phenyl)-benzidine (NPB)/Tris(8-hydroxyquinolinato)aluminium (Alq_3) OLED deposited on top of a BHJ OSC to image the underlying morphology, as detailed in the Supplemental Information (**Appendix 2.1**). X-ray photoelectron spectroscopy (XPS) is performed using a Thermo-VG Scientific ESCALab 250

Microprobe with a monochromatic Al KR source (1486.6 eV), capable of an energy resolution of 0.4-0.5 eV full width at half maximum.

3.10. Device Stability Experiments

All tests and stability experiments are conducted in a dry N_2 environment unless stated otherwise. Light-stress stability tests are carried out with white light from a halogen lamp at an intensity of 100 mW/cm^2, during which the sample is fan-cooled to maintain a temperature 40 ^{o}C. Note that the halogen lamp lacks a significant UV component as exists with AM1.5 solar illumination. As such UV-induced variations occur much more slowly and are specifically observed over longer aging periods, as described in **Chapter 10**. The light output intensity is monitored with the use of a calibrated pyranometer. . The temperatures of the devices are monitored using k-type thermocouples, as read from an Omega panel monitor. Heat-stress stability tests are carried out in the dark, with the devices similarly maintained at 40 ^{o}C. Electrical stress stability tests are accomplished by driving a constant current of 7.5 mA/cm^2 and measuring the corresponding device voltage using an Agilent HP4155C Semiconductor Parameter Analyzer (with ICS Metrics control software).

Chapter Four:

Materials Selection[1]

This chapter provides the rationale for the materials selection for the research in this thesis, which is particularly important in the field of organic electronics due to the vast number of materials available. To this end, BHJ OSCs with different m-Pc donors are studied in consideration of their intrinsic physical properties, such as the valency of their central moiety and their molecular energy levels. Trivalent m-Pc:C60 OSCs (especially ClInPc:C_{60} and ClGaPc:C_{60}) and SubPc:C_{60} OSCs are specifically identified for research on OSC charge transport and charge extraction phenomena, owing to their reasonable performance, their good reproducibility from device to device, and their high relevance/research impact. For understanding the variations of charge transport with time (i.e. photo-stability studies), materials selection was driven by the need for experimental data relevant to a very wide range of OSCs. As such, both the ClInPc:C_{60} materials system and the solution processable materials system, P3HT:PCBM, were selected. Additional observations are made throughout this chapter regarding the performance of m-Pcs as donors in OSCs, especially considering the resurgence of interest in these materials in the OPV research community and the high performance of non-traditional m-Pcs in fullerene-based Schottky OSCs.

4.1. Introduction

Substantial research efforts have been dedicated to the synthesis of new materials for OSCs. These materials developments have allowed for substantial improvements in the efficiencies of single junction OSCs in the past decade, from the landmark 5% efficient OSCs in 2005,[28-30] up to the 8-10% efficient OSCs established more recently.[120-124] Recent progress with OSCs has seen a shift from

[1] The majority of the material in this chapter was published in:
G. Williams, S. Sutty, R. Klenkler,H. Aziz, Sol. Energy Mater. Sol. Cells, 2014, 124, 217.
, reproduced here with permission.

intensive research on P-OSCs toward the development of small molecule donor species,[17, 19, 27, 125, 126] an area of research that had been previously overshadowed by the rapid progress of polymer donors.[20, 127, 128] SM-OSCs are interesting from a manufacturing standpoint where they can provide high batch-to-batch reproducibility compared to their polymer counterparts. Such small molecule donors have been shown to provide efficiencies competitive with polymer donors for OSCs, whether the SM-OSCs are formed by solution processing,[129, 130] or by vacuum deposition.[69, 131-133] The OPV field now has access to hundreds of donor and acceptor materials. Beyond their sheer number of combinations, each specific material has a unique and optimal manner to be incorporated into a given device. Materials selection is thus critically important: one must choose materials such that experimental results are valid, reproducible and have broad impact (i.e. not limited to a very specific combination of materials and methodologies).

4.2. Donor and Acceptor Materials for Small Molecule and Polymer Organic Solar Cells

For the majority of the initial (time-zero) OSC performance studies, where the OSC properties are considered in terms of device structure, vacuum-deposited SM-OSCs are specifically examined (**Chapters 5** through **7**). Vacuum deposition allows for the realization of multi-layer OSCs, as one can easily control the thickness and composition of any number of sequentially deposited neat or mixed layers. The result is a simple method to finely control the vertical distribution of donor and acceptor species in the OSC, a feat that is much more difficult in solution-processed OSCs. To emphasize this point, one may consider the PM-HJ structure from **Chapter 1**, which is simple to fabricate by vacuum deposition, but is not practical to form by standard solution processing techniques. In order to form the mixed layer, one would require a solvent that does not dissolve the underlying donor layer, yet still suitably dissolves both the donor and the acceptor together (and likewise, for the subsequent acceptor

layer, one would need a solvent that dissolves the acceptor alone, but not the underlying donor:acceptor mixed layer). To address this problem there has been some work on crosslinking spincoated polymers,[134-136] or polymerizing monomers directly on the substrate to form hardened, un-dissolvable layers.[85, 137] However, these approaches warrant further research before they are employed for rigorous device physics studies, and are thus unsuitable for the work completed in this thesis. As was discussed in **Chapter 1**, while the vacuum deposition of SM-OSCs has been well-established since the beginning of OPV research, the study of SM-OSCs fell out of favour for much of the past decade compared to the significant research efforts dedicated to solution-coated P-OSCs. Therefore, there are still many insights that can be gleaned from studying SM-OSCs, especially in consideration of device structure, vertical distribution of donor-to-acceptor and overall charge transport properties.

Beyond the difficulty in forming device structures with more complexity than a simple mixed layer, solution-processed P-OSCs suffer from strong variability in their output performance values. This stems from batch-to-batch variations in the polymer source material (e.g. changes in molecular weight, polydispersity, purity, etc.) as well as unavoidable variations during device fabrication (e.g. changes in lab temperature/humidity can alter film forming properties). In contrast, vacuum-deposited OSCs are deposited in a controlled high vacuum environment (nearly identical conditions from device to device), and are fabricated with material of generally much higher purity (as purified by train sublimation). It follows that vacuum deposition, being highly controllable and capable of generating OSCs in a highly reproducible manner, is ideal for studies of fundamental device physics.

There are a very large number of small molecules readily available; however, it is well beyond the scope of this thesis to study every combination of materials in the field. Some notable materials with their approximate energy levels are shown in Figure 4-1 below. Note that there are often large discrepancies in reported energy levels, so a range of HOMO/LUMO values are shown in red.

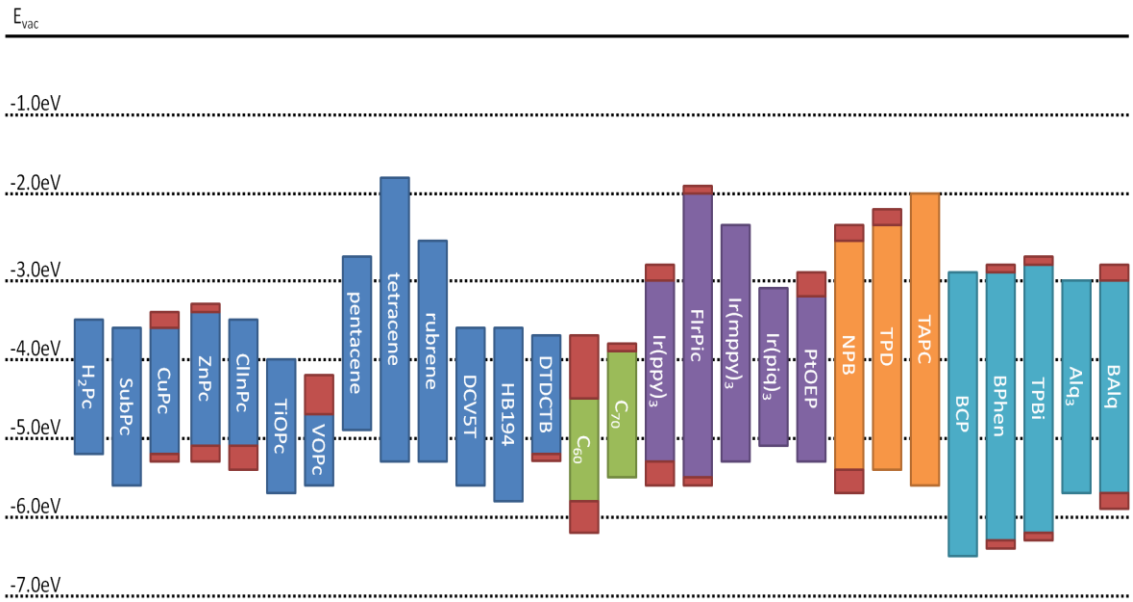

Figure 4-1 - HOMO and LUMO energy levels for common donors (blue), acceptors (green), phosphorescent dopants (purple), hole transport materials (orange) and electron transport materials (light blue).

To narrow the scope of this work, only the following small molecule materials are considered:

- C_{60}, fullerene (acceptor)
- Various m-Pcs – primarily obtained from Xerox Research Centre of Canada (XRCC) (donors)
- The high performance small molecule, DTDCTB[138] (donor)

This selection of small molecules provides a broad range of HOMO/LUMO values to provide a strong understanding of OSC properties and charge collection processes. C_{60} is a straightforward choice, as it is the most widely used acceptor in OPV research. To this end, fullerenes and fullerene derivatives offer relatively high electron mobilities, a large degree of electron delocalization and favourable film forming properties. There are currently no other acceptors that can compete in terms of efficiency and breadth of application. Divalent m-Pcs, such as CuPc and ZnPc, have been studied extensively in literature due to their strong visible absorption properties and their reasonable hole transport properties. The new or relatively unstudied m-Pcs developed by XRCC therefore make use of the general m-Pc materials system, which is well understood and has significant relevance in the OPV field, yet still offer new information in terms of optoelectronic properties and OSC performance. To further narrow the selection from within

the m-Pcs obtained from XRCC, a systematic study on the performance of OSCs with m-Pc donors and a C_{60} acceptor was performed. The results are discussed below in Section 4.3. DTDCTB is studied specifically in **Chapter 7** for its comparable energetic and optical properties as ClInPc, which provides useful information regarding charge transport in ternary mixture OSCs.

The research on solution-processed OSCs in this thesis is mainly focused on changes with charge transport/extraction with time, rather than the time zero performance. As noted above, this is largely due to the fact that it is difficult to solution process device structures that are more complicated than the basic BHJ in a controlled manner. From past work on other optoelectronic devices (OLEDs, organic photodiodes (OPDs), etc.), it has been established that a major and dominant degradation pathway involves organic-electrode interfacial degradation.[12, 13] For the research on solution-processed OSCs, it is therefore logical to choose a well-studied material with established time zero performance, and a materials system where the interfacial extraction layers can be easily varied. P3HT is thus chosen as the donor of interest and PCBM as the acceptor of interest. P3HT is the most heavily studied donor polymer in OSC research,[23] so work on this polymer has high relevance to other researchers. Furthermore, OSCs based on the ubiquitous P3HT and PCBM have proven to have some of the lowest energy payback times of any practical renewable energy technology.[139, 140] With regard to the acceptor, while there has recently been a significant push toward the development of new acceptor materials for OSCs,[141-144] as noted above, fullerene and fullerene derivatives remain the de facto standards in OPV research. It is thus logical to select $PC_{61}BM$ (from **Chapter 1** $PC_{61}BM$, or simply PCBM, is the soluble derivative of C_{60}) as the acceptor. It is worth noting that, in spite of the tremendous research efforts dedicated to P3HT-based OSCs, there remain many unknowns regarding the photo-stability of P3HT:PCBM OSCs, especially in regard to organic-electrode degradation phenomena. The studies from **Chapter 8** and **Chapter 9** are thus critical toward developing methodologies for obtaining OSCs with lifetimes that make them competitive with existing solar cell technologies.

4.3. Renewed Interest in Metal Phthalocyanine Donors for Small Molecule Organic Solar Cells

Metal phthalocyanines are historically some of the most studied donor materials in vacuum-deposited OSCs. Their success stems from their long-established hole transport properties, and their well-known capability as a sensitizer by photo-induced electron transfer to quenchers/acceptors.[145-147] For OSCs, this photo-induced electron transfer was employed most effectively when the m-Pcs were coupled with C_{60} and C_{70}, as has been studied in literature.[148, 149] CuPc was employed as a donor in the first bilayer heterojunction OSC reported in literature over two decades ago by C.W. Tang,[16] and subsequently studied for its use in OSCs in various configurations.[24, 26, 150, 151] Zinc phthalocyanine (ZnPc) may also be considered a traditional m-Pc, with its extensive use in OSCs by Gebeyehu et al.[25, 152-154] ZnPc was more recently chemically modified to F_4-ZnPc, where it achieved 3.9% PCE in a BHJ single cell architecture.[27] Since 2005, with the rise in popularity of solution-processable OSCs, the study of vacuum-deposited and thus m-Pc donor OSCs has been comparatively much less prevalent in literature. However, the development of alternative (non-traditional) m-Pc donors with high V_{oc} values and impressive PCE values has triggered a resurgence of interest in m-Pc-based OSCs. To this end, SubPc has shown promise as a donor material, granting 3.7% PCE when mixed with a C_{60} acceptor and 5.4% PCE in an optimized graded-BHJ device with a C_{70} acceptor.[133, 155] OSCs with a chloroaluminum phthalocyanine (ClAlPc)-C_{60} active layer have also been shown to grant good performance from 2% to greater than 4%, and ClAlPc has furthermore been highlighted for its near-infrared sensitivity.[156-159] The ClInPc donor can also be employed in simple BHJ OSCs to achieve reasonable device performance, providing 2.2% PCE when mixed with $C_{60,}$[72, 109] and 3.9% PCE when mixed with C_{70}.[72, 160] When coupled with their relatively simple synthesis and straightforward purification (by train sublimation), these m-Pcs show their promise as cost-effective and highly capable donor materials for highly efficient OPVs.

In previous work, Yuen et al. showed that a large set of m-Pcs, including both traditional m-Pcs (CuPc, ZnPc) as well as non-traditional (less-studied) m-Pcs, have some promise when used as donors in simple PHJ OSCs and 1:1 BHJ OSCs.[161] This work focused on establishing a basic understanding of the donors at a 1:1 mixing ratio and with non-ideal device thicknesses – generally too thin to provide reasonable efficiencies. As noted in **Chapter 1**, the fullerene-based Schottky device architecture has recently been highlighted in literature as a novel approach to grant high V_{oc} (>1 V) OSCs.[71] When employed for high performance OSCs, this device architecture relies on varied concentrations of the BHJ layer, usually with much higher C_{60} content than in the standard BHJ OSC.[42, 69, 72, 160, 162-165] The role of the Schottky architecture for the creation of high efficiency OSCs with traditional m-Pcs (CuPc, ZnPc) versus the more recently examined m-Pcs is currently unknown. To this end, a comprehensive study on the photovoltaic output characteristics of traditional versus non-traditional m-Pcs is highly valuable for the field of vacuum-deposited SM-OSCs, and further helps to identify the promising m-Pcs for study in this thesis. Thus, it is interesting to examine the untapped benefits of these non-traditional m-Pcs that have otherwise experienced success in other dye/pigment-related fields, such as xerography.[166]

In this section, OSCs comprising a m-Pc:C_{60} photo-active layer with substantially different mixing ratios are studied. These OSCs therefore span the traditional BHJ architecture to the Schottky architecture. The central moiety in the m-Pc is varied to gain an understanding of the role of the m-Pc donor in the OSC photovoltaic output properties. The present work encompasses the following donors: metal free phthalocyanine (H_2Pc), ZnPc, CuPc, ClAlPc, ClInPc, ClGaPc, titanium oxide phthalocyanine (TiOPc) and SubPc. In this manner, the impact of the m-Pc central moiety valency on achieving high efficiency OSCs primarily through mixed donor:acceptor (D:A) active layer optimization is elucidated. The results indicate that, while the traditional m-Pcs benefit most from a standard 1:1 D:A BHJ architecture, all non-traditional m-Pcs show substantially enhanced performance with a high C_{60}-content Schottky architecture. In-depth analysis of photovoltaic output parameters and EQE measurements are

used to explain these observations. ClInPc is highlighted as an especially promising small molecule donor, with very strong near-IR absorption and 2.5% PCE in a basic ClInPc:C_{60} BHJ. Further device optimization allows for 2.8% PCE ClInPc:C_{60} OSCs and V_{oc} values in excess of 1 V.

4.3.1. Overview of Metal Phthalocyanines of Interest

The m-Pcs in this section can be classified based on the valency of their central moiety in the molecule. To this end, monovalent (H_2- or metal-free), divalent (Cu, Zn), trivalent (ClIn, ClGa, ClAl) and tetravalent (TiO) phthalocyanines are studied. SubPc is also included in this study, which differs from the other m-Pcs in that it has three, instead of four, N-fused 1,3-diiminoisoindoline units around its central B-Cl moiety. The chemical structures are shown in Figure 4-2.A and B.

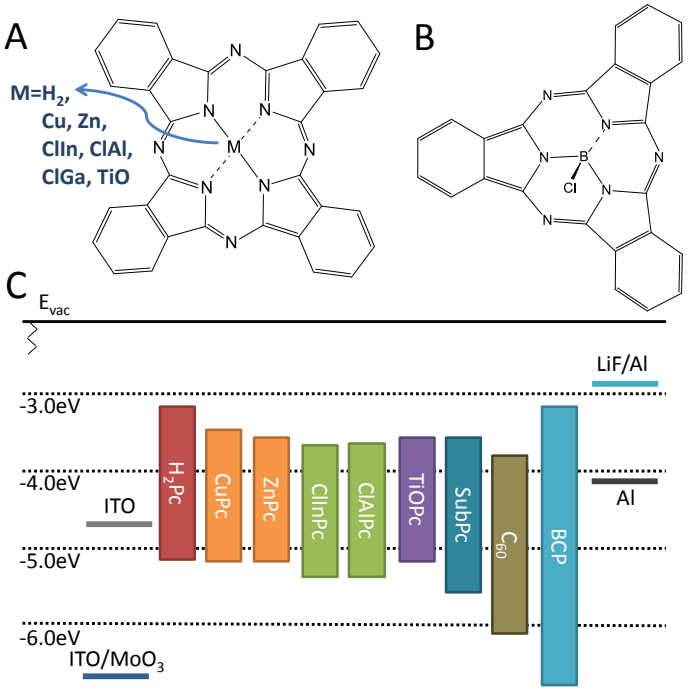

Figure 4-2 - Illustration of A) m-Pc and B) SubPc chemical structures. C) Energy level diagram of relevant species in the studied OSCs. m-Pc species are grouped/highlighted by the valency of their central moiety.

As noted previously, CuPc and ZnPc may be considered traditional phthalocyanines, as they have long been studied in literature for their application as donors in OSCs, while the other m-Pcs are considered non-traditional, as they have been comparatively much less studied for their use in OPV

devices. The energy levels for these m-Pc donors as well as the other species employed in the OSCs in this work are shown in Figure 4-2.C (a subset of Figure 4-1).[71, 150, 152, 155, 167-172] It is also worth noting that the HOMO values taken from recent literature (Figure 4-2.C) align well with the ionization energies established historically,[173, 174] as well as with the orbital energy diagrams found computationally.[175-177] Interestingly, the latter studies show that for H_2Pc, CuPc, ZnPc and TiOPc (among others) the HOMO is exclusively formed by C-2p_π characteristics, so that changes in the central metal atom have very little effect on the HOMO. Given that the HOMO has been experimentally found to be deeper for many of the non-traditional m-Pcs, such as ClInPc, ClAlPc, ClGaPc and SubPc, it is likely that the HOMO for these species may include orbital contributions from their central moiety.

4.3.2. Optical Properties of the Metal Phthalocyanines

The absorption spectra of 50 nm films of the presently examined m-Pc donors, as well as C_{60}, are presented in Figure 4-3. All m-Pcs exhibit two strong peaks, one in the UV and one in the visible (denoted as the B band and Q band respectively). The Q band also has a broad shoulder. The relative position and intensity of the peak and shoulder of the Q band depend on the valency of the m-Pc. Monovalent and divalent phthalocyanines have their peak visible absorption at 625 nm, with a shoulder at ~700 nm, as shown in the top panel of Figure 4-3. In contrast, trivalent and tetravalent phthalocyanines have their peak visible absorption from 720 to 750 nm, with a shoulder at 640 to 660 nm (Figure 4-3, middle panel). In effect, the trivalent and tetravalent species make for better red/near-IR absorbers, whereas the monovalent and divalent species are more effective for orange absorption. The capacity for near-IR absorption makes trivalent and tetravalent m-Pcs ideal candidates for semi-transparent solar cells, which have recently been highlighted as a promising application for OSCs.[157, 178] The strong absorption in this region also makes them useful for aesthetically pleasing blue/green-tinted OSC-coated windows – an area of obvious commercial importance in building construction.

With its reduced conjugation, SubPc's visible absorption peak is hypsochromatically shifted compared to traditional m-Pcs. Consequently, SubPc exhibits peak absorption at 588 nm and a much narrower shoulder at ~530 nm, as shown in the bottom panel of Figure 4-3, so that it is more suited for absorption of green/yellow light. Also observed from the bottom panel in Figure 4-3, the chosen acceptor for this study, C_{60}, has relatively poor tail absorption in the visible spectrum. C_{60} exhibits peak absorption at 350 nm and a secondary aggregate peak at ~440 nm that only arises for thin films with high C_{60} content.[72] The AM1.5G spectral irradiance shown in the same panel indicates that both the C_{60} aggregate absorption and the SubPc Q band absorption are ideally situated for generating photocurrent. Monovalent and divalent m-Pcs are also well-situated in the solar spectrum, but the trivalent and tetravalent m-Pcs show peak absorption in a region of comparatively reduced spectral irradiance.

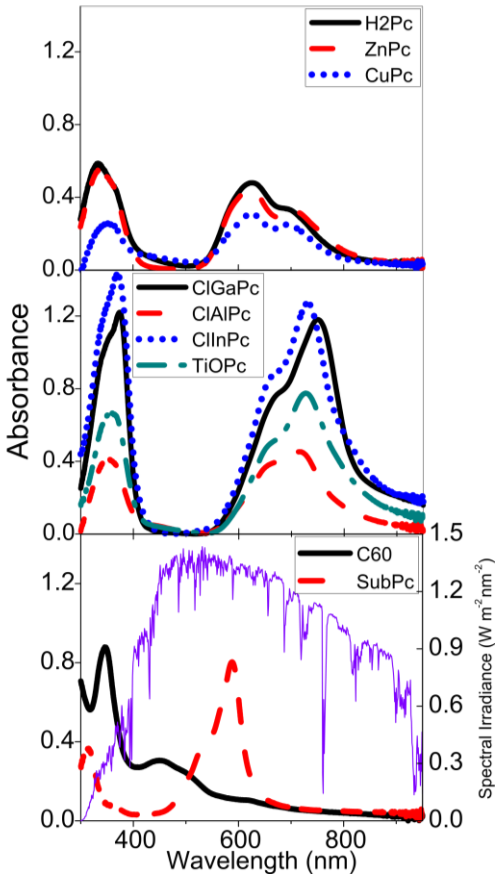

Figure 4-3 - Absorption Data for 50 nm Films of m-Pcs, SubPc and C_{60}-fullerene. Bottom panel also shows spectral irradiance from AM1.5G solar irradiation for comparison.

Since all absorption measurements from Figure 4-3 were obtained from 50 nm films of the respective donors and acceptor, and if one assumes similar film density/packing for all of these species, these data also provide a general understanding of the donors' molar extinction coefficients. Note that the scales of the three panels are identical. It is observed that the donors that absorb most strongly are ClInPc and ClGaPc, with peak absorption 1.5-times larger than that of the next candidates – SubPc and TiOPc. All other m-Pcs, including H_2Pc, ZnPc, CuPc and ClAlPc, show substantially reduced peak absorption – less than half of that of ClInPc. CuPc is found to have the lowest peak absorption, in spite of being studied so extensively in literature.

4.3.3. Principal Photovoltaic Output Properties of m-Phthalocyanine Organic Solar Cells

A basic mixed active layer device structure with a 40 nm active layer was employed for all OSCs fabricated in this section, as shown in Figure 4-4. It is worth noting that this is not necessarily the ideal device structure for each of the donor species examined in this study; however, standardizing the device structure greatly simplifies cross-comparisons and establishes a baseline for device behavior. Regardless, the chosen mixed layer thickness of 40 nm provides reasonably high J_{sc} values without substantially diminishing the FF. Since this device architecture does not use a neat donor or acceptor layer, as is employed in the PM-HJ devised by Xue et al.,[151] there is direct contact between the mixed D:A layer and hole/electron extracting contacts. To allow for efficient hole/electron extraction from the anode and cathode respectively, all devices employ a 5 nm MoO_3 HEL and an 8 nm BCP EEL. Such extraction layers are also critical for enhancing OSC photo-stability and ensuring long device lifetimes, as discussed in **Chapters 8** through **10**.[15, 109] Furthermore, the lack of a neat donor layer between the mixed D:A layer and the MoO_3 HEL allows for the realization of the fullerene-based Schottky OSC (with sufficient C_{60} content), which can have drastic implications toward device efficiency.

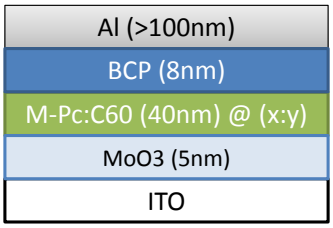

Figure 4-4 - Illustration of the standard mixed donor:acceptor (BHJ) device structure used in this chapter.

The PCE values of m-Pc:C_{60} OSCs at varying D:A ratios are shown in Figure 4-5. The data have been split into two panels in order to better illustrate the trends in device performances, with Figure 4-5.A showing divalent m-Pc donors (i.e. m-Pcs that are considered well-studied in literature), and Figure 4-5.B showing all other non-traditional m-Pc donors (i.e. m-Pcs that are less-studied in literature). The traditional divalent donors exhibit their highest PCE values at a 1:1 D:A mixing ratio. The use of any other mixing ratio strongly degrades the PCE. A peak PCE of 1% is achieved for CuPc:C_{60} OSCs, while 2% PCE is achieved for ZnPc:C_{60} OSCs. In contrast, OSCs with the non-traditional m-Pc donors all show strong improvements in PCE at much higher C_{60} concentrations (Figure 4-5.B). Maximum PCE values in this study are achieved by ClInPc and SubPc donors at 2.5% and 2.7% PCE respectively. In general, for all m-Pc donors examined (whether traditional or non-traditional), device performance is strongly reduced with very high donor concentration (75% donor content).

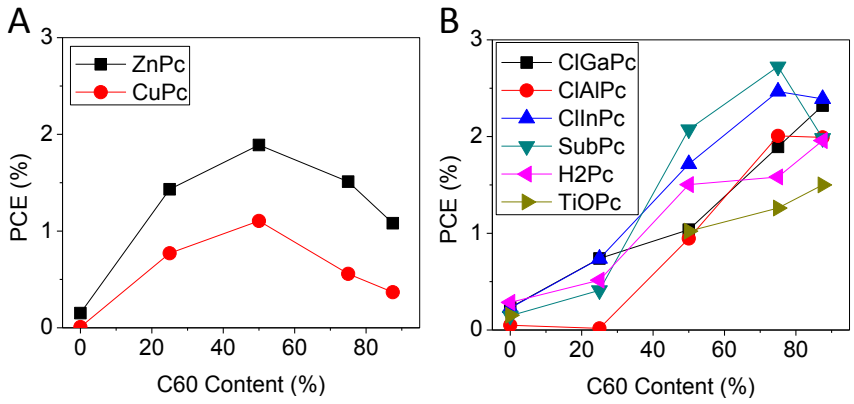

Figure 4-5 - PCE Values for ITO/MoO_3/m-Pc:C_{60}/BCP/Al OSCs at different donor:acceptor mixing ratios. A) Divalent m-Pc donors. B) Other valency m-Pc and SubPc donors.

In order to understand the improvements in PCE values at high C_{60} concentrations for the non-traditional m-Pc donors, it is necessary to further consider the formation of the MoO_3/C_{60} Schottky

junction. As noted in **Chapter 1** and established in literature, high V_{oc} Schottky OSCs arise from an interface formed between a high work function anode and a fullerene film. This has been demonstrated with anodes including ITO/MoO_3,[42, 71, 163] ITO/PEDOT:PSS,[162] and ITO/CF_4 (ie. where the ITO has been plasma treated with a CF_4:O_2 plasma).[72, 109, 160] The presence of donor within the active layer disrupts this Schottky junction, essentially acting as a charge trap and reducing the maximum possible V_{oc}. However, the donor has also been demonstrated to be essential for exciton dissociation, and thus to harvest photocurrent especially from the more strongly bound intermolecular excitons formed in C_{60} aggregates.[72] The presence of donor in the Schottky OSC is thus necessary for achieving broader spectral response from C_{60} and ultimately for achieving high J_{sc} values. Taking this into consideration, the fullerene acceptor contributes strongly to photocurrent in the Schottky architecture – from the EQE presented later in this chapter, these contributions are visibly much larger than the calculated 13% of J_{sc} observed with a standard 1:1 P3HT:PCBM BHJ.[179] It follows that Schottky OSCs that employ a C_{70} OSC, which is known to have excellent optical absorption properties and thus strong photocurrent generation capabilities,[180] can achieve very high J_{sc} values.[69, 165] In this regard, the study of exciton generation and subsequent hole transfer characteristics of acceptors is critically important to the overall performance of Schottky OSCs.[181] Regardless, even with the strong fullerene photocurrent contributions, it should be noted that phthalocyanine donors can provide reasonable photocurrent from their Q band absorption in the Schottky device architecture. In the present work, OSCs are examined at substantially different mixing ratios, spanning 3:1 to 1:7 D:A. As will be demonstrated below, the observed trends in PCE can be attributed to a transition from the traditional BHJ OSC to the fullerene-based Schottky OSC structure.

A strong indicator of the Schottky junction OSC is an increase in V_{oc} with increasing C_{60} content.[72] This effect can be observed for all m-Pc donors examined in this work, as shown in Figure 4-6, verifying that the Schottky architecture has a strong role in the ultimate efficiency of m-Pc:C_{60} OSCs. To briefly summarize this behavior, first consider an OSC with a 1:1 D:A active layer, which is generally

known as the standard BHJ device architecture. For a basic BHJ OSC, the maximum attainable V_{oc} is delineated by the offset between the HOMO of the donor and the LUMO of the acceptor – a more complete picture takes into consideration the various losses noted in **Chapter 1** (including the Coulombic exciton binding energy, energy level pinning at the organic-electrode contacts and spread in energy levels due to disorder in the organic films).[54, 182, 183] Now consider a pure Schottky OSC formed between an ITO/MoO_3 anode and a neat C_{60} film (0:1 D:A active layer). In this case, the V_{oc} is dictated by the effective work function of the ITO/MoO_3 contact and the energy levels of C_{60}.[71] For a simple ITO/MoO_3/C_{60}/BCP/Al Schottky device, the V_{oc} is found to be ~1.2 V. As the mixing ratio is varied between these two scenarios of BHJ versus Schottky architecture, the V_{oc} also varies between the values obtained for the two device architectures. In effect, the pure C_{60} Schottky devices set the upper limit on the V_{oc}, and the addition of donor to a 1:1 D:A mixing ratio lowers the V_{oc} to the BHJ value. Taking this explanation into account, the V_{oc} is expected to increase in the transition from the 1:1 D:A mixing ratio (BHJ architecture) to the 1:7 D:A mixing ratio (Schottky architecture).

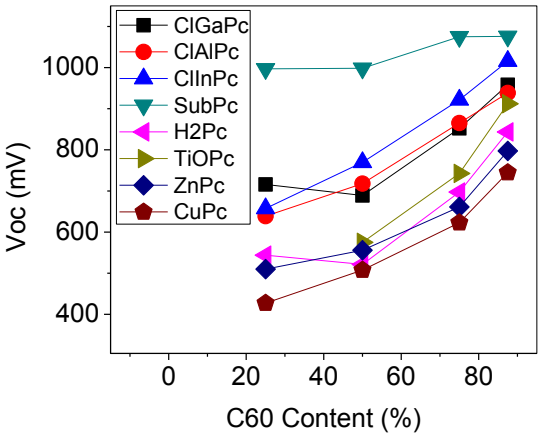

Figure 4-6 - V_{oc} values for ITO/MoO_3/m-Pc:C_{60}/BCP/Al OSCs at different donor:acceptor mixing ratios.

From Figure 4-6, donors with an initially low V_{oc} in the BHJ OSC architecture (CuPc, ZnPc, H_2Pc) have improvements to V_{oc} in the Schottky OSC architecture that can be substantial (40-60% increase). Likewise, for donors with an initially high V_{oc} in the BHJ OSC architecture, the improvements to V_{oc} in the Schottky OSC architecture are much lower (e.g. 8% for SubPc, 30% for ClInPc). At a 1:7 D:A mixing ratio,

there remains a ~350 mV spread in V_{oc} values among the different m-Pc donors. This is due to the fact that, even in low concentrations, the m-Pc donor species act as charge traps in the Schottky OSC device architecture, with their capacity for charge trapping associated with their HOMO energy levels. As the donor concentration is further reduced to zero, the V_{oc} values eventually converge to ~1.2 V. For SubPc and ClInPc donors, while the improvements to V_{oc} are not as significant in the transition from BHJ to Schottky device architecture, the ultimate V_{oc} values with the 1:7 D:A mixing ratio are quite high (1.08 V and 1.02 V respectively). As a point of note, the V_{oc} values for SubPc and ClInPc are quite similar in the Schottky architecture, in spite of being quite different in the BHJ architecture (1.00 V and 0.77 V respectively). This allows for substantial improvements in the efficiencies of ClInPc:C_{60} OSCs toward the same level as SubPc:C_{60} OSCs, evident from the PCE values shown previously in Figure 4-5. Further, with a slightly modified device structure (20 nm ClInPc:C_{60} (1:3)/30 nm neat C_{60}), the PCE values of ClInPc:C_{60} OSCs can be improved to 2.8%. This modified device structure shows strong improvements in FF at the cost of a slight decrease in J_{sc}, ultimately allowing for improved PCE, as discussed further in **Chapter 6**.

The J_{sc} values for m-Pc:C_{60} OSCs at varying D:A ratios are shown in Figure 4-7. The data have similarly been split into two panels, with Figure 4-7.A showing only divalent (traditional) m-Pc donors and Figure 4-7.B showing all other (non-traditional) donors. The OSCs that use divalent m-Pc donors maximize their photocurrent at a 1:1 D:A mixing ratio, with strong losses at any other mixing ratio. OSCs with monovalent and tetravalent donors similarly maximize their photocurrents at 1:1 D:A mixing ratios; however, their losses in photocurrent are not as severe with high C_{60} content. Specifically, the OSCs that employ divalent ZnPc and CuPc donors have 48% and 64% reduced J_{sc} respectively in the 1:7 compared to the 1:1 D:A mixing ratio. In contrast, OSCs with the monovalent H_2Pc donor show only a 17% reduction in J_{sc}, while OSCs with the tetravalent TiOPc donor show only a 6% decrease in J_{sc}. From the standpoint of generation of photocurrent, it is clear that the traditional divalent m-Pcs are most aptly suited for the 1:1 D:A mixing ratio (i.e. the BHJ structure).

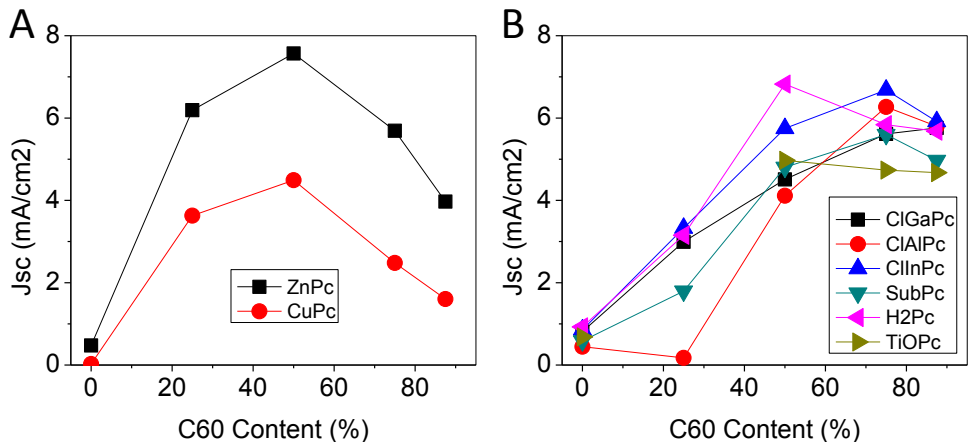

Figure 4-7 - J_{sc} values for ITO/MoO_3/m-Pc:C_{60}/BCP/Al OSCs at different donor:acceptor mixing ratios. A) Divalent m-Pc donors. B) Other valency m-Pc and SubPc donors.

OSCs with either the trivalent m-Pc or SubPc donors exhibit their highest J_{sc} values with high C_{60} content. Specifically, Figure 4-7.B shows that ClInPc, ClAlPc and SubPc all maximize their photocurrent at a 1:3 D:A mixing ratio, and ClGaPc maximizes its photocurrent at a 1:7 D:A mixing ratio. The transition from the BHJ device architecture to the Schottky device architecture thus allows for 16% improvements in J_{sc} values for OSCs using ClInPc and SubPc donors, and grants even more substantial 28% and 52% improvements in J_{sc} values for OSCs with ClGaPc and ClAlPc donors respectively. The slight drop in photocurrent in the transition from 1:3 to 1:7 D:A mixing ratio, observed for many of the non-traditional m-Pcs, is associated with a trade-off in photocurrent contributions from the m-Pc donor and the C_{60} acceptor (discussed further in the following section). In light of the improvements to J_{sc}, trivalent m-Pc and SubPc donors are better suited for OSCs with high C_{60} content (i.e. fullerene-based Schottky OSCs).

4.3.4. External Quantum Efficiency and Fill Factor Measurements of m-Phthalocyanine Organic Solar Cells

In order to better understand the trends in J_{sc} with changes in D:A mixing ratio, EQE measurements were performed for all of the examined m-Pc donors at the same mixing ratios examined in the previous section. In the present analysis, specific EQE data are highlighted for the m-Pc donors

that provide the most insightful conclusions; however, the remaining EQE spectra are also provided in the Supplemental Information (**Appendix 1.1**). The EQE spectra for OSCs with both the traditional m-Pc donors (CuPc and ZnPc) as well as high performance non-traditional m-Pc donors (ClInPc and ClAlPc) are provided in Figure 4-8.A-D respectively. It is useful re-establish the different photocurrent contributions in terms of their absorption bands. The m-Pcs examined in this work have photocurrent contributions in the visible range from 600 nm to 800 nm due to their Q band absorption. Both the m-Pcs and C_{60} have photocurrent contributions from UV light, with their combined EQE maxima at ~370 nm. The additional broad absorption band at ~450 nm that is present for OSCs with high C_{60} content (generally with the Schottky architecture) arises from intermolecular interactions among the C_{60} molecules.[72] For clarity, this intermolecular absorption band has been identified with an arrow on each sub-panel of Figure 4-8.

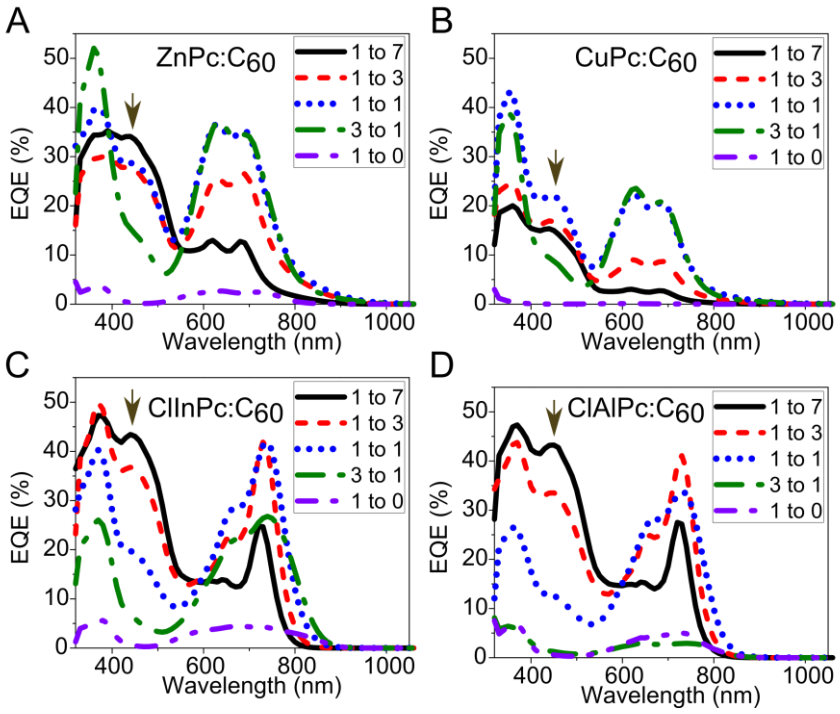

Figure 4-8 - EQE Spectra of ITO/MoO_3/m-Pc:C_{60}/BCP/Al OSCs at different donor:acceptor mixing ratios. A) ZnPc:C_{60}, B) CuPc:C_{60}, C) ClInPc:C_{60} and D) ClAlPc:C_{60}. C_{60} aggregate peak is highlighted with an arrow.

For the ZnPc:C_{60} OSC at a 1:1 D:A mixing ratio (Figure 4-8.A), all of the photocurrent contributions noted above are present and contribute strongly to the J_{sc}, allowing for greater than 30%

EQE across most of the visible spectrum. Peak EQE at this mixing ratio is ~40% at both 370 nm and 620 nm. This particular mixing ratio also corresponds to the maximum J_{sc} for ZnPc:C_{60} OSCs, and the broad EQE further explains why ZnPc:C_{60} OSCs exhibit some of the highest photocurrents among all of the m-Pc:C_{60} OSCs tested. As the ZnPc donor concentration is increased (3:1 D:A mixing ratio), the UV photocurrent contribution from ZnPc increases, and the Q band contributions remain largely unchanged. However, the reduction of C_{60} content at the 3:1 D:A mixing ratio suppresses the formation of C_{60} aggregates. As such, at a 3:1 D:A mixing ratio, the broad absorption at ~450 nm disappears. The loss of the C_{60} aggregate band strongly degrades the overall photocurrent, and so the J_{sc} decreases at high donor loadings (shown in Figure 4-7.A). If the ZnPc donor concentration is instead decreased relative to the C_{60} concentration (e.g. 1:7 D:A – Schottky architecture), the 600 nm to 800 nm photocurrent contributions from ZnPc logically decrease. Furthermore, the C_{60} aggregate band becomes slightly broader and provides more photocurrent. Interestingly, the UV photocurrent contributions at 370 nm for both the 1:3 and 1:7 D:A mixing ratios decrease relative to the 1:1 mixing ratio. Since both ZnPc and C_{60} absorb strongly in this region, the photocurrent is not expected to decrease drastically. This change at high C_{60} loadings is thus suggested to be from an overall loss in photocurrent throughout the cell due to poor charge extraction, which may arise due to charge trapping and charge recombination effects, as will be discussed further below.

From Figure 4-8.B, CuPc:C_{60} OSCs show similar behavior to ZnPc:C_{60}, with stronger m-Pc photocurrent contributions in the BHJ architecture and stronger C_{60} aggregate photocurrent contributions in the Schottky architecture. However, the absolute EQE values are much lower for the CuPc:C_{60} OSCs when compared to the ZnPc:C_{60} OSCs. For example, CuPc:C_{60} (1:3) OSCs show <10% EQE at the 625 nm m-Pc Q band absorption peak, whereas ZnPc:C_{60} (1:3) OSCs show >25% EQE at the same peak. At a 1:7 D:A mixing ratio, the photocurrent contributions from CuPc are almost completely absent. Similar to the ZnPc:C_{60} OSCs, the EQE values are also strongly reduced at 370 nm with high C_{60}

loadings, again implying the possibility of hindered charge extraction from the device. To better understand this effect, it is useful to examine the FF, which can be a strong indicator of losses due to charge accumulation or recombination effects.[67] The FF values for m-Pc:C_{60} OSCs at varying D:A ratios are shown in Figure 4-9. As with the previous data, the figures have been split into two panels in order to better illustrate the trends in device performances, with Figure 4-9.A showing only divalent (traditional) m-Pc donors and Figure 4-9.B showing all other (non-traditional) donors.

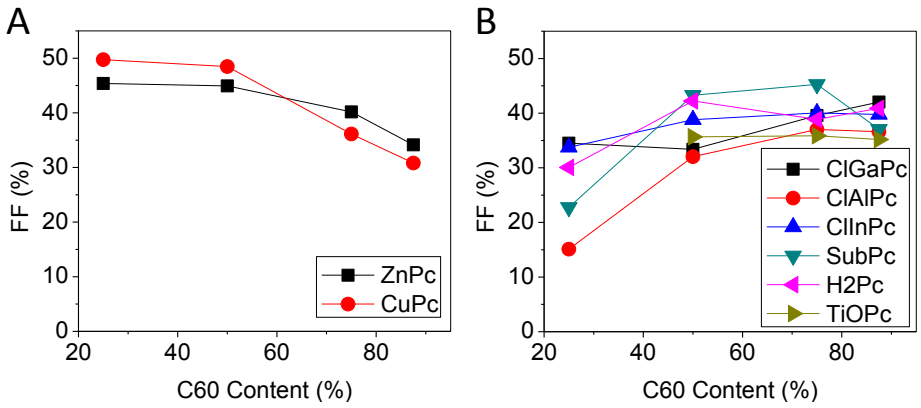

Figure 4-9 - FF values for ITO/MoO_3/m-Pc:C_{60}/BCP/Al OSCs at different donor:acceptor mixing ratios. A) Divalent m-Pc donors. B) Other valency m-Pc and SubPc donors.

For OSCs with traditional m-Pc donors, increasing the C_{60} content decreases the FF quite significantly. In the case of CuPc, the FF drops drastically from 50% to 30% in the transition from 3:1 to 1:7 D:A mixing ratio. This decrease in FF correlates with higher levels of charge recombination within the OSC (i.e. to create an opposing recombination current), which ultimately reduces the photocurrent and EQE throughout the entire visible spectrum. The source of this recombination current may stem from charge accumulation effects due to substantially unbalanced mobilities within the mixed film, or due to the non-optimal HOMO position of the donors (especially with the Schottky structure, as discussed in greater detail at the end of this section). The decrease in mobility in mixed donor:acceptor films compared to their neat donor or acceptor films, such as for CuPc:C_{60} materials systems as well as with other vacuum-deposited donor:acceptor materials systems, is commonly observed in literature.[42, 164, 184] In fullerene-rich active layers, this loss in mobility is also accompanied by a substantial disparity

in hole and electron mobility – from [184], a 1:3 CuPc:C_{60} mixing ratio can result in a hole mobility six orders of magnitude lower than that of the electron mobility. It is further expected that corresponding charge accumulation effects would be manifested as an increase in R_s due to space charge effects. This stipulation is thus supported by the substantial increase in R_s – from 14 to 40 Ω cm^2 for ZnPc:C_{60} OSCs and 12 to 74 Ω cm^2 for CuPc:C_{60} OSCs. An additional consideration may relate to the molecular organization of the donor and acceptor species, especially adjacent to the carrier collecting contacts, which has recently been shown to be critically important in device performance for PHJ OSCs with certain m-Pc donors.[185] Such subtleties in active layer morphology may play a role for the OSCs with mixed layers comprised of either substantially more donor or more acceptor content, as is the case in the present work. Therefore, when employing the fullerene-based Schottky OSC architecture with the traditional m-Pc donors, the potential gains in photocurrent arising from increased light absorption by the C_{60} aggregates cannot offset the losses in photocurrent that arise due to the decreased m-Pc content and due to undesired charge accumulation/recombination effects.

The EQE spectra for two non-traditional m-Pc:C_{60} OSCs (ClInPc:C_{60} and ClAlPc:C_{60} OSCs) at varying mixing ratios are shown in Figure 4-8.C and Figure 4-8.D. With a 1:1 D:A mixing ratio (BHJ architecture), the ClInPc:C_{60} OSCs provide reasonable EQE (20-40%) over UV/blue and red wavelengths, with photocurrent contributions extending into the near-IR due to the ClInPc Q band peak absorption at 720 nm. However, unlike the traditional m-Pc donors, the ClInPc donor lacks strong photocurrent contributions at 625 nm, ultimately limiting the J_{sc} of 1:1 ClInPc:C_{60} OSCs. This is especially critical when considering the AM1.5G spectral irradiance, shown earlier in Figure 4-3, which decreases in intensity beyond ~650 nm. As established in the previous section, many of the non-traditional m-Pc donors maximize their J_{sc} with high C_{60} content (1:3 and 1:7 D:A mixing ratios). In support of this observation, it is observed that the EQE due to the C_{60} aggregate band in ClInPc:C_{60} OSCs increases strongly to 37% and to 44% for the 1:3 and 1:7 mixing ratios respectively. Furthermore, at a 1:3 D:A mixing ratio, the EQE

due to ClInPc absorption at 720 nm remains largely unchanged compared to the 1:1 mixing ratio – there is only a small decrease in EQE at the ClInPc Q band shoulder at 650 nm. As the C_{60} concentration is further increased to the 1:7 D:A mixing ratio, the photocurrent contributions from ClInPc begin to decrease. Consequently, the photocurrent from the C_{60} aggregate band cannot offset the reduced contributions from ClInPc, and so the J_{sc} is observed to decrease slightly (6.7 mA/cm^2 to 5.9 mA/cm^2 for 1:3 to 1:7 D:A mixing ratio). ClAlPc:C_{60} OSCs generally show the same trends in EQE versus mixing ratio as ClInPc:C_{60} OSCs; however, ClAlPc:C_{60} OSCs exhibit much lower EQE values at the 1:1 D:A mixing ratio. More specifically, 1:1 ClAlPc:C_{60} OSCs have substantially reduced photocurrent contributions from C_{60} and much lower m-Pc Q band EQE compared to the equivalent 1:1 ClInPc:C_{60} OSCs. At a 1:3 D:A mixing ratio, ClAlPc:C_{60} OSCs have EQE values nearly on par with that of ClInPc:C_{60} OSCs, allowing for J_{sc} values up to 6.3 mA/cm^2. As the C_{60} content is increased further, ClAlPc:C_{60} OSCs similarly suffer from a trade-off between ClAlPc Q band absorption and C_{60} aggregate absorption. Likewise, in the transition from a 1:3 to a 1:7 D:A mixing ratio the improvements in photocurrent from C_{60} aggregate absorption cannot offset the losses in photocurrent due to reduced m-Pc absorption.

For both ClInPc:C_{60} and ClAlPc:C_{60} OSCs, if the C_{60} content is instead decreased (1:1 to 3:1 D:A mixing ratio), the EQE decreases across the entire spectrum, which corresponds well to the low J_{sc} values for the 3:1 D:A mixing ratio. Since C_{60}, ClInPc and ClAlPc all absorb strongly at 370 nm, the EQE in this region is again not expected to vary substantially with mixing ratio, and so the overall loss in EQE at the 3:1 D:A mixing ratio is similarly attributed to charge accumulation and recombination within the device. This is clearly represented in the FF of ClInPc:C_{60} and ClAlPc:C_{60} OSCs measured at varying mixing ratios, shown in Figure 4-9.B. Such variations may be explained by the substantially diminished charge transport properties in mixed films. Specifically, ClInPc is known to have a reduction in hole mobility by more than a factor of four when mixed with C_{60} at a 1:1 mixing ratio,[161] and C_{60} similarly shows reduced electron mobilities in mixed BHJ films [184]. It follows then that in Figure 4-9.B, ClInPc:C_{60} and ClAlPc:C_{60}

devices have low FF values with low C_{60} content. In fact, for any OSC with either a trivalent m-Pc donor or a SubPc donor, the FF decreases strongly in the transition from 75% C_{60} to 25% C_{60} – in the case of SubPc:C_{60} OSCs, the FF decreases remarkably from 45% to 23%. Note that this trend is exactly opposite to the trend observed for the traditional m-Pc donors, which showed a strong decrease to FF with increasing C_{60} content in the mixed active layer. Interestingly, OSCs with the monovalent (H_2Pc) and tetravalent (TiOPc) m-Pc donor show little change in FF between the 1:1 D:A and 1:7 D:A OSCs, although the FF for the H_2Pc:C_{60} OSC is much lower with high donor content (3:1 D:A mixing ratio). Therefore, in terms of both J_{sc} and FF, the traditional (divalent) m-Pc donors are better suited for the BHJ OSC device architecture, whereas the non-traditional trivalent m-Pc and SubPc donors are better suited for the Schottky OSC device architecture. Tetravalent and monovalent m-Pc donors may be used with reasonable success in either configuration according to their J_{sc} and FF values; however, when also considering the V_{oc}, these donors perform best with the Schottky device architecture.

In previous work, it was established that the suitability of a donor for the Schottky device architecture relates strongly to its HOMO position.[72] To this end, it was demonstrated that donors with HOMO energy levels either too close or too far from that of C_{60} are ineffective for use in Schottky OSCs. When the HOMO energy levels are too close (i.e. ΔHOMO < 0.2 eV), the donor-acceptor interface is incapable of separating strongly bound intermolecular C_{60} aggregate excitons, which are shown here to generate a large amount of photocurrent in the ~450 nm wavelength region. When the HOMO energy levels are instead too far apart (i.e. the donor has a shallow HOMO, ΔHOMO > 0.9 eV), the donor acts as a trap for holes (in light of the Schottky device architecture), and negatively affects all of the photovoltaic output parameters – V_{oc}, FF and ultimately the J_{sc} due to poor charge extraction and associated charge recombination. Since the V_{oc} is fundamentally related to the $HOMO_{donor}$-$LUMO_{acceptor}$ offset in the BHJ architecture,[54, 182, 183] the V_{oc} (at a 1:1 D:A mixing ratio) provides a rough estimate for the m-Pc HOMO. Interestingly, the traditional (divalent) m-Pc:C_{60} OSCs that show a decrease in FF with

increasing C_{60} content are among the OSCs with the lowest V_{oc} values (510 to 555 mV), and thus have the m-Pcs with the shallowest HOMO energy levels (also supported by the HOMO values obtained in literature, Figure 4-2). The remaining m-Pc:C_{60} OSCs with low V_{oc} values, H_2Pc and TiOPc, show very little change in FF with the transition from the BHJ architecture (1:1 D:A mixing ratio) to the Schottky architecture (1:3 or 1:7 D:A mixing ratio). It is suggested that the poor performance of the traditional m-Pc donors in mixed layers with high C_{60} content is, at least in part, due to the non-ideal position of their HOMO energy levels. In terms of their molecular properties, the traditional divalent species lack strong electron withdrawing groups to sufficiently lower their HOMO values for proper use in Schottky OSCs. In contrast, the non-traditional m-Pc:C_{60} OSCs with high V_{oc} values, including those employing ClInPc, ClGaPc and SubPc donors, have deeper HOMO energy levels, associated with the presence of the strong electron withdrawing group (Cl) in their molecular structures. It follows that these non-traditional m-Pc:C_{60} OSCs show improvements to FF in the transition from the BHJ architecture to the Schottky architecture, and ultimately exhibit superior performance with the Schottky OSC structure. The result is that SubPc as well as the trivalent m-Pcs, such as ClInPc and ClGaPc, yield generally higher performance OSCs, and are good candidates for further studies in this thesis.

4.4. Conclusions

In this chapter, the rationale for the materials selection for the research completed throughout this thesis was provided, which is particularly important due to the vast number of materials available in the OSC field. This chapter also served to introduce basic OSC performance data and associated output parameters, especially considering OSCs employing m-Pc donors and OSCs that make use of the fullerene-based Schottky device structure. The following major conclusions were drawn:

- Trivalent m-Pc:C_{60} OSCs (especially ClInPc:C_{60} and ClGaPc:C_{60}) and SubPc:C_{60} OSCs were specifically identified for research on time-zero charge transport and extraction properties, owing to their

reasonable performance, their good reproducibility from device to device, and their high relevance/research impact. ClInPc is employed for the studies in **Chapter 5**, while ClGaPc is used for studies in **Chapter 6**. SubPc is used in combination with ClInPc for ternary OSCs in **Chapter 7**.

- Both the ClInPc:C_{60} materials system (for research in **Chapter 9** and **Chapter 10**), as well as the solution processable P3HT:PCBM materials system (for research in **Chapter 8** and **Chapter 9**) were selected for understanding the variations of charge transport with time. This selection allows for deductions that are highly applicable to a very wide range of OSCs.
- From device performance data, it was demonstrated that there are many non-traditional m-Pcs that can contribute to impressive photovoltaic properties. It was shown that SubPc and trivalent m-Pcs are optimally employed in Schottky architecture OSCs, where they benefit from enhanced V_{oc}, J_{sc} and FF. This contrasts strongly with the traditional divalent m-Pcs, such as CuPc and ZnPc, which are best employed in the standard BHJ device architecture with a 1:1 D:A mixing ratio.
- Considering their relatively simple synthesis and purification in general, the use of non-traditional m-Pcs in OSCs offers a promising route toward cheap and efficient solar energy.

Chapter Five:

Insights into Interfacial Electron and Hole Extraction Layers[1]

This chapter examines efficiency variations due to the choice of interfacial extraction layers in vacuum-deposited SM-OSCs. This chapter thus serves to address many of the questions regarding the suitability of the interfacial extraction layer for efficient charge collection. The combination of exciton blocking properties and the presence of metal deposition-induced defect states are shown to be necessary for EELs in SM-OSCs. In this regard, both BCP and Alq_3 can act as EELs, but their efficacies relate strongly to deposition conditions. Thick MoO_3 HELs alone are shown to be suitable for inverted vacuum-deposited OSCs, provided the HEL thickness is sufficient to prevent metal deposition-induced damage to the photo-active layer. It is furthermore shown that the characteristics of the MoO_3 film change with repeat evaporation runs from the same source material. These variations have strong effects on P-OSCs, with an effective halving of the power conversion efficiency after only three MoO_3 evaporation runs. SM-OSCs are instead shown to be prone to large changes in efficiency and device lifetime as a function of the delay time in between deposition of the MoO_3 HEL and subsequent photo-active materials. The results emphasize subtleties in interfacial layer deposition processes that play significant roles in obtaining reproducible and scientifically relevant data.

5.1. Introduction

In **Chapter 4**, it was noted that OSCs have experienced vast improvements in their efficiencies due to concurrent research in materials synthesis, with the development of hundreds of photo-active organic electronic materials,[17] and in the optimization of the OSC device structure. **Chapter 6**

[1] The majority of the material in this chapter was published in:
G. Williams,H. Aziz, *SPIE Organic Photovoltaics XIV Proceedings*, 2013, p. 88301.
G. Williams,H. Aziz, *SPIE Organic Photonics XV Proceedings*, 2014, pp. 91841Q.
, reproduced here with permission.

elaborates on the optimization of the OSC device structure, providing a more comprehensive understanding of charge collection with changes to the bulk photo-active layers. However, before examining charge collection in varied OSC architectures, it is worthwhile to gain a better understanding of the other critical components within a modern OSC, specifically the contacts and interfacial extraction layers placed at the organic/electrode interfaces. To this end, EELs and HELs have proven to play a vital role in both device efficiency,[119] and in device lifetime.[102] One must ensure that photo-generated carriers are transported across the organic-electrode interface to the external circuit. Interfacial extraction layers are therefore crucial in the final step in the charge collection process. Traditional extraction layers, such as PEDOT:PSS, LiF and BCP, have been shown to be fundamental in achieving high efficiency OSCs.[40, 186, 187] The baseline performance of both P-OSCs and SM-OSCs employing standard interfacial extraction layers are described in more detail throughout **Chapter 9**. The implementation of interfacial extraction layers in OSCs, however, is not straightforward. EELs and HELs also add to device complexity and, when used without proper foresight, they can even have an opposite (detrimental) effect on OSC efficiency or lifetime. To this end, PEDOT:PSS has been suggested to have deleterious effects on stability due to inter-electrode degradation,[11, 109, 188] and LiF has been shown to suffer from light-induced variations in an organic/LiF/metal configuration.[189] Furthermore, wide bandgap organic materials, such as BCP, are liable to cause exciton-induced degradation at adjacent metal interfaces,[190] which may negatively impact OSC lifetime.[191] Such interfacial layer stability considerations are addressed in **Chapters 8**-**10**, where OSCs are studied in consideration of changes in device performance and charge collection properties with time.

As discussed in **Chapter 1**, the primary role of most extraction layers is to better align the electrode work function with the energy level of the adjacent organic material – that is, to align the cathode work function to the LUMO of the acceptor and the anode work function to the HOMO of the donor. EELs in vacuum-deposited SM-OSCs, however, play additional roles, where they are also used to

block excitons from the organic-electrode interface, and to prevent damage of the organic film during top electrode deposition. While there have been a number of studies on the main purpose of the wide bandgap organic EEL in vacuum-deposited OSCs,[39, 40, 192] many questions remain regarding the qualification of suitable interfacial extraction materials. Further questions remain regarding their use in new or non-traditional device structures, such as SM-OSCs built in the inverted configuration. In a similar vein, MoO_3 has become an increasingly important HEL for OSCs, especially with the advent of the fullerene-based Schottky OSC device architecture. However, there remain uncertainties regarding the reproducibility and quality of MoO_3 films, especially when the film is formed by vacuum deposition. In light of these realizations, it is beneficial to obtain a more thorough understanding of new and alternative interfacial extraction layers as they are discovered and implemented in OSCs.

In this chapter, the finer working points of the EEL and the HEL in both upright and inverted vacuum-deposited SM-OSCs are elucidated. As noted above, these SM-OSCs traditionally employ a wide bandgap organic EEL in the standard OSC configuration. Several organic extraction layer materials are examined to determine their role in OSC performance, and for their impact on photo-stability and thermal stability. It is demonstrated that the diffusion of metal into the extraction layer is a requirement for conduction, and it is the combination of wide bandgap organic extraction layers and subsequent metal deposition that generates high performance SM-OSCs. It follows that a wide bandgap organic HEL placed between the anode and the photo-active materials in a standard upright OSC blocks both excitons and holes (i.e. in the absence of metal deposition-induced defect states), and thus severely degrades device performance. Finally, it is shown that many of the requirements applied to EELs in standard configuration OSCs can be extended to HELs in inverted OSCs. However, the HEL thicknesses required in inverted OSCs are much larger than the EEL thicknesses used in upright OSCs. This work establishes fundamental design rules for the HEL and EEL in modern OSCs.

As a secondary objective of this chapter, several frequently overlooked facets of OSC fabrication with a vacuum-deposited MoO_3 HEL are examined. It is shown that P-OSCs have strong dependence on the quality of the MoO_3 used for evaporation, and that evaporating multiple times from the same evaporative source/material can strongly impact efficiency. SM-OSCs do not show this same dependence, but instead have a dependence on the time between evaporating MoO_3 and the deposition of subsequent organic layers. This time delay is further shown to affect the SM-OSC stability. The results thus stress that the quality of MoO_3 HEL film quality can alter charge collection properties within the OSC. Such variations could have significant implications for scaling up MoO_3 HEL-based OSCs for practical commercial applications.

5.2. Results and Discussion

5.2.1. The Role of Electron Extraction Layers

As described in **Chapter 1**, a large number of EEL materials have been applied to P-OSCs, including LiF,[32] Cs_2CO_3,[34], poly(ethylene glycol) (PEG),[193] TiO_x,[36] and ZnO[38]. In contrast, vacuum-deposited SM-OSCs usually employ 5-10 nm of wide bandgap organic materials, most commonly BCP.[24, 39, 40] BCP has been proposed to satisfy a number of critical roles:

- to protect the underlying organic materials from damage during top electrode deposition
- to act as an exciton blocking layer to prevent exciton quenching during device operation
- to prevent metal diffusion into the C_{60} layer and thereby prevent the formation of metal donor states that can cause charge recombination and exciton quenching
- to allow for the conduction/collection of electrons through metal deposition-induced defect states

Researchers have since studied a wide number of alternative OSC EEL materials for vacuum-deposited devices; [41, 194-197] however, these studies have produced mixed results, with varying degrees of success reported for both the efficiency and stability of OSCs with the same EEL.

To better understand the qualification of EELs in SM-OSCs, ClInPc:C_{60} OSCs employing a MoO_3 HEL and a variable EEL are first examined with three candidate EELs: BCP, Alq_3 and NPB. These materials have been shown to have similar electron mobility values.[198, 199] Further, as the conduction is expected to be due to metal deposition-induced defect states, slight variations in mobility should have little effect on the present analysis. The materials do, however, vary in their structure, their intermolecular packing and in their energy levels, which may alter the formation of metal deposition-induced defect states during top cathode deposition. The energy band diagram for these materials and the associated OSC device structure used in the present analysis are shown in Figure 5-1.

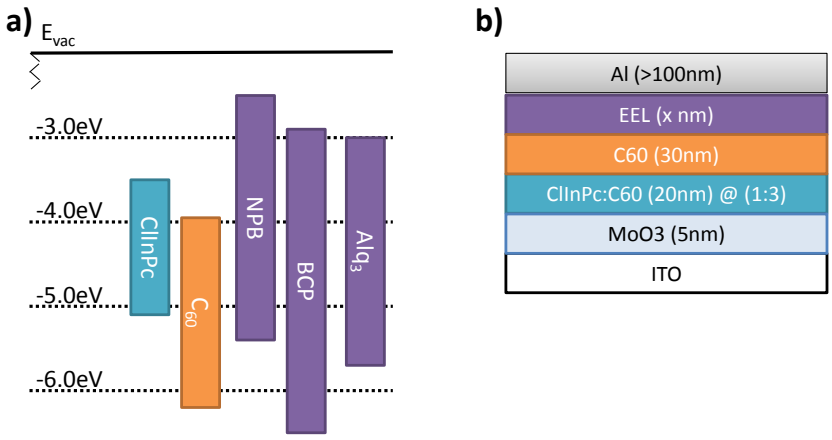

Figure 5-1 - a) Energy band diagram for the OSC donor (ClInPc), acceptor (C_{60}) and several potential EEL materials b) Illustration of a standard upright ClInPc:C_{60} device structure.

The solar cell output parameters for ClInPc:C_{60} OSCs using BCP, Alq_3 and NPB EELs with 8 nm and 12 nm thicknesses are shown in Table 5-1 below. As expected, OSCs with 8 nm and 12 nm of BCP work well to provide 2% PCE. The reasonable FF of ~50% suggests that charge accumulation near the cathode is not significant, in spite of the relatively thick EEL. OSCs with an 8 nm Alq_3 EEL show similar performance with 2.2% PCE; however, their performance decreases rapidly to 1.3% PCE as the thickness

of Alq_3 is increased to 12 nm. Finally, 8 nm NPB EEL devices show a poor PCE of 0.93%, which decreases even further to 0.17% PCE at 12 nm. By using 12 nm NPB instead of 12 nm BCP, a 70% decrease in FF, a 55% decrease in J_{sc} and a 35% decrease in V_{oc} are observed. At first glance, this may seem intuitive, as Alq_3 and BCP are both traditional electron transport materials in organic light emitting diodes (OLEDs), whereas NPB is traditionally used as a hole transport material. However, from the energy band diagram in Figure 5-1a, it is clear that there is a substantial barrier to electron transport for all materials. It follows that metal deposition-induced defect states are the most realistic possibility for carrier transport through the wide bandgap EEL.[24, 192]

Table 5-1 - Solar cell output parameters for ITO/MoO_3/ClInPc:C_{60}(1:3)/C_{60}/EEL/Al solar cells. EELs that provide reasonable performance are shaded in grey.

EEL	t (nm)	Jsc [mA/cm2]	Voc [mV]	FF [%]	Eta [%]
BCP	8	4.1	998	49	2.0
BCP	12	4.0	998	50	2.0
Alq3	8	4.4	1001	49	2.2
Alq3	12	3.7	902	38	1.3
NPB	8	3.7	750	34	0.93
NPB	12	1.8	649	14	0.17

As a point of note, the Alq_3 EEL devices generally required some form of a gentle 'activation' to operate efficiently. To this end, exposing these devices to a gentle heat treatment for a brief period of time (40-50 ^{o}C for an hour) improved their PCE by nearly 100% (~1% to over 2% PCE). Since conduction through the EEL is essentially dictated by metal deposition-induced defect states,[24, 192] it is suggested that the heat treatment allows for better diffusion of Al into the Alq_3 layer, which grants conduction through the otherwise electron-blocking layer. It also follows that the ability of the top electrode metal to diffuse through EEL is strongly affected by factors such as deposition rate/power and the total time of deposition. Given that these deposition parameters vary among research groups, this is likely the cause for the large variations in photovoltaic output parameters observed for the same EELs in OSCs from different research groups in literature.

In order to better understand the variations observed for the different EEL materials discussed above, it is useful to look at the dark IV characteristics, as shown in Figure 5-2a. OSCs with 8 nm of BCP clearly show diode-like behavior with very little leakage current. OSCs with 8 nm of Alq_3 also show diode-like IV characteristics; however, they also show substantial leakage current in reverse bias, indicative of shunting – perhaps due to excess diffusion of Al into the photo-active layers. OSCs with 8 nm of NPB have essentially no current flow from -1 V to 1 V, which implies poor injection/extraction into/out of the device. As such, NPB clearly acts as a blocking layer. For regular OSC operation, this barrier results in high R_s values, large recombination currents and, as a consequence, reduced FF and J_{sc} values, as observed in Table 5-1. This blocking effect is also observed with an Alq_3 EEL when its thickness is increased to 12 nm, as shown in Figure 5-2.b.

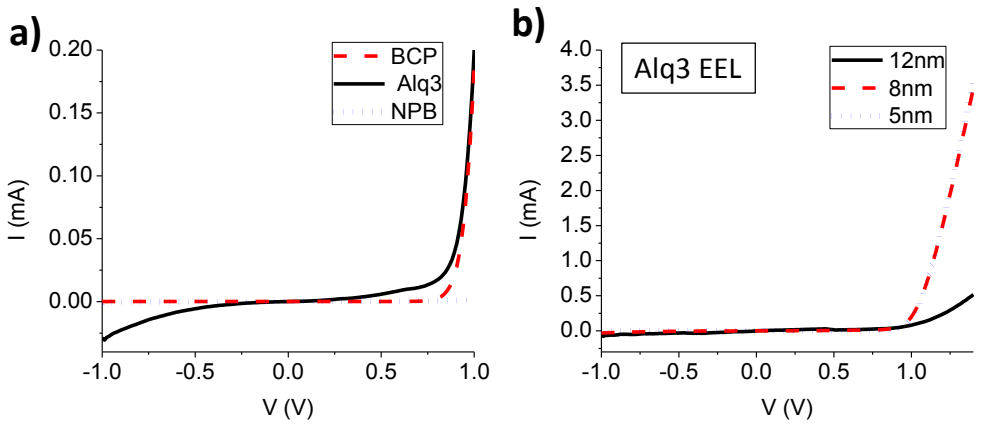

Figure 5-2 - Dark IV curves of ITO/MoO_3/ClInPc:C_{60} (1:3)/C_{60}/EEL/Al devices with a) 8 nm BCP, Alq_3 and NPB EELs, and b) 5 nm, 8 nm and 12 nm Alq_3 EELs.

Based on this analysis, BCP is shown to be the most reliable EEL material of the three examined. Alq_3 is a suitable EEL provided it is made thin enough to allow for metal diffusion, and provided there is sufficient driving energy to allow for the metal atoms to diffuse through the entirety of the EEL. Finally, NPB acts as a blocking layer even at a thickness of 8 nm, indicating that it is less capable of forming a conductive pathway. One can thus outline the most significant criterion for EELs when considering device efficiency: the EEL material and thickness must allow for good penetration of metal atoms for good conduction; however, one must avoid metal diffusion into the active layer. Such a stringent

requirement on the EEL thickness presents a significant challenge to the manufacturing industry, and, as a consequence, provides a critically important area of research: the study of EEL materials that can be made thicker without compromising device performance.

Given that Alq_3 and BCP EELs can yield similar levels of efficiency in ClInPc:C_{60} OSCs, and noting BCP's propensity to crystallize and adversely affect OSC performance,[41, 200] it is interesting to test the photo- and thermal-stability of OSCs with 8 nm EELs of either Alq_3 or BCP. To this end, the use of Alq_3 instead of BCP has been shown to substantially enhance ambient stability (i.e. with moisture and oxygen)[201]; however, the intrinsic photo- and thermal-stability of OSCs with BCP versus Alq_3 EELs is still unknown. ClInPc:C_{60} OSCs with BCP and Alq_3 EELs were thus exposed to 1-sun intensity light in a dry N_2 environment for 400 hours. The PCE values for these devices were tracked during light exposure are shown in Figure 5-3a. A second set of ClInPc:C_{60} OSCs with BCP and Alq_3 EELs were heated on a hot plate (60 ^{o}C) in a dry N_2 environment for 36 hours, and their PCE values are shown in Figure 5-3b. From Figure 5-3a, it is clear that, when kept in a controlled environment with low O_2/H_2O content, the Alq_3 EEL does not offer any substantial benefits to photo-stability compared to the BCP EEL. Further, from Figure 5-3b, the BCP EEL is shown to have similar thermal-stability as the Alq_3 EEL even when the device is heated at 60 ^{o}C. Note that, in Figure 5-3b, the Alq_3 EEL devices showed an initial improvement in PCE for reasons discussed previously (the diffusion of Al through the EEL to allow for better electron conduction). As such, on the basis of photo- and thermal-stability, both Alq_3 and BCP are suitable candidates for EELs when kept in a dry N_2 environment.

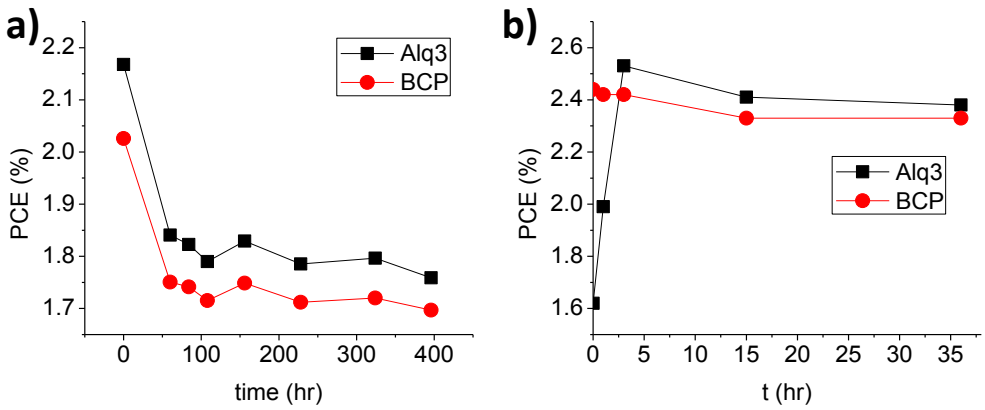

Figure 5-3 - a) PCE values of ITO/MoO_3/ClInPc:C_{60} (1:3)/C_{60}/EEL/Al OSCs with Alq_3 and BCP EELs over 400 hours of light exposure. b) Normalized PCE values of a second set of the same devices over 36 hours of heat exposure (60 °C).

5.2.2. The Role of Hole Extraction Layers

To further understand charge collection processes across wide bandgap organic extraction layers, the present analysis is extended to the HEL. 2,6-bis(3-(carbazol-9-yl)phenyl)pyridine (DCzPPy) is an ambipolar wide bandgap semiconductor, which, similar to BCP at the EEL, may serve to block excitons at the HEL, thereby preventing exciton recombination at the anode. Since the HEL is placed between the ITO bottom electrode and the organic layers, it has no metal deposition-induced defect states to aid with carrier transport/conduction. The use of a DCzPPy HEL thus helps verify the impact and the importance of the subsequent metal deposition in forming a proper extraction layer. More specifically, this experiment can help to rule out other mechanisms for conduction, such as tunneling across thin regions of the extraction layer (e.g. due to non-uniformity of deposition or film roughness). The energy level diagrams and associated device structure for the DCzPPy HEL devices are shown in Figure 5-4. Note that this device employs a 1:1 donor:acceptor ratio, instead of the 1:3 ratio used in the previous analysis. Since an organic HEL is employed in lieu of MoO_3, it is not possible to make use of the Schottky/band-bending effects that allow for V_{oc} enhancement in high acceptor content cells,[72] and so the better performing cells comprise an active layer with a 1:1 donor:acceptor mixing ratio.

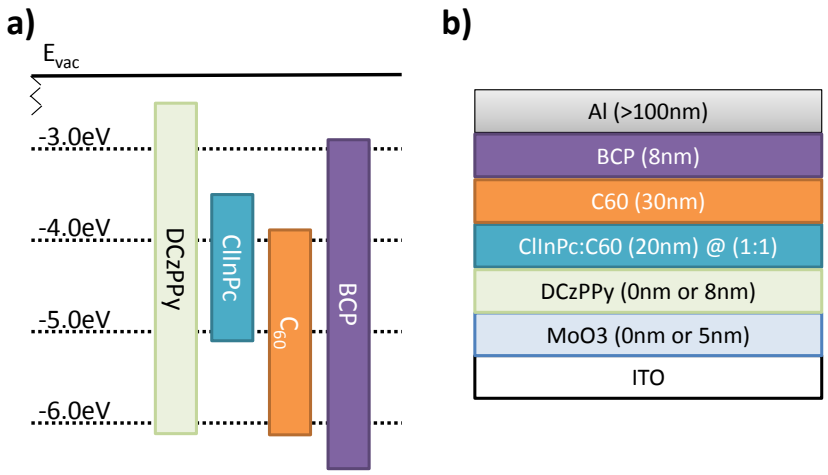

Figure 5-4 - a) Energy band diagram showing the relative HOMO/LUMO of the DCzPPy HEL to the donor, acceptor and EEL. b) Illustration of the upright device structure used to verify the efficacy of DCzPPy as a HEL.

The output parameters for the ClInPc:C_{60} OSCs with a DCzPPy HEL are listed in Table 5-2. The OSC with no HEL shows very poor performance due to poor alignment of the ITO work function with the HOMO of ClInPc. This is manifested as a 63% reduction in V_{oc} and a 44% reduction in Jsc compared to the control device employing a 5 nm MoO_3 HEL. As a point of note, the 5 nm MoO_3 HEL control device (at a 1:1 donor:acceptor ratio) achieves a PCE of ~1.6%, slightly lower than the ~2% PCE of the Schottky OSCs examined previously (at a 1:3 donor:acceptor ratio), in agreement with results from **Chapter 4** and **Chapter 6**. The use of a DCzPPy HEL directly on ITO strongly degrades the J_{sc} and FF, resulting in poorer overall performance than the device without any HEL. The use of a MoO_3 / DCzPPy HEL also shows reduced J_{sc} and FF compared to the MoO_3 HEL control. From these data, one can conclude that it is not sufficient to merely employ an extraction layer that blocks excitons. It is the metal deposition-induced defect states that allow for conduction, and it is the combination of this property with the exciton blocking property that determines the suitability of the wide bandgap organic extraction layer.

Table 5-2 - Solar cell output parameters for ITO/HEL/ClInPc:C_{60}(1:1)/C_{60}/BCP/Al OSCs.

HEL	Jsc [mA/cm2]	Voc [mV]	FF [%]	Eta [%]
No HEL	2.55	321	40	0.33
5 nm MoO_3	4.57	871	40	1.59
8 nm DCzPPy	0.74	536	5	0.02
5 nm MoO_3 / 8 nm DCzPPy	3.40	914	23	0.72

Metal deposition on top of a wide bandgap organic extraction layer has been shown to be necessary for conduction, so it is natural to extend the present analysis to inverted devices where the top anode is deposited on the HEL (instead of the top cathode being deposited on the EEL). Inverted OSCs were fabricated with the structure: ITO/Cs_2CO_3/ClInPc:C_{60} (1:1) (40 nm)/HEL/MoO_3(5 nm)/Al. The placement of the organic HEL between the MoO_3/Al contact and the mixed ClInPc:C_{60} layer again prevents the realization of fullerene-based Schottky OSCs, and so a 1:1 donor:acceptor ratio is employed. The PCE values for these inverted OSCs with both DczPPy and NPB HELs at varying thicknesses are shown in Figure 5-5a. DCzPPy HEL OSCs exhibit very low PCE values at both 6 nm and 12 nm – lower than the control device with no HEL. This is due to DCzPPy acting as a blocking layer, even at low thicknesses. The NPB HEL devices, however, have a reasonable PCE of 1.4% with 12 nm of NPB. Since these OSCs use both an NPB and a 5 nm MoO_3 HEL, this performance is achieved at an effective HEL thickness of 17 nm – more than double that of the BCP EEL thickness in the upright device configuration. It is also interesting that inverted devices employing an NPB HEL perform reasonably well, whereas the upright devices with an NPB EEL examined earlier showed rather poor performance (PCE values always less than 1%). It is feasible that the relative energy levels of the metal deposition-induced defect states within the extraction layer vary from material to material. Such an effect is, as of yet, poorly understood, and the capacity of any given material to form suitable energy levels for charge transport merits further investigation.

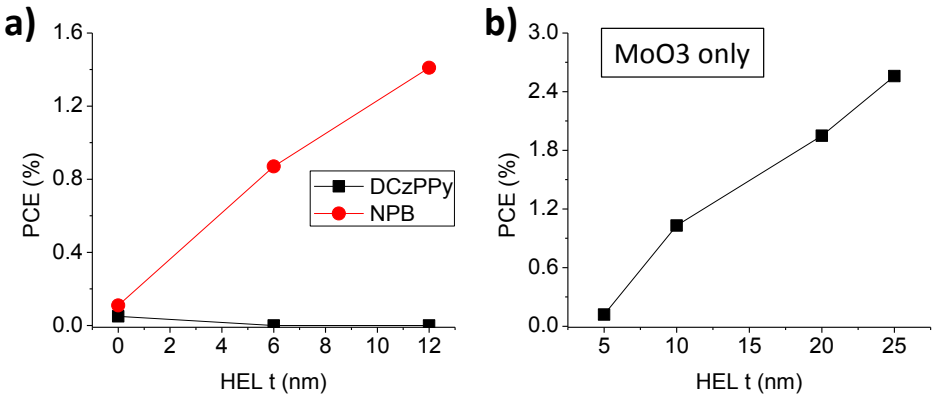

Figure 5-5 - Power conversion efficiencies for inverted OSCs with different HELs. Two HEL configurations are presented a) organic/MoO_3 HEL: ITO/Cs_2CO_3/ClInPc:C_{60} (1:1)/DCzPPy or NPB (x nm)/MoO_3 (5 nm)/Al, and b) pure MoO_3 HEL: ITO/Cs_2CO_3/ClInPc:C_{60} (1:3)/MoO_3 (x nm)/Al.

ClInPc:C_{60} OSCs without a wide bandgap organic HEL, but rather with a varying thickness MoO_3 HEL, were also investigated. The PCE values for these devices with different MoO_3 thicknesses are shown in Figure 5-5b. For these devices, there is direct contact between the MoO_3/Al electrode and the mixed ClInPc:C_{60} layer, so a 1:3 donor:acceptor ratio is used. In this manner, it is also possible to determine if Schottky OSCs are possible in an inverted configuration. These devices show poor efficiency at 5 nm MoO_3 – the typical MoO_3 HEL thickness used in upright devices. However, the PCE increases strongly with increasing MoO_3 thickness, allowing for a final PCE of 2.6% with 25 nm MoO_3. It is again worth noting that this effective HEL thickness is substantially higher than the EEL thickness in upright devices at more than three times the typical BCP thickness. Further, given the high V_{oc} of ~970 mV, it is clear that this inverted configuration also benefits from the Schottky OSC device structure.

One possible reason for the thicker HEL requirement in the inverted architecture may relate to the alignment of the contact work function to the relevant molecular orbital. To this end, aluminum has a work function of 4.1 eV, which is relatively close to the LUMO of C_{60} (~3.9 eV), but very far from the HOMO of ClInPc (~5.3 eV). As such, it is absolutely critical to form a complete surface coverage of MoO_3 on the generally rough organic layers in the inverted architecture to ensure good hole extraction. For the standard architecture, the EEL must protect the underlying organics, but the relative alignment of

the extraction layer's energy levels is less critical, so a thinner layer thickness is feasible (and necessary to allow for conduction via metal deposition-induced defect states). Furthermore, for the inverted architecture, MoO_3 may be made quite thick since MoO_3 and Al are known to undergo a reaction to generate a conductive transport layer.[202]

A comparison of the standard and converted configuration OSCs is provided in Table 5-3 below. The device structures are summarized as follows:

- Standard Configuration (x:y donor:acceptor)
    - 1:1 – ITO/MoO_3 (5 nm)/ClInPc:C_{60} (1:1) (40 nm)/BCP (8 nm)/Al
    - 1:3 – ITO/MoO_3 (5 nm)/ClInPc:C_{60} (1:3) (40 nm)/BCP (8 nm)/Al
- Inverted Configuration (x:y donor:acceptor)
    - 1:1 – ITO/Cs_2CO_3(<1 nm)/ClInPc:C_{60} (1:1) (40 nm)/NPB (12 nm)/MoO_3 (5 nm)/Al
    - 1:3 – ITO/Cs_2CO_3 (<1 nm)/ClInPc:C_{60} (1:3) (40 nm)/MoO_3 (25 nm)/Al

For both donor:acceptor ratios, the inverted configuration devices can achieve similar PCE values as the upright device configurations, indicating that there is sufficient conduction through the chosen HELs. Given their superior performance and their simple fabrication, 25 nm MoO_3 HELs are proposed as optimal for inverted vacuum-deposited OSCs.

Table 5-3 - Comparison of output parameters for representative upright and inverted ClInPc:C_{60} OSCs at different donor:acceptor concentrations.

	Upright Configuration		Inverted Configuration	
Donor:Acceptor	1:1	1:3	1:1	1:3
Jsc	5.8	6.7	5.3	6.3
Voc	770	920	770	970
FF	39	40	34	42
PCE	1.7	2.5	1.4	2.6

5.2.3. Reducing Variability in Vacuum-Deposited MoO_3 Extraction Layers

In spite of their many improvements in efficiency and lifetime, OSCs suffer from a high amount of variability in their performance from device to device. The unpredictability in the device performance of OSCs is exacerbated in more advanced device structures, such as those employing HELS, EELs or dedicated charge transport layers. MoO_3 has recently arisen as a strong candidate to replace the widely used PEDOT:PSS as an HEL material. When deposited on ITO, it is known to increase the effective work function allowing for enhanced hole extraction properties.[71, 203] MoO_3 has further been demonstrated to have generally positive effects on device stability by minimizing degradation that otherwise occurs at the organic-metal interface.[15, 109] However, there still remain many unknowns regarding its use in OSCs, especially regarding its processing considerations and its capacity to make highly reproducible devices. By obtaining a more rigorous understanding of the fabrication of MoO_3 HELs, the material can be used with confidence in subsequent charge transport studies in **Chapters 6** and **7**, as well as the extensive photo-stability studies in **Chapters 8** through **10**.

5.2.3.1. Materials Systems for MoO_3 Quality Studies

In this section, the impact of vacuum-deposited MoO_3 HEL film quality is examined for both P-OSCs and SM-OSCs (specifically P3HT:PCBM and ClInPc:C_{60} OSCs, as discussed in **Chapter 4**). The OSC materials' corresponding energy levels are provided in Figure 5-6 below. From literature, when the MoO_3 film is deposited in high vacuum, the resulting effective work function of the ITO/MoO_3 contact can be as deep as 6.8 eV.[71] However, the work function of MoO_3 is also known to decrease when the MoO_3 film is exposed to ambient or N_2 environments.[203, 204] By studying both SM-OSCs and P-OSCs it is possible to test, from a MoO_3 quality standpoint, two very different fabrication scenarios. In the case of the SM-OSC, the organic active layers are deposited on a MoO_3 film that is always kept in high vacuum

(<5x10^{-6} torr base pressure). In the case of the P-OSC, the active layers are spincoated on a MoO_3 film that is necessarily exposed to N_2.

It should be noted that several researchers have examined solution processable MoO_3 films,[205-208] with the objective to easily integrate MoO_3 HELs with solution-coated polymer active layers. In the present work, the focus is instead placed on vacuum-deposited MoO_3 films, which have been employed many times successfully in literature,[118, 203] but are less studied in the role that film quality plays in device performance and charge collection. Such efforts are particularly important because they help to reduce possible experimental variability that may be inherent in OSCs that use vacuum-deposited MoO_3.

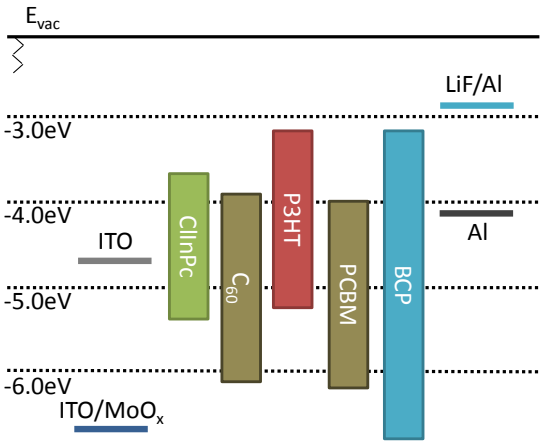

Figure 5-6 - Energy levels and contact work functions of the species studied in this section.

The UV-Vis absorbance spectra of films of C_{60}, ClInPc and P3HT:PCBM (1:1) are shown in Figure 5-7. The ClInPc:C_{60} OSCs are effective at near-IR absorption due to ClInPc's 720 nm peak absorption, whereas the P3HT:PCBM OSCs are better suited for broad visible light absorption. As discussed in **Chapter 4**, the use of high C_{60} content in the ClInPc:C_{60} OSCs grants additional C_{60} aggregate absorption in the visible regime, and enhances overall device performance through Schottky band bending effects.[72, 209, 210] Such band bending effects are heavily dependent on the MoO_3 film's deep work function, and so this structure serves as an ideal platform to examine the role of MoO_3 quality in device performance.

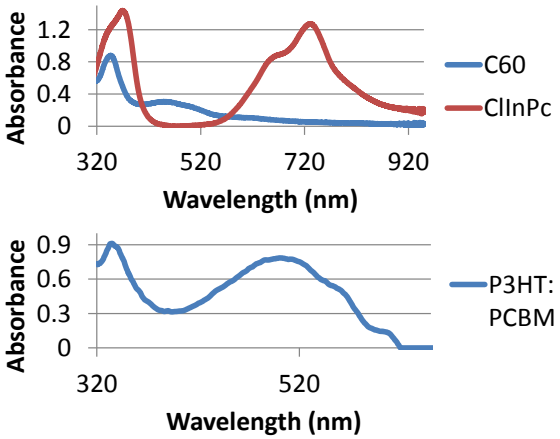

Figure 5-7 - Absorbance spectra of thin films of C_{60}, ClInPc and P3HT:PCBM (1:1).

As a first point of interest, the effect of MoO_3 thickness on PCE was investigated in 40 nm ClInPc:C_{60} (1:3) OSCs. When varying the MoO_3 thickness between 2 nm and 15 nm, the PCE did not change in any significant manner, with values pinned between 2.33% and 2.40%. In general, however, when the MoO_3 thickness is set below 5 nm, sporadic device shorting (catastrophic failure) becomes more common. This is suggested to be due to the inherent roughness of the ITO film, and the lack of conformal coverage of the ultra-thin MoO_3 film. When the MoO_3 thickness is set to be 5 nm or larger, OSCs are fabricated with high reproducibility and no immediate failures (near-100% yield).

5.2.3.2. MoO_3 Quality Effects on P3HT:PCBM Polymer Solar Cells

P3HT:PCBM P-OSCs were fabricated on ITO/MoO_3 contacts following the standard procedure detailed in **Chapter 3** (devices were pre-annealed and used an LiF EEL). The resulting OSCs achieve an average PCE of 2.2%, with a FF of 66%, a J_{sc} of 6.3 mA/cm^2 and a V_{oc} of 0.52 V. In contrast to standard fabrication methodologies, where MoO_3 is replaced between fabrication runs, a second set of P3HT:PCBM P-OSCs were then fabricated using the same MoO_3 source. It is worth noting that, since the evaporation chamber is equipped with a load lock for sample transfer, the MoO_3 evaporation source was kept at high vacuum (<5x10^{-6} torr) at all times. This process was repeated a second time, allowing

for the fabrication of 3 identical sets of devices, but with different MoO_3 quality: fresh (deposition #1), 1x'used' (deposition #2) and 2x'used' (deposition #3). The PCE, J_{sc} and FF values for these devices are shown in Figure 5-8.

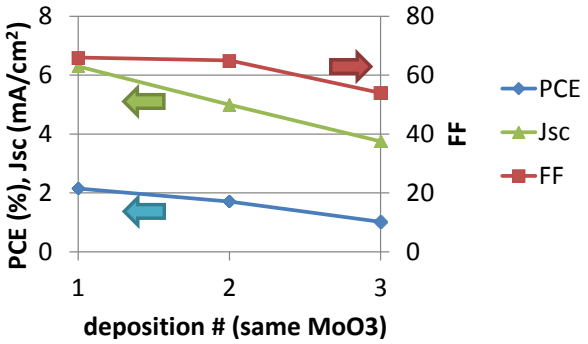

Figure 5-8 - PCE, J_{sc} and FF values for P3HT:PCBM P-OSCs fabricated with the same MoO_3 source material.

From Figure 5-8, each successive deposition from the same MoO_3 source material decreases the PCE of the otherwise identical P-OSCs. By the third deposition from the same MoO_3 source, the PCE is 1.0%, less than half of the PCE of the first P-OSC fabricated with fresh MoO_3. This is due to the decrease in J_{sc} from 6.3 mA/cm^2 to 3.8 mA/cm^2, and the decrease in FF from 66% to 54%. Interestingly, the V_{oc} for these devices did not change with the quality of MoO_3, remaining at ~0.5 V. The unchanged V_{oc} is not wholly obvious – since the MoO_3 HEL is employed primarily to obtain a deeper effective work function, it would be expected that any deterioration of the HEL would strongly affect the V_{oc}. More specifically, as noted in **Chapter 1**, the V_{oc} is dependent on proper alignment of the anode and the donor HOMO, and changes in the work function of the HEL due to varying MoO_3 source material quality could impact this alignment. However, as an addendum to this statement, as long as the anode's effective work function is deeper than the HOMO of the donor, the V_{oc} should be pinned due to the formation of the integer charge transfer state at the organic/anode interface.[211] From literature, when briefly exposing the MoO_3 film to ambient conditions, the effective work function of ITO/MoO_3 can decrease to 5.24 eV,[71] which is still within reasonably good alignment with the P3HT HOMO. As such, unless the work function

shifts considerably, which is not expected to occur with the brief exposure to N_2 in the present work, the V_{oc} is expected to remain constant, as is observed presently.

To better understand the variation in J_{sc}, FF and PCE with MoO_3 HEL quality, it is worthwhile to examine literature on solution-processed MoO_3 layers, as these studies are largely concerned with MoO_3 film quality. To this end, Tremolet de Villers et al. encountered a similar J_{sc} and FF dependence on MoO_3 quality when preparing solution-processed MoO_3 contact layers.[206] The researchers found that the quality of the MoO_3 HEL can affect the vertical phase distribution of P3HT and PCBM. To this end, MoO_3 films with lower oxygen content due to higher annealing temperatures were found to result in the preferential accumulation of PCBM near the anode of the device. A similar effect is suggested to occur in the present work, especially given that the MoO_3 source material loses oxygen content during vacuum thermal evaporation. This well-known oxygen loss phenomenon[212] was confirmed in the present study by monitoring material outgassing during the MoO_3 source heating, and also by noting the color change from light gray to dark gray of the MoO_3 source powder. In the ensuing P-OSC, the high concentration of PCBM near the anode acts as a barrier to charge transport, leads to charge recombination losses, and degrades the J_{sc}, FF and PCE. The data thus suggest that history of the MoO3 source material can influence P-OSC morphology and, as a consequence, alter P-OSC photovoltaic output parameters.

5.2.3.3. MoO_3 Quality Effects on ClInPc:C_{60} Small Molecule Organic Solar Cells

Given the strong dependence of P-OSCs on MoO_3 source quality, the performance of ClInPc:C_{60} SM-OSCs deposited sequentially from the same MoO_3 source material was also investigated. The results are shown in Figure 5-9 below. The SM-OSCs show very small changes in performance when using the same MoO_3 evaporation source. In fact, the J_{sc} is shown to improve very slightly with the 4x-used MoO_3 source. The relatively constant performance is reasonably straightforward to understand. Since the

ClInPc:C_{60} active layer is deposited by vacuum thermal evaporation (and not by spincoating), there is little possibility for rearrangement of the C_{60} and ClInPc molecules – the substrate is kept cool, so the molecules stick to the MoO_3 HEL and remain relatively stationary. In contrast, when P-OSCs are spincoated onto an ITO/MoO_3 contact, the residual solvent and subsequent thermal annealing treatment allow for vertical phase separation and the observed trends described previously. Therefore, it is found that the method of device fabrication (vacuum thermal deposition versus spincoating) can have a significant role in the inter-compatibility of layers within the OSC: an HEL that is ideal for a SM-OSC may feasibly result in poor device performance when implemented in a P-OSC.

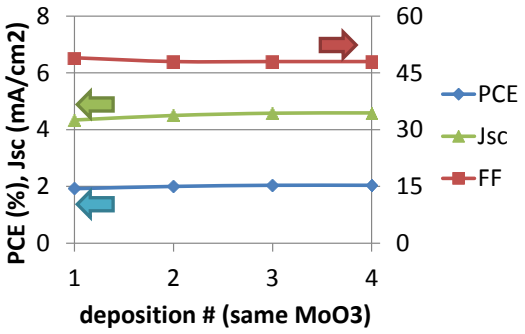

Figure 5-9 - PCE, J_{sc} and FF values for ClInPc:C_{60} SM-OSCs fabricated with the same MoO_3 source material.

While the performance of the SM-OSC may not be dependent on the quality of the source MoO_3 material, it is worthwhile to further examine how MoO_3 deposition methodologies may impact device performance. Of particular note, it is interesting to know the effect of delaying deposition of the organic layers after deposition of the MoO_3 HEL. It is also interesting to see the effect (if any) of exposing the MoO_3 source material to air/ambient in between depositions. Four different fabrication methods of the MoO_3 layer, while studying the same ClInPc:C_{60} active layer, were therefore devised. Note that the different methods were all implemented on the same substrate, so the ClInPc:C_{60} layer is identical (40 nm, 1:3 donor:acceptor) across the four methods. The corresponding photovoltaic output parameters for these devices are shown in Table 5-4 below.

- Method A: Fresh MoO_3, with t=17 hours delay between deposition of MoO_3 and ClInPc:C_{60}

- Method B: 1x'used' MoO_3, MoO_3 source material exposed to air, with t=12.5 hours delay
- Method C: 2x'used' MoO_3, MoO_3 source material exposed to air twice, with t=2.5 hours delay
- Method D: Fresh MoO_3, with t=0 hours delay

Table 5-4 - Photovoltaic output parameters for ClInPc:C_{60} OSCs with varying MoO_3 HEL deposition conditions.

	Jsc [mA/cm^2]	Voc [mV]	FF [%]	PCE [%]
A	4.6	780	45	1.6
B	4.7	880	46	1.9
C	4.8	930	47	2.1
D	4.8	940	47	2.1

In agreement with Figure 5-9 and the discussion above, the quality of the MoO_3 source material has very little impact on the SM-OSC photovoltaic parameters, even if the MoO_3 source is exposed to air/ambient in between deposition cycles. To this end, it is observed that the 2x'used' MoO_3 (method C) has roughly the same PCE as the fresh MoO_3 in method D, with only a small difference in V_{oc}. Furthermore, both methods A and D use fresh MoO_3, yet they have drastically different PCE values. This difference in performance can instead be attributed to the delay between deposition of the MoO_3 HEL and the subsequent deposition of the organic active materials (i.e. ClInPc:C_{60}). To visualize this phenomenon better, the PCE and V_{oc} versus this time delay are shown in Figure 5-10 below.

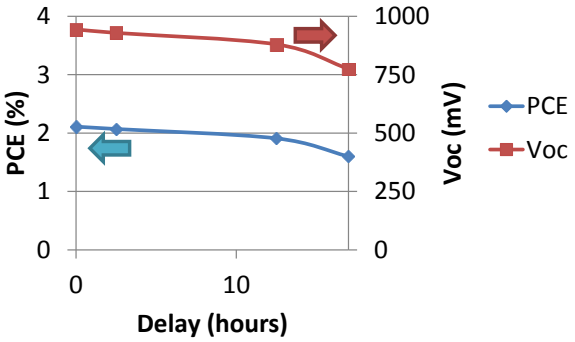

Figure 5-10 - PCE and V_{oc} values of ClInPc:C_{60} OSCs versus time delay after deposition of MoO_3.

From Figure 5-10, as the time delay between deposition of MoO_3 and subsequent organic layers increases, the performance of the SM-OSC decreases. This is shown to be largely due to a reduction in

V_{oc}, although the J_{sc} is also affected for very long delays. This decrease in performance is therefore different than that observed for the P-OSCs described previously. Specifically, the P-OSCs showed a strong reduction in J_{sc} and FF due to the quality of the MoO_3 source material and ultimately due to the active layer morphology. For the SM-OSCs, since the reduction in PCE in Figure 5-10 is largely due to a decrease in V_{oc}, the observed variations are not expected to be due to changes in the ClInPc:C_{60} active layer. Given the sensitivity of the fullerene-based Schottky device architecture to the very deep work function of the anode,[42, 71] the reduction in V_{oc} is instead suggested to be due to a reduction in the MoO_3 work function. To this end, even though the ITO/MoO_3 film is kept in high vacuum (<$5x10^{-6}$ torr), the effective work function of the anode decreases over time. This decrease in work function occurs in a manner analogous to the decrease observed with MoO_3 air exposure,[203, 204] but to a lesser extent due to the low pressure environment. The deterioration of the MoO_3 HEL compromises the Schottky band bending effects in the device and results in an overall reduction in V_{oc} by ~160 mV.

To further understand the implications of delaying deposition of the organic layers after deposition of the MoO_3 HEL, the photo-stability of these SM-OSCs was also studied. The ClInPc:C_{60} SM-OSCs fabricated using MoO_3 HELs by methods A through D were exposed to 1-sun intensity white light in an inert N_2 environment over 264 hours. The photovoltaic output parameters over this period, normalized to their initial values, are shown in Figure 5-11. For SM-OSCs where there was no delay (0 hrs), the PCE decreased by 10%, whereas devices with the longest delay (17 hrs) exhibited a reduction in PCE by 30% over the same period. Most critically, devices with only a 2.5 hour delay, which showed comparable initial performance to the no-delay devices (Table 5-4), showed a 20% reduction in PCE over the 264 hours of light exposure. In all cases, the majority of the reduction in PCE can be attributed to a loss in V_{oc}. In order to minimize these effects, and other similar effects that may be present (e.g. at the EEL, especially in inverted architectures), OSCs should be fabricated with minimal delay between deposition of layers. This is especially pertinent as OSC structures increase in complexity, and more

auxiliary layers are added to OSCs to enhance performance and stability. As such, for the the work described in this thesis, fresh MoO_3 source material is always used and there is minimal delay between deposition of the various layers of the OSC.

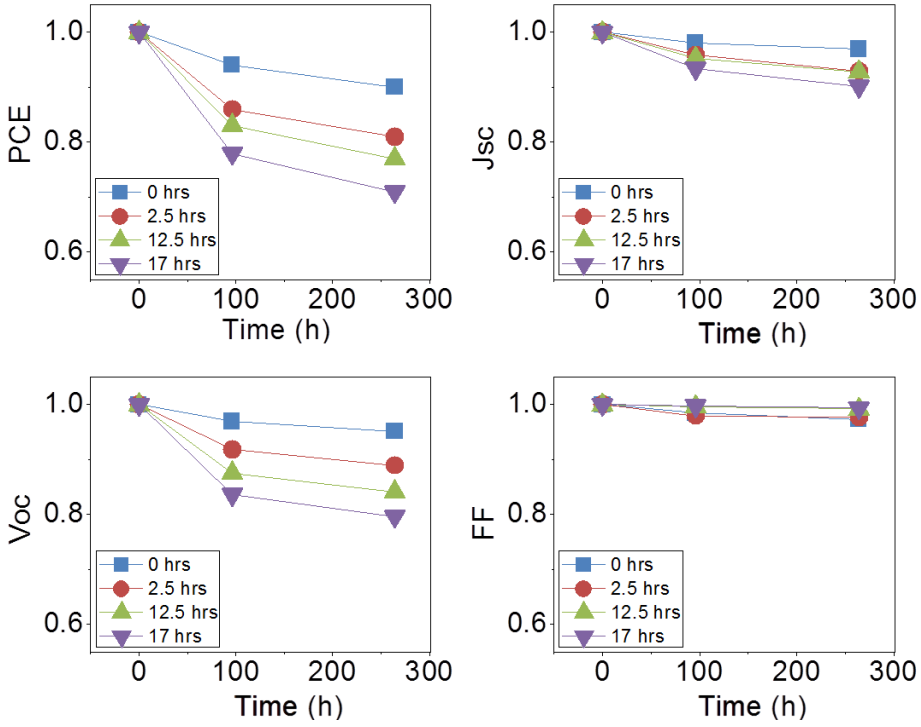

Figure 5-11 - Normalized photovoltaic output parameters of ClInPc:C_{60} SM-OSCs during light-stress experiments. Legend denotes time delay between deposition of MoO_3 and subsequent layers.

5.3. Conclusions

In this chapter, vacuum-deposited SM-OSCs were studied to better understand charge transport across interfacial layers. The results helped to identify the criteria for efficient extraction layers, and furthermore identified several experimental considerations to obtain reproducible and scientifically relevant OSC performance data. The major conclusions drawn from this work are detailed below:

- BCP and Alq_3 are both suitable EEL candidates, with similar levels of efficiency and stability, while the use of NPB generally results in lower PCE values. The combination of exciton blocking properties and the presence of metal deposition-induced defect states make a suitable SM-OSC EEL candidate.

- The use of a thick wide bandgap organic HEL in an upright OSC creates a blocking contact and severely deteriorates device performance. Inverted device structures, which have the HEL deposited immediately prior to the top metal anode, can employ a wide bandgap organic HEL (in combination with a MoO_3 layer) or, alternatively, a thick MoO_3 HEL alone. The HEL in an inverted device must be substantially thicker than the EEL used in an upright device.
- Re-using MoO_3 source material can have implications in the quality of the MoO_3 film, which strongly alters P-OSC device performance. Delays between deposition of MoO_3 and subsequent organic materials degrade both the efficiencies and lifetimes of SM-OSCs.
- To minimize concerns regarding the quality of the MoO_3 film, new MoO_3 source material should be used for every deposition, and the time spent between deposition of the MoO_3 layer and subsequent organic layers should be minimized. As will be discussed in **Chapter 8** and **Chapter 9**, by employing these standards in MoO_3 HEL deposition, MoO_3 HELs can allow for highly stable and efficient OSCs while minimizing concerns regarding device reliability and reproducibility.

Chapter Six:

Interplay between Efficiency and Device Architecture for Small Molecule Organic Solar Cells[1]

This chapter presents a systematic study on OSC device architecture, thus providing a base of knowledge on the role of the photo-active layer composition on OSC performance. As such, this chapter helps to identify limiting factors in charge collection in modern OSCs, and discusses how charge accumulation and recombination effects can be understood in terms of device structure. Five different SM-OSC structures are investigated, including the simple PHJ and BHJ, as well as several planar-mixed structures. The different OSC structures are studied over a wide range of donor:acceptor mixing concentrations. Transient photocurrent decay measurements are used to provide crucial information regarding the interplay between charge sweep-out and charge recombination, and ultimately hint toward space charge effects in planar-mixed structures. The results show that the BHJ/acceptor architecture, with a BHJ layer with high C_{60} acceptor content, generates OSCs with the highest performance by balancing charge generation with charge collection. The performance of other device architectures is largely limited by hole transport, with associated hole accumulation and space charge effects.

6.1. Introduction

In **Chapter 5**, the role of interfacial layers on the performance of OSCs was examined, and it was shown that they play a critical role in charge collection and ultimately in the OSC's photovoltaic output parameters. To better understand potential limitations in charge collection processes in OSCs, one must

[1] The majority of the material in this chapter was published in:
G. Williams, S. Sutty,H. Aziz, *Physical Chemistry Chemical Physics,* **2014,** *16*, 11398.
, reproduced here with permission of the PCCP Owner Societies.

naturally also study the role of the photo-active organic layers in device performance, especially in consideration of how the donor and acceptor layers are mixed (or not mixed) and positioned relative to each other. Vacuum-deposited SM-OSCs are of particular interest in this regard, as this device fabrication methodology lends itself to multi-layer devices with precise control over both layer thicknesses and BHJ layer composition – a significantly more difficult feat with solution processing. Understanding the physics of the various device architectures can provide insights into factors governing charge transport, charge extraction and stability in OSCs, with consequences that apply to both vacuum deposition and solution processing fabrication methodologies. For example, the PM-HJ was initially developed using vacuum deposition methods, and was shown to allow for efficient charge generation and charge collection.[213] More recently, an approximation of this device structure has been realized with solution processing to allow for 75% FF OSCs.[214] A more comprehensive understanding of the role of device architecture in device performance is thus invaluable for achieving high performance OSCs. It follows that a systematic study on device architecture as it relates to OSC performance also allows for simpler cross comparisons within the wealth of different device structures studied in literature. To this end, such a study can isolate the reasons that a particular device architecture may be best suited for a particular donor:acceptor materials system.

In this chapter, SM-OSCs with varying device architectures are examined, with active regions comprising: a PHJ, a BHJ, a BHJ/acceptor, a donor/BHJ and a donor/BHJ/acceptor. Within this subset of device architectures, a constant total device thickness is maintained while the acceptor (C_{60}) content is varied from 25% to 87.5%. The inclusion of devices with high C_{60} content allows for research on the Schottky OSC, an emerging device architecture discussed in **Chapters 1** and **4** above, known for its high efficiencies and high V_{oc} values.[42, 71, 72, 109, 209] The different devices are tested for their photovoltaic output parameters, their EQE spectra and their transient photoresponse to provide a complete picture of the operation and the inherent limitations of the various device architectures. Transient

photocurrent decay measurements, known from literature to be a powerful technique for investigating charge transport as well as charge trapping effects,[206, 215-217] help to clarify charge sweep-out and charge recombination effects in the different structures. These measurements further elucidate the role of space charge effects in regular device operation.

The results of this work demonstrate that potential improvements in performance with device architecture are strongly associated with minimizing charge trapping and the associated charge recombination. To this end, the donor/BHJ/acceptor device architecture is shown to reduce charge recombination effects compared to a simple BHJ with equivalent thickness; however, the limited charge transport properties of the constituent materials result in space charge effects that ultimately degrade device performance. The results thus lend credence to the heavily doped organic layers employed in p-i-n OSCs.[25, 154, 218] Basic Schottky OSCs are shown to offer a fast transient response and are thus less prone to space charge effects, but are ultimately limited by the poor charge transport properties and associated charge recombination within the thick mixed donor:acceptor layer. It follows that, due to limited donor hole mobility and the absence of doped organic layers, the highest performing OSCs employ a Schottky architecture OSC with an additional neat C_{60} acceptor layer. This architecture optimizes the trade-off between charge generation and charge collection. The comprehensive set of devices and the associated characterization techniques employed in this work are shown to allow for judicious determination of the device architecture required to achieve high efficiency OSCs with optimal charge collection characteristics.

6.2. Results and Discussion

In the present study, ClGaPc and C_{60} are incorporated into various device architectures, as detailed in Figure 6-1, while maintaining a total device thickness of 40 nm. As discussed in **Chapter 4**, ClGaPc has very similar properties compared to ClInPc, with similar absorption spectra and with similar

device performance in basic BHJ OSCs. The device thickness of 40 nm is specifically chosen to provide reasonable efficiencies – thicker devices generally suffer from poor FF values, while thinner devices suffer from poor J_{sc} values. In all devices, a 5 nm MoO_3 HEL and an 8 nm BCP EEL are used.

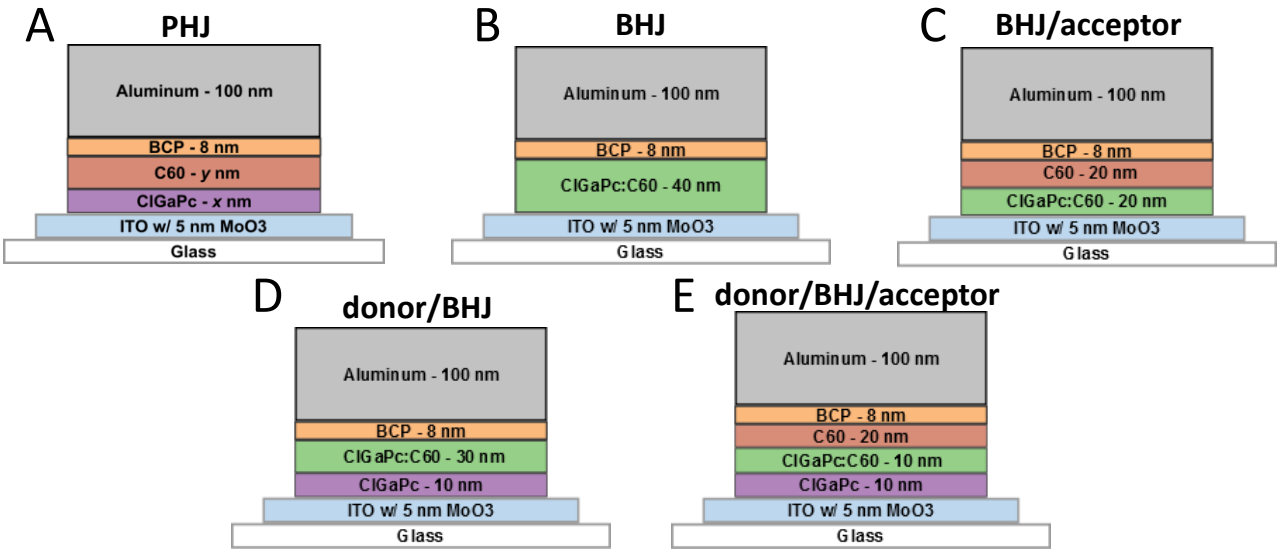

Figure 6-1 - Illustration of OSC Device Architectures, including: a) PHJ, b) BHJ. c) BHJ with a neat acceptor layer, d) BHJ with a neat donor layer and e) BHJ with both a neat donor and a neat acceptor layer.

The devices are labelled 'A' through 'E', corresponding to the PHJ, BHJ, BHJ/acceptor (BHJ/a), donor/BHJ (d/BHJ) and donor/BHJ/acceptor (d/BHJ/a, also known as a full PM-HJ) device architectures respectively. In the case of the PHJ, the thicknesses of the donor and acceptor layers are varied in order to vary the acceptor (C_{60}) content within the device. In devices B through E, only the mixing concentration within the BHJ layer is varied. As noted in **Chapter 4** and discussed further below, for the cases where high C_{60} content is used and the mixed BHJ layer is in direct contact with the ITO/MoO_3 anode, a Schottky contact is formed. In effect, the structures presented in Figure 6-1 represent the full spread of viable device architectures available with the constituent materials, and thus provide a full picture of charge transport as it relates to OSC efficiency. The energy level diagram for the various species employed in the OSCs in this chapter as well as the absorption spectra for both ClGaPc and C_{60} are provided in Figure 6-2.

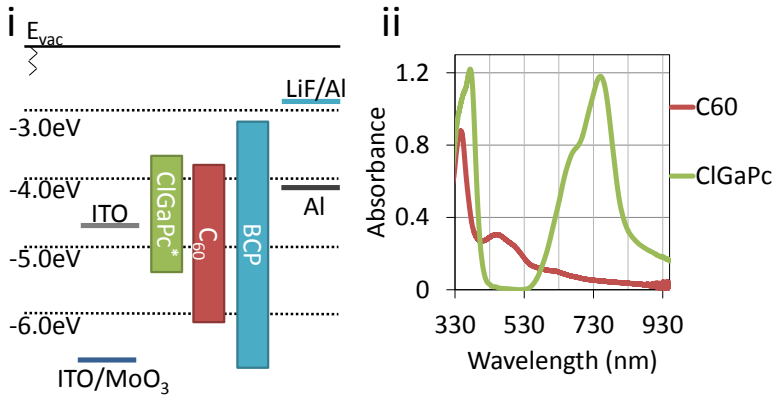

Figure 6-2 - i. Energy level diagram for ClGaPc/C_{60} OSCs. ii. Absorption spectra of 50 nm films of C_{60} and ClGaPc.

The photovoltaic output parameters for devices A through E as a function of C_{60} content are shown in Figure 6-3 (current density-voltage (JV) characteristics are provided in the Supplemental Information (**Appendix 1.2**)).

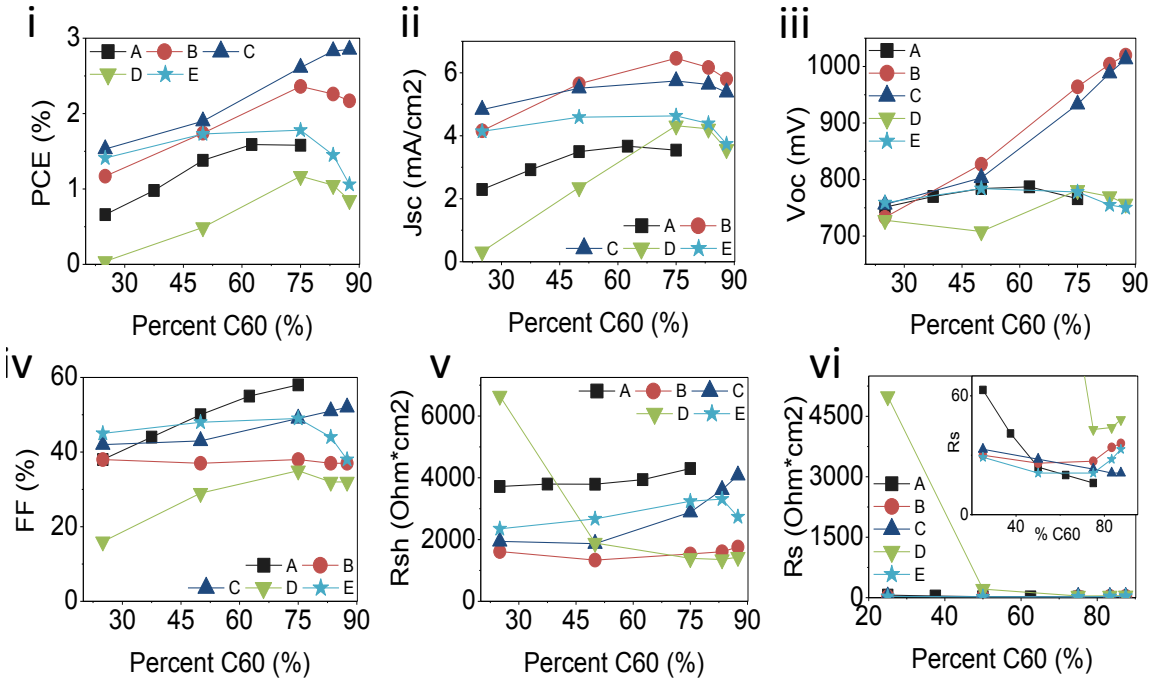

Figure 6-3 - Photovoltaic output parameters of ClGaPc:C_{60} OSCs with varying device architectures and varying acceptor (C_{60}) content. Devices A through E correspond to the PHJ, BHJ, BHJ/acceptor, donor/BHJ and donor/BHJ/acceptor device architectures respectively.

From panel i in the figure, it is clear that the BHJ and BHJ/acceptor device architectures (structures B and C respectively) offer the highest efficiencies – the latter demonstrating 2.9% PCE at 87.5% C_{60} content. The worst performing devices are those that employ a donor/BHJ device architecture

(structure D), with PCE values substantially lower than the BHJ/acceptor architecture for the same mixing concentrations. The donor/BHJ/acceptor device architecture (structure E) grants slightly improved efficiencies compared to that of equivalent PHJ devices (structure A). However, the donor/BHJ/acceptor structure drops in efficiency at higher C_{60} content, so it cannot compete with devices B and C for BHJ layers with 75% to 87.5% C_{60} content. In general, all devices show improvement in PCE when they have more C_{60} content than ClGaPc donor content, in agreement with results from **Chapter 4**. To better understand these trends in efficiency, it is necessary to examine the photovoltaic output parameters (J_{sc}, FF and V_{oc}) in greater detail and in combination with EQE measurements as well as transient photoresponse measurements. To accomplish this task in a meaningful manner, the device architectures are compared incrementally in terms of their structural complexity.

6.2.1. Bulk Heterojunction versus Planar Heterojunction Structures

To begin the analysis, a comparison of the most straightforward device architectures, the PHJ and BHJ (structures A and B respectively from Figure 6-1), is provided. This follows naturally from the historical development of OSCs in literature, which evolved from the simple bilayer heterojunction (PHJ)[16] to the BHJ.[219-221] Such comparisons have also recently been made from a theoretical standpoint to better understand photocurrent generation.[222] This basic comparison serves as an ideal starting point to allow for later analysis of the more complicated device architectures (structures C through E) in light of the chosen suite of characterization techniques. For the PHJ, the C_{60} content is varied by changing the individual donor and acceptor layer thicknesses while maintaining a summative active layer thickness of 40 nm. In contrast, the BHJ comprises a fully mixed 40 nm active layer with varied donor-to-acceptor content.

The PHJ device (structure A) shows moderate PCE values, varying from 0.7% to 1.6% with higher performance for thicker C_{60} layers (thinner ClGaPc layers). Improvements in PCE with a thicker C_{60} layer are largely due to the improvements in FF with increasing C_{60} content, as shown in Figure 6-3-iv. This enhanced FF is associated with a decrease in R_s, as is visible from Figure 6-3-vi. The stark decrease in R_s and increase in FF with a thicker C_{60} layer is indicative of improved charge transport properties of C_{60} compared to ClGaPc. It is worth noting that optimal PHJ configurations that employ relatively thick C_{60} layers in bilayer heterojunction devices have been used for numerous other small molecule donor species in literature, so the comparatively poor mobility of ClGaPc is not believed unique to this specific donor.[171, 223, 224] In fact, the relatively poor hole mobility of CuPc, a close relative of ClGaPc, compared to C_{60} is also well established in literature, and is even more strongly evident when considering hole/electron mobilities in mixed layers.[184]

Interestingly, the J_{sc} is also shown to improve with increasing C_{60} layer thickness and decreasing ClGaPc layer thickness. This is counterintuitive, as ClGaPc absorbs much more strongly in the visible wavelengths compared to C_{60}. Therefore, it would seem that decreasing the ClGaPc content should decrease the amount of photocurrent generated within the OSC. In order to understand this effect, it is useful to examine the EQE spectra, as shown in Figure 6-4-i. It is clear that the photocurrent contributions from ClGaPc quickly reach their maximum levels even at the smallest ClGaPc thickness (10 nm ClGaPc / 30 nm C_{60}), suggesting that the ClGaPc exciton diffusion length is the most critical limitation for this device architecture (i.e. excitons generated greater than 10 nm from the heterojunction do not yield photocurrent). Furthermore, the increase in J_{sc} with increasing C_{60} layer thickness is found to be largely due to the strong increase in EQE at 450 nm, which was previously shown to be due to C_{60} aggregate absorption.[72] It follows that increasing the thickness of the C_{60} layer increases the number of C_{60} aggregates, and hence also increases their contributions to photocurrent. An additional contributor to photocurrent with increasing C_{60} layer thickness (decreasing ClGaPc thickness) is the broad increase in

EQE from 530 nm to 720 nm. While this appears as a hypsochromatic shift of the 750-nm ClGaPc absorption, the improved EQE in this region is due to tail-end absorption from low energy C_{60} Frenkel excitons,[162, 225] as shown and discussed further in the Supplemental Information (**Appendix 1.2**).

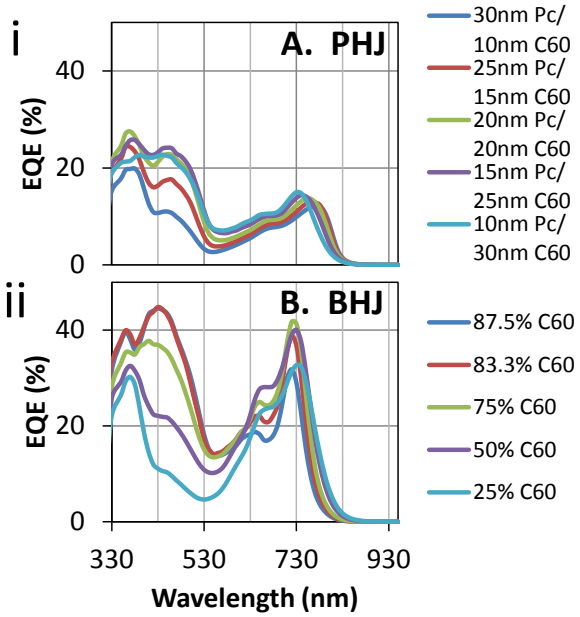

Figure 6-4 - EQE spectra of the i) ClGaPc/C_{60} PHJ and ii) ClGaPc:C_{60} BHJ OSCs with different layer thicknesses (PHJ) and C_{60} content (BHJ).

It is now interesting to compare the PHJ device architecture (structure A) to those devices that use a 40 nm BHJ (structure B), beginning with their photovoltaic output parameters in Figure 6-3. While the PHJ reaches its maximum PCE at 1.6% with 62.5% C_{60} content, the BHJ reaches a substantially higher PCE of 2.4% at 75% C_{60} content. The most significant improvement in the transition from the PHJ to the BHJ structure is the increase in J_{sc}, owed to the improved exciton collection efficiency from the interpenetrating donor:acceptor network. In terms of EQE, shown in Figure 6-4-ii, it is clear that the BHJ shows much improved photocurrent contributions from both ClGaPc and C_{60} at nearly all mixing concentrations. As the BHJ is varied from ClGaPc-rich to C_{60}-rich, there is a clear trade-off between photocurrent from ClGaPc in the red/near-IR wavelengths and from C_{60} aggregates at 450 nm. It is more difficult to form C_{60} aggregates with high ClGaPc content, and so the 450 nm absorption disappears with only 25% C_{60} content. Furthermore, the J_{sc} is optimized at 75% C_{60} content, which balances the ClGaPc

and C_{60} photocurrent contributions optimally. The transition from the PHJ to the BHJ structure offers an additional benefit to the V_{oc}, as shown in Figure 6-3-iii. For the PHJ, the V_{oc} remains at ~770 mV regardless of C_{60} content; however, for the BHJ, the V_{oc} is observed to increase with increasing C_{60} content to a maximum value of 1020 mV at 87.5% C_{60} content. This enhancement in V_{oc} occurs as a consequence of the Schottky junction formed between the BHJ layer and the high work function ITO/MoO_3 anode, established in **Chapter 1** and **Chapter 4**, which occurs when the BHJ layer contains a high concentration of C_{60}.[42, 71, 72] The PHJ, using a neat donor layer adjacent to the anode, cannot possibly benefit from this Schottky interface. Consequently, the PHJ V_{oc} is dictated by the $HOMO_{donor}$-$LUMO_{acceptor}$ offset (minus energy losses noted in **Chapter 1** and **Chapter 4**), whereas the fullerene-based Schottky V_{oc} is set by band-bending at the organic/anode interface – essentially by the C_{60} energy levels and the anode's effective work function.[71]

While the transition from the PHJ to the BHJ device architecture enhances the J_{sc}, it also degrades the FF due to the poor charge transport properties of the mixed organic layers compared to neat organic layers.[42, 164, 184] From Figure 6-3-iv, the BHJ shows a ~40% FF compared to the ~60% FF for the PHJ when both OSCs have 75% C_{60} content. This loss in FF is primarily manifested as a lower R_{sh}, suggesting that the BHJ is generally more prone to charge recombination. To better understand these charge recombination effects, it is useful to employ transient photoresponse measurement techniques. To this end, the OSCs are excited with a pulse of light from an LED, and the photocurrent decay is measured immediately after the light pulse. Single exponential fits are used to characterize the photocurrent decay, as per equation (6.1) below, to calculate the relevant fall time constant τ. In equation (6.1), I is the current measured at time t, following the end of the light pulse, and C_1 & C_2 are fitting parameters.

$$I = C_1 \cdot \exp(-C_2 t), \qquad C_2 = 1/\tau \tag{6.1}$$

The specific details of the transient photoresponse measurement technique are described in the experimental section; however, some crucial notes for analysing these data are discussed presently. When considering transient photocurrent decay, there are two major pathways that significantly alter τ: sweep-out of free carriers and charge recombination. Faster sweep-out of charge carriers is generally beneficial, and helps to prevent charge trapping and space charge effects. Increased recombination, however, also serves to reduce the fall time, and is a harmful effect that can lower the FF and degrade the OSC performance. It is thus emphasized that faster devices do not always correspond to more efficient devices, and so it is necessary to examine the transient photocurrent measurements in the context of their device architectures and all of their photovoltaic output parameters. To this end, the presented transient photocurrent measurements do not individually provide concrete information regarding recombination, but they can allow for a much more robust understanding of carrier dynamics, especially when examined with the FF, R_{sh}, R_s and EQE. This is in contrast to transient photovoltage techniques, which can be used as a more direct probe of charge recombination,[65, 216, 226] but at open circuit conditions that may alter carrier dynamics compared to regular operation (e.g. by suppressing field-assisted de-trapping of charges).

The extracted τ values as a function of the C_{60} content within the OSC for both the PHJ (structure A) and the BHJ (structure B) are shown in Figure 6-5. In both cases, it is clear that the τ values decrease with increasing C_{60} content (i.e. C_{60}-rich devices are 'faster'). For the PHJ, the faster photocurrent transient can be explained simply: C_{60} exhibits superior electron transport properties compared to the hole transport properties of ClGaPc. This conclusion corresponds well to the previous analysis of the OSC photovoltaic output parameters, which showed an increase in FF and decrease in R_s with increasing C_{60} content. The reduced R_s results in a smaller voltage drop over the active layers of the device, and so the sweep-out of free carriers is expected to be more effective. With a faster sweep-out of free carriers, the transient photocurrent decay time decreases, as is observed in Figure 6-5.

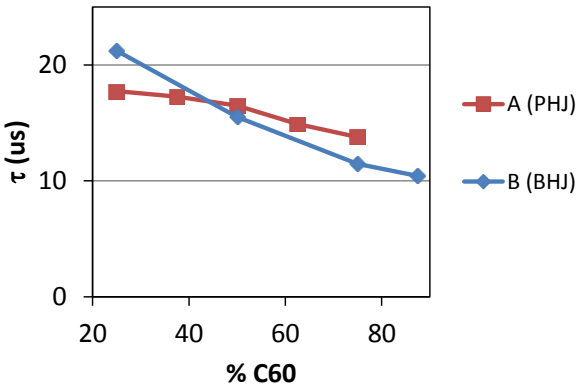

Figure 6-5 - Single exponential fit τ values for transient photocurrent decay (falling current) after illumination with a white LED pulse. τ values are plotted vs. C_{60} content for ClGaPc/C_{60} PHJ (A) and ClGaPc/C_{60} BHJ (B) OSCs.

The τ values for the BHJ OSC are found to change more strongly with varying C_{60} content compared to the PHJ OSC. With low C_{60} content (25% C_{60}), the BHJ OSCs are slower than the PHJ OSCs – 21 μs versus 18 μs for the two structures respectively. This is attributed to the generally poor carrier mobilities in the ClGaPc-rich BHJ layer as compared to the neat layer counterparts. With high C_{60} content, the BHJ is faster than the PHJ – the BHJ has a τ value of 10 μs at its highest C_{60} concentration. The ultimately faster transient photoresponse of the BHJ is attributed to an increase in charge trapping and recombination within the device. Such stipulations are supported by the generally low FF values of the BHJ OSCs compared to the PHJ OSCs. Charge trapping and recombination effects are likely prevalent in C_{60}-rich ClGaPc:C_{60} BHJs, where poor hole mobility coupled with incomplete percolation of donor material (i.e. islands of donor) make it difficult for holes to reach the anode. Hence, hole transport in C_{60}-rich OSCs would be problematic for holes formed far (up to 40 nm away) from the anode. In light of these findings, the increased rates of recombination (due to trapped holes deep within the BHJ layer) are suggested to be responsible for the 10 μs τ values in 87.5% C_{60} BHJ OSCs. The enhanced sweep-out, which also occurs as a consequence of higher C_{60} content (and potentially due to Schottky band bending effects), may also play a role in reducing the transient fall times. These stipulations are revisited and bolstered in the subsequent section, where neat donor and acceptor layers bordering the BHJ layers are considered for their effect on transient photocurrent.

6.2.2. Planar-Mixed versus Bulk Heterojunction Structures

6.2.2.1. BHJ/Acceptor Structures

It is now interesting to consider the performance of OSCs that employ the BHJ device architecture (structure B) relative to the OSCs that employ a BHJ in combination with a neat donor and/or a neat acceptor layer (Figure 6-1, structures C through E for the BHJ/acceptor, donor/BHJ and donor/BHJ/acceptor respectively), starting with the BHJ/acceptor structure. The BHJ/acceptor structure is particularly interesting given its very high performance in literature, with recent tetraphenyldibenzo-periflanthene (DBP):C_{70}/C_{70} OSCs granting 8.1% PCE single cell efficiencies.[68] In the present work, the BHJ/acceptor structure employs a 20 nm ClGaPc:C_{60} BHJ adjacent to a 20 nm neat C_{60} layer, as compared to the 40 nm simple BHJ discussed in the previous section. As shown in Figure 6-3-i, both the BHJ and the BHJ/acceptor structures offer similar PCE values when the BHJ layer has 25% to 75% C_{60} content. Within this range, the BHJ/acceptor structure generally has PCE values ~0.2 to 0.3% higher than the BHJ structure. The BHJ/acceptor structure is further the only device architecture that improves in PCE from 75% to 87.5% C_{60} content. At 87.5% C_{60}, the BHJ/acceptor structure obtains the highest PCE values for this study at 2.9%.

Following the same approach as in the previous section, these trends are expounded by first examining the individual photovoltaic output parameters in greater detail. From Figure 6-3-iii, both the BHJ and the BHJ/acceptor structures share nearly identical V_{oc} values for all donor:acceptor ratios, increasing strongly with increasing C_{60} concentration. This follows naturally, as both device structures include a MoO_3/ClGaPc:C_{60} interface, with their V_{oc} values dictated by the Schottky band bending effects described earlier. From Figure 6-3-ii, the J_{sc} values are also similar among the two device structures,

with the BHJ having slightly better J_{sc} values compared to the BHJ/acceptor structure for BHJ layers with higher C_{60} content. In terms of EQE, shown in Figure 6-6-i versus Figure 6-6-ii, this can be understood from the small increase in ClGaPc photocurrent contributions and a larger increase in C_{60} aggregate photocurrent contributions.

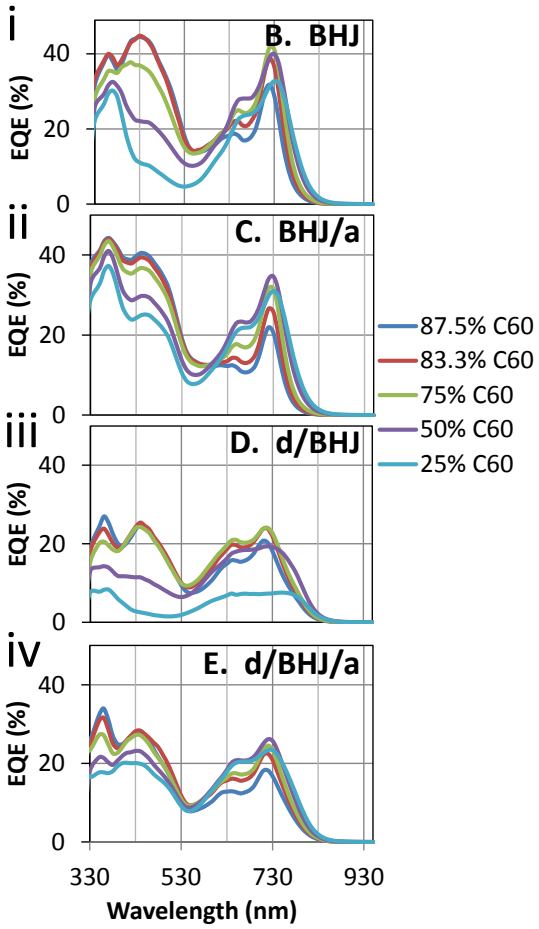

Figure 6-6 - EQE spectra of the BHJ (B), BHJ/acceptor (C), donor/BHJ (D) and donor/BHJ/acceptor (E) ClGaPc:C_{60} OSCs with varying C_{60} content.

The improvement in C_{60} aggregate photocurrent with the simple BHJ is particularly interesting – it was initially expected that the (overall) higher C_{60} content in the BHJ/acceptor structure, due to the presence of the neat C_{60} layer, would result in higher photocurrent contributions from C_{60}. Instead, it is observed that intermolecular C_{60} (aggregate) excitons are more efficiently separated into free carriers when the C_{60} aggregates are mixed with the donor, rather than being present in a pure layer and adjacent to a donor/mixed layer. This stipulation is supported by past work, which showed that a small concentration

of a suitable donor is required for harvesting photocurrent from the C_{60} aggregates,[72] thus implying that photocurrent generation from C_{60} aggregates is strongly reliant on the presence of a donor species. Interestingly, when the BHJ layer instead has very low C_{60} content, the BHJ/acceptor structure shows higher J_{sc} values compared to the BHJ structure. This variation can also be explained from the EQE in Figure 6-6. For structure B, it is observed that C_{60} aggregates cannot be formed in the BHJ layer at 25% C_{60} (due the very low C_{60} content) and so the photocurrent contributions at 450 nm are suppressed. However, in structure C, the neat C_{60} layer, which is not present in structure B, still consists of C_{60} aggregates. It follows that this added C_{60} layer allows for meagre C_{60} aggregate photocurrent contributions, as is evident from the EQE near 450 nm for 25% C_{60} OSCs (augmenting the J_{sc}).

Since the V_{oc} is nearly identical for both the BHJ and BHJ/acceptor structures, and the changes in J_{sc} between the structures are not significant, the main source of differences in PCE between these two device architectures is due to the FF. The BHJ/acceptor structure exhibits strongly improved FF values compared to the BHJ, as shown in Figure 6-3-iv. Furthermore, while the BHJ structure shows relatively constant FF values with variations in BHJ layer C_{60} content, the BHJ/acceptor structure shows strong improvements to FF with increasing C_{60} content. This difference in FF can be readily explained in terms of the high electron mobility in neat C_{60} compared to the poorer electron mobility in mixed (BHJ) layers. Replacing 20 nm of ClGaPc:C_{60} with C_{60} serves to reduce the R_s and enhance the FF. This trend in R_s is also visible from Figure 6-3-vi for devices with high C_{60} content. A second consequence of the BHJ/acceptor structure is that the BHJ layer is only present in close proximity to the anode since a neat C_{60} layer replaces the region near the cathode. In the previous section, it was stipulated that isolation and subsequent accumulation of holes within the BHJ layer, especially in regions far from the hole-collecting electrode, can cause recombination effects. As such, it is logical that removing the BHJ layer from this region of the device substantially improves the FF. This fact is further supported by the

increase in R_{sh} for the BHJ/acceptor structure compared to the BHJ structure, especially for BHJ layers with high C_{60} content, as shown in Figure 6-3-v.

To further verify and explain the improvement in FF, R_s and R_{sh} in the BHJ/acceptor structure compared to the BHJ structure, transient photocurrent decay measurements are employed, extending the analysis from the previous section. The single exponential τ values from transient photocurrent decay experiments for the BHJ and the BHJ/acceptor device are shown in Figure 6-7, alongside the data for the remaining device structures (D and E, the donor/BHJ and donor/BHJ/acceptor respectively). As with the simple BHJ, the BHJ/acceptor structure exhibits decreasing τ values with increasing C_{60} content. This can again be attributed to more efficient sweep-out of free carriers due to the superior transport properties of the C_{60}-rich films, as compared to ClGaPc-rich films.[184] Of more critical interest, the τ values for the BHJ/acceptor structure are found to be generally higher than those for the simple BHJ structure, especially when the BHJ layer has high C_{60} content. This can be explained in terms of the fact that replacing 20 nm of the BHJ layer with neat C_{60} (i.e. comparing structure B to structure C) reduces hole accumulation and, as a consequence, reduces the associated recombination effects. To understand this phenomenon, consider that the BHJ/acceptor structure is essentially a BHJ structure that has no donor material present deep within the device (far from the anode). As such, holes cannot become isolated and subsequently accumulate in the sparsely distributed donor regions deep in the BHJ layer. Rather, holes are only formed in the 20 nm BHJ layer adjacent to the anode, where they may be more effectively collected. Reducing recombination effectively slows the device, and so the BHJ/acceptor structure is observed to have a slower transient response (larger τ) compared to the simple BHJ. This observation coincides well with the fact that the BHJ/acceptor structure has higher FF values than the simple BHJ structure at all C_{60} concentrations.

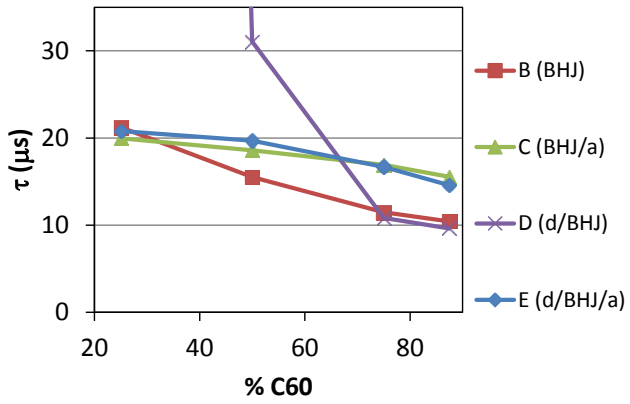

Figure 6-7 - Single exponential fit τ values for transient photocurrent decay (falling current) after illumination with a white LED pulse. τ values are plotted vs. C_{60} content for BHJ (B), BHJ/acceptor (C), donor/BHJ (D) and donor/BHJ/acceptor (E) ClGaPc:C_{60} OSCs.

6.2.2.2. Donor/BHJ Structures

Given the strong enhancement in device performance with the addition of the neat C_{60} layer to the simple BHJ structure, it is natural to question the effect of instead adding a neat donor layer. As such, it is now interesting to study the donor/BHJ (structure D) as compared to the simple BHJ (structure B). From Figure 6-1, structure D replaces 10 nm of the BHJ layer adjacent to the anode in the simple BHJ with a neat ClGaPc layer. The photovoltaic output parameters for this structure are plotted in Figure 6-3, where it is immediately clear that the inclusion of the neat donor layer strongly degrades OSC performance. The donor/BHJ structure is shown to be the worst-performing device architecture, with only 0.3% PCE when the BHJ layer has 25% C_{60} content, and PCE values much less than half of those of the simple BHJ structure at all other mixing concentrations. The most immediate hint for this decrease in efficiency is the generally high R_s for the donor/BHJ structure, as shown in Figure 6-3-vi, which increases drastically with 25% and 50% C_{60} content in the BHJ layer. The strong increase in R_s follows from the generally poor charge transport properties of ClGaPc compared to C_{60}, established with the PHJ above. The effect of poor charge transport in the donor/BHJ structure, however, is further intensified by two additional factors:

- the poor charge transport properties of the donor:acceptor BHJ layer, as compared to the neat C_{60} film that is employed in the PHJ
- the much higher increase in photogenerated carriers due to the innumerable donor/acceptor interfaces in the BHJ layer, as compared to the single PHJ interface

The combination of these factors results in a device architecture that is incredibly susceptible to space charge effects, and consequently suffers from poor charge extraction. To this end, upon illumination, a large number of holes are generated within the BHJ layer of the device and traverse to the donor/BHJ layer interface. The generally poor transport properties of the donor layer result in an accumulation of holes to cause space charge effects and to further degrade OSC performance. As the BHJ layer increasingly becomes acceptor-rich, the device performance approaches that of the 10 nm ClGaPc/30 nm C_{60} PHJ studied in the previous section.

Taking this explanation into consideration, the performance of the donor/BHJ structure may be broken into two different regimes: BHJ layers with low/moderate C_{60} content, and BHJ layers with high C_{60} content. For the low C_{60}-content devices, the R_s is very high for the reasons discussed above. Furthermore, comparing the donor/BHJ structure to the simple BHJ structure at 25% and 50% C_{60} content, the addition of the neat donor layer ultimately results in charge blockage, leading to an increase in R_{sh}, as observed in Figure 6-3-v. With a near-complete loss of diode characteristics and small photocurrents, the device operates less like an efficient heterojunction solar cell, but instead more like a resistive (albeit photo-sensitive) organic film. It follows that both the FF and J_{sc} suffer strongly with these mixing concentrations. As shown by the EQE in Figure 6-6-iii, photocurrent contributions are strongly decreased across all wavelengths for these mixing concentrations. The photocurrent contributions also lose their fine spectral detail, with the peak and shoulder of the ClGaPc photocurrent merged together. Furthermore, the OSCs with 25% and 50% C_{60} content provide virtually no C_{60}

aggregate photocurrent contributions, since it is more difficult to form C_{60} aggregates at these mixing concentrations. The poor FF at these mixing concentrations is supported by the substantial increase in the time constant of the transient photoresponse of the donor/BHJ device, shown in Figure 6-7. Specifically, the τ values increase drastically to 31 μs for 50% C_{60} content and 520 μs for 25% C_{60} content (the latter point not shown in the figure). While the poor charge transport properties of the neat donor layer and the donor-rich BHJ layer clearly limit the performance of these OSCs, it is worth noting that the charges present within these devices are incredibly long-lived. This shows that the photogenerated carriers are not being swept out quickly; however, they are also not undergoing rapid recombination.

While increasing the C_{60} content in the BHJ layer can alleviate charge transport problems in the donor/BHJ structure, the ultimate performance of this device architecture is still quite poor. Specifically, since this structure employs a neat donor layer, and thus lacks the interface between the BHJ layer and the high work function anode, it no longer benefits from the Schottky interface enhancement to V_{oc}. This is observed clearly in Figure 6-3-iii, where the V_{oc} for structure D tracks the V_{oc} values set by the PHJ (structure A). The J_{sc} for the donor/BHJ structure is also lower than that of the BHJ, as the excitons that are formed in the neat ClGaPc layer far from the BHJ layer interface do not generate photocurrent (established with the PHJ earlier). This effect is clearly visible in the EQE in Figure 6-6, where the peak photocurrent contributions from ClGaPc in the donor/BHJ structure (75% to 87.5% C_{60} content) are much lower than that of the simple BHJ device, in spite of the 10 nm neat ClGaPc layer. It is also observed that, with the replacement of 10 nm ClGaPc:C_{60} with 10 nm of ClGaPc (again comparing structures B and D), the C_{60} photocurrent contributions are reduced accordingly. Interestingly, the τ values extracted from the transient photocurrent experiments for the donor/BHJ structure are nearly identical to those of the simple BHJ when both structures employ high C_{60} content in their BHJ layer. This is observed clearly in Figure 6-7 for 75% and 87.5% C_{60} content. The fast response at these mixing concentrations follows from the high level of recombination due to holes formed in isolated pockets of

donor deep within the BHJ layer. This is the same effect established for the simple BHJ in earlier sections – essentially trapped holes formed far from the anode are unable to traverse the BHJ layer due to the BHJ layer's low donor content.

6.2.2.3. Full Donor/BHJ/Acceptor Structures

The final device architecture studied in this work is the donor/BHJ/acceptor (structure E), which makes use of both a neat donor and a neat acceptor layer. When compared to the simple BHJ (structure B), 10 nm of the BHJ layer near the anode is replaced with neat ClGaPc and 20 nm of the BHJ layer near the cathode is replaced with C_{60}. Therefore, this final device structure encompasses both of the alterations made for the BHJ/acceptor structure and the donor/BHJ structures examined above. From Figure 6-3-i, the donor/BHJ/acceptor structure generates devices with moderate PCE values in between those of the other device structures examined in this work. Furthermore, the donor/BHJ/acceptor structure has PCE values that are the least dependent on C_{60} content in the BHJ layer – between 1.4% and 1.8% for C_{60} content varying from 25% to 83%. One major contributor to this independence of PCE on mixing concentration is that the donor/BHJ/acceptor structure exhibits a relatively constant V_{oc} (Figure 6-3-iii). As noted for the donor/BHJ structure, this is due to the neat ClGaPc layer separating the high work function anode from the BHJ layer. As a consequence, the V_{oc} is simply set by the $HOMO_{donor}$-$LUMO_{acceptor}$ offset (minus relevant energy losses noted in **Chapter 1** and **Chapter 4**), and does not benefit from the Schottky interface enhancement observed in structures B and C. In Figure 6-3-ii, the donor/BHJ/acceptor structure's J_{sc} is also shown to be relatively constant with variations in C_{60}, with values near ~4 mA/cm^2 for all mixing concentrations. This is also consistent with observations from Figure 6-6, where EQE spectra show much less drastic variations in intensity, especially when compared to the simple BHJ. This is due to the fact that, with neat layers of both ClGaPc and C_{60}, there are always moderate contributions to photocurrent from both the ClGaPc and C_{60}. Furthermore, as the C_{60} content

is increased in the BHJ layer, any loss in photocurrent from ClGaPc is compensated by an increase in photocurrent from the C_{60} aggregate band (and vice versa). Regardless, the J_{sc} for the donor/BHJ/acceptor structure is, as expected, shown to be lower than that of the simple BHJ, since the simple BHJ has a much thicker mixed donor:acceptor layer to generate a substantially larger number of free carriers from photogenerated excitons.

Intriguingly, while the donor/BHJ/acceptor structure makes use of a neat donor layer, it does not suffer from the same increases in R_s as observed for the donor/BHJ structure. It is thus shown to be the combination of the neat donor layer and a thick (> 10 nm) BHJ layer (especially when the BHJ layer has low C_{60} content) to be the cause of the strongly increased R_s for the donor/BHJ structure. In fact, the donor/BHJ/acceptor structure is shown to have the some of the best R_{sh} and R_s values (highest and lowest in Figure 6-3-v and Figure 6-3-vi respectively) for the various device architectures studied in this work. The devices that outperform the donor/BHJ/acceptor in this regard are those that employ the PHJ structure, and those that use the BHJ/acceptor structure with high C_{60}-content – the latter was shown to be the highest performing structure in the present study. The donor/BHJ/acceptor structure's high R_{sh} and low R_s values translate to a relatively high FF for the donor/BHJ/acceptor OSC for most mixing concentrations, as shown in Figure 6-3-iv (especially when compared to the simple BHJ). The high FF is explained by the fact that this device structure replaces a large portion of the BHJ layer, known to have poor charge transport characteristics and a higher propensity for charge recombination, with neat layers that lessen such issues. The operation of the donor/BHJ/acceptor is thus similar to that of the PHJ examined previously, but with a higher capacity for photocurrent generation due its 10 nm BHJ layer. At very high C_{60} concentrations in its BHJ layer, however, the donor/BHJ/acceptor shows a slight reduction in FF, which can be attributed to poor hole transport characteristics through the BHJ layer, and increased hole accumulation/recombination effects.

The transient photocurrent response for the donor/BHJ/acceptor as a function of the BHJ layer's C_{60} content is similar to that of the other device structures examined throughout this study. As shown in Figure 6-7, increasing the C_{60} content in the BHJ layer serves to decrease the time constant τ, implying that the C_{60}-rich donor/BHJ/acceptor device is faster. As with the simple BHJ, this is attributed to enhanced sweep-out of free carriers, owing to the superior charge transport characteristics of C_{60} compared to ClGaPc. The τ value for the donor/BHJ/acceptor at the highest C_{60} concentration, however, is slower than that of the simple BHJ and the donor/BHJ structure. This further verifies previous stipulations regarding the accumulation and trapping of holes deep within the BHJ layer (i.e. far from the anode). Since the donor/BHJ/acceptor employs only a 10-nm thin BHJ layer, and has a neat 20-nm C_{60} layer near the cathode, isolated donor domains can only be formed 10 to 20 nm away from the anode. As such, isolated holes are not formed far away from the anode, and hole recombination effects are reduced. With reduced recombination in the donor/BHJ/acceptor structure, charge carriers are observed to have longer lifetimes.

In structures B through D (those that employ a BHJ layer), the observed maximum FF of ~50% leaves significant room for improvement, especially with optimized P-OSCs proven to be capable of FF values up to 75%.[214] To further understand these limitations, the transient photocurrent analysis is explained by employing coloured LEDs with much higher brightness values at the materials' major absorption wavelengths (blue and red LEDs, for C_{60} and ClGaPc respectively). The effect is to substantially increase the number of excitons generated at a given LED power compared to the white LED since the emission spectrum overlaps more strongly with the absorption spectrum. In literature, it has been shown that increasing the number of excitons, and thus the number of photogenerated carriers, can lead to space charge effects visible in transient photocurrent experiments.[66, 215-217] In a transient photocurrent experiment, space charge effects are manifested as a peak increase in photocurrent and subsequent stabilization at lower photocurrents with the initial pulse of light. In some

cases, researchers have noticed a negative photocurrent peak recovery at the end of the light pulse. The negative photocurrent implies the injection of carriers from the contacts to neutralize carriers that remain within the device due to insufficient sweep-out, essentially arising from space charge effects.[215] It is also worth noting that this negative recovery is strongly dependent on the device architecture, as the carriers must favour accumulation over various potential avenues for recombination (i.e. the charge carrier lifetime must be quite long). This negative photocurrent recovery is demonstrated in Figure 6-8, which shows the transient photocurrent decay for a ClGaPc:C_{60} OSC (with the donor/BHJ/acceptor device structure) after being exposed to both dim and bright light pulses. In the case of a dim LED pulse, no negative transient is observed, but in the case of a bright LED pulse, a significant negative spike and subsequent recovery is observed. In fact, all of the mixing concentrations in the donor/BHJ/acceptor structure show this negative photocurrent recovery at the end of the bright light pulse. However, this behaviour is not observed for any of the other device architectures – it is unique to the structure E, the full donor/BHJ/acceptor, and it emphasizes the generally low recombination rates and high FF with this device architecture.

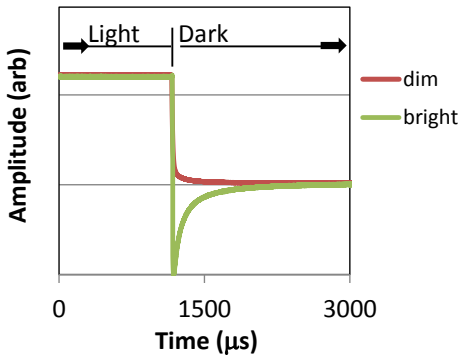

Figure 6-8 - Transient photocurrent decays of a ClGaPc:C_{60} donor/BHJ (87.5% C_{60})/acceptor OSC after illumination from a bright LED pulse and a dim LED pulse.

Upon illumination, the interface between the BHJ layer and the neat donor or acceptor layer is a region of high charge density, as this interface contains charges from two sources:

- excitons formed throughout the full thickness of the BHJ layer

- excitons formed in the neat layer and within the exciton diffusion length of the mixed/neat interface

The large concentration of free carriers at the mixed/neat interface is a potential contributor to space charge effects, especially in consideration of the generally poor hole transport within the presently studied materials. Structure E has both donor/mixed and mixed/acceptor interfaces present, and so it suffers from these effects most strongly. As further evidence of these effects, it is observed that all structures that have a neat donor or acceptor layer adjacent to a BHJ layer have both a fast and slow decay component with a dim LED pulse when fitted with a bi-exponential fit. The slow decay components are suggested to be attributed to space charge effects, as described in greater detail in the Supplemental Information (**Appendix 1.2**). While space charge effects have been noted as a strong limiter toward device performance for the donor/BHJ/acceptor structure, the remarkably long free carrier lifetimes in this device architecture are re-emphasized. The donor/BHJ/acceptor structure is therefore a promising device architecture for high performance OSCs, but only in the case where both the donor and acceptor materials are optimized for high free carrier mobilities and thus to prevent space charge effects. The success of more complicated device structures in literature, such as the p-i-n architecture,[27] or those that employ gradient mixed layers,[227] can at least in part be attributed to their tackling space charge effects. In the prior case, this is accomplished explicitly by bolstering the charge transport properties of the neat layers. In the latter case, space charge effects are minimized implicitly by minimizing the accumulation of charges at any specific region within the photo-active layers. In this chapter, it was shown that a much simpler device architecture, with an active region comprising BHJ/acceptor layers (structure C), can achieve a high level of performance for similar reasons.

6.3. Conclusions

In this chapter, a wide variety of OSC device architectures were studied, and their photovoltaic properties were examined in consideration of their transient photoresponse characteristics. By considering the different device structures incrementally in terms of structural complexity, a more robust understanding of charge collection processes in modern OSCs was obtained. The following major conclusions were discussed:

- The BHJ/acceptor device structure generates the highest PCE values. Its high performance is strongly associated with enhanced sweep-out, and with minimizing both charge trapping and charge recombination effects. This is further accomplished while maintaining a relatively high J_{sc}, by balancing ClGaPc photocurrent with C_{60} aggregate photocurrent, and obtaining a high V_{oc} due to Schottky interface effects.
- The donor/BHJ/acceptor device structure, another frequently studied device structure in literature, minimizes charge recombination, but ultimately suffers from hole accumulation and space charge effects that limit its sweep-out.
- Transient photocurrent measurements suggest that space charge effects may be present and potentially problematic for any device architecture that employs BHJ layers in combination with neat donor or acceptor layers. These effects are most prevalent for donor-rich OSCs, further highlighting the hole transport limitations in these vacuum deposited SM-OSCs.
- The results emphasize the significant impact that the choice of device architecture plays on charge collection and OSC device performance.

Chapter Seven:

Vacuum-Deposited Ternary Mixture and Cascade Organic Solar Cells[1]

In this chapter, ternary mixtures of vacuum deposited small molecules are studied for their charge transport and charge collection properties. This chapter thus addresses the use of advanced OSC device architectures for enhanced performance and altered charge transport behaviour. The two-donor, one-acceptor mixed layer composition is systematically varied to study all possible film configurations, and the resulting OSCs are successful in harvesting photocurrent from all three components to grant broad spectral photoresponse. However, the performances of ternary OSCs are generally poorer than binary OSCs, largely due to reduced fill factors. By examining transient photocurrents, as well as studying multi-layer PHJ cascade OSCs, ternary OSCs are shown to be strongly affected by the energy levels of their constituent materials. Small differences in the two donor materials' HOMO values are demonstrated to degrade hole transport. In light of the insights in this chapter, and with proper design of small molecules with highly specific energy levels, ternary OSCs can provide an alternative pathway to low cost, high efficiency photovoltaics in lieu of more complicated device architectures.

7.1. Introduction

As noted in **Chapter 4**, the intensive research efforts on OSCs have generated a vast number of opto-electronic organic materials with varied absorption and charge transport properties. Unfortunately, these organic materials are limited by their relatively narrow absorption bands, at least compared to the broad absorption of silicon used in first generation solar cells. From discussions in

[1] The majority of the material in this chapter was published in:
G. Williams,H. Aziz, *Org. Electron.,* **2015,** *17*, 229.
, reproduced here with permission.

Chapter 1, the logical approach for bolstering OSC performance in literature has been to employ more than one primary absorber. The simplest method is to use a C_{70} fullerene acceptor instead of the traditional C_{60} fullerene acceptor (analogously, $PC_{70}BM$ versus $PC_{60}BM$ for solution-coated OSCs). Given C_{70}'s stronger visible absorption properties compared to C_{60}, this method allows both the donor and the acceptor to absorb light and generate meaningful photocurrent.[180, 228, 229] Unfortunately, even with C_{70}, the breadth of absorption in OSCs is unsatisfactory compared to silicon, and the substantially increased costs of C_{70} make it presently impractical for manufacturing scale-up. Non-fullerene acceptors have also been investigated, but generally have lower efficiencies.[142, 230-232] As a consequence, many researchers have shifted their focus toward alternative device structures that allow for more than two primary absorbers, such as the tandem solar cell approach that has granted 11-12% OSCs,[233-235] and the more recently studied ternary OSC.

OSCs compete with first-generation silicon photovoltaics by substantially reduced materials costs, but they also require relatively simple device structures for ease of fabrication (e.g. through reel-to-reel methods). As such, while the tandem OSC structure can grant impressive efficiencies, its use of 10-15 individual layers – each requiring optimization of highly controlled fabrication recipes – makes it a difficult structure to implement in practical OSCs, especially in consideration of costs due to device complexity. Two much simpler alternatives to the tandem OSC are the ternary OSC and the cascade OSC described in **Chapter 1**, which have both garnered significant interest in the past few years.[91, 236] This chapter focuses primarily on ternary OSCs; however, cascade OSCs are also discussed in Section 7.3. Researchers have examined ternary OSCs with multiple donors (more prevalent in literature),[74, 82, 237-242] as well as multiple acceptors.[86, 87, 243] Initial results have been generally positive, with most researchers demonstrating enhanced J_{sc} values due to broader spectral responses. Further, some ternary OSCs have been shown to have tunable V_{oc} values dependent on the composition of the mixed layer,[89] instead of being pinned to the lowest V_{oc} dictated by the energy levels of the comprising donors/acceptors. The

combination of enhanced J_{sc} and intermediate value V_{oc} can thus allow ternary OSCs to achieve reasonably high performances while greatly simplifying device fabrication.

To date, ternary OSCs in literature have been formed by solution coating methods, while vacuum-deposited ternary OSCs have remained virtually unstudied. This is likely due to limitations with equipment (i.e. the need for multi-source evaporators), and the relative difficulty of simultaneously depositing three materials in a controlled manner. However, as the simultaneous deposition of three to four materials becomes more prevalent in white OLED fabrication,[244, 245] it is also more accessible to OSC research. In this work, ternary OSCs comprised of a BHJ with two m-Pc donors and a C_{60}-fullerene acceptor, with the active layer deposited by vacuum deposition, are studied. Vacuum deposition is specifically employed to minimize concerns regarding morphology. To this end, in a solution-coated OSC, the choice of solvent/co-solvent for the 'ink' can have tremendous impact on the morphology of the film, which has critical implications regarding device performance. It is therefore expected that the addition of an additional species to the ink, whether it is an extra donor or acceptor, will have drastic repercussions on the morphology of the film (this is further suggested by recent research focusing on active layer morphology in ternary OSCs).[81] Furthermore, these alterations to morphology are likely present even when using a very small amount of the third photo-active species, considering that solvent additives can substantially impact device performance at very low concentrations.[246-248] For ternary OSCs, it is therefore difficult to discriminate whether changes in photovoltaic parameters are solely due to the opto-electronic properties of the third component in the mixed layer, or related to changes in the morphology of the film. In the event that the morphology of the film changes considerably, direct comparisons of OSCs with and without the third component (binary versus ternary) may not be entirely valid. In contrast to solution processing, co-deposition by vacuum thermal evaporation (i.e. without substrate heating / post-processing steps) results in films that are inter-molecularly dispersed.[249, 250] It follows that vacuum-deposited ternary OSCs can provide a clearer understanding of the roles of the

three components in the OSC, including a more robust knowledge of the impact of their fundamental opto-electronic properties. Therefore, vacuum-deposited ternary OSCs provide a platform to study the impact of adding a third photo-active species, while minimizing concerns related to morphological variations that may otherwise obfuscate the data.

For the present study, the composition of the ternary mixture is systematically varied using a matrix approach, which allows for the study of all possible and relevant mixing ratios. The results demonstrate that ternary mixed films can be used to generate photocurrent over the entire visible spectrum at wavelengths from 300 nm up to 800 nm. However, in all mixtures, the ternary OSCs have poorer FF values than equivalent binary (one-donor, one-acceptor) OSCs. The reduced performance is attributed to an offset in the HOMO levels between the two donor materials, which ultimately results in hole trapping and poorer hole sweep-out to reduce the FF. Cascade OSC structures (multi-layer PHJ OSCs) are employed to emphasize this concept. The results suggest that the ideal alignment of energy levels is critical for ternary OSCs, and that the enhancements more commonly observed for solution-processed ternary OSCs may in part be due to morphological changes associated with the addition of the third component to the BHJ. Nevertheless, with intelligent molecular design, ternary OSCs should allow for significant improvements in the J_{sc} of OSCs with minimal impact to other photovoltaic parameters, thereby providing a simple, cost-effective device structure.

7.2. Results and Discussion

The ternary OSCs in this study are comprised of a C_{60} acceptor and two donor materials: ClInPc and SubPc. The energy levels for these materials, along with the energy levels and work functions for other relevant species in the OSCs for this chapter, are shown in Figure 7-1.A. As noted in **Chapter 4**, SubPc is reasonably well studied in literature, providing high V_{oc} values (owed to its deep HOMO) and high performance vacuum-deposited SM-OSCs.[133, 155, 169, 251] Furthermore, ClInPc is less studied in

literature, but it has also been highlighted for its high V_{oc} OSCs, while granting near-IR absorption.[72, 191, 209] The UV/Vis absorbance spectra of ClInPc, SubPc and C_{60} are provided in Figure 7-1.B. These three photo-active materials are shown to have ideal (complementary) positions for a ternary OSC, with C_{60} absorbing from 400 nm to 500 nm, SubPc absorbing from 500 nm to 600 nm, and ClInPc absorbing from 600 nm to 800+ nm.

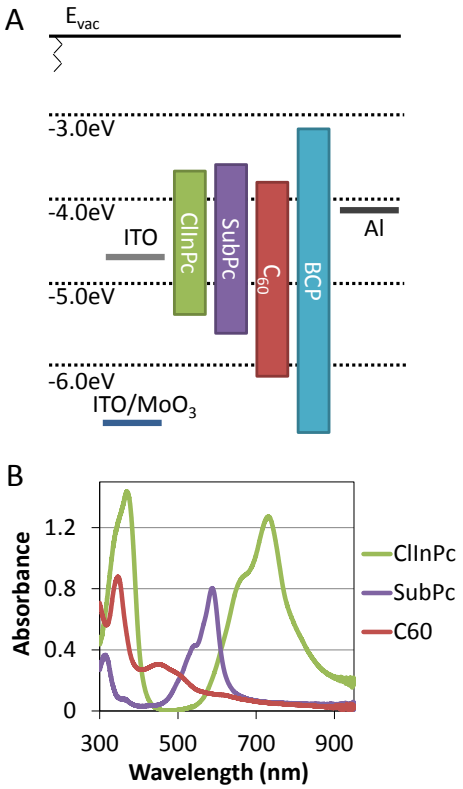

Figure 7-1 - A. Energy levels and work functions of the materials studied in this chapter. B. UV-Vis absorbance of 50 nm films of the photo-active materials studied in this chapter.

The OSC device structure employed in this research is a 40 nm BHJ sandwiched between a 5 nm MoO_3 HEL and an 8 nm BCP EEL, with an ITO anode and an aluminum cathode. The thickness of the BHJ was chosen to be 40 nm since it provides good performance for binary m-Pc:C_{60} BHJ OSCs, as established in previous work and discussed in **Chapter 4**.[209] It should also be noted that a neat layer of C_{60} in between the BHJ and the BCP layer could be employed in these devices to further bolster the PCE of the OSCs, as described in **Chapter 6**.[210] However, this architecture would also make data analysis,

particularly with the EQE spectra, more complicated than necessary. Since the ultimate goal of this work is to obtain a more fundamental understanding of the operation of the ternary mixed layer, the study is limited to the basic BHJ device structure.

7.2.1. Device Performance of Binary Mixture Controls

Binary BHJ OSCs with ClInPc:C_{60} and SubPc:C_{60} active layers are first considered to re-establish a baseline for device performance (see also the discussions in **Chapter 4**). The photovoltaic output parameters for these OSCs with varying donor-to-acceptor content are shown in Figure 7-2.

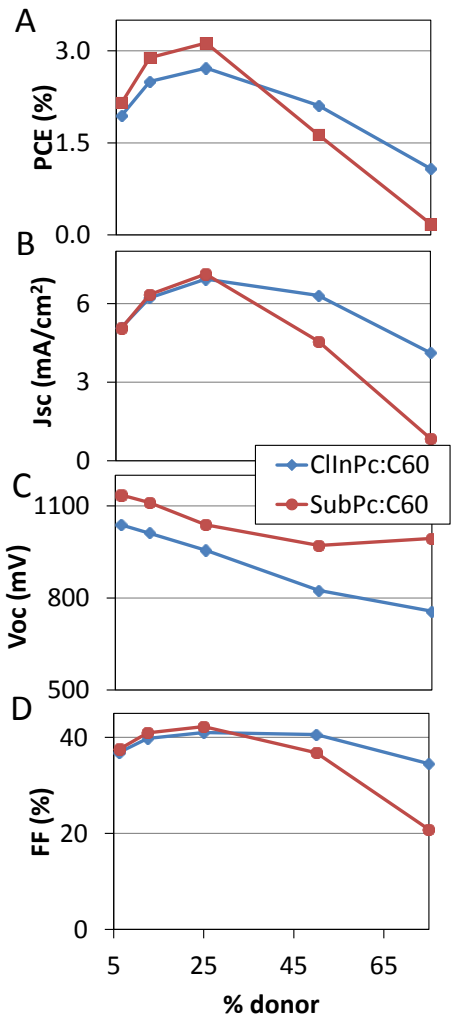

Figure 7-2 - Photovoltaic output parameters for binary ClInPc:C_{60} and SubPc:C_{60} BHJ OSCs with varying donor content (A through D correspond to PCE, J_{sc}, V_{oc} and FF respectively).

The ClInPc:C_{60} and SubPc:C_{60} OSCs maximize their performance at 25% donor content with peak PCE values of 2.7% and 3.1% respectively. At even lower donor content, the OSCs experience reductions in J_{sc} and FF (essentially due to hole trapping and recombination effects, as per discussions in **Chapter 6**).[210] An increase in V_{oc} with decreasing donor content due to Schottky band bending effects is also observed, as has been established in **Chapter 4**.[42, 72, 210] At 50% donor content, where Schottky band bending effects are not notably present, the V_{oc} of the SubPc:C_{60} OSC is ~970 mV and the V_{oc} of the ClInPc:C_{60} OSC is ~820 mV. At this 1-to-1 donor-to-acceptor mixing ratio, the V_{oc} is dictated primarily by the difference between the HOMO of the donor and the LUMO of the acceptor (minus energy losses noted in **Chapter 1**). Since the acceptor in both OSCs is C_{60}, and assuming similar exciton binding energies with ClInPc vs. SubPc, the ~150 mV offset corresponds to a ~150 meV offset in the HOMO positions between ClInPc and SubPc. This correlates reasonably well with the values shown in Figure 7-1. Finally, it is observed that at very high donor content, device performance decreases due to reductions in J_{sc} and FF, largely associated with the poor electron transport properties of the donor-rich BHJ layer (and in consideration of the associated charge recombination effects), as discussed in **Chapter 6**.[209, 210] It is worth noting that SubPc:C_{60} OSCs are generally more sensitive to varying donor content than ClInPc:C_{60} OSCs (with poorer performance at >50% donor content), suggesting that there may be some slight differences in the charge transport properties in the two materials systems.

The EQE spectra of the binary ClInPc:C_{60} and SubPc:C_{60} OSCs are shown in Figure 7-3.A and Figure 7-3.B respectively. As noted in **Chapter 4**, there are three spectral features of interest: The m-Pc Q band (peak at ~720 nm for ClInPc, ~580 nm for SubPc), the broad C_{60} aggregate band (peak at ~450 nm) and the UV band (peak at ~370 nm). The latter UV band comprises contributions from both C_{60} and the m-Pc B bands. The C_{60} aggregate band is only present at low donor concentrations (conversely, high C_{60} concentrations),[72, 210] and is best observed at ≥75% C_{60} within the mixed layer. By balancing the C_{60} aggregate photocurrent with the m-Pc Q band photocurrent, the EQE is optimized at 25% donor

content, which corresponds to the peak J_{sc} from Figure 7-2. In accordance with the UV/Vis absorbance from Figure 7-1.B, the SubPc:C_{60} OSCs generate photocurrent more strongly in the green region of the spectrum, whereas the ClInPc:C_{60} OSCs generate photocurrent in the red/near-IR region of the spectrum.

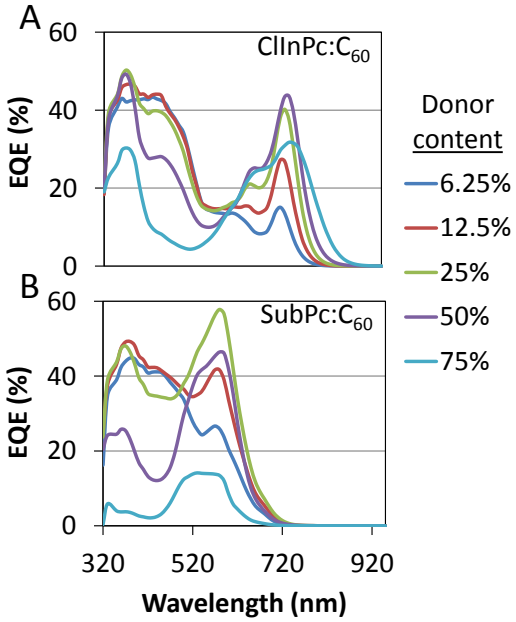

Figure 7-3 - EQE spectra of binary A) ClInPc:C_{60} and B) SubPc:C_{60} BHJ OSCs with varying donor content.

7.2.2. Device Performance of Ternary Organic Solar Cells

In order to obtain a comprehensive understanding of the vacuum-deposited ternary OSCs, a matrix approach is employed to vary the composition of ClInPc, SubPc and C_{60}. To this end, the concentration of ClInPc within the BHJ is varied, specifically considering values of 0%, 6.25%, 12.5%, 25%, 37.5% and 50%, while the SubPc concentration is varied with the same values. The balance (remainder) of the film concentration comprises C_{60}. This matrix approach thus consists of 36 different composition OSCs, with several duplicates at each point to establish average values. The OSCs were studied in a similar manner as in the previous section – extracting their photovoltaic parameters and

EQE spectra. Transient photocurrent measurements were also performed to obtain a better understanding of potential charge trapping effects. To visualize the trends in photovoltaic performance with active layer composition, surface plots were generated by interpolating values from the discrete data set, as shown in Figure 7-4. The x- and y-axes correspond to the ClInPc and SubPc concentrations respectively (with the remainder concentration as C_{60}), and the specific values are shown via color bars.

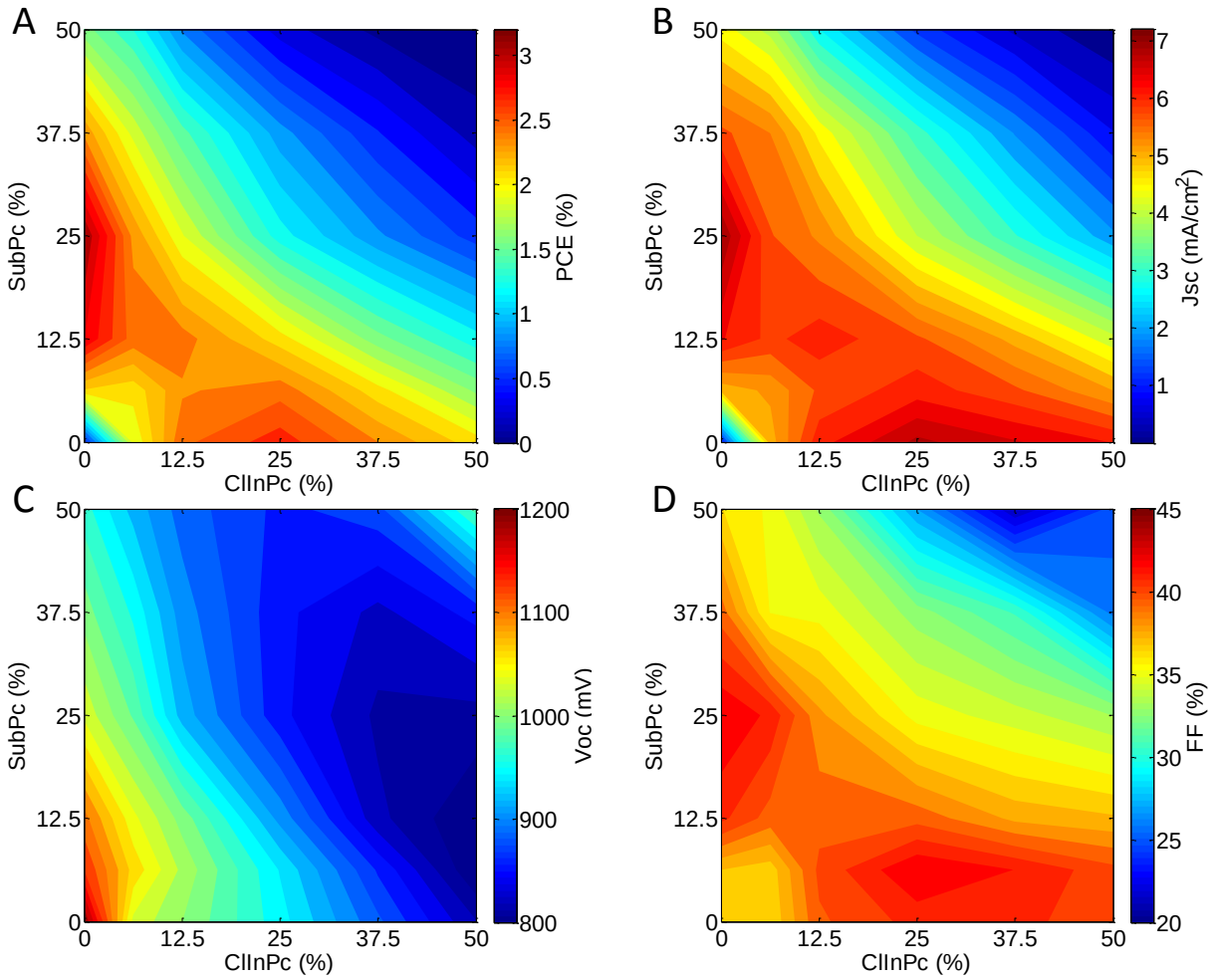

Figure 7-4 - Photovoltaic output parameter mapping of ternary ClInPc:SubPc:C_{60} OSCs (composition shown by x/y-axes, balance is C_{60}). Panels A through D correspond to the PCE, J_{sc}, V_{oc} and FF respectively.

From the plot of PCE as a function of film composition in Figure 7-4.A, the ternary OSCs clearly underperform when compared to the binary OSCs. To this end, the ClInPc:C_{60} OSCs with 0% SubPc concentration (data lying on the x-axis) show higher PCE than the OSCs with a small concentration of SubPc. Similarly, the SubPc:C_{60} OSCs with 0% ClInPc concentration (data lying on the y-axis) show higher

PCE than the OSCs with a small concentration of ClInPc. Interestingly, the performance data are rather symmetric since both the ClInPc:C_{60} and SubPc:C_{60} OSCs optimize their performance at 25% donor concentration. The device performance decreases rapidly as the donor concentration decreases from 6.25% to 0%. On the other hand, the device performance decreases more gradually as the acceptor concentration decreases from 50% to 0%. The result is a band of good performance OSCs (2.5% to 3% PCE) stretching across the 25% donor content region, with slight variations in performance within this band due to the distribution of ClInPc to SubPc.

Since one of the key motivations for studying ternary OSCs is their potentially broader photoresponse, it is logical to examine the J_{sc} versus film composition, shown in Figure 7-4.B. The J_{sc} is observed to follow a similar trend as the PCE, except that the band of good J_{sc} values is slightly broader than the band of good PCE values. This indicates that reasonable J_{sc} values (5.5 mA/cm^2 to 6.5+ mA/cm^2) can be obtained between 12.5% to 37.5% donor content. Within this band, the highest J_{sc} values are obtained nearest the binary ClInPc:C_{60} and SubPc:C_{60} OSCs. As a consequence, the J_{sc} is found to decrease in the ternary OSC in spite of the third photo-active component in the mixed layer. This is opposite to the desired trend, so it is necessary to study the EQE of the samples to verify that all three species can contribute to the photocurrent in the ternary OSC. Figure 7-5 shows the EQE spectra of OSCs with equal concentrations of SubPc and ClInPc (e.g. such that 25% donor content = 12.5% ClInPc, 12.5% SubPc and 75% C_{60}).

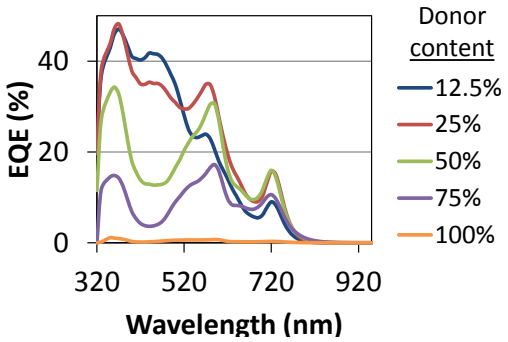

Figure 7-5 - EQE spectra of ternary OSCs with varying donor content ([ClInPc] = [SubPc], balance is C_{60}.

The data confirm that ClInPc, SubPc and C_{60} all contribute to the photocurrent simultaneously and thus provide photocurrent across the entire visible spectrum (300 nm to 800 nm). It is worth noting that, at 100% donor content (no C_{60}), the EQE logically decreases to ~0% because the mixed layer no longer has a donor-acceptor interface to efficiently separate excitons (the ~150 meV HOMO offset between ClInPc and SubPc is not sufficient in this capacity). While Figure 7-5 shows that all three components can generate photocurrent in the ternary OSC, there are two critical deficiencies visible from the EQE spectra:

- the magnitude of EQE is significantly lower across all wavelengths – at the m-Pc Q band, the binary OSCs exhibit peak EQE values of 40-60% (Figure 7-3) while the ternary OSCs have peak EQE values of 10-35% (Figure 7-5)
- the C_{60} aggregate absorption disappears completely for OSCs with >25% donor content

While the latter point is an important factor in binary OSCs as well, its impact on the photocurrent generation for the ternary OSCs is substantially more critical. In the ternary OSC, the 25% donor content must be split between two different absorbing species, so the individual donor components cannot generate the same magnitude of photocurrent. Unfortunately, increasing the total donor content beyond 25% serves to reduce the V_{oc} (due to Schottky band bending effects),[209] hinder charge transport,[191, 210] and reduce C_{60} aggregate photocurrent,[72] thus degrading OSC performance. These observations highlight one of the more critical aspects of the ternary OSC: one must carefully

tune the mixed layer composition to balance photocurrent contributions from all three species. By increasing the concentration of one component in the OSC, one necessarily decreases the concentration of the other component, thereby reducing its impact on device performance and its role in generating photocurrent. This is even more critical when certain species, such as C_{60}, require a minimum concentration (i.e. to form C_{60} aggregates) to contribute meaningfully to the photocurrent, and therefore place further compositional restrictions on the BHJ.

The limitations regarding photocurrent in the ternary device architecture are clearly visible from the EQE spectra mappings as a function of OSC composition, as shown in Figure 7-6. Figure 7-6 provides the magnitude of EQE at several critical regions in the EQE spectra, including the ClInPc Q band at ~720 nm, the SubPc Q band at ~580 nm and the C_{60} aggregate band at ~450 nm (panels A through C respectively – the UV peak EQE is also mapped and provided in the Supplemental Information (**Appendix 1.3**)). As stipulated, the maximum EQE values for these bands essentially never overlap. Furthermore, these regions of high magnitude EQE are found to decrease rapidly away from their peak efficiency. Specifically, considering a constant 25% ClInPc concentration and then increasing the SubPc concentration from 0% to 25%, the EQE is found to decrease from 40% to 15%. Likewise, considering a constant 25% SubPc concentration and then increasing the ClInPc concentration from 0% to 25%, the EQE is found to decrease from 60% to 30%. In order for the ternary OSC to be useful in generating significant photocurrent, the individual absorbing species must each be able to generate photocurrent at relatively low concentrations (at least half of their typical concentrations in a binary OSC). Since there is no substantial overlap in the EQE plots for the present materials system, the OSC photocurrent generation is indeed broad, but not very efficient.

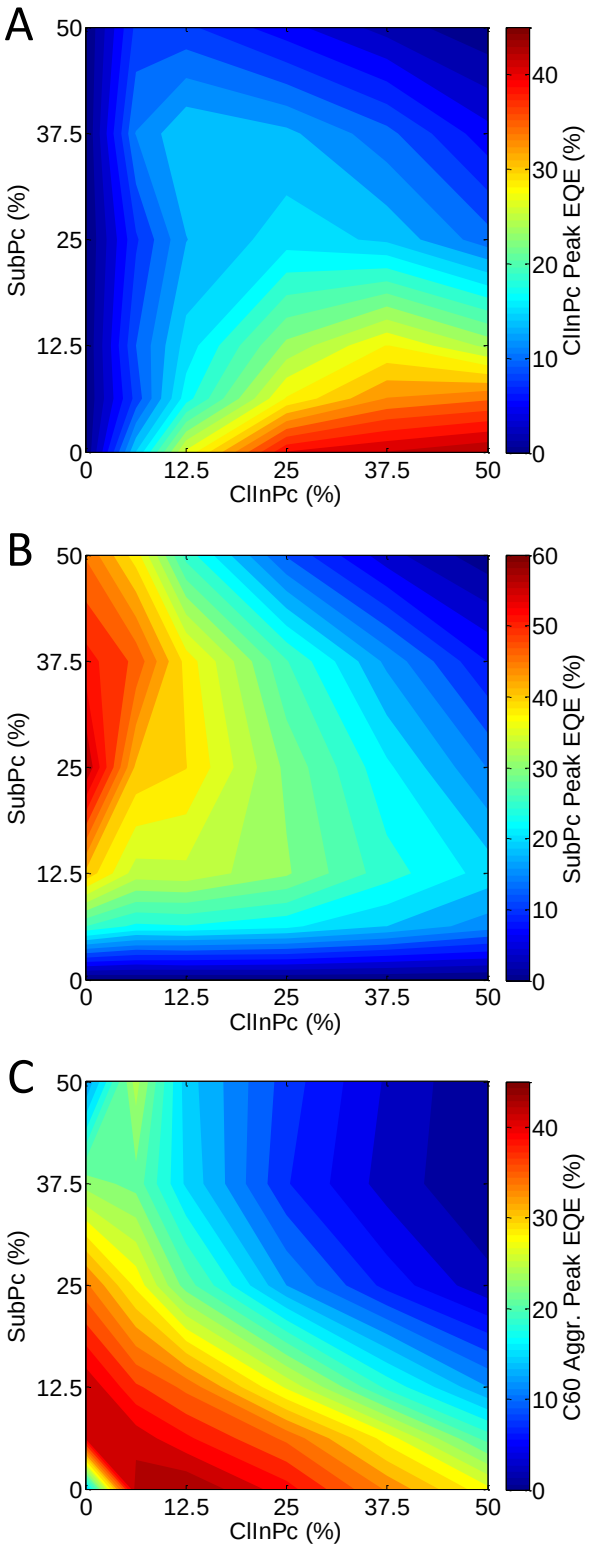

Figure 7-6 - EQE spectra mapping of ternary ClInPc:SubPc:C_{60} OSCs (composition shown by x/y-axes, balance is C_{60}). Panels A through C correspond to the ClInPc peak (~720 nm), SubPc peak (~580 nm) and C_{60} aggregate peak (~450 nm) respectively.

While the effective splitting of photocurrent contributions among two donors is a significant issue to overcome in ternary OSCs, it cannot in itself account for the decrease in efficiency observed for ternary OSCs. If this was the sole factor, one would expect equivalent performance between ternary and binary OSCs, not the decreased performance shown in Figure 7-4.A. It is therefore necessary to study the two remaining photovoltaic output parameters from Figure 7-4, the V_{oc} and the FF (panels C and D respectively). Figure 7-4.C is relatively straightforward to understand from the background provided in **Chapter 4** and **Chapter 6**. Namely, SubPc:C_{60} OSCs have slightly higher V_{oc} values than ClInPc:C_{60} OSCs due to SubPc's deeper HOMO, and both OSCs benefit from Schottky band bending effects that occur at very high C_{60} concentrations. For this reason, a peak V_{oc} value of 1.2 V can be obtained when no donor is present (at the origin of Figure 7-4.C). Naturally, as the C_{60} concentration is increased, regardless of the donor composition, the V_{oc} approaches this maximum value that is ultimately defined by the anode's effective work function (as set by ITO/MoO_3) and the energy levels of C_{60}.[71] When the mixed layer has more ClInPc content, the V_{oc} is closer to that of ClInPc:C_{60} OSCs, and when the mixed layer has more SubPc content, the V_{oc} is closer to that of SubPc:C_{60} OSCs. Interestingly, in accordance with previous results from literature,[89] the V_{oc} values of the ternary OSCs are generally at some intermediate state between the low V_{oc} floor and the high V_{oc} ceiling set by the ClInPc:C_{60} and SubPc:C_{60} OSCs respectively. However, given the complications with the varying V_{oc} due to Schottky band bending effects, it is unclear if this effect is similarly due to the formation of an organic alloy.

The changes in FF with active layer composition, shown in Figure 7-4.D, follow similar trends as the PCE and the J_{sc}. The FF is maximized for the binary OSCs, and maintains reasonably high values near 25% donor concentration. However, when the ClInPc concentration equals the SubPc concentration (for any given mixing ratio), the FF for the ternary OSC is always found to be lower than the equivalent donor-to-acceptor content binary OSC. For example, considering a 25% donor content OSC, the binary ClInPc:C_{60} device has a FF of 41%, the binary SubPc:C_{60} device has a FF of 42%, but the ternary OSC

(12.5% ClInPc, 12.5% SubPc) only has a FF of 37%. Similarly, at 12.5% donor content, the binary OSCs have FF values of 40% to 41%, but the ternary OSC has a FF of 35%. This degradation to the FF is thus a strong contributor toward the reduced performance of the ternary OSCs in general. To better understand the cause of this reduction in FF, it is useful to consider hole transport in ternary OSCs in terms of the energy levels of ClInPc, SubPc and C_{60}, shown in Figure 7-1. Any hole formed on ClInPc will remain on ClInPc molecules due to the energetic barrier to hop onto SubPc molecules. If the donor concentration is kept constant at 25%, which allows one to harvest photocurrent from C_{60} aggregates, any addition of SubPc to the ClInPc:C_{60} OSC necessarily requires a reduction in ClInPc content. Since holes formed on ClInPc molecules cannot hop to SubPc molecules, the number of pathways for hole transport is effectively reduced. The result is an increased path length that the hole must traverse to reach the anode, as the hole must meander through the sparsely distributed ClInPc. Furthermore, an exciton formed on SubPc may reach a SubPc/C_{60} interface to generate a hole on SubPc. However, if there are any adjacent ClInPc molecules, the hole will preferentially hop to ClInPc due to its shallower HOMO. As such, by incorporating two donors with different HOMO levels, hole transport throughout the mixed layer is strongly hindered.

To better visualize the limitations for hole transport in ClInPc:SubPc:C_{60} ternary OSCs, multi-donor PHJ OSCs were fabricated with two different configurations: ClInPc (0, 5 or 20 nm)/SubPc (10 nm)/C_{60} (30 nm) and SubPc (0 or 10 nm)/ClInPc (20 nm)/C_{60} (30 nm). The use of the PHJ (neat layers) structure instead of the BHJ (mixed layer) structure helps to emphasize charge transport limitations due to the mismatch in the donors' HOMO energy levels. In the first device structure, the ClInPc layer merely acts as an additional hole transport layer, and cannot contribute to photocurrent due to the wider bandgap SubPc layer separating ClInPc from C_{60} (this is verified by EQE measurements, shown in Section 7.3 and the Supplemental Information (**Appendix 1.3**)). This device structure is therefore analogous to forcing holes to be transported along an extra length of ClInPc, which is essentially the end

result of decreasing ClInPc content in the ternary OSC. In the second device structure, the SubPc layer acts as a blocking layer, restricting hole transport from ClInPc to the anode. This device structure therefore verifies that once a hole is present on a ClInPc molecule, it cannot hop to a SubPc molecule due to the offset in HOMO energy levels (unless it is a sufficiently hot carrier). The current-voltage characteristics for these PHJ devices are shown in Figure 7-7. It is worth noting that the SubPc/ClInPc/C_{60} structure exhibits cascading donor exciton energies to potentially allow for long distance energy transfer processes, as will be discussed further in Section 7.3.

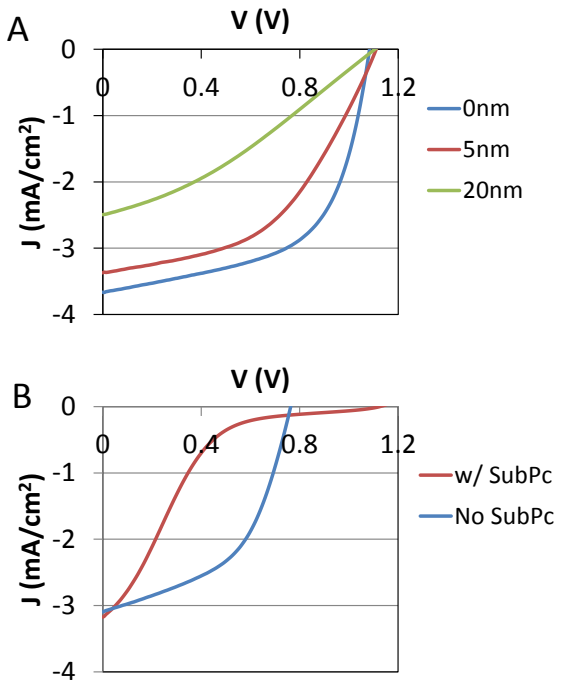

Figure 7-7 - JV characteristics of A) ClInPc (x nm)/SubPc (10 nm)/C_{60} (30 nm) and B) SubPc (0 or 10 nm)/ClInPc (20 nm)/C_{60} (30 nm) multi-donor PHJ OSCs.

As seen from Figure 7-7.A, both the FF and J_{sc} are strongly degraded with the addition of a neat layer of ClInPc between the anode and the SubPc layer. As noted above, this is due to the added length that holes must traverse to reach the anode, which serves to increase the R_s, cause undue charge recombination effects, and ultimately decrease the R_{sh}. In Figure 7-7.B, the addition of 10 nm of the wider bandgap SubPc between ClInPc and the anode blocks holes and creates the s-shaped JV characteristic that is now well studied in literature and can be attributed to space charge build-up.[59, 215,

[252] The multi-donor PHJ OSCs therefore verify the stipulations made previously: the HOMO offset between SubPc and ClInPc limits the charge transport properties of ternary mixed film and ultimately degrades ternary OSC performance. Interestingly, this effect is generally not observed as strongly for the solution-processed ternary OSCs studied in literature, where ternary OSCs usually provide a slight improvement in performance. It is thus suggested that additional morphological variations in solution-processed ternary OSCs, which are not present in the vacuum-deposited (molecularly mixed) ternary OSCs, may account for some degree of improvement in device performance.

Given that the HOMO position of the two donors is a critical factor in the performance of ternary OSCs, OSCs comprising two donors with similar HOMO energy levels were also examined. Specifically, ternary OSCs with a 40 nm mixed layer of ClInPc, C_{60} and the donor-acceptor-acceptor molecule DTDCTB were examined.[138, 253] Both DTDCTB and ClInPc have HOMO values on the order of ~5.2 eV to 5.3 eV, which corresponds well to their similar V_{oc} values of ~0.8 V (+/- 20 mV) when incorporated into 1:1 donor:C_{60} BHJ OSCs. Unfortunately, since both DTDCTB and ClInPc were designed to absorb in the red and near-IR, they have overlapping absorbance spectra (shown in the Supplementary Information(**Appendix 1.3**)), so these ternary OSCs are not expected to improve the J_{sc} (since ternary ClInPc:DTDCTB:C_{60} OSCs do not absorb more broadly than binary ClInPc:C_{60} OSCs). Nevertheless, the overlapping HOMO values of the donors provide critical information with regard to charge transport. Furthermore, DTDCTB:C_{60} OSCs yield similar performance values as compared to ClInPc:C_{60} OSCs, so DTDCTB is particularly appropriate for this analysis. It is expected that holes on ClInPc can easily hop to DTDCTB and vice versa, so that mixing DTDCTB into ClInPc:C_{60} will not negatively affect the FF. The FF of a 12.5%:87.5% ClInPc:C_{60} OSC is 40%. As noted previously, adding SubPc to the mixture decreases the FF, such that a ternary 6.25%:6.25%:87.5% ClInPc:SubPc:C_{60} OSC has a FF of 35%. Interestingly, adding DTDCTB to the mixture to create a ternary 6.25%:6.25%:87.5% ClInPc:DTDCTB:C_{60} OSC instead yields a small improvement in FF to 42%. This effect is repeated for a 50%:50% ClInPc:C_{60}

OSC, which has an initial FF of 41%. Adding SubPc to create a 25%:25%:50% ClInPc:SubPc:C_{60} OSC reduces the FF to 34%, while adding DTDCTB again increases the FF very slightly to 43% (with a 25%:25%:50% ClInPc:DTDCTB:C_{60} OSC). The full set of photovoltaic parameters for these devices is available in the Supplementary Information (**Appendix 1.3**). Based on this analysis, it is reasonable to emphasize the stringent requirements on the energy levels of the components used in a ternary OSC. To this end, the HOMO values of the donors used in a donor:donor:acceptor ternary OSC must be very close to each other in order to generate films with reasonable hole transport properties (and thus to yield OSCs with high FF values). Furthermore, in a HOMO-matched ternary OSC, any significant differences in hole mobilities between the two donors may cause additional charge transport limitations. Likewise, it can be stipulated that the LUMO values and mobilities of the acceptors in a donor:acceptor:acceptor ternary OSC would have to be very close for the same reasoning.

As further validation of the hole transport limitations discussed above, microsecond transient photocurrent responses of ternary ClInPc:SubPc:C_{60} OSCs were also studied. Transient photocurrent measurements have been used in a number of studies to examine charge transport phenomena in OSCs,[66, 206, 215] and such measurements were used in **Chapter 6** to examine charge transport in binary donor:acceptor OSC structures.[191, 210] These measurements thus serve as an ideal platform to understand the charge transport limitations of ClInPc:SubPc:C_{60} OSCs. The full details of the transient photocurrent measurements are provided in the Experimental section. Single exponential fits are used to characterize the photocurrent decay, as per equation (7.1) below, to calculate the relevant fall time constant τ. In equation (7.1), I is the current measured at time t, following the end of the light pulse (as shown in Figure 7-8.A), and C1 and C2 are fitting parameters.

$$I = C_1 \cdot \exp(-C_2 t), \quad C_2 = 1/\tau \tag{7.1}$$

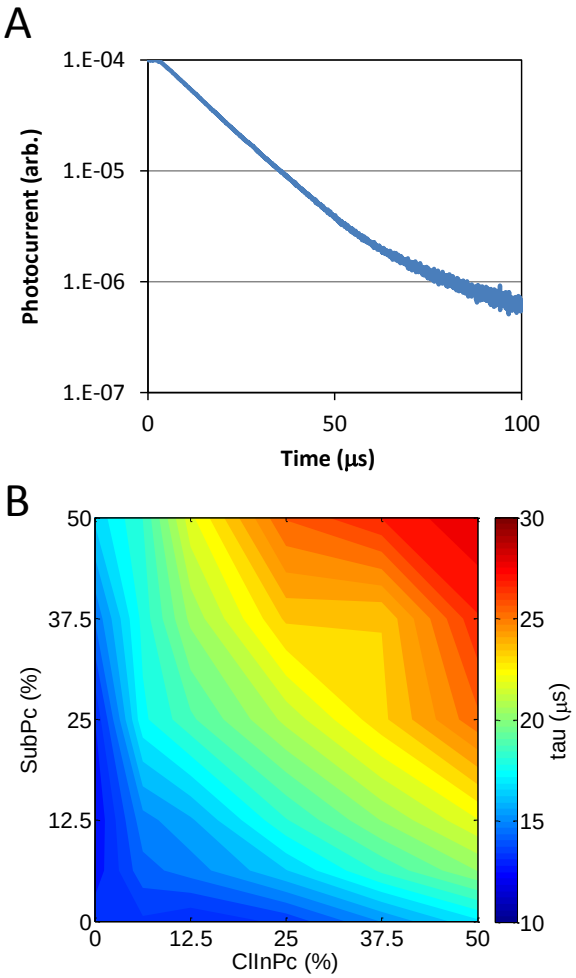

Figure 7-8 - A) Sample transient photocurrent decay for a ternary ClInPc:SubPc:C_{60} OSC. B) Transient photocurrent τ mapping of ternary ClInPc:SubPc:C_{60} OSCs (composition shown by x/y-axes, balance is C_{60}).

The transient photocurrent responses of the ternary ClInPc:SubPc:C_{60} OSCs at all of the relevant mixing ratios are shown in Figure 7-8.B. The resulting plot is rather symmetric, with binary OSCs providing the fastest transient photoresponse, and ternary OSCs being substantially slower. In light of the previous discussions, it is suggested that ternary ClInPc:SubPc:C_{60} OSCs suffer from poor hole sweep out due to hole transport limitations, which slows the transient photocurrent response. As noted previously, by mixing ClInPc and SubPc together and considering constant donor:acceptor content, one effectively decreases the number of ClInPc molecules in a ternary film compared to a binary film. Given its shallower HOMO, ClInPc is naturally the primary hole transporter in ClInPc:SubPc:C_{60} ternary OSCs. Charge trapping is therefore especially problematic for holes on isolated ClInPc molecules. Furthermore,

the reduction of ClInPc content serves to limit the number of hole-conductive pathways for hole transport, thereby hindering sweep-out. Coupling this information with the knowledge that ClInPc has generally poorer hole transport properties compared to fullerene's electron transport properties,[209, 210] it is observed that the slowest devices are the ternary ClInPc:SubPc:C_{60} OSCs with high donor content. The results thus support the earlier conclusions, which suggest that the energy levels of ternary OSCs must be well matched in order to retain reasonable charge transport properties, and thus to allow for rapid sweep out of charges.

7.3. Cascade Organic Solar Cells with ClInPc, SubPc and C_{60}

In the previous section, several multi-layer PHJ OSCs were examined to better understand charge transport difficulties in two-donor-one-acceptor ternary OSCs. It is worthwhile to further examine these systems for their own merit, given that they can also qualify as cascade OSCs, a topic of significant interest in recent literature.[91, 94, 95, 254-256] Considering ClInPc, SubPc and C_{60}, there are four practical and interesting device configurations:

A. ITO/MoO_3/ **SubPc (10 nm)/ClInPc (x nm)/C_{60} (30 nm)** /BCP/Al

B. ITO/MoO_3/ **SubPc (x nm)/ClInPc (20 nm)/C_{60} (30 nm)** /BCP/Al

C. ITO/MoO_3/ **ClInPc (20 nm)/SubPc (x nm)/C_{60} (30 nm)** /BCP/Al

D. ITO/MoO_3/ **ClInPc (x nm)/SubPc (10 nm)/C_{60} (30 nm)** /BCP/Al

, where each defined thickness has been optimized for an associated bilayer PHJ OSC (e.g. 20 nm ClInPc / 30 nm C_{60} and 10 nm SubPc / 30 nm C_{60} provide the highest efficiencies). Configurations B and D were examined briefly in Section 7.2. The current voltage curves for five different thicknesses of each configuration are shown in Figure 7-9.

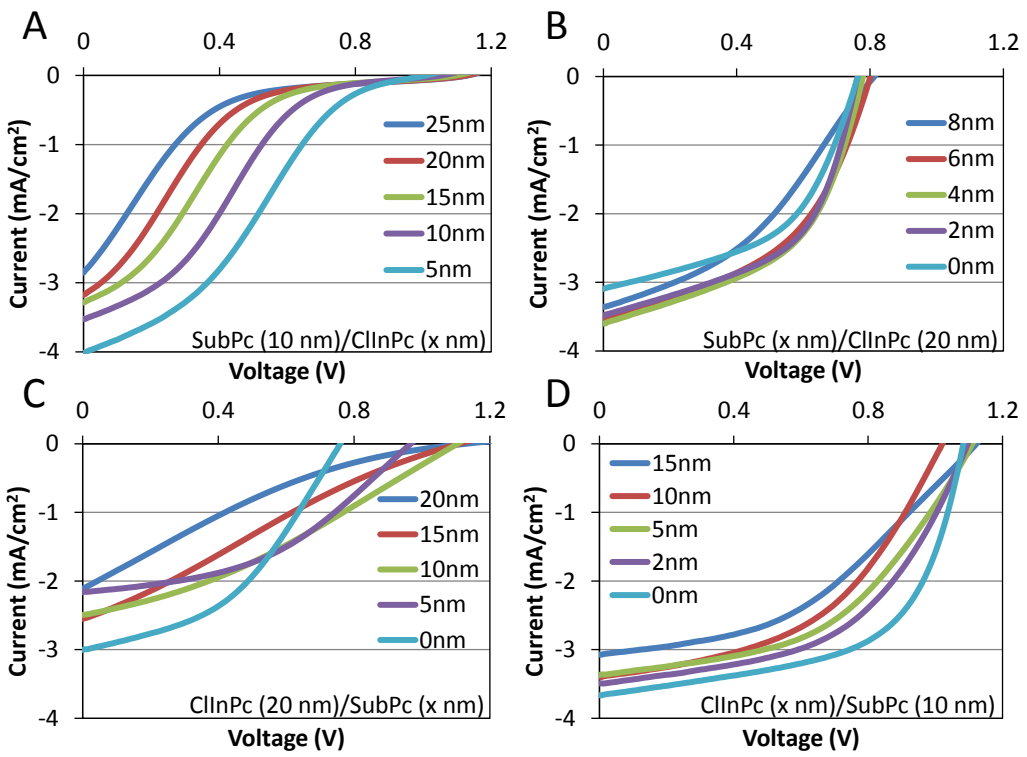

Figure 7-9 - JV characteristics of multi-layer PHJ OSCs, with photo-active layers comprising: A) SubPc (10 nm)/ClInPc (x nm)/C_{60} (30 nm), B) SubPc (x nm)/ClInPc (20 nm)/C_{60} (30 nm), C) ClInPc (20 nm)/SubPc (x nm)/C_{60} (30 nm), and D) ClInPc (x nm)/SubPc (10 nm)/C_{60} (30 nm).

Device configurations A and B employ a ClInPc/C_{60} donor/acceptor junction, placing SubPc between the anode and ClInPc. For these configurations, an exciton can be generated on either ClInPc or SubPc following the absorption of light. In the case of ClInPc, the exciton diffuses to the ClInPc/C_{60} heterojunction to generate a hole on ClInPc and an electron on C_{60}. In the case of SubPc, the exciton must first diffuse to ClInPc, and then subsequently diffuse to the ClInPc/C_{60} interface. As noted in the previous section, the exciton cascade from SubPc to ClInPc is energetically favourable due to SubPc's wider bandgap compared to ClInPc. As such, ClInPc and SubPc both contribute to photocurrent and these configurations may be considered cascade OSCs. The photocurrent contributions from both ClInPc and SubPc can be verified by EQE measurements, as shown in Figure 7-10. For SubPc thicknesses equal to and greater than 4 nm (Figure 7-10.B), there are EQE peaks visible from all three active layer components: ClInPc (720 nm), SubPc (580 nm), and C_{60} (450 nm).

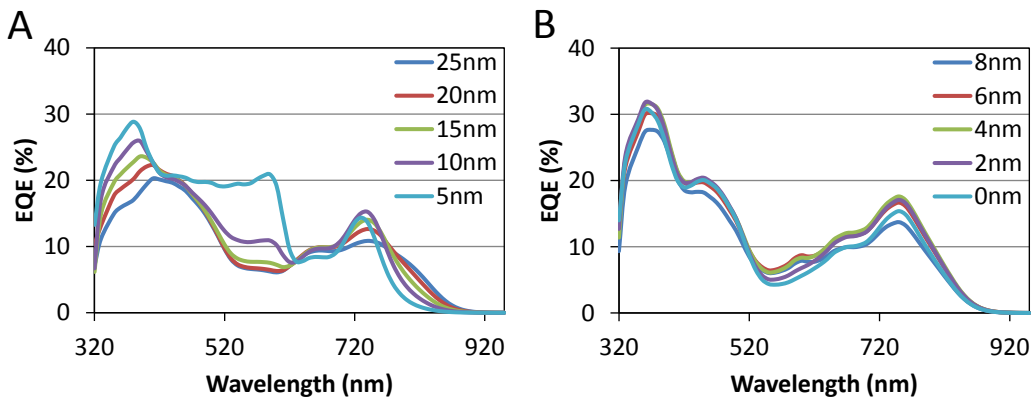

Figure 7-10 - EQE Measurements of various multi-layer PHJ OSCs, with photo-active layers comprising: A) SubPc (10 nm)/ClInPc (x nm)/C_{60} (30 nm), B) SubPc (x nm)/ClInPc (20 nm)/C_{60} (30 nm).

As described in the previous section, once a hole is formed on ClInPc, it has difficulty being swept to the anode due to the HOMO offset at the ClInPc/SubPc interface. This leads to the s-shape JV characteristics in Figure 7-9.A that are well studied in literature.[59, 60, 215, 252] For device configuration A, where the SubPc is kept constant at 10 nm and the ClInPc thickness varies from 5 to 25 nm, the highest J_{sc} values are obtained with the thinnest ClInPc. From the EQE spectra in Figure 7-10.A, there is a strong reduction in SubPc photocurrent with thicker ClInPc. Beyond ~15 nm ClInPc, the SubPc photocurrent contributions are almost completely suppressed. From these data, it can be concluded that excitons initially formed on SubPc can only diffuse ~15 nm on ClInPc before recombining. Finally, as a point of interest, it is worth noting that both configurations A and B pin the V_{oc} to the $ClInPc_{HOMO}$-$C_{60\text{-}LUMO}$ offset. However, when the SubPc layer is suitably thick to strongly suppress hole transport (resulting in s-shape JV characteristics), the V_{oc} shifts to the value set by the $SubPc_{HOMO}$-$C_{60\text{-}LUMO}$ offset. In this mode of operation, only hot (high energy) holes are able to overcome the HOMO offset between ClInPc and SubPc, which further explains the strong reduction in photocurrent near the V_{oc} and the overall s-shape characteristic. It can be concluded that the HOMO offset for cascade OSCs needs to be much lower than the ~150 meV offset in the presently studied system – likely on the order of the thermal energy of the system (~25 meV at room temperature).

For device configuration B, the SubPc layer thickness is varied from 0 to 8 nm, while the ClInPc layer thickness is kept constant at 20 nm. From Figure 7-9.B, increasing the SubPc thickness from 0 nm to 2 nm serves to increase device performance, with improved FF, J_{sc} and PCE. This improvement is initially counterintuitive, as it was established that the HOMO offset between SubPc and ClInPc results in hole blocking/accumulation. From the EQE in Figure 7-10.B, the improvement in J_{sc} is primarily due to improved ClInPc photocurrent contributions, and secondarily due to slight contributions from SubPc. It has been established that MoO_3 is an effective HEL because it can generate high work function electrodes; however, MoO_3 is also very efficient at quenching excitons.[69] As such, while MoO_3 can substantially improve hole extraction from OSCs, it also interferes with the fundamental photocurrent generation processes. Thus, by incorporating a very thin film of the wider bandgap SubPc at the anode, one may effectively reduce the exciton recombination rate at the ClInPc/MoO_3 interface, while still allowing for hole transport to the anode. Naturally, following the results from device configuration A, as the SubPc layer thickness is further increased, it begins to hinder hole transport and thus degrade device performance. To this end, with 8 nm of SubPc, the s-shape characteristic becomes more visible, and by 10 nm (Figure 7-9.A), hole transport is strongly suppressed.

Device configurations C and D employ a SubPc/C_{60} donor/acceptor junction, placing ClInPc between the anode and SubPc. As noted previously, since SubPc has a wider bandgap than ClInPc, excitons generated on ClInPc cannot be transferred across SubPc to the donor/acceptor interface. These device configurations are not considered true cascade OSCs, as only SubPc contributes to the photocurrent. This can be observed more clearly from their EQE spectra in Figure 7-11.

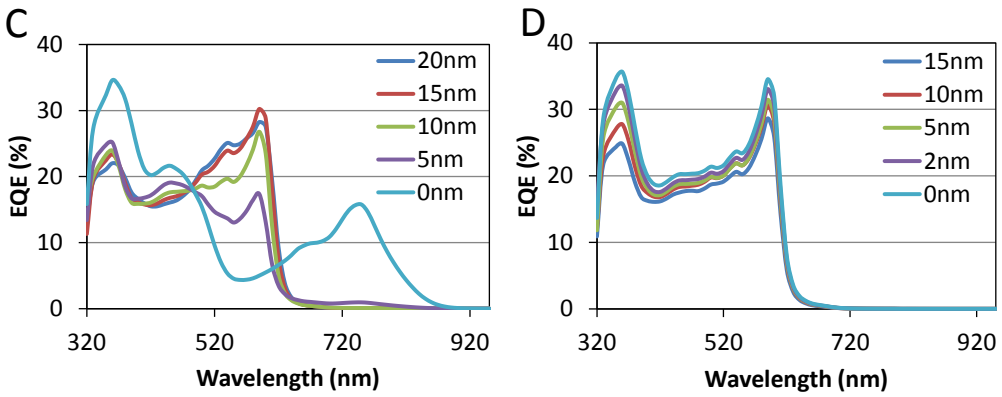

Figure 7-11 - EQE Measurements of various multi-layer PHJ OSCs, with photo-active layers comprising: C) ClInPc (20 nm)/SubPc (x nm)/C_{60} (30 nm), and D) ClInPc (x nm)/SubPc (10 nm)/C_{60} (30 nm).

For configuration C, the transition from 0 nm SubPc to 5 nm SubPc between ClInPc and C_{60} results in complete suppression of photocurrent from ClInPc (720 nm). The photocurrent remains suppressed for all other thicknesses and for all of the devices in configuration D, indicating that SubPc efficiently blocks ClInPc excitons. Likewise, this transition from a ClInPc/C_{60} OSC to a SubPc/C_{60} OSC results in a corresponding increase in the V_{oc}, as shown in Figure 7-9.C. As noted in the discussion on ternary OSCs in Section 7.2.2, once the SubPc/C_{60} interface is formed, the role of ClInPc is solely to act as a hole transport layer. Increasing the thickness of ClInPc only serves to hinder hole sweep out and thus degrade FF and J_{sc}, shown in Figure 7-9.D.

7.4. Conclusions

In this chapter, vacuum-deposited ternary OSCs were investigated by systematically varying the composition of their comprising two-donor, one-acceptor mixed films. The data from this work notably complement studies in literature on solution-processed ternary OSCs by alleviating many of the morphological considerations that are inherent in spincoating, doctor blading, etc. The following major conclusions were drawn from this chapter:

- Ternary OSC can be effective in providing broad photocurrent across the entire visible spectrum, with ClInPc:SubPc:C_{60} OSCs exhibiting photocurrent contributions from 300 nm to 800 nm.

- By incorporating a third material into the photo-active layer, one unavoidably reduces the amount of the other two materials in the mixture, and therefore reduces their light absorption and photocurrent generation. Correspondingly, it is challenging to adjust the mixing ratios of the ternary mixed film to achieve high EQE values from all three photo-active components simultaneously. This limitation may be partially addressed by employing thicker active layers; however, thicker active layers would reduce the FF and exacerbate the already complicated charge transport processes within the ternary mixture.
- Ternary OSCs have stringent requirements for the comprising molecules' energy levels, especially since a slight mismatch in the HOMO levels of the two donors can strongly hinder charge transport and thus degrade the FF.
- With intelligent molecular design to achieve ideal energy levels, thereby minimizing charge transport limitations, ternary OSCs are a simple and cost-effective device architecture that can allow for broad and intense photocurrents that ultimately grant high power conversion efficiencies.

Chapter Eight:

The Photo-stability of Polymer Solar Cells: Contact Photo-degradation and the Benefits of Interfacial Layers[1]

In this chapter, P3HT:PCBM OSCs are studied for their light, heat and electrical stability in inert atmosphere. This chapter therefore examines changes in charge collection with time to identify the major contributors to reduced OSC performance under regular operation. Various extraction layers are examined for their effect on device stability. The organic/metal interface is shown to be inherently photo-unstable and is identified as the primary source of deterioration in OSC performance, resulting in significant losses in device efficiency with photo-irradiation. XPS measurements of the organic/aluminum interface suggest that the photo-induced changes are chemical in nature. In general, interfacial layers are shown to substantially reduce photo-degradation of the active layer/electrode interface. In spite of their photo-stability, several interfacial layers present at the active layer/cathode interface suffer from thermal degradation effects due to OSC temperature increases while exposed to light. Electrical aging effects are demonstrated to be negligible in comparison to other major modes of degradation.

8.1. Introduction

As discussed in **Chapter 1**, limited device stability remains one of the most significant roadblocks toward the wide success and commercialization of OSCs. Gradual changes in an OSC's comprising

[1] The majority of the material in this chapter was published in:
G. Williams, Q. Wang,H. Aziz, Adv. Funct. Mater., 2012, 23, 2239
Q. Wang, G. Williams, H. Aziz, Org. Electron., 2012, 13, 2075 (secondary)
Q. Wang, G. Williams, T. Tsui,H. Aziz, J. Appl. Phys., 2012, 112, 064502 (secondary)
, reproduced here with permission.

materials can cause its PCE to decrease with time, thus limiting its useful (i.e. service) life. The vast majority of OSC stability research to date has focused on degradation due to ambient moisture and oxygen, which affects both the bulk active layer as well as the organic-electrode interface.[4-7, 193, 257, 258] Ambient stability measurements provide very relevant information regarding degradation of the end-product solar cell. In addition, some efforts have been made to understand the stability behavior of OSCs under illumination, even in an inert environment, referred to as intrinsic device photo-stability.[8, 11, 36, 259] In inert atmosphere one may simply isolate the major pathways toward OSC photo-degradation: direct photo-induced changes, changes induced by the associated thermal stresses, and changes induced by the flow of photo-generated charge carriers and/or their accumulation in trap sites in the various layers of a device (due to electrical stress). It was recently found that the organic layer/electrode interfaces in organic optoelectronic devices can degrade rapidly under illumination, even in inert environments.[12, 13] To this end, it was shown that OLEDs and OPDs made of small molecule organic semiconductor materials are sensitive to photochemical changes at the metal and ITO interfaces, ultimately playing a major role in charge collection behaviour with time.

In this chapter, the stability of P-OSCs under illumination is studied, focusing on the organic/electrode contacts and their influence on device photo-stability behaviour. The archetypical OSC system based on a blend of P3HT and PCBM is employed for this work, following the rationale established in **Chapter 4**. Namely, the goal of this chapter is to establish major degradation phenomena that alter charge collection processes and are highly relevant to the OPV community at large. In **Chapter 9**, these observations are expanded to study both P-OSCs and SM-OSCs, allowing for the identification of variations in device performance that can occur regardless of the fabrication methodology.

Since interfacial layers are regularly used at organic/electrode interfaces in OSCs, their influence on P3HT:PCBM OSC stability is systematically investigated throughout this chapter. As discussed in

Chapter 1 and **Chapter 5**, interfacial layers are generally used in OSCs to facilitate the extraction of the photogenerated charge carriers (holes and electrons) from the active layer to the corresponding hole- and electron-collecting electrodes. Commonly used HEL and EEL materials include PEDOT:PSS [28-30] and MoO_3 [11, 31] for HELs, and LiF [8, 32], Cs_2CO_3 [33, 34], PEG [193, 257], TiO_x [31, 35, 36] and ZnO [37, 38] for EELs – the latter two materials are usually used in inverted solar cells, i.e. where the top electrode serves as the hole-extracting electrode. Since the studied devices were made in the more widely studied upright architecture, PEDOT:PSS and MoO_3 were used for the HELs, and LiF and Cs_2CO_3 were used for the EELs. A new EEL material, Liacac, was also studied, which was found to provide slight enhancements in device stability when compared to the ubiquitous LiF EEL. Furthermore, a CF_4 plasma treatment was also investigated to act as an HEL. The results demonstrate that the active layer/metal interface is inherently photo-unstable and limits the OSC photo-stability. The results also show that the use of HELs and EELs can substantially enhance photo-stability, but they may impact thermal stability. Further, MoO_3 HELs bolster the device stability compared to PEDOT:PSS. Electrical aging effects are found to be of minor concern when compared to other degradation mechanisms. The results accentuate the need for new HEL and EEL materials, and shed a new light on the reasons behind the higher stability of inverted OSCs.

8.2. Results and Discussion

8.2.1. Photo-Stability Tests on Polymer Solar Cells with PEDOT:PSS Hole Extraction Layers and Variable Electron Extraction Layers

A group of P3HT:PCBM solar cells with a PEDOT:PSS HEL and various (or no) EELs was irradiated continuously by white light (100 mW/cm^2) over a period of 168 hours in a N_2 atmosphere. In order to monitor changes in their performance as a result of the light stress, the photovoltaic characteristics of

the OSCs were measured at fixed time intervals during this period. For comparison, a second group of samples, made of the same materials and structures, was kept in the dark (in a N_2 atmosphere) for the same period of time. This group was used to test for aging effects that may occur in the devices with time regardless of the irradiation. Furthermore, in order to distinguish between photo-induced changes and any changes that may be caused by thermal stresses arising from the exposure to light, a third group of samples was studied. This group of samples was kept in N_2 in the dark, but heated to a temperature of ~40 ^{o}C, which is a few degrees above the measured temperature of the photo-irradiated samples (the first group). This allowed for thermal effects to be slightly more pronounced in the data set from the third group versus that in the first group. Therefore all solar cells were fabricated in triplicate: one group of samples for exposure to light stress (denoted 'light stress'), a second group of samples to be kept in the dark (denoted 'dark') and a third group of samples for exposure to thermal stress (denoted 'heat stress'). The average solar cell parameters for these devices (prior to aging) are detailed in Table 8-1. In general, the PCE values were around 2% for devices with EELs and 1% for the control devices that did not have any EEL. The PCE improvement by inclusion of an EEL is due to an increase in all relevant solar cell parameters, including J_{sc}, V_{oc} and FF. Such PCEs are in line with the large body of published data for devices with these materials, specific fabrication methodologies and device architectures, indicating that these devices can be treated as good representatives of the majority of OSCs made with this material system by other research labs.[23]

Table 8-1 - Summary of PEDOT:PSS HEL / variable EEL P3HT:PCBM OSC photovoltaic output parameters before aging.

Device Description	J_{sc}	V_{oc}	FF	PCE	R_{sh}	R_s
	[mA/cm^2]	[mV]	[%]	[%]	[Ohm.cm^2]	[Ohm.cm^2]
No EEL (control)	5.9	505	38	1.1	1700	31
LiF	6.5	623	46	1.9	3300	25
Liacac	7.2	626	50	2.3	3500	18
No EEL (post-anneal)	7.4	612	48	2.2	4200	19

The normalized PCE, FF, V_{oc} and J_{sc} values for these devices over the 168-hour aging scheme are shown in Figure 8-1, all normalized to the original values to facilitate cross-comparisons. Note that each point in Figure 8-1 and Table 8-1 represents the average value from four to six samples in each group. It is further noted that the data presented in this figure (and in Figure 8-2 below) comprise only a small sub-set of a larger body of data collected over a period of 18 months. The specific sub-set of data presented here was obtained from samples fabricated and tested over a shorter period of time (6 months) to minimize experimental variation.

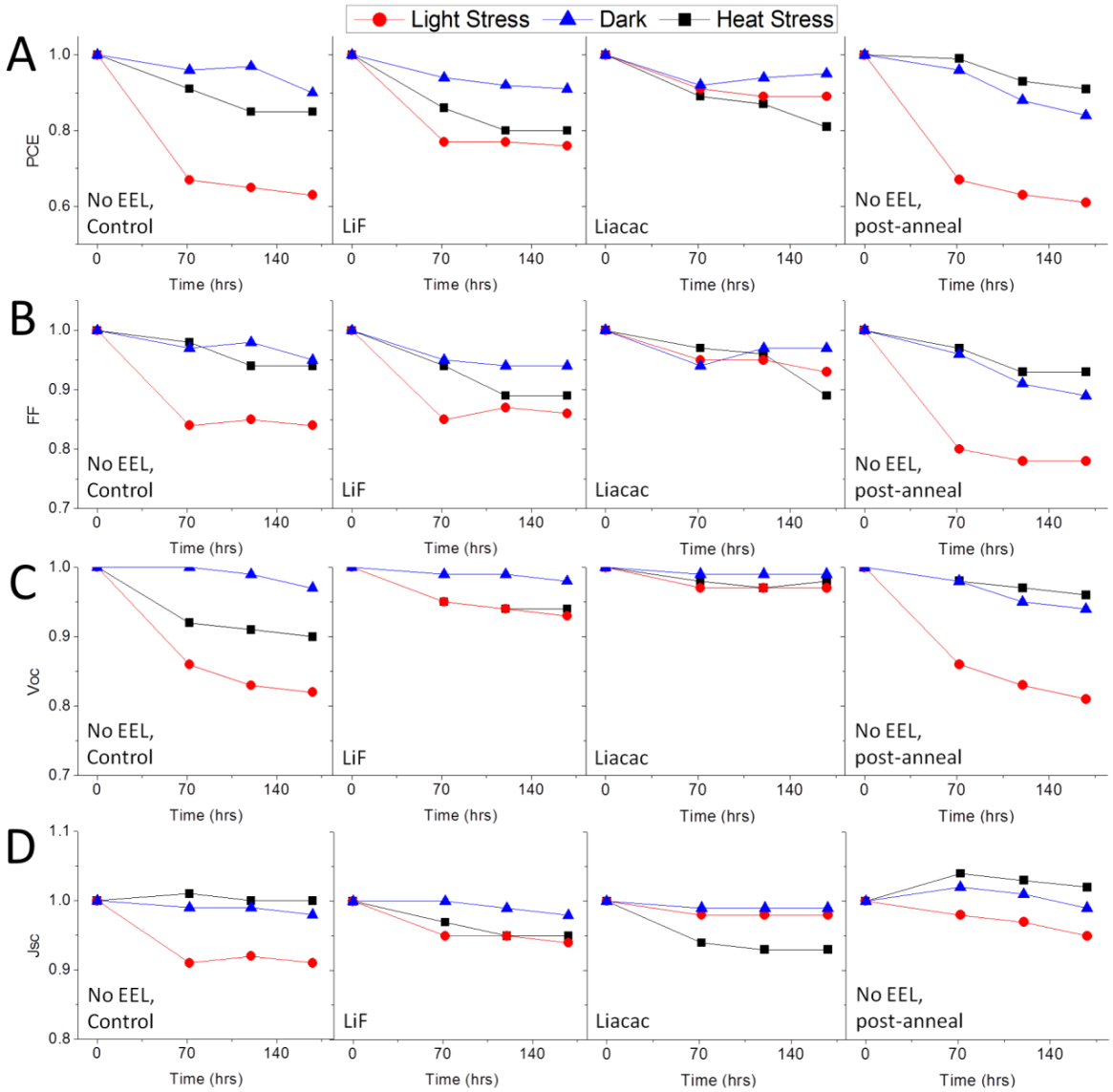

Figure 8-1 - Normalized PCE (A), FF (B), V_{oc} (C) and J_{sc} (D) values of ITO/PEDOT:PSS/P3HT:PCBM/x/Al OSCs during 168-hour aging studies. x=LiF, Liacac or nothing. All points are taken as averages from 4-6 devices.

As shown in Figure 8-1, light stress leads to significant degradation in the performance of all devices, and the effect is more severe in the control devices without the EEL, which exhibit a decrease in PCE to 60% of their initial values after exposure to light for 168 hours. For control devices, this degradation is not substantially due to thermal effects, as devices exposed to heat stress alone (i.e. without the light) displayed a decrease in their PCEs to only ~85% of their initial values over the same period of time, despite the slightly higher temperature of the heat-stressed devices relative to that caused by the illumination of the light-stressed devices. In contrast, the OSCs employing LiF and Liacac EELs show substantially improved photo-stability compared to the control devices. To this end, the LiF devices decreased to ~75% of their original PCE values within 168 hours of light stress, and the Liacac devices decreased to only ~90% of their original PCE values. These results clearly show that the photo-stability of OSCs is limited by some photo-induced changes that occur at the organic/Al interface, and that EELs can have significant benefits to photo-stability by minimizing these changes. It is furthermore noteworthy that Cs_2CO_3 was initially included in this investigation as a potential EEL. However, Cs_2CO_3-based devices generally exhibited much lower efficiencies (roughly 50% of that of LiF-based devices) and much poorer stabilities compared to other materials. As such, Cs_2CO_3 is only noted here as a rather poor EEL choice for standard configuration solar cells (at least compared to more common EEL materials). It has, however, been demonstrated as a reasonable EEL in inverted geometries.[33, 34]

While the LiF and Liacac EELs improve photo-stability, they are also found to affect the thermal stability. Considering the degradation of the LiF-based devices, shown in Figure 8-1, the heat-stressed devices exhibit a nearly identical reduction in PCE as the light-stressed devices. This convincingly shows that the reduction in PCE for these devices arises primarily from thermal degradation. Although the large portion of degradation for LiF EEL devices appears to be purely due to thermal effects, the light-stressed devices have a slightly stronger reduction in PCE compared to the heat-stressed devices (decreasing to 75% vs. 80% PCE, due to a stronger reduction in FF for the light-stressed devices).

Finding that device photo-stability is governed by the organic/Al interface, and that introducing an EEL at the interface can significantly improve OSC stability, it is interesting to see if altering the interface without using an EEL may have a similar effect. Therefore, devices were also studied where the annealing step in the device fabrication process was conducted after the Al metal deposition (referred to as "post-annealed") instead of the more common scenario where the annealing step is done prior to the top electrode deposition, as is the case with the other devices in this study (referred to as "pre-annealed"). The post-annealing process has been shown to drastically improve device performance.[30, 260, 261] These improvements, especially the shift in V_{oc} from 0.4 to 0.6 V, have been attributed to vertical segregation of the active layer, resulting in a more coherent interface with fewer shunt paths.[262] As detailed above and has been shown in literature,[32] a similar improvement in solar cell parameters can also be realized using pre-annealed devices in combination with an EEL, such as LiF. It is thus reasonable to conclude that the post-annealing step causes a change at the organic/Al interface, forming a quasi-EEL that helps improve electron extraction. It is interesting to see if such devices may have different photo-stability behaviour in comparison to the control (i.e. pre-annealed) devices.

The normalized PCE, FF, V_{oc} and J_{sc} values for the post-annealed devices over the 168-hour aging scheme are also shown in Figure 8-1. The average solar cell parameters for these devices (prior to aging) are likewise detailed in Table 8-1. As expected, annealing after Al deposition results in an improvement to all major solar cell parameters, allowing for a two-fold improvement in PCE. The enhancement of FF was manifested as both an increase in R_{sh} and a decrease in R_s.

Quite interestingly, despite the performance improvement, the post-annealed devices have generally poor photo-stability, similar to that of the control devices, showing a decrease to 60% of the initial PCE within 168 hours of light stress. As shown in Figure 8-1, this degradation is due to a deterioration in all relevant solar cell parameters (FF, V_{oc} and J_{sc}), with the FF and V_{oc} most strongly

affected. The post-annealed sample experiences a slightly smaller reduction in J_{sc} compared to the control sample, but this is compensated by a larger drop in FF. The post-annealed devices do, however, exhibit slightly enhanced thermal stability compared to the control devices. This variation is shown to be exclusively due to added stability in the V_{oc}, where the V_{oc} of the heat-stressed post-annealed sample remained relatively constant. In contrast, the V_{oc} of the heat-stressed control sample decreased to ~90% of its original value within the first 72 hours. It is thus likely that this instability is due to heat-induced degradation at the organic/Al interface.

It is clear that in spite of the added thermal stability with post-annealing treatments, the active layer/Al interface is still very susceptible to photo-degradation. This suggests that simply altering the physical characteristics of the organic/Al interface (e.g. by annealing after the metal has been deposited) has little effect on the contact photo-stability, and that only changing the chemical nature of the interface, such as by introducing an inorganic EEL, improves OSC photo-stability. It should also be noted that although, for these samples, Al was used as the top electrode material due to its wide use in OSCs, interfacial photo-degradation is not specific to P3HT:PCBM/Al contacts, but rather occurs at the interfaces of various metals and organic materials,[13] suggesting that the phenomenon may be of a universal nature. To this end, it is suggested that the only requirements for photo-degradation are an organic/metal interface and the presence of photo-induced excitons.

8.2.2. Photo-Stability Tests on OSCs with MoO_3 Hole Extraction Layers and Variable Electron Extraction Layers

Finding that the organic/Al contact strongly influences OSC photo-stability it is natural to question if similar effects take place at the ITO contact. This section therefore examines the effect of

changing the HEL. MoO_3 is an attractive candidate in this regard, as it has recently been identified as a replacement to the traditional PEDOT:PSS HEL (per discussions in **Chapter 5**). In line with the present analysis, MoO_3 HELs have been shown to offer superior stability to PEDOT:PSS HELs by preventing inter-electrode degradation phenomena otherwise caused by moisture retained in PEDOT:PSS.[11] Given that many EELs are essentially salts that may be strongly affected by the presence of moisture in the OSC, it is highly relevant to extend the present analysis to P3HT:PCBM OSCs made with a MoO_3 HEL. The initial photovoltaic output parameters (prior to aging) for P3HT:PCBM OSCs with a MoO_3 HEL and a variable EEL are shown in Table 8-2 below. Comparing the MoO_3 HEL versus PEDOT:PSS HEL OSCs, the MoO_3 devices tend to have slightly lower J_{sc} values that are compensated by corresponding increases with FF. Otherwise, the V_{oc} values and the PCEs of MoO_3 HEL OSCs are generally in the same range as PEDOT:PSS HEL OSCs. As noted in **Chapter 5**, the MoO_3 thickness can be varied from 0.5 nm to 15 nm with little variation in OSC output parameters – for all of the devices detailed in this work, a thickness of 5 nm MoO_3 was used.

Table 8-2 - Summary of MoO_3 HEL / variable EEL P3HT:PCBM OSC photovoltaic output parameters before aging.

Device Description	J_{sc}	V_{oc}	FF	PCE	R_{sh}	R_s
	[mA/cm^2]	[mV]	[%]	[%]	[Ohm.cm^2]	[Ohm.cm^2]
No EEL (control)	5.3	453	46	1.1	2600	21
LiF	5.3	622	56	1.8	3300	16
Liacac	5.7	621	56	2.0	3300	13
No EEL (post-anneal)	6.4	623	52	2.1	4500	18

The normalized PCE, FF, V_{oc} and J_{sc} values for the MoO_3 HEL OSCs over the 168-hour aging period are shown in Figure 8-2. As with the previous data, each point in Figure 8-2 and Table 8-2 represents the average value from four to six samples. The most noticeable difference between the stability of devices with PEDOT:PSS HELs versus those with MoO_3 HELs is the near complete lack of degradation of the latter when kept in the dark. For the duration of this study, MoO_3 HEL OSCs that were kept in the dark

retained 96% to 100% of their original PCE (with the exception of the control devices without an EEL). The other major contrast when using MoO_3 is the behaviour of J_{sc} for the heat-stressed devices. For PEDOT:PSS HEL OSCs, J_{sc} increased during the heat stress when no EEL was used, but decreased for LiF- and Liacac-EEL OSCs. For MoO_3 HEL OSCs, heat stress resulted in an increase to J_{sc} of 2%-10% for both the 'No EEL' devices as well as those devices employing LiF and Liacac EELs.

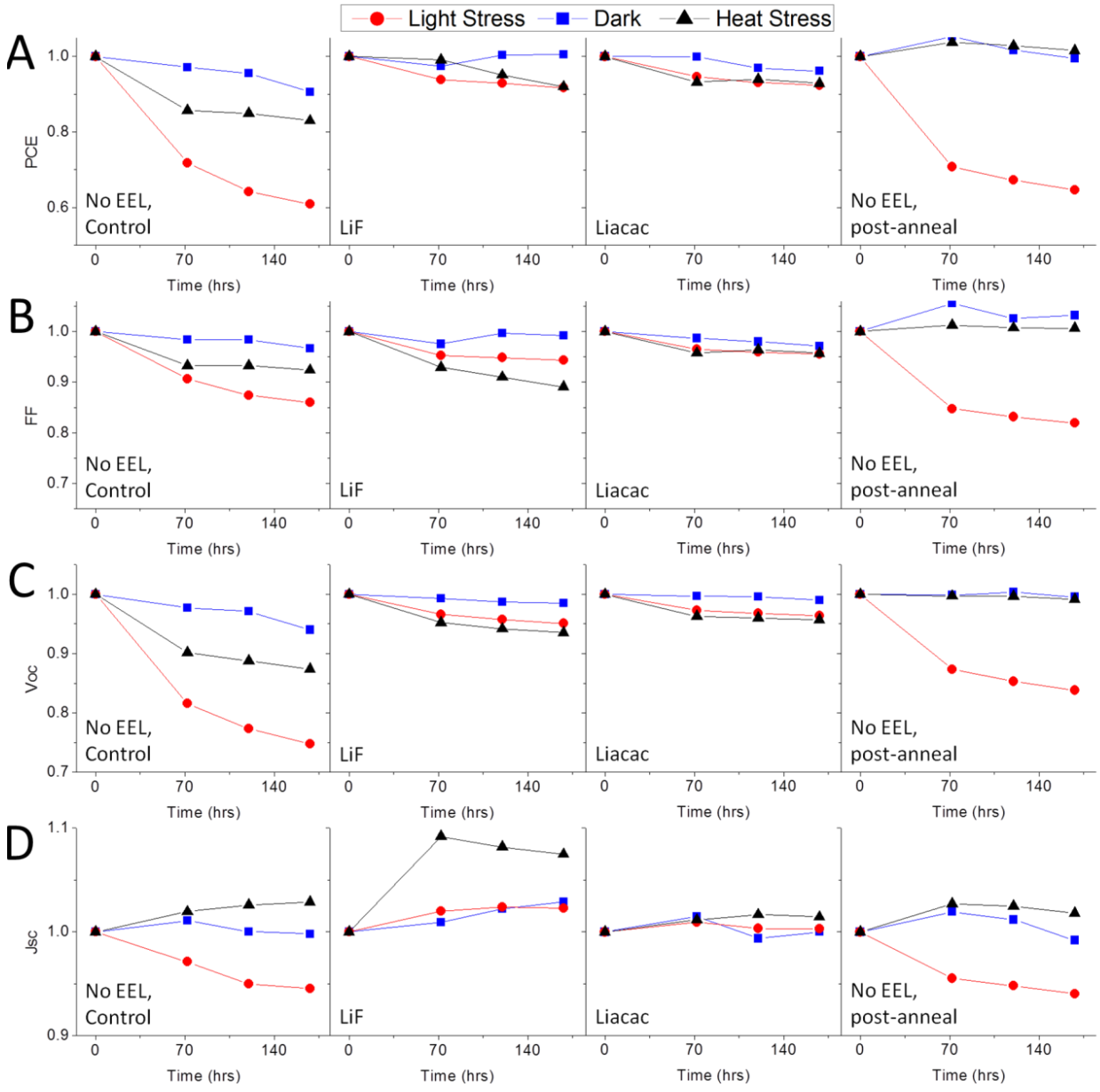

Figure 8-2 - Normalized PCE (A), FF (B), V_{oc} (C) and J_{sc} (D) values of ITO/MoO_3 /P3HT:PCBM/x/Al OSCs during 168-hour aging studies. x=LiF, Liacac or nothing. Note: All points are taken as averages from 4-6 devices.

The differences between MoO_3 vs. PEDOT:PSS HEL devices can perhaps be explained by the presence of residual moisture in the PEDOT:PSS film. For degradation in the dark, residual moisture would ultimately degrade all solar cell parameters over time, analogous to OSCs that have been exposed to ambient moisture.[263] Further, heating may result in the gradual release of residual moisture from the PEDOT:PSS HEL, which could significantly affect the ultra-thin LiF or Liacac EELs, considering their chemical nature as salts, and may cause them to release some species into the active layer of the OSC.[189] This could lead to the creation of recombination centres that would reduce J_{sc}, as observed for the PEDOT:PSS HEL devices. The contrasting increase in J_{sc} for the MoO_3 HEL devices may be attributed to further improvement in the P3HT:PCBM layer morphology with heat, or due to a thermally induced change in the MoO_3 film.

The degradation behaviour of the MoO_3 HEL OSCs was otherwise very similar to the PEDOT:PSS HEL OSCs. As shown in Figure 8-2, both the control and post-annealed 'No EEL' devices showed substantial photo-degradation. The control device similarly showed heat stress degradation to V_{oc} not observed in the post-annealed device. Introduction of an LiF or Liacac EEL substantially reduced direct photo-degradation, but the devices still suffered from thermal effects. This is shown for both the LiF and Liacac EEL devices, which have very similar final PCE values for the light-stressed and heat-stressed samples. As a point of note, the light-stressed and heat-stressed PCEs for both LiF and Liacac EEL devices were somewhat higher when making use of the MoO_3 HEL. Specifically, when employing an LiF or Liacac EEL, the MoO_3 HEL devices never dropped below 90% of the original PCE, whereas the PEDOT:PSS HEL OSCs ranged between 75% and 90%. The results therefore show that using MoO3 instead of PEDOT:PSS as an HEL material can lead to some stability improvements, and that the benefits appear to be mostly due to lower moisture retention and/or improved thermal stability. Ultimately, however, both MoO_3 and PEDOT:PSS offer a similar level of photo-stability. These results can perhaps

provide new insights on the reasons behind the general higher stability of inverted OSCs.[113] In this regard, inverted OSCs always employ interfacial layers to more efficiently extract holes/electrons. The absence of the organic active layer/metal interface, which appears to be strongly susceptible to photo-degradation and detrimental to the photo-stability, can therefore enhance the inverted OSC stability. Furthermore, since MoO_3 is typically used instead of PEDOT:PSS as an HEL material in inverted OSCs, additional stability benefits can be expected in consideration of the present observations.

8.2.3. The Role of Surface Treatments on ITO/Organic Interface Photostability

To further probe the photo-stability of the ITO-organic interface, additional light stress experiments were made on P3HT:PCBM OSCs, comparing CF_4:O_2plasma treatments (PT-ITO) to MoO_3 HELs and samples without HELs. An LiF EEL was applied in order to minimize any immediate photo-degradation at the organic-Al interface. In this manner, it is possible to better isolate ITO-contact-specific variations that occur as a consequence of photo-irradiation. Only recently have CF_4 treatments been reported as a replacement to PEDOT:PSS for P3HT:PCBM solar cells;[264] however, the stability of CF_4-treated ITO has yet to be reported when used in OSCs.

As with the devices in the previous sections, the OSCs were aged by constant exposure to 100 mW/cm^2 white light, during which they were kept in an N_2 environment and cooled by a fan to prevent excessive heating. For this set of experiments, the OSCs were exposed to light over an 8-day period. Figure 8-3 below shows the before- and after-aging dark IV characteristics of the ITO-, PT-ITO- and ITO/MoO_3-based OSCs. All OSCs show relatively normal diode behavior before aging, and the PT-ITO and ITO/MoO_3 OSCs show very little change in their IV characteristics after aging. The untreated ITO OSCs, however, exhibit a strong variation in their IV characteristics, losing their diode shape and

behaving more like a simple resistor. These data suggest substantial degradation of the untreated ITO-organic interface, with less degradation of the PT-ITO- and ITO/MoO_3-organic interfaces.

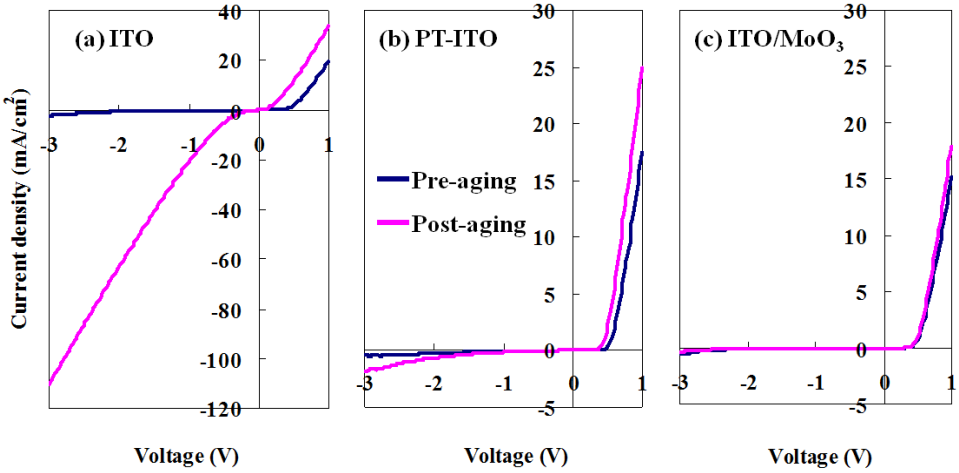

Figure 8-3 - Changes in the dark JV characteristics from OSCs utilizing (a) ITO, (b) PT-ITO and (c) ITO/MoO_3 as contacts after exposure to 100 mW/cm^2 light from a halogen lamp.

Elucidation of the OSC photovoltaic parameters supports the above conclusions. The untreated ITO contact yields OSCs with very poor photovoltaic properties, presenting an initial PCE of 0.01%. Within an hour of irradiation, the untreated ITO OSC exhibits no measurable photo-response (PCE~0%). Figure 8-4 shows the changes in J_{sc}, V_{oc} and PCE extracted from the remaining PT-ITO and ITO/MoO_3 OSCs (FF is not shown as it was relatively constant for both devices for the duration of the experiment). A strong variation in the properties of the PT-ITO versus the ITO/MoO_3 devices is observed. In general, PT-ITO OSCs exhibit slight deterioration in PCE, largely owing to a decrease of V_{oc}. ITO/MoO_3 devices, however, remain unaffected in this regard, even showing a slight improvement to PCE due to a slight increase in J_{sc}. It is thus clear that, like the organic/metal contact, the ITO/organic contact requires some form of interfacial layer in order to reduce photo-degradation effects. Further, the ITO/MoO_3 contact appears to be more suitable for stable OSCs than the PT-ITO contact.

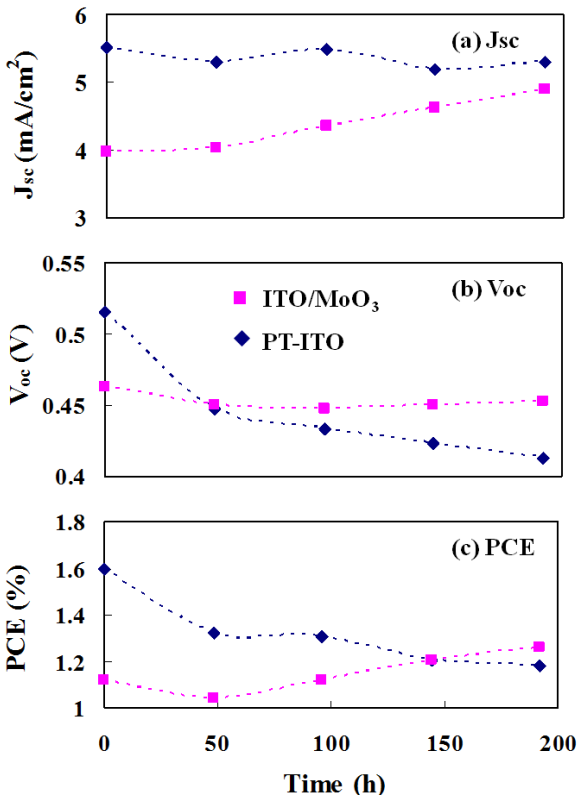

Figure 8-4 - Changes in (a) J_{sc}, (b) V_{oc} and (c) PCE, respectively, from OSCs utilizing PT-ITO and ITO/MoO_3 as contacts as a function of time exposed to 100 mW/cm^2 white light.

8.2.4. X-Ray Photoelectron Spectroscopy Analysis of the Organic-Aluminum Interface

To gain some insight about the nature of the photo-induced changes at the active layer/metal interface, and whether the underlying processes are photochemical in nature, XPS was used to probe changes in the chemical characteristics of the P3HT:PCBM/Al interface. The Al 2p binding energy spectra of P3HT:PCBM(70 nm)/Al(5 nm) samples are shown in Figure 8-5 below.

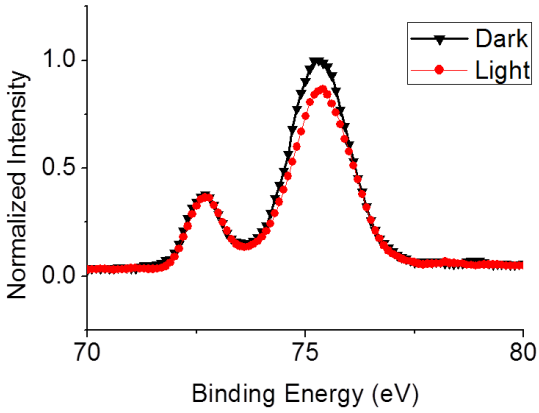

Figure 8-5 - Al 2p binding energy spectra (by XPS) of P3HT:PCBM(70 nm)/Al (5 nm) samples kept in dark and the same irradiated at 100 mW/cm^2 for 24 hours.

In Figure 8-5, the 'light' sample was irradiated with 100 mW/cm^2 white light from a halogen lamp for 24 hours. Since both the light-stressed samples and the samples kept in the dark were fabricated on the same substrate (later cleaved for light aging and testing), the elemental aluminum peak at 72.7 eV has been normalized to the same intensity for both curves. A second peak is also observed at 75.3+/-0.1 eV, which is shown to decrease significantly in intensity after irradiation. Note that aluminum oxide bonds form in this binding energy region, and some aluminum oxide is necessarily present due to the loading of the sample into the XPS chamber; however, a control/pure Al films on glass (without the P3HT:PCBM layer) showed negligible change in this region. It is thus suggested that the origin of this peak is due to Al-S by the thiophene component in P3HT,[265, 266] and/or Al-O-C by the carbonyl groups in PCBM (analogous to the peak observed in Alq_3[267]). Given the tendency of P3HT to accumulate at this interface,[268] the Al-S bond may be more likely. The reduction of peak intensity post-irradiation suggests a decrease in bond density, indicating that the photo induced changes may indeed be chemical in nature. This implies that the active organic layer/aluminum interface is inherently susceptible to photo-degradation. These results also agree with previous work,[12, 13] and add merit to the notion that the photo-degradation of organic-electrode interfaces is universally applicable, and occurs due to a change that is chemical in nature and detectable by XPS.

8.2.5. Electrical Aging Effects in Solar Cell Degradation

Although the above results clearly indicate that the major mode of degradation for the contact interfaces is photo-induced, it is possible that the degradation is caused by the flow of electrical current (photo-generated carriers) through the OSCs – i.e. primarily due to electrical stress. Degradation due to charge accumulation and the associated electrical aging of organic layers has been identified as a significant mode of efficiency loss for OLEDs.[269] It is thus worth studying electrical stress effects in OSCs to ascertain their relative impact on device efficiency. To this end, electron-only and hole-only devices with the following structures were fabricated and studied:

- electron-only: ITO/Cs_2CO_3/P3HT:PCBM/(LiF, Liacac or No EEL)/Al
- hole-only: ITO/(PEDOT:PSS or MoO_3)/P3HT:PCBM/MoO_3/Ag

As both contacts in the first device are capable of injecting electrons efficiently into the P3HT:PCBM layer, but are much less efficient in injecting holes, the flow of current across the layers of the device under an external bias, regardless of the polarity, will occur predominantly through the transport of electrons, making it an "electron-only" device. Similarly, the hole-only device makes use of hole-injecting contacts allowing for only hole current with an applied bias.

The current density-voltage (J-V) characteristics of these devices are shown in Figure 8-6. On these figures, a positive bias voltage corresponds to a bias where the ITO is at a more positive potential with respect to the Al. Considering the electron-only devices, the use of LiF or Liacac results in the highest level of injected current from the Al into the P3HT:PCBM layer, as shown in the positive bias region of Figure 8-6.A. The LiF and Liacac EELs also exhibit very similar capacities to extract electrons from the P3HT:PCBM, as is evident from their similar current densities at any given voltage in the negative bias region of the J-V curve. Further, both LiF and Liacac were more efficient in extracting electrons versus the No EEL control. Note: in the negative bias region, electrons are injected into

P3HT:PCBM from the ITO/Cs_2CO_3 contact, and hence any differences in the current density at any voltage among the devices in this region reflects differences in the current extraction capacities at the Al top electrode.

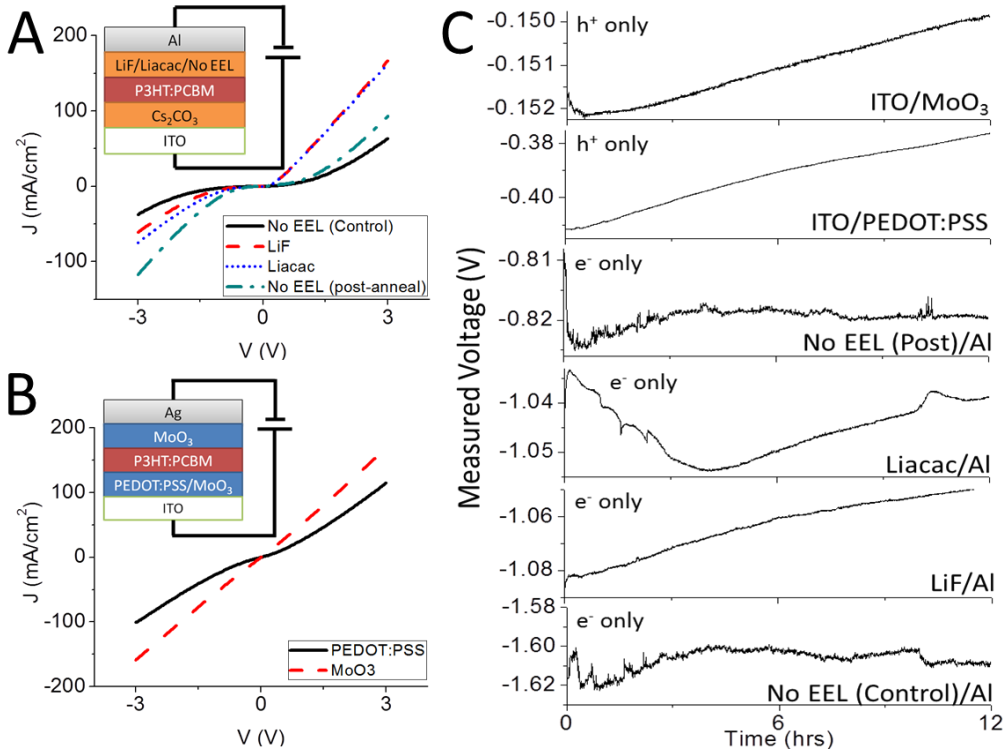

Figure 8-6 - JV curves of A) electron- and B) hole-only devices respectively. Insets: device structures and biasing scheme (Note: negative bias = regular current flow during photovoltaic operation across interfaces of interest). C) Measured device voltages with -7.5 mA/cm^2 driving current over 12 hours for various interfaces of interest.

These observations are in full agreement with the data in Table 8-1 and Table 8-2, where the increase in PCE upon using the EELs is associated with higher Voc and lower Rs, both indicative of improved charge extraction and smaller V_{oc} losses at the contact. The most efficient contact for extracting electron current, however, is the 'No EEL' + post-annealed sample, which is consistent with its high J_{sc} noted in Table 8-1. For the hole-only devices, the ITO/MoO_3 contact is shown to have no observable Schottky barrier, providing slightly higher injected and extracted current compared to the PEDOT:PSS film. In general, the barriers to injection/extraction and the associated contact resistances were found to be much lower for the hole-only devices than for the electron-only devices.

In order to investigate possible degradation effects due to the prolonged flow of current, the electron-only and hole-only devices were subjected to a negative bias sufficient to maintain a continuous flow of current of -7.5 mA/cm^2 for 12 hours in the dark, which is slightly higher than the highest J_{sc} observed with the OSCs subjected to the light stress tests in the first section of this chapter. A negative bias was used in order to make the flow direction of electrons and holes in these test devices the same as that of the photo-generated carriers in OSCs under normal conditions (i.e. electrons flowing from the P3HT:PCBM layer to the Al contact in the case of the electron-only device, and holes flowing from the P3HT:PCBM layer to the ITO contact in the case of the hole-only device). The required voltages to maintain the -7.5 mA/cm^2 current density for the duration of these measurements are shown in Figure 8-6.C. In general, the measured voltages remained relatively stable, varying only by 2 mV to 20 mV. Furthermore, subsequent current-voltage measurements after electrical stress showed insignificant variations from the original measurements – these data are not shown in Figure 8-6.A-B, as the curves essentially overlap. These results indicate that electrical stress effects are relatively limited in OSCs, at least in the timeframe of the present experiment, and cannot account for the fast degradation in OSC performance observed with illumination.

The conclusion that the electrical stresses are insignificant is further supported by observations made during light-stress tests, where the OSCs were placed under both open circuit and short circuit conditions. In the open circuit scenario, photogenerated charge carriers can be expected to exist in the active layer of the OSC, but since the electrodes are electrically isolated and hence cannot dissipate charges from the active layer, the photogenerated charges remain largely immobile. In contrast, in the short circuit scenario, the photogenerated charges are able to flow through the organic layers and across the various interfaces to the electrodes/external circuit. As such, should electrical stresses be significant, one would expect some differences in the rate of PCE decrease between these electrically different scenarios. The results, however, showed that devices aged in both conditions gave very similar

trends. Therefore, it is shown that the photo-induced changes in the previously examined OSCs are not due to the photo-induced flow of current or as a consequence of electrical stresses. Given these results, it is suggested that electrical stresses pale in comparison to other degradation mechanisms, such as light-, heat- and ambient H_2O/O_2-induced losses.

8.3. Conclusions

In this chapter, the stability behavior of P3HT:PCBM OSCs was studied in inert atmosphere considering various stresses, including light, heat and electrical stresses. This chapter also provided a base of knowledge for understanding photo-degradation mechanisms and variations in charge collection with time, topics that are further examined in **Chapter 9** and **Chapter 10**. The major conclusions discussed in this chapter are described below:

- The main source of the deterioration in the charge collection properties of OSCs with time is found to be photo-induced changes at the organic/electrode interface, with thermal and electrical stresses generally shown to be less significant. XPS measurements suggest that these changes are photochemical in nature. The use of EELs and HELs in between the organic layer and the electrodes can largely suppress contact photo-degradation and enhance OSC photo-stability.
- Liacac is proposed here as a new EEL material that is shown to provide efficiency improvements on par with the ubiquitous LiF, but with some additional stability improvements.
- MoO_3 can be used instead of PEDOT:PSS as an HEL to improve stability, likely due to its lower moisture retention and/or improved thermal stability. Both HELs, however, provide substantial stability and efficiency improvements over untreated samples.
- The results of this chapter thus uncover a major degradation mechanism that limits OSC stability under illumination and accentuates the need for research on new HEL and EEL materials.

Chapter Nine:

The Effect of Charge Extraction Layers on the Photo-Stability of Vacuum-Deposited versus Solution-Coated Organic Solar Cells[1]

In this chapter, P3HT:PCBM P-OSCs are studied in parallel with ClInPc:C_{60} SM-OSCs for their photo-stability behaviour. To further examine organic/electrode interactions, a wide set of traditional HELs and EELs are examined for their role in OSC performance and stability. The inter-compatibilities and incompatibilities of these extraction layers in SM-OSCs versus P-OSCs are explored. Certain extraction layer combinations are highlighted for resulting in strong inter-electrode degradation. The results suggest that the presence of excitons at the organic-electrode interface plays a critical role in contact photo-degradation in both vacuum-deposited and solution-coated materials systems. By minimizing contact photo-degradation, which dominates the majority of short-term OSC degradation, a new avenue for studying OSC stability behavior and opportunities to focus on other losses in OSCs become possible.

9.1. Introduction

As noted in previous chapters, the umbrella term 'OSC' may be broken up into SM-OSCs and P-OSCs. While P-OSCs are always solution-coated, SM-OSCs can be either vacuum-deposited or solution-

[1] The majority of the material in this chapter was published in:
G. Williams,H. Aziz, *Org. Electron.,* **2013,** *15*, 47.
, reproduced here with permission.

coated. Despite the different fabrication methodologies, high efficiency OSCs can be achieved for all of these cases,[233, 234, 270] usually in combination with suitable extraction layers. It is thus intriguing that the various approaches in device fabrication (solution-coated versus vacuum-deposited) generally employ different extraction layers, while making use of the same electrode materials – this point was addressed briefly in **Chapter 1** and **Chapter 5**. P-OSCs and solution-coated SM-OSCs usually employ a PEDOT:PSS HEL and a thin (~1 nm) LiF EEL.[186] In contrast, vacuum-deposited SM-OSCs often use a plasma treatment-based HEL,[72, 271] and a BCP EEL.[39, 40] The relative stabilities and efficacies of these and several other extraction layers (such as CF_4 plasma treatment,[72, 264, 272] and MoO_3[31, 273]) when directly comparing the different fabrication methodologies are, as of yet, unstudied.

In this chapter, a systematic study is conducted on the effect of commonly employed extraction layers on OSC photo-stability, as well as on the inter-compatibilities of these extraction layers in both solution-coated P-OSCs and vacuum-deposited SM-OSCs. By illuminating SM-OSCs and P-OSCs in a controlled N_2 environment, the impact of the interfacial layers on device lifetime and photovoltaic parameters is elucidated. The results further demonstrate that, although both SM-OSCs and P-OSCs suffer from contact photo-degradation, the use of extraction layers generally improves their photo-stability. This is in agreement with the results presented in **Chapter 8**, and confirms that the photo-degradation phenomenon occurs regardless of fabrication methodology (vacuum-deposited vs. solution-coated). Optimal HEL/EEL combinations are identified for both vacuum-deposited SM-OSC and P-OSC materials systems. Incompatible HEL/EEL combinations, as observed by inter-electrode degradation, are also highlighted. The presence of excitons at the organic-electrode interface is suggested to be fundamentally important in contact photo-degradation. By minimizing contact photo-degradation, which dominates the majority of short-term OSC degradation, opportunities to focus on other losses in OSCs become possible.

9.2. Results and Discussion

9.2.1. Photo-Stability of Organic-Electrode Interfaces with Various Interfacial Layers

Illustrations of the relevant devices structures for the P-OSCs and SM-OSCs examined in this chapter are provided in Figure 9-1.A and B respectively. The comprising materials are chosen for their high degree of OSC performance reproducibility, and also because their initial PCE values are roughly equivalent (~2 to 2.2% PCE for optimized HEL/EEL), allowing for simpler comparisons across the two different fabrication methodologies. While the acceptor materials are fundamentally similar (C_{60} versus PCBM), the donor materials for the two systems are different in their structure and their energy levels, the latter illustrated in Figure 9-1.C.[71, 167-169, 264, 274, 275] As such, the present work considers two very different OSC systems – in fabrication methodology, constituent materials and device structure – to elucidate possible commonalities regarding their stability. As will be proven in this chapter, in spite of these differences, both of the examined SM-OSCs and P-OSCs show strong similarities in their device stability that are largely associated with photo-induced organic-electrode interfacial degradation.

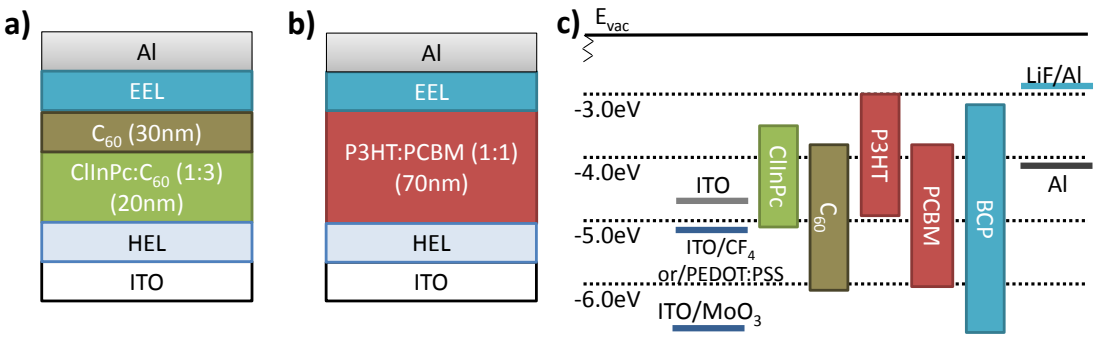

Figure 9-1 - Illustration of the OSC device structures used in this chapter for a) vacuum-deposited SM-OSCs and b) solution-coated P-OSCs. c) Energy level diagram for the constituent materials in a) and b).

P-OSC and SM-OSC samples were continuously illuminated over a period of 84 hours in a dry N_2 environment, and the photovoltaic output parameters were measured at fixed time intervals. To gauge

any degradation simply due to the storage of the devices, identical samples were kept in the dark in a dry N_2 environment and measured at the same time intervals. The initial photovoltaic parameters for representative SM-OSC and P-OSC samples (prior to illumination) are detailed in Table 9-1 and Table 9-2.

Table 9-1 - Initial (t=0) PCE values for ITO/HEL/ClInPc:C_{60}/C_{60}/EEL/Al SM-OSCs with various HELs and EELs. J_{sc}, V_{oc} and FF are shown in smaller text.

HEL	EEL							
	None			BCP			BCP + LiF		
None	**0.01%**	0.19 mA/cm^2 59 mV 25%		**0.27%**	3.18 mA/cm^2 213 mV 34%		**0.14%**	2.70 mA/cm^2 151 mV 29%
PEDOT:PSS	**0.30%**	2.54 mA/cm^2 511 mV 23%		**1.24%**	4.51 mA/cm^2 652 mV 42%		**1.25%**	4.58 mA/cm^2 660 mV 41%
CF_4	**0.27%**	2.52 mA/cm^2 420 mV 25%		**2.17%**	4.57 mA/cm^2 919 mV 52%		**2.12%**	4.44 mA/cm^2 921 mV 52%
MoO_3	**0.42%**	2.98 mA/cm^2 516 mV 28%		**2.15%**	4.63 mA/cm^2 982 mV 47%		**2.17%**	4.67 mA/cm^2 985 mV 47%

Table 9-2 - Initial (t=0) PCE values for ITO/HEL/P3HT:PCBM/EEL/Al p-OSCs with various HELs and EELs. J_{sc}, V_{oc} and FF are shown in smaller text.

HEL	EEL							
	None			LiF			BCP			BCP + LiF		
None	**0.02%**	0.58 mA/cm^2 135 mV 22%		**0.04%**	1.26 mA/cm^2 201 mV 18%		**0.04%**	1.43 mA/cm^2 188 mV 17%		**0.03%**	1.05 mA/cm^2 160 mV 18%
PEDOT:PSS	**1.72%**	6.18 mA/cm^2 553 mV 50%		**2.07%**	6.22 mA/cm^2 615 mV 54%		**1.99%**	6.29 mA/cm^2 610 mV 52%		**1.85%**	6.12 mA/cm^2 617 mV 49%
CF_4	**0.44%**	5.27 mA/cm^2 277 mV 29%		**1.83%**	6.60 mA/cm^2 584 mV 47%		**2.08%**	6.89 mA/cm^2 609 mV 50%		**1.94%**	6.75 mA/cm^2 608 mV 47%
MoO_3	**0.94%**	5.37 mA/cm^2 382 mV 46%		**1.87%**	5.72 mA/cm^2 593 mV 55%		**2.11%**	5.80 mA/cm^2 630 mV 58%		**2.06%**	5.86 mA/cm^2 632 mV 56%

It is immediately obvious that, in nearly all cases, using either no HEL or no EEL results in very poor device performance, as is well established in the field.[119] The following general observations can be made regarding the initial performance of OSCs made by the two different fabrication methodologies (vacuum-deposited and solution-coated OSCs):

- *HEL:*
    - CF_4 plasma treatment gives performance on par with MoO_3, and both HELs work for SM-OSCs and P-OSCs
    - PEDOT:PSS works well for P-OSCs, and it may work for SM-OSCs; however, it is incompatible with ClInPc:C_{60} SM-OSCs that rely on the fullerene-based Schottky junction architecture (discussed further in Section 9.2.5)
    - P-OSCs that use a PEDOT:PSS HEL and no EEL can show reasonable performance
- *EEL:*
    - LiF works well for P-OSCs, but does not work well for SM-OSCs because it does not suitably protect the organic layers from damage during metal deposition, especially given the relatively high roughness of films including C_{60}
    - BCP works well for both SM-OSCs and P-OSCs; however, it suffers from incompatibilities with PEDOT:PSS (discussed further in Section 9.2.3)

9.2.2. Vacuum-Deposited Small Molecule Organic Solar Cells

Since the majority of stability studies have focused primarily on P-OSCs,[4, 7, 15] it is of immediate interest to observe the photo-stability of vacuum-deposited SM-OSCs. The normalized PCE values of the ClInPc:C_{60} SM-OSCs with varying HELs/EELs during the 84-hour light illumination scheme are plotted in Figure 9-2. In order to better isolate the effects of illumination on the samples, the data presented in

Figure 9-2 have been normalized relative to the PCE values of identical devices kept in the dark at the given time. This normalization helps to remove any degradation effects or other variations in efficiency simply due to storage of the devices, and therefore it allows one to better observe degradation purely due to light exposure. The original non-normalized data, including data for both the illuminated samples and the samples kept in dark, are provided in the supplemental information (**Appendix 1.5**). It is worth noting that the devices that had suitable interfacial layers and that were kept in the dark generally degraded very little, immediately suggesting that the shelf life of these devices is much longer than the lifetime of illuminated devices. As it will become evident from the vast amount of raw data (as provided in the supplemental information), this normalization methodology assists in cleanly analyzing and identifying trends, while avoiding the obvious consequences of 'big data.'

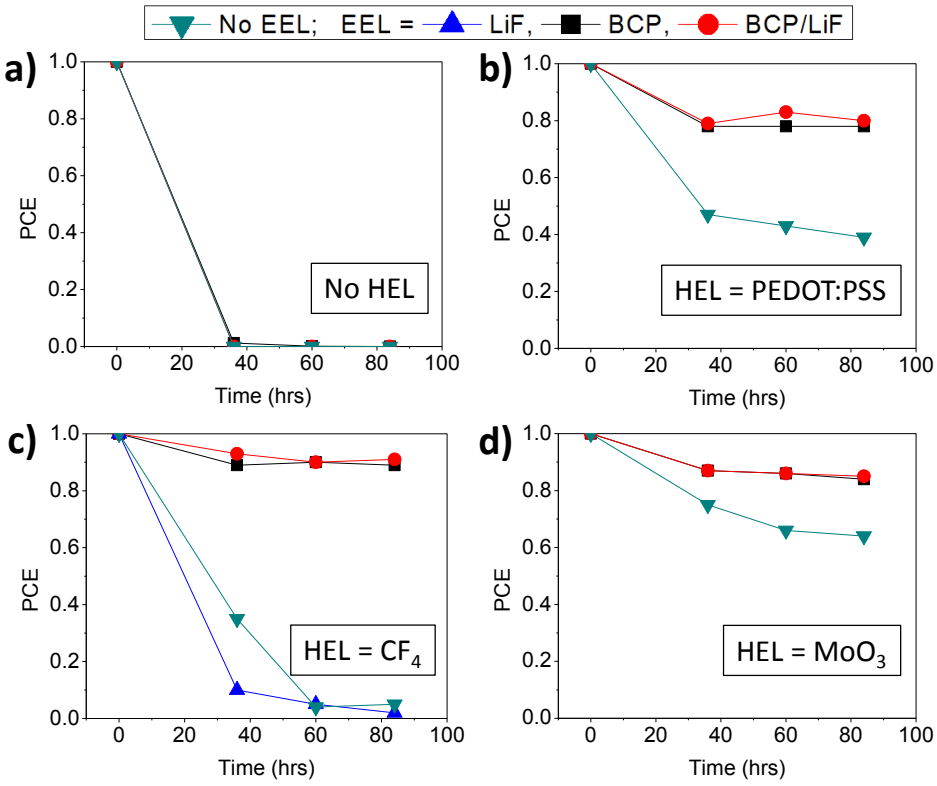

Figure 9-2 - Normalized PCE values for ClInPc:C_{60} SM-OSCs with varying HELs (a->d) and EELs over 84 hours of illumination. HELs include: a) No HEL, b) PEDOT:PSS, c) CF4 plasma treatment, d) MoO3.

From Figure 9-2, it is clear that, without some form of HEL or EEL, the ClInPc:C_{60} SM-OSCs are very photo-unstable. Within 36 hours, the PCE values for all devices without an HEL (Figure 9-2.a) decrease to ~0% due to a strong deterioration in J_{sc}, V_{oc} and FF. Similarly, those devices with no EEL suffer very strong photo-deterioration, although not as severe as the devices with no HEL. To this end, the 'No EEL' devices with PEDOT:PSS and MoO_3 HELs decrease to ~40% and ~65% of their original PCE within 84 hours of continuous light exposure. In contrast, the use of either no HEL or a CF_4 HEL with no EEL results in complete degradation of photovoltaic characteristics in the 84 hours of illumination. It is also worth noting that the initial efficiencies of devices without HELs and EELs are quite poor, as shown in Table 9-1, which makes them very sensitive to further decreases in J_{sc}, V_{oc} and FF. The results strongly demonstrate the photo-instability of these devices.

It is useful to now examine those devices with both an HEL and an EEL, shown in Figure 9-2.b-d. As per discussions in **Chapter 5**, it is worth emphasizing that SM-OSCs generally employ an organic EEL – typically BCP – in contrast to the most commonly used inorganic EEL for P-OSCs: LiF. As noted in **Chapter 8**, it is observed that light harvesting devices with organic-metal interfaces are photo-unstable;[13, 15] however, in those experiments, the organic material also served as a photo-active component in the device operation and thus contained excitons during illumination. The use of an organic extraction layer (i.e. BCP) that has no role in the generation of photocurrent can help show whether this interfacial degradation is merely due to the weak chemical nature of organic-metal interfaces in general, or due to exciton interactions at the organic-cathode interface. To better understand the effect of the EEL in the stability of SM-OSCs three EEL variants are included in this study: BCP (8 nm), LiF (1 nm) and BCP(8 nm)/LiF(1 nm). Comparisons of BCP with BCP/LiF immediately show whether an organic/inorganic/cathode interface offers stability enhancements over the simple organic/cathode interface.

Upon examination of Figure 9-2.b-d, it is clear that the presence of a BCP or BCP/LiF EEL significantly improves the photo-stability of ClInPc:C_{60} OSCs with all three of the examined HELs (PEDOT:PSS, CF_4 plasma treatment and MoO_3). PEDOT:PSS/…/BCP and PEDOT:PSS/…/BCP/LiF configurations lose 20% of their original PCE after 84 hours of illumination, with a ~5% loss to FF and more severe ~10% losses to both J_{sc} and V_{oc}. The use of a MoO_3 HEL instead grants slightly better photo-stability, with only 15% reduced PCE after 84 hours, due to only minor (few percent) losses to V_{oc}, but the same 5% loss to FF and a 10% loss to J_{sc}. The most stable ClInPc:C_{60} device, however, employs a CF_4 HEL and a BCP or BCP/LiF EEL, allowing for only a 10% reduction in PCE after 84 hours of illumination. In this case the PCE reduction is due to few-percent losses to both J_{sc} and V_{oc}, and the same 5% loss to FF. Plots of these major photovoltaic parameters (PCE, J_{sc}, V_{oc} and FF) versus illumination time are available in the supplemental information (**Appendix 1.5**). Therefore, the most stable SM-OSC in this study employs CF_4 plasma treatment as an HEL and a BCP EEL. Based on the XPS data from **Chapter 8**, the organic-electrode interfaces are known to be especially susceptible to photo-induced chemical changes.[12, 13] Consequently, the instabilities of the organic-electrode interfaces observed here are suggested to be due to detrimental photo-chemical interactions between the photo-active organic species and the electrode. These interactions are found to occur due to exposure to light, as samples kept in dark showed either no change or substantially smaller changes in their photovoltaic parameters when compared to those devices exposed to light. In all configurations, the SM-OSCs lose ~5% in FF, indicating the likelihood of an additional degradation mechanism beyond the photo-instability of the organic-electrode interface. This additional degradation mechanism is studied in greater detail in **Chapter 10**, where SM-OSCs are studied for variations in their charge collection properties with time as a function of their device structure.

Interestingly, the SM-OSCs with an LiF EEL showed degradation behavior very similar to that of a device with no EEL. Note that the photo-stability data for SM-OSCs with LiF EELs are not provided for

PEDOT:PSS and MoO_3 HELs because the initial performances of these devices were generally too low to be meaningful. Furthermore, the combined BCP/LiF EEL showed stabilities similar to that of BCP alone – the curves of BCP and BCP/LiF EEL devices largely overlap. To understand the inefficacy of LiF here, it is useful to re-examine the function of the EEL in SM-OSCs as discussed in **Chapter 5**:

- to aid in work function alignment of the cathode and/or aid with conduction of electrons to the cathode, same as with P-OSCs[187, 276]
- to block excitons from reaching the adjacent electrode, unique to SM-OSCs (generally not considered for P-OSCs)[39, 192]
- to protect the underlying organic layers from damage during deposition of the top metal cathode, also unique to SM-OSCs[39, 192]

While LiF may help to satisfy the first role of work function alignment, a 1 nm LiF layer is insufficient to protect the underlying organic layers from metal damage during cathode deposition or to physically block excitons from reaching the adjacent electrode. This is particularly relevant when considering the RMS roughness values of the organic layer adjacent to the EEL, as determined by AFM. An AFM scan of the C_{60} layer (i.e. the layer adjacent to the EEL in the SM-OSC) is provided in Figure 9-3.a. For reference, an AFM image of the 1:1 P3HT:PCBM layer (i.e. the layer adjacent to the EEL in the P-OSC) is also provided in Figure 9-3.b. From these data, the roughness of the neat C_{60} layer is found to be quite high (3.3 nm RMS roughness), especially when compared to that of the 1:1 P3HT:PCBM BHJ in the P-OSC (1.4 nm RMS roughness). It is worth noting that using a 1:1 BHJ of ClInPc:C_{60} does decrease the roughness slightly (2.5 nm RMS roughness), but not to the same level as with the P-OSC BHJ (LiF is similarly ineffective for a simple 1:1 ClInPc:C_{60} BHJ SM-OSC). The penetration of aluminum through 1 nm thick LiF to create an organic/Al interface would further result in reduced OSC stability and lifetime. Finally, in the case of the BCP/LiF EEL, the presence of LiF does not have any effect, whether positive or negative,

on the device characteristics or photo-stability, indicating that the BCP EEL is already sufficient to carry out all of its functions denoted above.

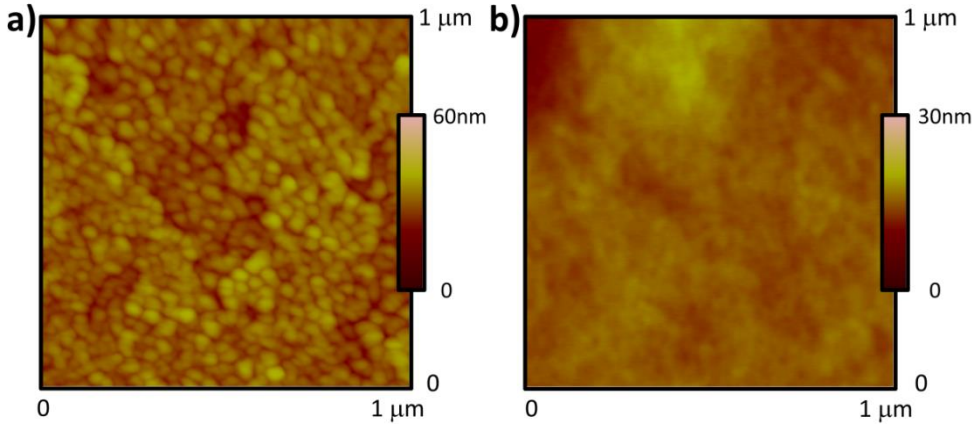

Figure 9-3 - AFM image of a) C_{60} and b) 1:1 P3HT:PCBM films. RMS roughness values are 3.3 nm and 1.4 nm for a) and b) respectively.

From these results, it is becoming clear that the cathode photo-degradation phenomenon is strongly linked to the presence of excitons at the organic-metal interface (and not merely due to the creation of a 'weak' organic-metal interface). BCP, with its large bandgap compared to either the donor or acceptor material, provides a necessary buffer to physically separate excitons from this interface and thus it can effectively limit photo-degradation. As such, there are two viable strategies for the selection of extraction layers for high stability OSCs: either form highly stable interfaces (e.g. through the use of inorganic layers, as is the case with LiF in P-OSCs), or prevent direct contact between the electrode and the photo-active species (e.g. with a wide bandgap organic extraction layer).

9.2.3. Solution-Coated Polymer Solar Cells

The normalized PCE values of the P3HT:PCBM P-OSCs with varying HELs/EELs during the 84-hour illumination scheme are plotted in Figure 9-4. Following the same approach as in the previous section, the data have been normalized relative to the PCE values of identical devices kept in the dark at the given time. The original non-normalized data, including data for both the illuminated samples and the

samples kept in dark, are provided in the supplemental information (**Appendix 1.5**). As with the ClInPc:C_{60} OSCs, the storage of the devices with suitable HELs/EELs yields only small variations in photovoltaic parameters (with only one exception, PEDOT:PSS/P3HT:PCBM/BCP devices, which are discussed further below). In concurrence with the results from **Chapter 8**,[15] P3HT:PCBM P-OSCs with either no EEL or no HEL exhibit poor photo-stability. Devices with no HEL suffer a significant decrease in PCE to ~0-20% of their initial PCE within 84 hours of illumination regardless of the choice of EEL. P-OSCs with no EEL also photo-degrade, but not nearly as much as SM-OSCs, losing only ~40%, ~20% and ~15% of their initial PCE for CF_4 plasma treatment, PEDOT:PSS and MoO_3 HELs respectively.

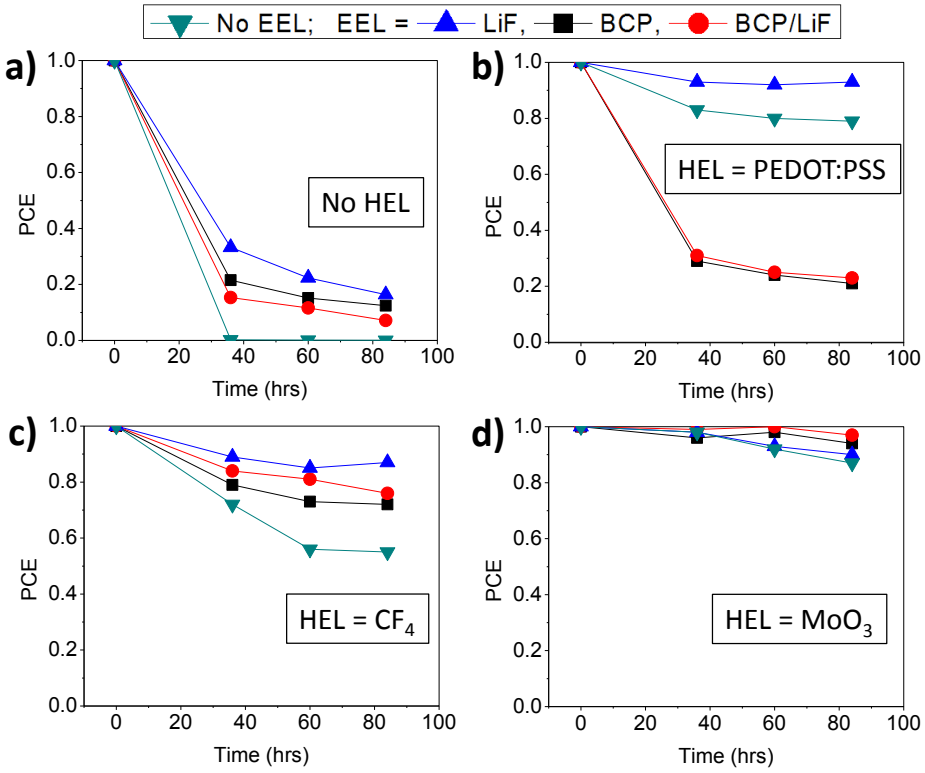

Figure 9-4 - Normalized PCE values for P3HT:PCBM P-OSCs with different HELs and EELs over 84 hours of illumination. HELs include: a) No HEL, b) PEDOT:PSS, c) CF4 plasma treatment, d) MoO_3.

P-OSCs that employ both an HEL and an EEL exhibit a significantly enhanced photo-stability. Following similar behavior as the SM-OSCs, BCP and BCP/LiF EELs give roughly the same trends during illumination, so the latter are not discussed in depth here. As shown in Figure 9-4.b, PEDOT:PSS/…/LiF P-

OSCs are relatively photo-stable, with only a 5-10% decrease in PCE after 84 hours of light exposure. In this case, the reductions are due to slight losses in V_{oc} and FF. From Figure 9-4.c, devices with either LiF or BCP in combination with a CF_4 HEL are shown to exhibit reasonable stability. The CF_4/…/BCP configuration allows for only a ~20% reduction in PCE, while the CF_4/…/LiF configuration shows only a ~10% decrease in PCE after 84 hours of illumination. From Figure 9-4.d, MoO_3/…/LiF P-OSCs are also reasonably stable with only a 10% loss in PCE. The highest stability P-OSCs employ the MoO_3/…/BCP configuration, allowing for only a 5% reduction in PCE over 84 hours of illumination, which appears to arise primarily from losses in FF. Therefore, the most stable P-OSCs from this study employ a MoO_3 HEL and a BCP EEL.

From Figure 9-4.b, PEDOT:PSS/…/BCP devices are demonstrated to exhibit very poor stability, losing ~80% of their original PCE within 84 hours of light exposure – a trend in direct contrast to all other devices with a BCP EEL. Since PEDOT:PSS HEL devices show reasonable stabilities with an LiF EEL, and BCP EEL devices show reasonable stabilities with both CF_4 and MoO_3 HELs, it is clear that BCP and PEDOT:PSS cannot be employed simultaneously. As discussed in **Chapter 8**, PEDOT:PSS has been suggested to contain residual humidity that can adversely affect device performance.[11] Furthermore, BCP has been shown to suffer from moisture-induced degradation.[201] It is thus logical to study the thermal stability of these devices, on the basis that any thermally assisted out-diffusion of moisture from PEDOT:PSS would adversely affect the OSC lifetime by interacting with BCP. As such, PEDOT:PSS/…/BCP P-OSCs were heated in the dark in a N_2 environment at the temperature that the illuminated samples reach (40 ^{o}C). Their output parameters were measured periodically up to a period of 36 hours (i.e. the first point in the concurrent photo-stability experiments). The normalized PCE values for the heated samples are plotted alongside illuminated data (for the same structure P-OSC) in Figure 9-5.a.

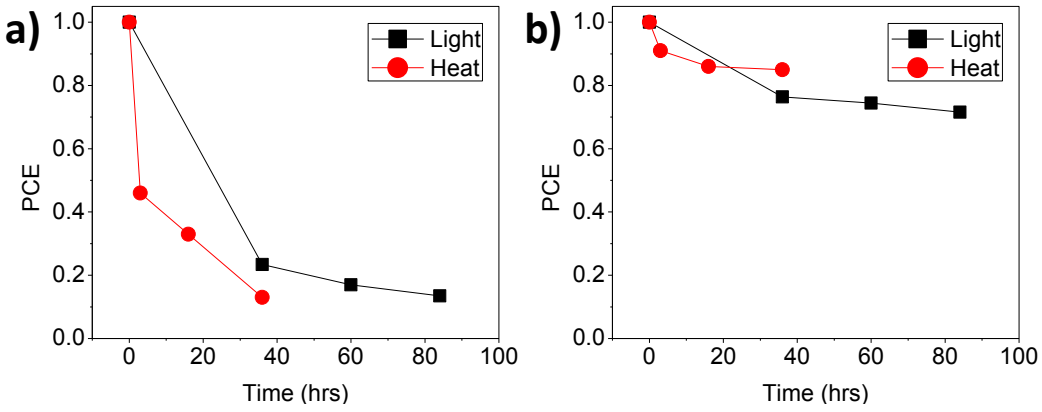

Figure 9-5 - Normalized PCE values for a) P3HT:PCBM and b) ClInPc:C60 OSCs with a PEDOT:PSS HEL and a BCP EEL while illuminated and heated.

The PEDOT:PSS/…/BCP samples are shown to degrade rapidly with heat, with a 90% loss in PCE in only 36 hours. Furthermore, the 36-hour heated sample point matches reasonably well with the 36-hour illuminated sample point. This indicates that, for this particular combination of materials, heat-induced degradation likely dominates photo-degradation. The results suggest that this poor stability may be largely due to the heat-mediated release of moisture from PEDOT:PSS and its subsequent interaction with the BCP interlayer. While heat plays a major role in the OSC losses for P-OSCs with a PEDOT:PSS HEL and a BCP EEL, it is worth recalling that heat-induced degradation is not always the primary cause of OSC contact degradation and the associated PCE losses. To this end, in **Chapter 8**, it was established that P-OSCs with no HEL and no EEL have similar PCE versus time behavior whether they are heated or simply kept in the dark in N_2.[15] These same devices, however, showed strong reductions in PCE when illuminated. XPS measurements have further shown that various organic-electrode interfaces are susceptible to photo-induced chemical changes.[12, 13] In these latter experiments, the light intensities were generally low enough that the devices did not experience any significant heating. The results thus stress the importance of considering all possible avenues toward device degradation in OSC stability studies.

Interestingly, for the ClInPc:C_{60} SM-OSCs, the PEDOT:PSS/…/BCP combination did not show as significant deterioration, with only a ~20% loss in PCE after 84 hours of illumination. Since it is unknown

if this loss is similarly due to heat-induced effects, the same heat-stress experiment was conducted for the SM-OSCs, and the PCE values for the heated and illuminated devices are both plotted in Figure 9-5.b. From these data, it is clear that ~15% of the reduction in PCE in the first 36 hours can be attributed exclusively due to thermal effects. Thus, it is supposed that this moisture release still affects SM-OSCs, but not to the same degree as P-OSCs. Work completed by Voroshazi and coworkers suggests that C_{60} may act as a form of 'getter' material for residual moisture in OSCs.[11] Since the SM-OSCs employ both a high concentration of C_{60} and a neat C_{60} layer, this may explain the higher stability compared to the P-OSCs. If this caveat holds true, it implies that PCBM is not capable of acting in the same regard as a getter, at least when mixed with P3HT with a 1:1 mixing ratio.

From these data, it is shown that the reduction in the PCE of OSCs under illumination is a widespread phenomenon, as it is observed in both SM-OSCs and P-OSCs and for all HEL/…/EEL configurations. It is also clear that the contacts play a critical role in the photo-stability behavior of these devices, with proper choices of HEL and EEL allowing for considerable stability improvements for illuminated samples. Finally, there is interplay between the HEL and the EEL that must be considered when studying the photo-stability behavior of OSCs, whether solution-coated or vacuum-deposited. It follows that the HEL and the EEL must be chosen carefully when considering the device's ultimate stability.

9.2.4. Observations for the Photo-Stability of Small Molecule versus Polymer Organic Solar Cells

It was established that the most stable configuration of SM-OSC employs a CF_4 plasma treatment HEL and a BCP EEL. The most stable configuration of P-OSC, however, employs a MoO_3 HEL and a BCP EEL. It is worthwhile to examine the different features of these two HELs that make them suitable for SM-OSCs and P-OSCs respectively, and thus make them suitable for the two different OSC

fabrication methodologies (with either vacuum-deposited or solution-coated photo-active layers). For CF_4 plasma treatments, the ITO surface is passivated with fluorine atoms; however, spincoating is a mechanically harsh process that may disrupt or alter the ITO surface chemistry compared to vacuum deposition. In contrast, MoO_3 is much more suited as a foundation for subsequent spincoating processes, and is thus less likely to show regions of uncovered/untreated ITO. Such untreated regions in CF_4 HEL-based P-OSCs would ultimately undergo photo-degradation processes to lead to a strong reduction in photovoltaic output properties – essentially due to a loss in active device area. Given the similarity between the CF_4 plasma surface treatment and self-assembled monolayer surface treatments, it is also feasible that the variations observed here are related to the selectivity of the contact,[277] which may vary for the different materials systems and for the different fabrication methodologies. Regardless, given that inorganic oxides can be deposited as much thicker, denser films, it is suggested that they provide a more reliable platform for subsequent device fabrication and are therefore much more reliable extraction layers in general.

In this chapter and in **Chapter 8**, it was established that a majority of the photo-degradation of the photovoltaic output parameters, especially in the short-term, can be minimized through the choice of certain combinations of extraction layers. Once the optimum HEL/EEL combinations have been chosen, the losses to J_{sc} and V_{oc} during illumination are strongly reduced. However, in spite of extraction layer optimization, all device configurations show a few percent decrease in V_{oc} and a ~5% decrease in FF. This trend is observed more clearly in Figure 9-6.a, which shows the pre-/post-illumination light IV characteristics of SM-OSCs and P-OSCs with optimal HELs and EELs.

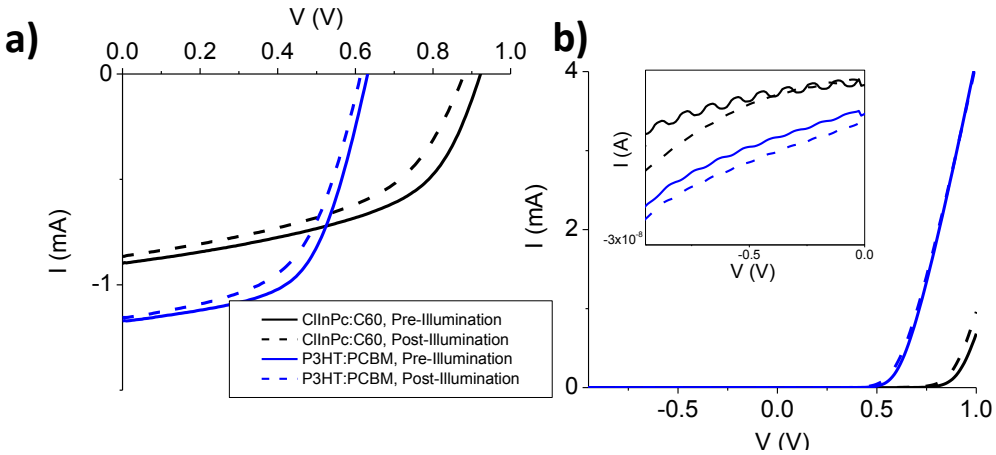

Figure 9-6 - a) Light IV and b) dark IV curves for ClInPc:C_{60} and P3HT:PCBM OSCs before and after illumination (Inset of B shows the dark current at negative bias at a magnified scale). Device structures are ITO/CF_4/ClInPc:C_{60}/C_{60}/BCP/Al and ITO/MoO_3/P3HT:PCBM/BCP/Al.

Further, from the dark IV characteristics of these devices, as plotted in Figure 9-6.b, post-illuminated devices have more leakage current in both forward and reverse bias. As the V_{oc} is fundamentally related to the reverse saturation current,[58] leakage current under reverse bias necessarily leads to a reduction in V_{oc}. Since an increase in current in both forward bias as well as reverse bias is observed, it is suggested that there are additional shunts through the post-illuminated devices. This shunting and the associated decrease in FF merit further investigation. To this end, by minimizing this fast photo-induced contact degradation, it is now feasible to focus on additional degradation pathways that happen over a larger time scale, including photo-deterioration of the organic bulk materials or even photo-induced alterations at the organic-organic interfaces throughout the mixed donor-acceptor active layer.

9.2.5. Further General Observations

As established above, ClInPc:C_{60} SM-OSCs that employ a PEDOT:PSS HEL exhibit a reduced initial PCE of ~1.24%, which is much lower than the CF_4 and MoO_3 HEL OSCs. To understand this effect, it is necessary to examine each photovoltaic parameter in greater detail. SM-OSCs with a PEDOT:PSS HEL have J_{sc} values on par with those of the CF_4 and MoO_3 HEL devices; however, their FF values are lower

and their V_{oc} values are strongly reduced (650 mV for PEDOT:PSS vs. 920 mV and 980 mV for CF_4 and MoO_3 respectively). The 650 mV V_{oc} observed with the PEDOT:PSS HEL is near (slightly lower than) the V_{oc} set by the $HOMO_{ClInPc}$-$LUMO_{C60}$ offset (in consideration of other energy losses, as described in **Chapter 1**). The V_{oc} enhancements observed for MoO_3 and CF_4 HELs are due to the Schottky junction effect that arises when a high work function electrode contacts a BHJ with high fullerene content, as discussed in **Chapters 1**, **4** and **6**.[42, 71, 72] It can thus be concluded that PEDOT:PSS may act as a suitable HEL for these SM-OSCs, but it does not provide a sufficiently deep work function to allow for the band bending and the subsequent V_{oc} improvement inherent in fullerene-based Schottky OSCs. In contrast, both MoO_3 and CF_4 plasma treatment HELs have sufficiently high work functions to allow for the fullerene-based Schottky OSC structure. It is also worth noting that PEDOT:PSS has been used successfully in Schottky P-OSCs employing high concentrations of PCBM in P3HT:PCBM cells. [162] As such, the HELs that may allow for the formation of a Schottky OSC must also be considered in the context/choice of the principal photo-active materials.

Throughout this chapter, BCP was shown to be a suitable EEL for both SM-OSCs and P-OSCs, granting good initial PCE values and high OSC lifetimes. This implies that BCP satisfies all of the EEL criteria established previously – exciton blocking, metal damage protection and work function alignment. However, the role of BCP in work function alignment is, as of yet, unclear. To this end, considering P3HT:PCBM P-OSCs, Reese et al. previously demonstrated that the high work function of an Al cathode causes a reduction in both V_{oc} and FF; however, the use of an LiF/Al contact recoups these losses to grant good performance, near that of P-OSCs employing a Ca/Al or Ba/Al cathode.[32] The observed improvements with the use of an LiF EEL are attributed to the shallow work function of LiF/Al compared to Al alone, which is due to dipole formation at the LiF/Al interface.[187] Given that a similar level of performance enhancement is observed for P3HT:PCBM P-OSCs with a BCP EEL, especially with regard to the V_{oc} (>~600 mV), it is suggested that the thin BCP EEL must also help in some regard with

work function alignment. Such a possibility was recently shown by Xiao et al. who observed that solution-coated films of a similar wide bandgap electron transport material, Bphen, can be used as an EEL for inverted P3HT:PCBM P-OSCs.[278] For these inverted OSCs, the adjacent cathode is ITO (work function of ~4.3 eV to 4.8 eV [279]), so the Bphen EEL must necessarily result in a low work function contact to grant good device performance and the observed V_{oc} of ~600 mV.

9.3. Conclusions

In this chapter, a systematic comparison of the photo-stability of vacuum-deposited SM-OSCs versus solution-coated P-OSCs was provided to further elucidate the photo-instability of the organic-electrode interface. The results reinforced the observations observed in **Chapter 8**, and clarified the suitability of common interfacial extraction layers in P-OSCs and SM-OSCs. The major conclusions from this work are detailed below:

- The use of both an HEL and an EEL can drastically suppress contact photo-degradation for both SM-OSCs and P-OSCs, suggesting that the organic/electrode interface poses a serious source of device instability regardless of fabrication methodology (solution-coated versus vacuum-deposited).
- Common HELs and EELs in SM-OSCs (CF_4 plasma treatment and BCP) can be applied to P-OSCs, but the opposite is not necessarily true, as both PEDOT:PSS and LiF result in low efficiency SM-OSCs.
- The data suggest that it is not merely the existence of the organic-electrode interface in OSCs that leads to photo-unstable devices, but rather the direct contact between the photo-active layer and the electrode. It is thus hinted that the presence of excitons at the organic-electrode interface is the root cause behind contact photo-degradation.
- Minimizing the short-term contact photo-degradation grants the opportunity to address other degradation mechanisms that may occur over a larger timescale.

Chapter Ten:

Implications of the Device Structure on the Photo-Stability of Organic Solar Cells[1]

In this chapter, long-term photo-stability experiments are conducted on SM-OSCs with strongly varied mixing ratios. Comparisons are made between the fullerene-based Schottky device structure and the standard BHJ structure. The results therefore help to ascertain the impact of photo-induced changes in the bulk photo-active layer as compared to variations at the organic/electrode interfaces. Losses in V_{oc} with light exposure are observed for both Schottky and standard BHJ OSCs. In agreement with previous results, these losses are attributed to organic-electrode degradation. Smaller variations in the other photovoltaic parameters are found to be dependent on the active layer composition and the associated device structure. Schottky OSCs are slightly more resilient to variations in short circuit current compared to standard BHJ OSCs, but they suffer from losses in fill factor. Microsecond transient photocurrent and EQE measurements show that these fill factor losses are due to increased recombination. The choice of device architecture is thus shown to alter degradation mechanisms, and so it can have implications on the overall OSC photo-stability.

10.1. Introduction

As described in **Chapter 1**, the fullerene-based Schottky structure is an emergent device architecture with impressive efficiencies and high V_{oc} values. The finer working points of the Schottky device architecture have only recently begun to be investigated,[42, 72, 160, 162, 209] while its stability in

[1] The majority of the material in this chapter was published in:
G. Williams,H. Aziz, *Sol. Energy Mater. Sol. Cells,* **2014,** *128*, 320.
, reproduced here with permission.

relation to more traditional device architectures remains largely untested. Given that the Schottky device architecture is responsible for some of the highest efficiency single-cell vacuum-deposited OSC-OSCs,[68, 69, 280] it is beneficial to gain a better understanding of its photo-stability. In this chapter, SM-OSCs are studied for their photo-stability in an inert N_2 environment. By employing mixed BHJ layers with drastically different mixing ratios, from donor-rich to acceptor-rich, comparisons are made between the traditional/standard BHJ OSC structure and the more recently developed fullerene-based Schottky OSC structure. The OSCs are tested over a period of four weeks, and their photovoltaic parameters are measured in parallel with their EQE spectra, UV/Vis absorbance spectra and microsecond transient photocurrent behavior. This full suite of characterization techniques provides a more fundamental understanding of the intrinsic device photo-degradation behavior.

From the results in this chapter, it is found that thermal stresses at relevant temperatures (those that the OSCs typically reach during light-stress experiments) have only small effects on device performance, regardless of the device architecture (i.e. the active layer mixing ratio). However, light stress results in 10-15% losses in PCE after four weeks of continuous 1-sun intensity illumination. This finding is in agreement with the results from **Chapter 8** and **Chapter 9**. Schottky OSCs generally suffer from losses in FF, but are slightly more resilient to variations in J_{sc} compared to their standard (1:1 donor:acceptor) BHJ counter-parts. Transient photocurrent measurements indicate that the losses in FF are due to increased recombination within the devices after aging, suggested to be due to photo-induced degradation of C_{60}. Photo-induced losses in V_{oc} are associated with a slower transient photo-response, as observed in standard BHJ structure OSCs, and are posited to be due to degradation at the contacts and interfacial extraction layers. The results thus demonstrate that the choice of device architecture can have an impact on OSC degradation mechanisms and, as a consequence, can have implications on the ultimate OSC photo-stability.

10.2. Results and Discussion

10.2.1. Initial Performance of Standard Bulk Heterojunction and Schottky Organic Solar Cells

In this chapter, the photo-stability of ClInPc:C_{60} SM-OSCs is further examined to elucidate less obvious degradation phenomena, especially those related to the organic photo-active layers. The device structure and associated energy band diagram for the constituent materials used in the OSCs in this chapter are shown in Figure 10-1 (A and B respectively).

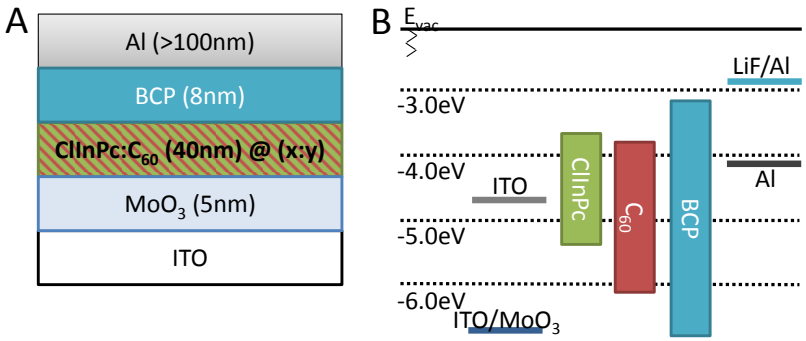

Figure 10-1 - A) ClInPc:C_{60} OSC device structure used for experiments in this chapter. B) Energy level diagram for the constituent materials used in the ClInPc:C_{60} OSCs.

All devices studied in this work employ a 40 nm donor:acceptor mixed layer between a MoO_3 HEL and BCP EEL. MoO_3 and BCP are specifically chosen for this series of experiments, as they are known to be effective in creating SM-OSCs with high photo-stability, as discussed in **Chapter 9**.[109] The use of a MoO_3 HEL also allows for the creation of fullerene-based Schottky OSCs, as discussed in **Chapter 1**. The 40 nm photo-active layer allows for reasonable power conversion efficiencies at most mixing ratios, demonstrated in **Chapter 4**, by balancing photocurrent generation with charge transport. The composition of the mixed layer is varied from donor-rich to acceptor-rich, including 3:1, 1:1, 1:3 and 1:7 donor:acceptor mixing ratios. The comparison of a 1:1 donor:acceptor mixed layer to an acceptor-rich mixed layer (e.g. 1:3 or 1:7 donor:acceptor) allows one to explicitly test the standard BHJ device

architecture as it relates to the Schottky device architecture. The UV-Vis absorbance spectra of the 40 nm films at these various mixing ratios are shown in Figure 10-2, which show three major peaks (established in **Chapter 4**): UV contributions from C_{60} as well as the m-Pc B band (~350 nm), fullerene aggregate absorption (~450 nm) and ClInPc Q band absorption (~720 nm peak, ~650 nm shoulder). It is worth noting that the Q band absorbance of ClInPc is quite strong, especially compared to C_{60} – at a 1:3 ClInPc:C_{60} mixing ratio, the absorbance from ClInPc is twice as strong as the C_{60} 450 nm band.

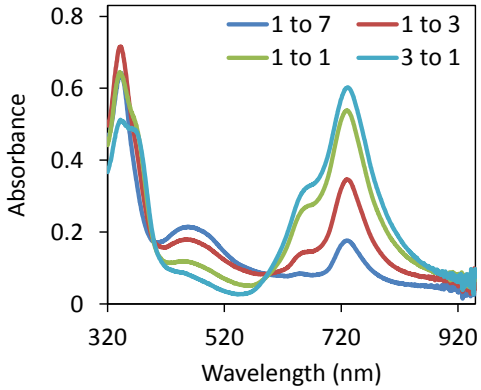

Figure 10-2 - UV/Vis absorbance of the various mixing ratio films employed in the ClInPc:C_{60} OSCs in this study.

The initial photovoltaic output parameters for the ClInPc:C_{60} OSCs at varying mixing ratios are provided in Table 10-1. Note that the performance of as-fabricated ClInPc:C_{60} OSCs (not aged, at t=0) with varying mixing ratios has been addressed at depth in previous chapters,[72, 209] and so the data are only discussed briefly here. The V_{oc} is observed to increase strongly with increasing C_{60} content due to the shift from the standard BHJ device architecture to the Schottky architecture.[72] To this end, in the standard BHJ device architecture, the V_{oc} is set by the $HOMO_{donor}$-$LUMO_{acceptor}$ offset, whereas in the Schottky device architecture, the V_{oc} is dictated by band bending at the MoO_3/C_{60} interface.[71] As the donor:acceptor ratio is altered, the V_{oc} varies between these two scenarios. The J_{sc} reaches its maximum value at a 1:3 ClInPc:C_{60} mixing ratio due to balancing photocurrent contributions from the ClInPc Q band and the C_{60} aggregate absorption. The culmination of these trends shows that the PCE is

maximized for devices with higher C_{60} content, largely owing to the drastic improvements in V_{oc} with increasing C_{60} concentration (due to the fullerene-based Schottky device architecture).

Table 10-1 - Initial (t=0) photovoltaic parameters for ClInPc:C_{60} OSCs at various donor:acceptor mixing ratios.

Mixing Ratio (D:A)	Jsc [mA/cm^2]	Voc [mV]	FF [%]	Eta [%]	Rshunt [Ohm.cm^2]	Rseries [Ohm.cm^2]
1 to 7	5.4	1000	43	2.3	2870	25
1 to 3	5.8	900	43	2.2	2270	20
1 to 1	5.2	770	38	1.5	1460	26
3 to 1	4.1	760	36	1.1	1570	35

10.2.2. PCE, Voc and Jsc Stability in Schottky versus Standard Bulk Heterojunction Organic Solar Cells

In order to make meaningful conclusions regarding the stability, one must consider several degradation pathways (as was done in **Chapter 8**). Since the present study focuses on the stability of OSCs in an inert environment, degradation due to ambient (O_2 or H_2O) effects are generally much less critical. In past work it was shown that purely electrical stresses have little impact on OSC lifetimes,[15] so these effects are also not examined explicitly. A first set of samples is fabricated in order to test the effect of simply storing the devices in the dark and in N_2 (i.e. to test the device shelf-life), and thus to act as a control for these experiments. A second set of samples is fabricated for studying the photo-stability, and so these samples are placed under 1-sun intensity light as described in **Chapter 3**. A final, third set of samples is fabricated for studying thermal stability effects, accomplished by placing the samples in the dark at 40 ^{o}C (approximately the temperature that the OSCs reach during the light-stress experiments). In each case, the samples are aged over 28 days and measured periodically for their photovoltaic output parameters, EQE spectra and microsecond transient photocurrent response. UV/Vis absorption and AFM measurements are also conducted at the beginning and the end of the study in order to provide further information regarding potential degradation to the active material itself (e.g. photo-bleaching effects), as well as further information on morphological variations.

The normalized PCE, V_{oc} and J_{sc} values for these OSCs versus time exposed to both heat and light are shown in Figure 10-3 (FF values and associated R_s/R_{sh} values are addressed in Section 10.2.3). To better isolate the effects of light and heat on the samples, the data presented in Figure 10-3 have been normalized relative to the photovoltaic parameters of identical devices kept in the dark at the given times, as done in **Chapter 9**.[109] This normalization helps to remove any variations with time, independent of the light and heat stress, and therefore it allows one to better observe changes in the photovoltaic parameters purely due to light and heat stresses. The original non-normalized data, including data for both the illuminated/heated samples and the samples kept in dark, are provided in the Supplemental Information (**Appendix 1.6**). It is worth noting that the samples simply stored in the dark in N_2 showed very small (generally insignificant) variations in their photovoltaic output parameters, and so this process is primarily completed to more cleanly identify trends while avoiding the obvious consequences of 'big data.'

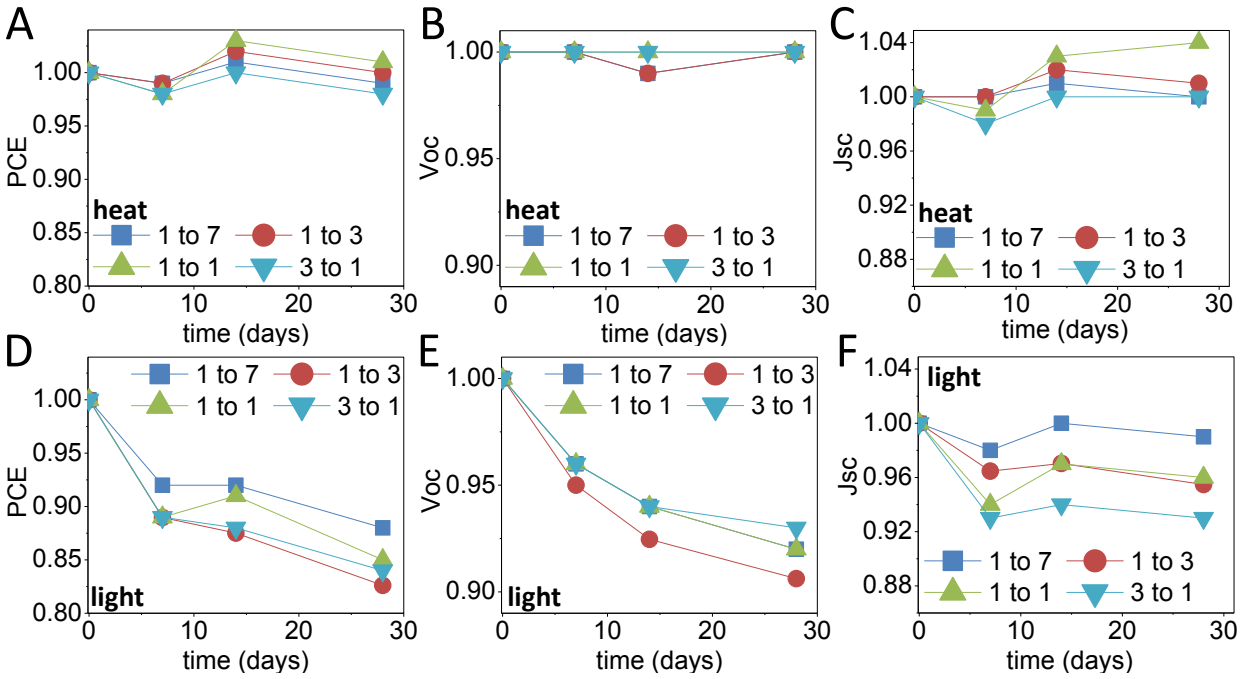

Figure 10-3 - PCE, V_{oc} and J_{sc} values of heated ((A) through (C)) and illuminated ((D) through (F)) ClInPc:C_{60} OSCs at various mixing ratios.

From Figure 10-3.A-C, all OSCs (regardless of mixing ratio) subjected to heating show very small variations in their photovoltaic parameters with time. Only few percent variations are observed around their initial PCE values (Figure 10-3.A), largely owing to changes in J_{sc} (Figure 10-3.C) – the V_{oc} values for these OSCs are remarkably stable (Figure 10-3.B). Interestingly, the OSCs that employ 1:1 and 1:3 ClInPc:C_{60} mixed layers show a slight improvement in PCE with time due to an increase in J_{sc}. This improvement can perhaps be attributed to a thermally induced rearrangement of the donor and/or acceptor species within the film, which serves to improve the film morphology, enhance charge collection and ultimately grant higher J_{sc} values. To further understand these variations in J_{sc}, EQE measurements for both Schottky samples (1:7 ClInPc:C_{60}) and standard BHJ samples (1:1 ClInPc:C_{60}) are provided in Figure 10-4, with spectra measured immediately prior to the heat stress (fresh samples) compared to spectra measured after the heat stress experiment.

In the case of the Schottky device (1:7 ClInPc:C_{60}, Figure 10-4.A), heat stress results in a visible increase in EQE at the 450 nm absorption band. While the improvements are relatively small, they are non-negligible and are well within the sensitivity of the experimental set-up. Full EQE data for all of the different mixing ratios for the heat stress as well as the devices kept in the dark are provided in the Supplemental Information (**Appendix 1.6**), where the devices kept in the dark show no change in EQE after storage (perfect overlap of the pre- and post-storage curves). Note that this broad absorption band at 450 nm is due to the presence of C_{60} aggregates,[72] which were demonstrated to grant substantial photocurrent in high C_{60} content OSCs in previous chapters. It is thus logical that, for the Schottky architecture, this band is most strongly affected during stress tests. Since the absorption of light at 450 nm is contingent on the formation of fullerene aggregates, it is strongly suggested that the observed changes are related to the partial phase separation of donor and acceptor within the mixed layer (this point is elaborated below with AFM measurements, but also revisited in Section 10.2.3 with transient photocurrent measurements). This improvement in C_{60} aggregate photocurrent, however,

does not result in an equivalent increase in J_{sc}. To this end, the observed variations in EQE should result in a ~5% increase in J_{sc} (as calculated by integration of the EQE with the AM1.5G solar spectrum), and yet only a 1% improvement is observed at the 1:7 ClInPc:C_{60} mixing ratio.

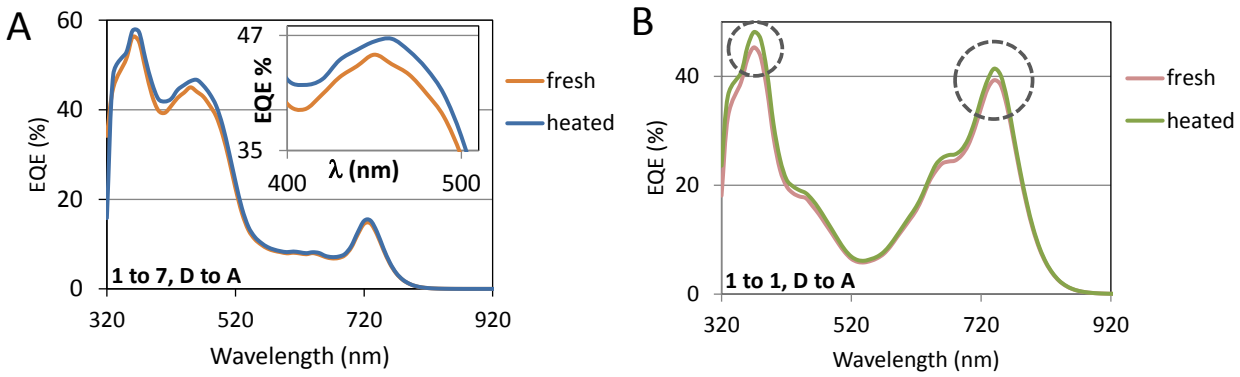

Figure 10-4 - EQE spectra of ClInPc:C_{60} OSCs with different mixing ratios as-made (fresh) and heated in N_2 for 28 days. (A) Schottky device structure, inset: zoom-in of the C_{60} aggregate photocurrent. (B) Standard BHJ device structure, with major variations highlighted.

Given that EQE measurements are conducted at much lower light intensities than the 1-sun measurements used to collect the photovoltaic output parameters, it is feasible that the additional photocurrent measured by EQE is not translated proportionally to higher J_{sc} values at much higher light intensities. At high light intensities, the higher exciton or charge carrier density may result in recombination effects that temper the improvements in photocurrent observed during the low light intensity EQE measurements. In comparison, for the standard BHJ structure device (1:1 ClInPc:C_{60}, Figure 10-4.B), heat stress results in increases in both the ClInPc Q band as well as the UV absorption at 350 nm. This improvement is also logical, as ClInPc contributes much more strongly to photocurrent in the BHJ structure as compared to the Schottky architecture. Only slight improvements are observed in the C_{60} aggregate band. In this case, the 1:1 ClInPc:C_{60} OSC shows a ~5% improvement in J_{sc} during heat stress, which corresponds reasonably well to the ~4% improvement calculated from the EQE spectrum.

To further study possible morphological changes with heat, AFM was employed to measure the surfaces of the heated devices. The measurements were taken away from the Al cathode, but still on

top of the organic stack (i.e. on ITO/MoO_3/ClInPc:C_{60}/BCP). The AFM images for the 28-day-heated devices at 1:7, 1:1 and 3:1 ClInPc:C_{60} mixing ratios are shown in Figure 10-5.A-C respectively.

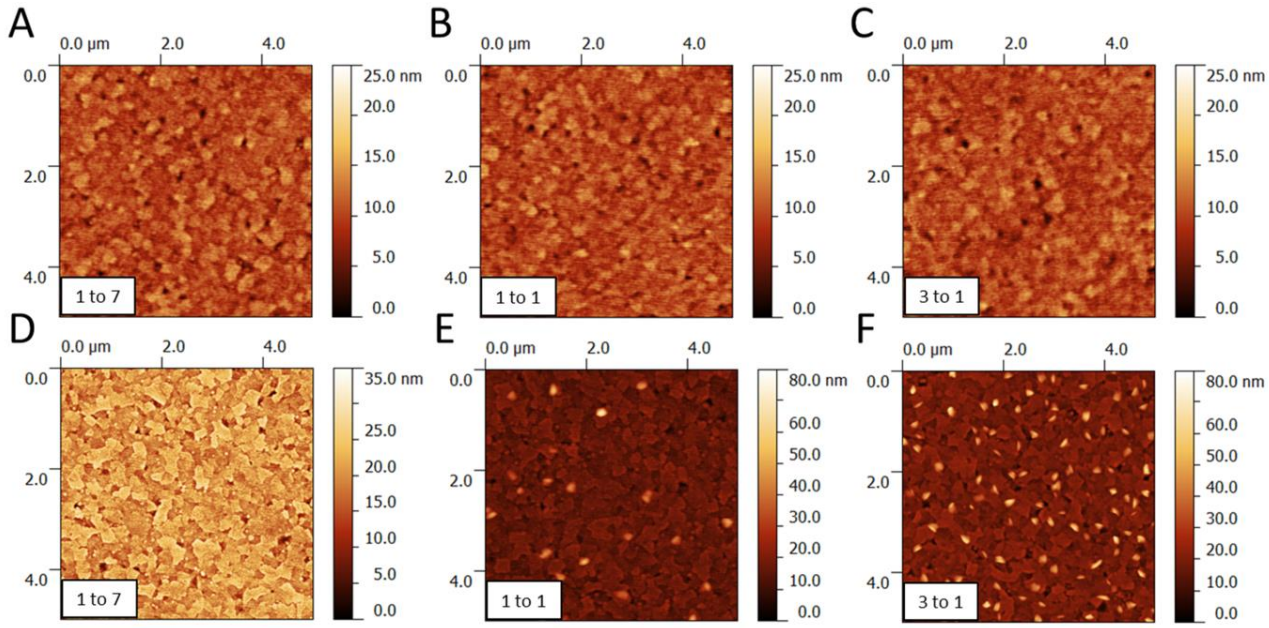

Figure 10-5 - AFM measurements of 28-day heated ITO/MoO_3/ClInPc:C_{60}/BCP films ((A) through (C)) and 7-day heated ITO/MoO_3/ClInPc:C_{60} films ((D) through (F)) at varying mixing ratios (all films heated at 40 ^{o}C).

The morphology looks quite similar across the three mixing ratios, and generally follows that of the underlying ITO. However, there are no noticeable differences between the heated devices and the devices kept in dark (AFM images of devices stored in dark are provided in the Supplemental Information (**Appendix 1.6**)). This suggests that the changes identified by EQE are too small to provoke a measurable morphological change, which is perhaps likely given the small magnitude of the observed changes. AFM was also performed on ITO/MoO_3/ClInPc:C_{60} films (without the BCP layer) after 7 days of heat stress, with the AFM images for 1:7, 1:1 and 3:1 ClInPc:C_{60} mixing ratios shown in Figure 10-5.D-F respectively. Fascinatingly, these films show a drastic change after being heated when compared to the films measured before heat (pre-heat AFM images are provided in the Supplemental Information (**Appendix 1.6**), and are generally similar to Figure 10-5.A-C). Specifically, films with higher ClInPc content show very large particles with heights on the order of 50 to 60 nm. Since the number of these particles increases with increasing ClInPc concentration, these particles are likely comprised of ClInPc.

Further, since such features were not visible on the heated films capped with BCP (Figure 10-5.A-C), it can be asserted that the formation of these large features is facilitated by the presence of the free ClInPc:C_{60} surface (i.e. the 8 nm BCP layer suppresses the formation of these large ClInPc features), and therefore does not occur, at least to a significant extent, in the OSCs. As such, these variations cannot provide direct information of the ClInPc:C_{60} morphology underneath the BCP layer while the samples are heated, but they do provide some critical hints. To this end, ClInPc molecules have been identified as incredibly mobile, and the heat experienced during 1-sun intensity illumination is sufficient to allow for remarkable morphological changes indicative of some form of ClInPc aggregation. It would therefore be unsurprising that ClInPc and C_{60} undergo heat-induced phase separation during the heat- and light-stress experiments. Such conclusions also coincide well with the EQE measurements noted above.

In contrast to the heated devices, all of the OSCs exposed to light show a ~10% loss to PCE within the first 7 days of light stress, as shown in Figure 10-3.D, and continued (slower) reduction in PCE beyond day 7. As such, over the 28-day aging experiment, a photo-dose of ~2.8 to 4 kJ can be calculated to elicit a 1% loss in normalized PCE. A large contributor to this reduced PCE is the decrease in V_{oc} that affects all OSCs regardless of the mixing ratio, shown in Figure 10-3.E. In the photo-stability experiments completed in **Chapter 8** and **Chapter 9**,[15, 109, 163] it was established that this degradation behavior and reduction of V_{oc} are generally associated with degradation at the organic-electrode interface, commonly due to the poor choice of interfacial extraction layers. It is worth noting that the losses observed in the present study occur in spite of the fact that a MoO_3 HEL and a BCP EEL are used, the combination of which are known to offer reasonable stability for SM-OSCs (from **Chapter 9**).[109] Since the present study is conducted over a longer period of time, the MoO_3/BCP HEL/EEL combination is thus posited to be non-ideal for long-term photo-stability. Considering the anode-organic interface first, the MoO_3 HEL itself can be prone to stability variations based on the quality of the deposited MoO_3 (as noted in **Chapter 5**), which is dependent on the time in between the deposition of MoO_3 and subsequent organic

layers (with the incomplete device kept in high vacuum < 5E-6 torr). This behavior is re-emphasized in Figure 10-6 below, where depositing MoO_3, waiting 17 hours, and then depositing the organic layers can have drastic consequences for device photo-stability (compared to devices where the MoO_3 HEL and organic layers are deposited in quick succession).

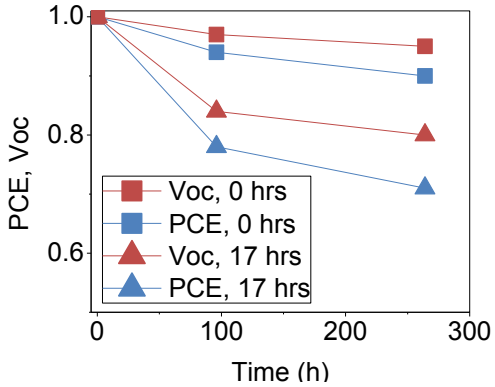

Figure 10-6 - Photostability of ITO/MoO_3/ClInPc:C_{60}/BCP/Al OSCs, with delays between deposition of MoO_3 and the ClInPc:C_{60} active layer. PCE and V_{oc} values are shown for 0 hr and 17 hr delays.

From Figure 10-6, this decrease in performance can be largely attributed to a decrease in V_{oc} for illuminated devices. Such behavior is likely associated with changes in the oxidation state of the MoO_3 film, as this has been shown to strongly impact device performance.[207, 281, 282] Thus, if irradiation can elicit a variation in the quality or composition of the MoO_3 film during the light-stress experiments, it would be unsurprising that the OSC performance is compromised. Considering instead the organic-cathode interface, a decrease in V_{oc} may be observed due to exciton-induced degradation through absorption of UV light by BCP, as has been demonstrated for other similar wide bandgap materials.[190] In **Chapter 8** and **Chapter 9**, the organic/metal interface was demonstrated to be susceptible to photo-induced degradation, essentially due to the presence of excitons at this interface, so it is logical that excitons generated in BCP directly may cause similar degradation.[13, 15] Since the UV component of the lamps used in the light stress experiments is quite low in intensity, this photo-degradation occurs over a much longer period of time, as is observed by the gradual loss in V_{oc} over the 28-day light stress experiment. This topic of interfacial degradation is revisited in Section 10.2.3 to address changes in the

sweep-out of photo-generated carriers for light-aged devices. Such observations highlight the continued requirement for more robust interfacial extraction layers, and further verify that organic-electrode interfacial degradation can occur regardless of the active layer composition. With organic-electrode interfacial degradation relatively well established, it is interesting to now examine the stability of the bulk (mixed donor:acceptor layer), as probed by studying the J_{sc}, EQE, FF and transient photoresponse of the OSCs.

While the J_{sc} for the 1:7 ClInPc:C_{60} Schottky OSC is generally unaffected by light exposure (Figure 10-3.F), OSCs with all other mixing ratios show a decrease in J_{sc} with light stress, especially those that employ more donor content than acceptor content (e.g. the 3:1 ClInPc:C_{60} OSC). As a first test for material photo-stability, it was verified that the absorbance of the ClInPc:C_{60} films showed no variations after the light stress experiments (spectra are provided in the Supplemental Information (**Appendix 1.6**) and overlap perfectly). This suggests that there are no significant photo-induced changes (e.g. photo-bleaching effects) that affect the bulk of the film. Therefore, it is useful to look toward EQE measurements for both Schottky and standard BHJ structure OSCs pre- and post-light stress, as shown in Figure 10-7. The EQE data for the remaining mixing ratios are provided in the Supplemental Information (**Appendix 1.6**). It is again emphasized that the dark control devices showed no variations in their EQE, so the observed changes in EQE during the light stress experiments are significant.

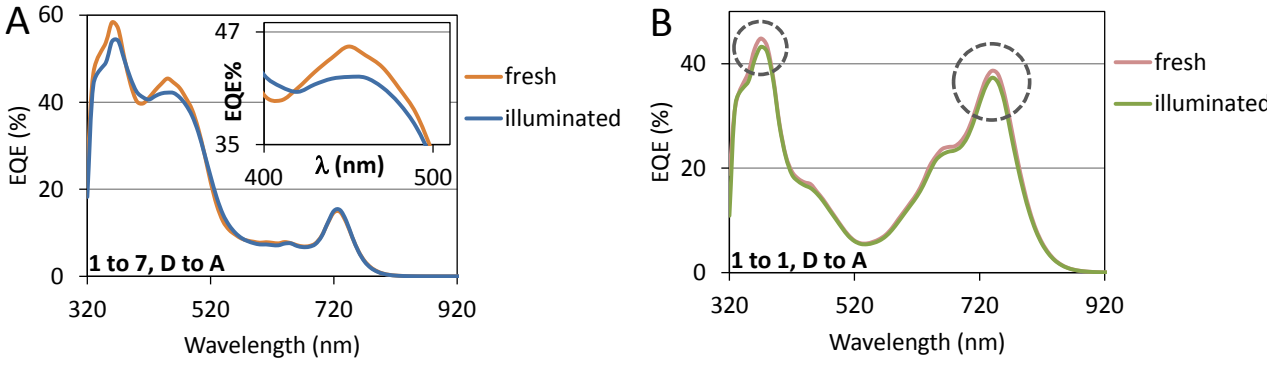

Figure 10-7 - EQE spectra of ClInPc:C_{60} OSCs with different mixing ratios as-made (fresh) and illuminated under 1-sun intensity light in N_2 for 28 days. (A) Schottky device structure, inset: zoom-in of the C_{60} aggregate photocurrent. (B) Standard BHJ device structure, with major variations highlighted.

Intriguingly, the changes in EQE observed due to the light stress are exactly opposite to those caused by the heat stress (for both Schottky and standard BHJ structures). For the Schottky device structure (1:7 ClInPc:C_{60}, Figure 10-7.A), the EQE at 450 nm is reduced after light stress when compared to the fresh device, and a slight reduction in the UV peak at 350 nm is also observed. Since the film's absorbance spectra did not change noticeably between pre- and post-irradiation, the observed decrease is suggested to be due to either morphological changes within the film or due to photo-chemical changes within fullerene, both of which may alter the film's charge transport characteristics. To test for morphological variations, the surfaces of light-stressed OSCs were probed by AFM in the same manner as with the heat-stressed devices. Similar to the heated devices, the ITO/MoO_3/ClInPc:C_{60}/BCP films showed no variations after light-stress. Likewise, the uncovered ClInPc:C_{60} films were more prone to variations in the exact same manner as the heat-stressed devices (the corresponding AFM images are provided in the Supplemental Information(**Appendix 1.6**)). Since the EQE data for the light-stressed OSCs show trends that are opposite to the heat-stressed devices, the presently observed changes for light-stressed devices are suggested to be more likely due to photo-chemical changes within fullerene. This point will be discussed further in Section 10.2.3, and is well in-line with previous studies that report exciton-induced degradation and subsequent trap formation in neat layers of C_{60}.[283]

For the standard BHJ structure device (1:1 ClInPc:C_{60}, Figure 10-7.B), there is a slight loss in both the ClInPc Q band and the UV absorption at 350 nm. As a consequence, the 1:1 ClInPc:C_{60} OSC shows a ~4% decrease in J_{sc} during light stress. This again corresponds well to the ~4% reduction calculated from the integrated EQE spectrum. This decrease in J_{sc} and overall reduction in EQE will be discussed further in Section 10.2.3 by examining the device's transient photocurrent to study the poor sweep-out of free carriers in photo-aged BHJ OSCs. This phenomenon may not affect the Schottky structure OSCs as strongly, owing to their inherently larger internal electric field and their extensive band bending near the anode.[71] Based on these observations, it can be concluded that for both the Schottky and standard

BHJ structure there is photo-induced degradation with time due to an initially rapid 'burn-in' loss, followed by more gradual losses. The degradation is largely attributed to reductions in V_{oc}, with only minor variations in J_{sc} that are generally more noticeable for the standard BHJ structure compared to the Schottky architecture. These variations are not substantially due to thermal effects.

10.2.3. FF and Transient Photocurrent Variations in Schottky versus Standard Bulk Heterojunction Organic Solar Cells

To better understand the role of charge transport variations in OSC stability with the light-stress and heat-stress experiments, the FF values are examined as they vary during the photo-stability experiments described in the previous section. The normalized FF, R_s and R_{sh} values for the light-stress and heat-stress experiments are shown in Figure 10-8.

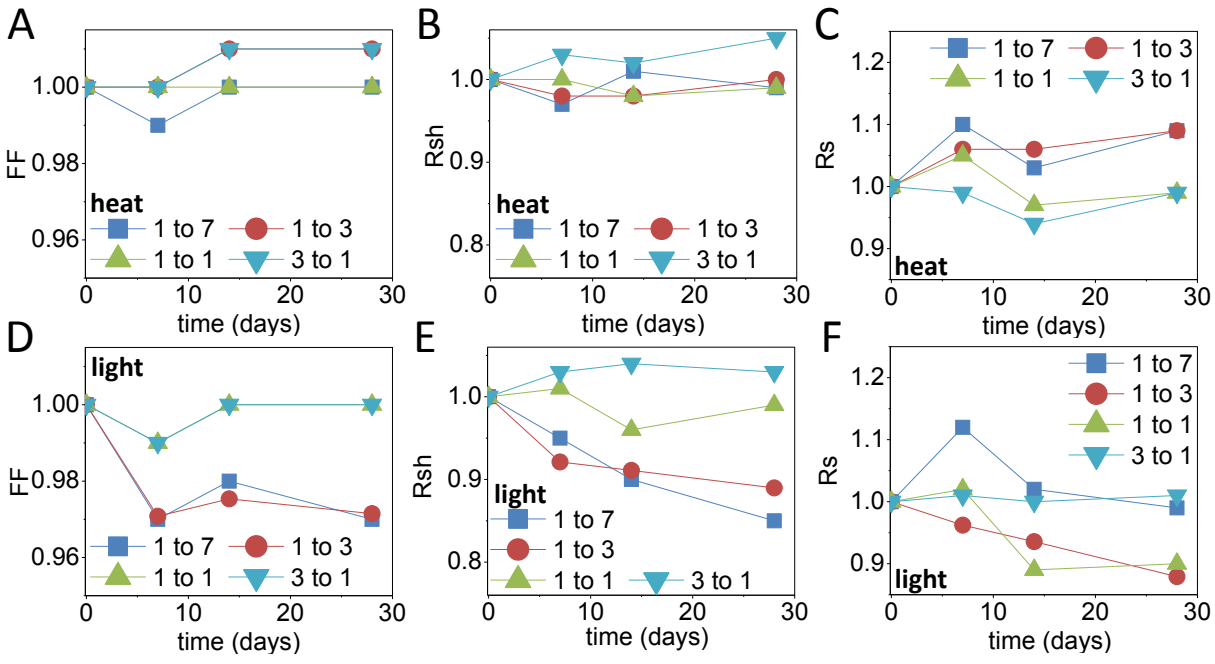

Figure 10-8 - FF, R_{sh} and R_s values of heated ((A) through (C)) and illuminated ((D) through (F)) ClInPc:C_{60} OSCs at various mixing ratios.

As with Figure 10-3, the data have been normalized relative to the photovoltaic parameters of identical devices kept in the dark at the given times to isolate the heat- and light-induced changes (i.e. versus time-dependent changes for the same parameters independent of stress). The non-normalized data are similarly provided in the Supplemental Information (**Appendix 1.6**, and again virtually no variations for dark/stored devices are observed). It is also worth noting that, while the FF is essentially defined by the R_s and R_{sh}, these resistances must change rather strongly to elicit variations in the FF. This is especially true for the R_s values, as these values are initially quite low (a 10% variation in R_s only accounts for a change of ~2 to 4 Ω*cm^2). For the heated devices, there are no significant variations in FF with aging, as is clearly visible in Figure 10-8.A. Note that this is in spite of the ~10% increase in R_s for the Schottky OSCs (1:3 and 1:7 ClInPc:C_{60}, Figure 10-8.C), which further emphasizes that more significant changes in R_s are required to have a substantial impact on the FF values for these particular OSCs. For the illuminated devices, the standard BHJ OSC (1:1 ClInPc:C_{60}) and the donor-rich OSC (3:1 ClInPc:C_{60}) show very small variations in FF with time. However, the Schottky OSCs (1:3 and 1:7 ClInPc:C_{60}) are observed to have a slight decrease in FF when illuminated. This decrease in FF is coupled with a more drastic (10 to 15%) reduction in R_{sh}, which suggests that the devices may suffer from increased recombination effects (i.e. to provide recombination current) as they are illuminated with time. Such observations are in accordance with the possibility for trap-related recombination caused by exciton-induced degradation of C_{60}, as previously observed by Tong et al. with OSCs employing neat films of C_{60}.[283] This exciton-induced degradation was more recently shown to be due to the photo-polymerization of C_{60} molecules.[284] It is also feasible that trap formation may be related to fullerene photo-oxidation,[223, 285, 286] by release of oxygen from a component within the solar cell (e.g. from ITO or organic impurities). The exciton-induced degradation of C_{60} was reported to be more prevalent when excitons were long-lived in neat C_{60} thin films. While Tong and coworkers did not observe significant photo-degradation in their mixed

SubPc:C_{60} OSCs (since the addition of SubPc decreased the exciton lifetime),[283, 284] it is likely that the effect is more predominant in the current study due to:

- the higher C_{60} content for these devices, specifically for the 1:7 ClInPc:C_{60} OSCs
- the lack of spectral overlap between the ClInPc Q band absorption and the C_{60} aggregate/cluster emission band, to strongly reduce any potential for FRET, which may otherwise serve as an avenue (beyond charge transfer) to reduce C_{60} exciton density

It is thus suggested here that, due to their very high concentration of C_{60}, exciton-induced degradation of C_{60} may be a potentially harmful factor toward the stability of Schottky structure OSCs.

To further support the stipulations regarding light-induced trap formation in C_{60}-rich (Schottky) OSCs, microsecond transient photocurrent measurements were also performed on the OSCs as they were heated and illuminated. Transient photocurrent measurements have been employed with increasing frequency in literature to analyze charge transport and charge extraction limitations in OSCs (as in **Chapter 6** and **Chapter 7**),[66, 206, 215, 216] and more recently for studying aged OSCs.[217, 287] This measurement technique is thus perfectly suited to elucidate the variations in FF, as the FF is strongly associated with charge transport and extraction. For the transient photocurrent measurements, OSCs are excited with a light pulse from a white LED, and the photocurrent decay is measured immediately after the light pulse. Single exponential fits are used to characterize the photocurrent decay, as per equation (10.1) below, to calculate the relevant fall time constant τ (I is the current measured at time t, following the end of the light pulse, and C1/C2 are fitting parameters).

$$I = C_1 \cdot \exp(-C_2 t), \qquad C_2 = 1/\tau \tag{10.1}$$

As discussed in **Chapter 6**, there are two major pathways that significantly alter τ: sweep-out of free carriers and charge recombination. Faster sweep-out of charge carriers is generally beneficial, and helps

to prevent weak charge trapping and space charge effects. Increased recombination, however, also serves to reduce the fall time, and is a harmful effect that can lower the FF and degrade the OSC performance. The extracted τ values for the ClInPc:C_{60} OSCs at varying mixing ratios, as tested prior to any stability or light-/heat-stress experiments, are shown in Figure 10-9. In accordance with previous results, the transient decay is observed to be much faster for the Schottky structure OSCs (1:3 and 1:7 ClInPc:C_{60} OSCs) compared to the standard BHJ structure OSC (1:1 ClInPc:C_{60}). The fast transient response is due to the generally superior charge transport properties of C_{60} compared to the m-Pc donor, especially in mixed layers, as established in previous chapters.[184, 209] Given the general improvement in charge transport for films with high C_{60} content, the sweep-out of free carriers is improved and so the transient response is faster. A second factor impacting the transient response is the potentially higher rate of recombination within the acceptor-rich material, especially in the Schottky architecture where isolated donor domains may form to strongly hinder hole transport. Therefore, the increased rate of recombination due to the presence of trapped holes deep within the mixed layer may also further hasten the transient photocurrent response (discussed in greater detail in **Chapter 6**).[210]

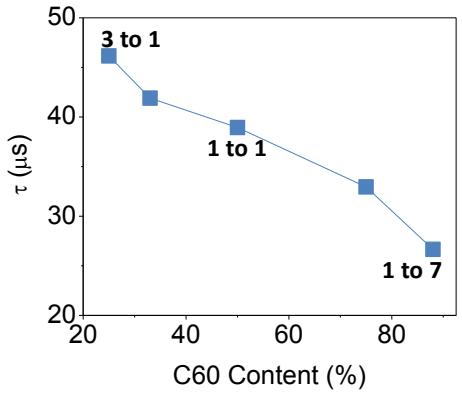

Figure 10-9 - Transient photocurrent decay τ values for ClInPc:C_{60} OSCs at various mixing ratios.

It is now interesting to examine the variations in transient photocurrent under the same three stability stress conditions presented above, where ClInPc:C_{60} OSCs are in one case kept in the dark, in another case kept in the dark while heated, and in the final case illuminated. The extracted τ values

(normalized to their initial values) for both Schottky structure (1:7 ClInPc:C_{60}) and standard BHJ structure (1:1 ClInPc:C_{60}) OSCs are shown in Figure 10-10. For the Schottky OSCs (Figure 10-10.A), it is clear that simply storing the devices has no effect on the transient photocurrent. Heating the OSCs results in a ~20% reduced τ (i.e. a faster device), with 15% of the reduction in τ occurring in the first 7 days, and an additional 5% occurring more gradually over the next 21 days. From the EQE and AFM measurements in Section 10.2.2, it was suggested that heat-stress may result in morphological changes within the mixed layer, potentially resulting in further separation of donor and acceptor phases within the Schottky device architecture. Such a morphological change would also result in further phase separation and thus produce more isolated donor domains, especially for mixed films with very high C_{60} concentrations. This would consequently increase recombination within the device and thus make the transient photoresponse faster (as is observed presently). These changes in the transient photocurrent, however, are not strong enough to cause an observable variation in the FF.

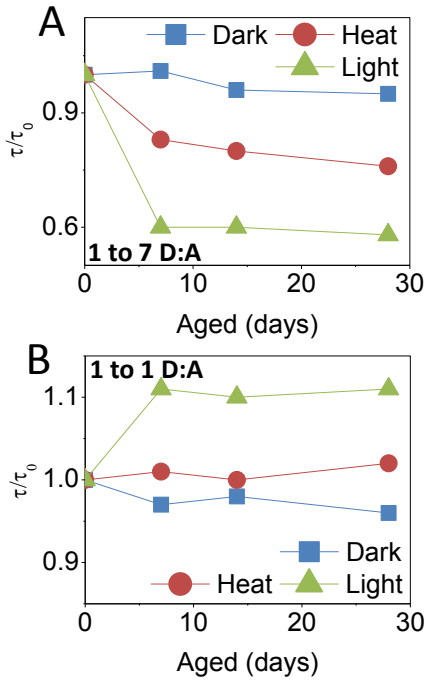

Figure 10-10 - Variations in transient photocurrent decay τ values (normalized) for (A) Schottky and (B) standard BHJ ClInPc:C_{60} OSCs under no stress (dark), heat-stress (40 ^{o}C) and light-stress (1-sun intensity light) conditions over 28 days in N_2.

In contrast, light exposure results in an even more significant 40% reduction in τ, with the full change occurring rapidly in the first 7 days of the light-stress experiment, and the faster response maintained for the remainder of the light-stress experiment. Combined with the slight reduction in FF as well as the fall in EQE near ~450 nm, this decrease in τ is suggested to be due to an increased rate of recombination within the device essentially due to trap formation. The photo-degradation occurs quickly, suggesting that the trap state formation occurs quickly and eventually saturates, where any photo-susceptible species are affected in the initial stages of illumination. Tong et al. noted that the number of traps in a neat C_{60} film after exposure to light similarly saturates, thus resulting in a burn-in loss,[283] and so the degradation observed in the present experiment is again strongly implied to be due to exciton-induced degradation of C_{60}.

For the standard BHJ structure OSCs (Figure 10-10.B), both the devices stored in the dark and the heated devices show virtually no changes in their transient photocurrent τ values. Only the light-stressed devices show variations, with ~10% larger τ values post-illumination (occurring within the first 7 days). This is the exact opposite trend as observed with the Schottky structure OSC. The increased τ value is believed to be associated with contact issues, potentially due to degradation of the interfacial extraction layers, which result in poorer sweep-out of free carriers. This stipulation follows from the observations regarding the reduction to V_{oc} with light stress, noted in Section 10.2.2. The reduced electric field and the associated hindrance to free carrier sweep-out also coincide well with the overall reduction in EQE observed for the light-aged standard BHJ OSCs, also noted in Section 10.2.2. Such a degradation mechanism, however, would affect both the standard BHJ structure as well as the Schottky structure OSC, although perhaps affecting the latter less strongly due to its larger internal electric field and extensive band bending. Rather, it is likely that the exciton-induced degradation of C_{60} dominates the transient photoresponse in the Schottky OSC. To support this stipulation, it is observed that for the

1:3 ClInPc:C_{60} OSC, which is a Schottky structure OSC, but with comparatively much more donor content, the effects are more balanced – the τ value changes only by 4%.

Based on these results, it is established that the transient photocurrent decay characteristics vary throughout the lifetime of OSCs, and furthermore, that these variations depend on the donor:acceptor mixing ratio. As a consequence, it is found that the light-induced changes in the transient photo-response depend strongly on the device architecture. The observed changes provide hints regarding sweep-out and recombination. To this end, OSCs at all mixing ratios have a susceptibility to organic-electrode contact degradation that can decrease V_{oc}, hinder sweep-out and slow the transient photoresponse. From the J_{sc} values and EQE data of Schottky versus standard BHJ OSCs, the extensive band bending within Schottky OSCs are suggested to make them slightly more resilient to the reduced internal electric field associated with interfacial degradation phenomena. It was further demonstrated that, while the Schottky architecture is responsible for some of the highest efficiency vacuum-deposited SM-OSCs, the very high C_{60} concentrations in this device structure make it susceptible to exciton-induced degradation of C_{60}. Fortuitously, with the presence of a small amount of donor within the mixed layer (to decrease the C_{60} exciton lifetime), the photovoltaic output parameters of Schottky OSCs are affected only slightly during light exposure stability experiments. As such, this device structure remains a strong competitor for highly efficient, stable and cost-effective OSCs.

10.3. Conclusions

In this chapter, ClInPc:C_{60} OSCs were examined for their photo- and thermal stability in an inert N_2 environment over a 28-day period, with a particular focus on comparing the acceptor-rich Schottky structure to the standard BHJ structure. By strongly varying the photo-active layer while keeping the interfaces the same, this work therefore helped to ascertain the relative impact of bulk versus interfacial

degradation, especially in consideration of the results from **Chapter 8** and **Chapter 9.** The major conclusions from this chapter are as follows:

- Light stress results in 10-15% losses in PCE, largely due to interfacial degradation. Photo-induced losses in V_{oc} can also be observed as reduced sweep-out in transient photocurrent experiments. This degradation occurs in spite of the use of relatively well-established interfacial layers, indicating that long-term stability in OSCs requires further research and development of interfacial extraction layers.
- Schottky OSCs are slightly more resilient to variations in J_{sc} compared to the standard (1:1 donor:acceptor) BHJ structure, but they suffer more strongly from losses in FF. Transient photocurrent measurements indicate that the losses in FF are due to increased recombination, likely due to photo-induced degradation of C_{60} and the associated increase in trap density.
- The choice of device architecture is shown to have an impact on photo-degradation mechanisms, and so it can have implications on overall OSC photo-stability.

Chapter Eleven:

Concluding Remarks and Future Research

11.1. Conclusions

The research described throughout this thesis serves to elucidate charge collection processes and limitations in modern OSCs, and offers insights regarding the changes in photovoltaic performance throughout the lifetime of OSCs. To this end, the factors affecting charge collection were studied in terms of both the organic-electrode interface (interfacial phenomena) as well as the distribution of donor and acceptor within the photo-active layers (bulk phenomena). This thesis established that interfacial charge collection processes are absolutely critical when considering the photo-stability and lifetime of the OSCs, and as such, organic-electrode interfacial degradation is the most significant avenue to reduced OSC performance when the devices are photo-aged in inert atmosphere. This interfacial degradation is independent of the OSC fabrication methodology – both solution-coated and vacuum-deposited OSCs require careful selection of interfacial layers to prevent photo-degradation. Bulk and structure-dependent degradation phenomena generally pale in comparison, and are therefore not as critical for addressing immediate OSC stability concerns.

The time-zero performance of OSCs was found to be less dependent on the choice of interfacial layer, as long as a suitable material was chosen from the wide number of available materials. Instead, the time-zero performance is highly dependent on the orientation/mixing of the photo-active layers. All relevant combinations of neat and mixed donor/acceptor layers were examined, and it was found that the fullerene-based Schottky OSC with an additional neat C_{60} layer offered the highest device performance. This research thus helps to explain why this device structure has achieved such high efficiencies in literature in recent years. The ternary OSC structure was also examined to understand its charge transport properties in light of the optoelectronic properties of its comprising donor materials. While this structure has some promise in offering large J_{sc} values by generating photocurrent across the entire visible spectrum, its practical implementation requires the use of designer donor molecules with well-matched HOMO values, identical mobilities and, furthermore, very high mobilities even in a mixed film. Further highlights and key conclusions drawn from this work are discussed below.

Interfacial extraction layers are known to be critical for achieving high initial performance (t=0) OSCs; however, the role and requirements for viable interfacial layers are not straightforward, particularly with SM-OSCs. SM-OSCs are more prone to metal deposition-induced defect states that cause undue charge recombination and therefore hinder device performance. This fact was stressed in **Chapter 9**, where it was shown that traditional HELs and EELs in P-OSCs could not be employed in SM-OSCs to achieve equivalent performance improvements, which was hinted to be related to the inherently rough surface morphologies of vacuum-deposited small molecule films (as compared to spin-coated polymer films). In SM-OSCs, many organic electronic materials can satisfy the EEL requirements, as discussed in **Chapter 5** (e.g. BCP, Alq_3, TPBi, NPB, etc.), and the differences in performance can be largely attributed to their propensity for forming metal deposition-induced defect states. In inverted SM-OSCs, both NPB/MoO_3 and pure MoO_3 were found to be suitable HELs, but only when they are made very thick (similarly, to prevent metal damage to the photo-active layer).

Considering the photo-active layers within the OSC, methodical experiments on OSCs with varied device architectures (**Chapter 6**) demonstrated that the BHJ/acceptor OSC is ideal for high efficiency SM-OSCs. This structure benefits strongly from the fullerene-based MoO_3/C_{60} Schottky interface, and is the principal structure employed for the high PCE SM-OSCs in recent literature. The BHJ/acceptor structure optimizes the trade-off between charge generation and charge collection, with band bending effects used to minimize charge trapping/recombination. High J_{sc} values are maintained by maximizing photocurrent contributions from the fullerene aggregates (usually requiring at least 75% fullerene content in the mixed layer). Other structures regularly employed in literature, such as the donor/BHJ/acceptor structure, suffer from hole accumulation and subsequent space charge effects that hinder free carrier sweep-out. These conclusions highlight a fundamental difference between vacuum-deposited SM-OSCs and P-OSCs: in SM-OSCs, many standard donor materials show poor hole mobilities that can strongly limit a researcher's choice in device structure. As a consequence, high PCE SM-OSCs usually rely more strongly on fullerene for both its charge transport and photocurrent generation capabilities (the latter point more critically with the use of C_{70} instead of C_{60}). Further improvement in vacuum-deposited SM-OSCs necessitates the synthesis of new small molecule donors with very high hole mobilities, and a capacity to retain high mobility values in mixed films.

Charge transport and charge extraction are further complicated in ternary OSCs, with the addition of a third component in the mixed BHJ layer, as discussed in **Chapter 7**. Vacuum-deposited ternary SM-OSCs were shown to be capable of producing photocurrent from three photo-active species (specifically two m-PC donors with C_{60}). However, ternary SM-OSCs are highly sensitive to any energy level offsets of their comprising materials. A slight offset in the HOMO values of the donors results in significant charge blocking and charge accumulation effects, and thus strongly hinders charge transport (manifested as reduced FF and J_{sc}). With intelligent molecular design to achieve matched energy

levels/mobility values, ternary OSCs may provide an avenue to simple and cost-effective OSCs that can allow for broad and intense photocurrents.

To understand how charge collection processes in OSCs vary with time, systematic and highly controlled device aging studies were conducted on P3HT:PCBM P-OSCs in **Chapter 8**. To this end, P-OSCs were shown to be strongly susceptible to photo-induced organic-electrode interfacial degradation even in an inert environment. XPS measurements verified that changes at the organic-electrode interface were photo-chemical in nature, related to a reduction in organic-metal bond density. The use of interfacial layers can largely suppress contact photo-degradation and thus enhance OSC photo-stability. To this end, for P3HT:PCBM P-OSCs, MoO_3 and Liacac were identified to bolster photo-stability. Further studies in **Chapter 8** demonstrated that both solution-coated P-OSCs and vacuum-deposited SM-OSCs suffer from contact photo-degradation. The data suggest that it is not merely the existence of the organic-electrode interface in OSCs that leads to photo-unstable devices, but rather the direct contact between the photo-active layer and the electrode. It is suggested that the presence of excitons at the organic-electrode interface is therefore the root cause behind contact photo-degradation. Reducing the exciton concentration at the organic-electrode interface can be accomplished with interfacial layers that effectively quench excitons (such as MoO_3), or that physically block excitons from the organic-electrode interface (such as with wide bandgap interfacial layers, like BCP). The organic-electrode interfacial degradation was therefore highlighted as the major degradation phenomenon in OSCs exposed to light in inert atmosphere. As such, minimizing the short-term contact photo-degradation with the development of new HEL and EEL materials can grant the opportunity to address other degradation mechanisms (e.g. bulk or structure-dependent degradation) that may occur over a larger timescale.

By employing relatively efficient and stable interfacial layers (MoO_3/…/BCP), SM-OSC photo-stability was studied as a function of device structure in **Chapter 10**, specifically comparing standard BHJ OSCs to Schottky OSCs. While these OSCs still exhibited some organic-electrode degradation to cause a photo-induced reduction in V_{oc}, slight differences in performance related to the bulk/photo-active layer were observed. To this end, Schottky OSCs were found to be slightly more resilient to variations in J_{sc} compared to the standard (1:1 donor:acceptor) BHJ structure, but they suffered more strongly from losses in FF. Transient photocurrent measurements indicated that the losses in FF were due to increased recombination, likely due to photo-induced degradation of C_{60} and the associated increase in trap density. This particular degradation phenomenon therefore affects Schottky OSCs more strongly, and may be relevant for very long-term photo-stability experiments, albeit once the HELs and EELs are further optimized such that organic-electrode interfacial degradation does not dominate device stability.

11.2. Future Research

The studies described throughout this thesis and summarized in Section 11.1 have laid the groundwork for future research on highly efficient and stable OSCs. Perhaps more critically, the research in this thesis serves to bridge the gap in research between SM-OSCs and P-OSCs, which occurred with the strong shift in focus from SM-OSCs to P-OSCs within the OSC research community since 2005. With a strong understanding of the fundamental limitations in OSC charge collection, both initially (t=0) and throughout the OSC lifetime, there are a number of interesting research studies that may be pursued. Some particularly relevant studies are described throughout this section.

The charge collection studies through **Chapters 4** to **7** employed vacuum deposition to form simple, highly mixed layers in SM-OSCs, granting a reasonably straightforward view of OSC device physics. In this regard, co-deposition of organic molecules yields heavily inter-mixed films with minimal phase separation. However, this is also a limiting factor for the overall performance in SM-OSCs. P-

OSCs benefit greatly from optimized phase separation with domain sizes on the same scale as the corresponding exciton diffusion lengths. Nano-crystalline donor polymers further offer substantially improved hole transport properties. With the baseline performance in standard OSCs now well established from results in **Chapters 4** to **6**, it becomes interesting to explore post-processing effects that can enhance mixed layer morphologies. Strategies such as thermal annealing have been used previously for high performance OSCs in literature.[27] Remarkably, there are only a few scattered reports in literature that discuss thermal annealing on vacuum-deposited SM-OSCs.[249, 288, 289] More rigorous studies on the impact of post-processing techniques, including thermal annealing and solvent annealing, are natural extensions to this thesis, and would further help fill in the gap in knowledge between SM-OSCs and P-OSCs. With a better understanding of post-processing techniques, these studies could also be extended to ternary OSCs.

The bulk of research in this thesis focused on m-Pc donors and fullerene acceptors, in order to simplify cross comparisons from study to study. m-Pcs are furthermore historically studied for use in OSCs, so they have wide impact in the field in general. However, in **Chapter 6**, it was established that the poor hole mobilities of donors is a limiting factor in device performance for SM-OSCs, and thus a force that dictates the optimal device architecture. In light of the robust understanding of the charge collection processes in modern OSCs established throughout this work, it is worthwhile to examine new donor molecules specifically engineered for high hole mobilities. Furthermore, for high PCE SM-OSCs, it is necessary to obtain small molecules that can maintain reasonable mobilities while mixed with fullerene acceptors – with donor content as low as 25% if the Schottky device structure is to be used. In a similar vein, the next step in vacuum-deposited ternary SM-OSCs is the use of new donor and acceptor materials with ideal HOMO/LUMO values to minimize charge accumulation and recombination effects.

The conclusions on photo-stability and the factors affecting charge collection with time in **Chapters 8** through **10** offer more straightforward suggestions for future research. To obtain photo-stable OSCs, it is critically necessary to research and develop more robust interfacial extraction layers. The research in this thesis established photo-degradation of the organic-electrode interface to be the most significant factor in OSC stability in inert atmosphere. While interfacial layers improve photo-stability, many interfacial layers are prone to their own degradation phenomena that ultimately hinder charge collection. For example, while BCP, Liacac and LiF are good EELs for performance and photo-stability, they also exhibit some small degree of thermal instability. MoO_3, the widely used HEL replacement to PEDOT:PSS, has recently been shown to suffer from UV-induced photo-induced degradation.[290] This latter point highlights the final recommendation of this thesis, which is to more comprehensively study photo-degradation phenomena for OSCs as a function of the spectra of the light used in photo-aging (and in consideration of interfacial layers). The photo-stability studies in this thesis use a halogen lamp at 1-sun intensity, which includes a small component of UV. Alarmingly, there are many contrasting reports on OSC photo-stability in literature. It is believed that the source of this ambiguity stems from the spectra of the lamps, especially in regard to their proportion of UV and their match to the absorption properties of the OSCs. By developing interfacial layers that are stable in both AM1.5 light as well as high UV conditions, it may be possible to obtain OSCs that do not require additional UV filters, thus allowing for significant reductions in OSC module fabrication costs. Furthermore, with the development of more stable and more robust interfacial layers, it is feasible to study more subtle degradation phenomena.

References

[1] Heliatek. (July 24, 2012, Accessed: December 17, 2014). *HeliaTek Sets New World Record Efficiency of 10.7% for its Organic Solar Cell*. Available: http://www.heliatek.com/newscenter/latest_news/heliatek-erzielt-mit-107-effizienz-neuen-weltrekord-fur-seine-organische-tandemzelle/?lang=en

[2] Mitsubishi Chemical. (2011, Accessed: December 17, 2014). *Progress Report 1: Solution-Processable Organic Photovoltaic (OPV) Modules*. Available: http://www.m-kagaku.co.jp/english/r_td/strategy/technology/topics/opv/index.html

[3] L. Doua, J. Youa, C. C. Chena, G. Lia,Y. Yanga, "Plastic Solar Cells: Breaking the 10% Commercialization Barrier," in *SPIE Organic Photovoltaics XIII*, 2012, p. 847702.

[4] N. Grossiord, J. M. Kroon, R. Andriessen,P. W. M. Blom, *Org. Electron.,* **2011,** *13*, 432.

[5] M. Hermenau, M. Riede, K. Leo, S. A. Gevorgyan, F. C. Krebs,K. Norrman, *Sol. Energy Mater. Sol. Cells,* **2011,** *95*, 1268.

[6] M. Wang, F. Xie, J. Du, Q. Tang, S. Zheng, Q. Miao, J. Chen, N. Zhao,J. Xu, *Sol. Energy Mater. Sol. Cells,* **2011,** *95*, 3303.

[7] M. Jorgensen, K. Norrman,F. C. Krebs, *Sol. Energy Mater. Sol. Cells,* **2008,** *92*, 686.

[8] M. O. Reese, A. J. Morfa, M. S. White, N. Kopidakis, S. E. Shaheen, G. Rumbles,D. S. Ginley, *Sol. Energy Mater. Sol. Cells,* **2008,** *92*, 746.

[9] Y. Kanai, T. Matsushima,H. Murata, *Thin Solid Films,* **2009,** *518*, 537.

[10] K. Kawano,C. Adachi, *Appl. Phys. Lett.,* **2010,** *96*, 053307.

[11] E. Voroshazi, B. Verreet, T. Aernouts,P. Heremans, *Sol. Energy Mater. Sol. Cells,* **2011,** *95*, 1303.

[12] Q. Wang, G. Williams,H. Aziz, *Org. Electron.,* **2012,** *13*, 2075.

[13] Q. Wang, G. Williams, T. Tsui,H. Aziz, *J. Appl. Phys.,* **2012,** *112*, 064502.

[14] S. Bertho, G. Janssen, T. J. Cleij, B. Conings, W. Moons, A. Gadisa, J. D'Haen, E. Goovaerts, L. Lutsen,J. Manca, *Sol. Energy Mater. Sol. Cells,* **2008,** *92*, 753.

[15] G. Williams, Q. Wang,H. Aziz, *Adv. Funct. Mater.,* **2012,** *23*, 2239.

[16] C. Tang, *Appl. Phys. Lett.,* **1986,** *48*, 183.

[17] A. Mishra,P. Bäuerle, *Angewandte Chemie International Edition,* **2012,** *51*, 2020.

[18] M. T. Lloyd, J. E. Anthony,G. G. Malliaras, *Mater. Today,* **2007,** *10*, 34.

[19] B. Walker, C. Kim,T. Q. Nguyen, *Chem. Mat.,* **2011,** *23*, 470.

[20] E. Bundgaard,F. C. Krebs, *Sol. Energy Mater. Sol. Cells,* **2007,** *91*, 954.

[21] C. J. Brabec, S. Gowrisanker, J. J. M. Halls, D. Laird, S. J. Jia,S. P. Williams, *Adv. Mater.,* **2010,** *22*, 3839.

[22] G. Dennler, M. Scharber, T. Ameri, P. Denk, K. Forberich, C. Waldauf,C. Brabec, *Adv. Mater.,* **2008,** *20*, 579.

[23] M. T. Dang, L. Hirsch,G. Wantz, *Adv. Mater.,* **2011,** *23*, 3597.

[24] P. Peumans, A. Yakimov,S. Forrest, *J. Appl. Phys.,* **2003,** *93*, 3693.

[25] B. Maennig, J. Drechsel, D. Gebeyehu, P. Simon, F. Kozlowski, A. Werner, F. Li, S. Grundmann, S. Sonntag, M. Koch, K. Leo, M. Pfeiffer, H. Hoppe, D. Meissner, N. S. Sariciftci, I. Riedel, V. Dyakonov,J. Parisi, *Appl. Phys. A-Mater. Sci. Process.,* **2004,** *79*, 1.

[26] J. Xue, B. P. Rand, S. Uchida,S. R. Forrest, *J. Appl. Phys.,* **2005,** *98*, 124903.

[27] M. Riede, C. Uhrich, J. Widmer, R. Timmreck, D. Wynands, G. Schwartz, W. M. Gnehr, D. Hildebrandt, A. Weiss, J. Hwang, S. Sundarraj, P. Erk, M. Pfeiffer,K. Leo, *Adv. Funct. Mater.,* **2011,** *21*, 3019.
[28] M. Reyes-Reyes, K. Kim,D. L. Carroll, *Appl. Phys. Lett.,* **2005,** *87*, 083506.
[29] G. Li, V. Shrotriya, J. S. Huang, Y. Yao, T. Moriarty, K. Emery,Y. Yang, *Nat. Mater.,* **2005,** *4*, 864.
[30] W. L. Ma, C. Y. Yang, X. Gong, K. Lee,A. J. Heeger, *Adv. Funct. Mater.,* **2005,** *15*, 1617.
[31] C. Tao, S. P. Ruan, X. D. Zhang, G. H. Xie, L. Shen, X. Z. Kong, W. Dong, C. X. Liu,W. Y. Chen, *Appl. Phys. Lett.,* **2008,** *93*, 193307.
[32] M. O. Reese, M. S. White, G. Rumbles, D. S. Ginley,S. E. Shaheen, *Appl. Phys. Lett.,* **2008,** *92*, 053307.
[33] H. H. Liao, L. M. Chen, Z. Xu, G. Li,Y. Yang, *Appl. Phys. Lett.,* **2008,** *92*, 173303
[34] G. Li, C. W. Chu, V. Shrotriya, J. Huang,Y. Yang, *Appl. Phys. Lett.,* **2006,** *88*, 253503
[35] S. J. Yoon, J. H. Park, H. K. Lee,O. O. Park, *Appl. Phys. Lett.,* **2008,** *92*, 143504
[36] A. Hayakawa, O. Yoshikawa, T. Fujieda, K. Uehara,S. Yoshikawa, *Appl. Phys. Lett.,* **2007,** *90*, 163517.
[37] N. Sekine, C. H. Chou, W. L. Kwan,Y. Yang, *Org. Electron.,* **2009,** *10*, 1473.
[38] M. S. White, D. C. Olson, S. E. Shaheen, N. Kopidakis,D. S. Ginley, *Appl. Phys. Lett.,* **2006,** *89*, 143517
[39] H. Gommans, B. Verreet, B. P. Rand, R. Muller, J. Poortmans, P. Heremans,J. Genoe, *Adv. Funct. Mater.,* **2008,** *18*, 3686.
[40] M. Vogel, S. Doka, C. Breyer, M. C. Lux-Steiner,K. Fostiropoulos, *Appl. Phys. Lett.,* **2006,** *89*, 163501.
[41] H. Wu, Q. Song, M. Wang, F. Li, H. Yang, Y. Wu, C. Huang, X. Ding,X. Hou, *Thin Solid Films,* **2007,** *515*, 8050.
[42] M. Zhang, H. Wang, H. Tian, Y. Geng,C. Tang, *Adv. Mater.,* **2011,** *23*, 4960.
[43] S. R. Forrest, *MRS bulletin,* **2005,** *30*, 28.
[44] L. A. A. Pettersson, L. S. Roman,O. Inganäs, *J. Appl. Phys.,* **1999,** *86*, 487.
[45] D. W. Sievers, V. Shrotriya,Y. Yang, *J. Appl. Phys.,* **2006,** *100*, 114509.
[46] P. Van Hal, R. Janssen, G. Lanzani, G. Cerullo, M. Zavelani-Rossi,S. De Silvestri, *Chem. Phys. Lett.,* **2001,** *345*, 33.
[47] M. Muntwiler, Q. Yang, W. A. Tisdale,X. Y. Zhu, *Physical review letters,* **2008,** *101*, 196403.
[48] R. A. Street,M. Schoendorf, *Physical Review B,* **2010,** *81*, 205307.
[49] K. Tvingstedt, K. Vandewal, F. Zhang,O. Inganäs, *The Journal of Physical Chemistry C,* **2010,** *114*, 21824.
[50] V. I. Arkhipov, P. Heremans,H. Bassler, *Appl. Phys. Lett.,* **2003,** *82*, 4605.
[51] R. A. Street, S. Cowan,A. J. Heeger, *Physical Review B,* **2010,** *82*, 121301.
[52] S. Gélinas, O. Paré-Labrosse, C. N. Brosseau, S. Albert-Seifried, C. R. McNeill, K. R. Kirov, I. A. Howard, R. Leonelli, R. H. Friend,C. Silva, *The Journal of Physical Chemistry C,* **2011,** *115*, 7114.
[53] D. Veldman, T. Offermans, J. Sweelssen, M. M. Koetse, S. C. J. Meskers,R. A. J. Janssen, *Thin Solid Films,* **2006,** *511*, 333.
[54] D. Veldman, S. C. J. Meskers,R. A. J. Janssen, *Adv. Funct. Mater.,* **2009,** *19*, 1939.

[55] M. Lenes, M. Morana, C. J. Brabec,P. W. M. Blom, *Adv. Funct. Mater.,* **2009,** *19*, 1106.
[56] K. Tvingstedt, K. Vandewal, A. Gadisa, F. Zhang, J. Manca,O. Inganas, *J. Am. Chem. Soc.,* **2009,** *131*, 11819.
[57] D. Veldman, O. İpek, S. C. J. Meskers, J. Sweelssen, M. M. Koetse, S. C. Veenstra, J. M. Kroon, S. S. Bavel, J. Loos,R. A. J. Janssen, *J. Am. Chem. Soc.,* **2008,** *130*, 7721.
[58] K. Vandewal, K. Tvingstedt, A. Gadisa, O. Inganäs,J. V. Manca, *Nat. Mater.,* **2009,** *8*, 904.
[59] J. Wang, X. Ren, S. Shi, C. Leung,P. K. L. Chan, *Org. Electron.,* **2011,** *12*, 880.
[60] A. Wagenpfahl, D. Rauh, M. Binder, C. Deibel,V. Dyakonov, *Physical Review B,* **2010,** *82*, 115306.
[61] L. Koster, V. Mihailetchi,P. Blom, *Appl. Phys. Lett.,* **2006,** *88*, 052104.
[62] J. R. Tumbleston, Y. Liu, E. T. Samulski,R. Lopez, *Adv. Energy Mater.,* **2012,** *2*, 477.
[63] G. F. A. Dibb, T. Kirchartz, D. Credgington, J. R. Durrant,J. Nelson, *The Journal of Physical Chemistry Letters,* **2011,** *2*, 2407.
[64] C. Shuttle, R. Hamilton, B. O'Regan, J. Nelson,J. Durrant, *Proceedings of the National Academy of Sciences,* **2010,** *107*, 16448.
[65] A. Maurano, R. Hamilton, C. G. Shuttle, A. M. Ballantyne, J. Nelson, B. O'Regan, W. Zhang, I. McCulloch, H. Azimi,M. Morana, *Adv. Mater.,* **2010,** *22*, 4987.
[66] I. Hwang, C. R. McNeill,N. C. Greenham, *J. Appl. Phys.,* **2009,** *106*, 094506.
[67] Y. Zhang, X. D. Dang, C. Kim,T. Q. Nguyen, *Adv. Energy Mater.,* **2011,** *1*, 610.
[68] X. Xiao, K. J. Bergemann, J. D. Zimmerman, K. Lee,S. R. Forrest, *Adv. Energy Mater.,* **2014,** *4*, 1301557.
[69] X. Xiao, J. D. Zimmerman, B. E. Lassiter, K. J. Bergemann,S. R. Forrest, *Appl. Phys. Lett.,* **2013,** *102*, 073302.
[70] Y. Zou, J. Holst, Y. Zhang,R. J. Holmes, *Journal of Materials Chemistry A,* **2014,** *2*, 12397.
[71] M. Zhang, H. Ding, Y. Gao,C. Tang, *Appl. Phys. Lett.,* **2010,** *96*, 183301.
[72] S. Sutty, G. Williams,H. Aziz, *Org. Electron.,* **2013,** *14*, 2392.
[73] S. Sutty, G. Williams,H. Aziz, *Journal of Photonics for Energy,* **2014,** *40999*, 1.
[74] P. C. Dastoor, C. R. McNeill, H. Frohne, C. J. Foster, B. Dean, C. J. Fell, W. J. Belcher, W. M. Canipbell, D. L. Officer, I. M. Blake, P. Thordarson, M. J. Crossley, N. S. Hush,J. R. Reimers, *J. Phys. Chem. C,* **2007,** *111*, 15415.
[75] D. Gupta, D. Kabra, N. Kolishetti, S. Ramakrishnan,K. S. Narayan, *Adv. Funct. Mater.,* **2007,** *17*, 226.
[76] J. Peet, A. B. Tamayo, X. D. Dang, J. H. Seo,T. Q. Nguyena, *Appl. Phys. Lett.,* **2008,** *93*, 163306.
[77] E. M. J. Johansson, A. Yartsev, H. Rensmo,V. Sundstrom, *J. Phys. Chem. C,* **2009,** *113*, 3014.
[78] S. Honda, H. Ohkita, H. Benten,S. Ito, *Chem. Commun.,* **2010,** *46*, 6596.
[79] M. Koppe, H. J. Egelhaaf, G. Dennler, M. C. Scharber, C. J. Brabec, P. Schilinsky,C. N. Hoth, *Adv. Funct. Mater.,* **2010,** *20*, 338.
[80] Z. X. Xu, V. A. L. Roy, K. H. Low,C. M. Che, *Chem. Commun.,* **2011,** *47*, 9654.
[81] H. Yan, D. Li, Y. Zhang, Y. Yang,Z. Wei, *The Journal of Physical Chemistry C,* **2014,** *118*, 10552.
[82] B. Lim, J. T. Bloking, A. Ponec, M. D. McGehee,A. Sellinger, *ACS Appl. Mater. Interfaces,* **2014,** *6*, 6905.

[83] L. Lu, T. Xu, W. Chen, E. S. Landry,L. Yu, *Nat Photon,* **2014,** *8*, 716.
[84] L. Ye, H. Xu, H. Yu, W. Xu, H. Li, H. Wang, N. Zhao,J. Xu, *The Journal of Physical Chemistry C,* **2014,** *118*, 20094.
[85] Y. J. Cheng, C. H. Hsieh, P. J. Li,C. S. Hsu, *Adv. Funct. Mater.,* **2011,** *21*, 1723.
[86] H. Kim, M. Shin,Y. Kim, *J. Phys. Chem. C,* **2009,** *113*, 1620.
[87] P. P. Khlyabich, B. Burkhart,B. C. Thompson, *J. Am. Chem. Soc.,* **2011,** *133*, 14534.
[88] Y. Kim, S. Cook, S. A. Choulis, J. Nelson, J. R. Durrant,D. D. C. Bradley, *Synth. Met.,* **2005,** *152*, 105.
[89] R. A. Street, D. Davies, P. P. Khlyabich, B. Burkhart,B. C. Thompson, *J. Am. Chem. Soc.,* **2013,** *135*, 986.
[90] S. Sista, Y. Yao, Y. Yang, M. L. Tang,Z. Bao, *Appl. Phys. Lett.,* **2007,** *91*, 223508.
[91] C. W. Schlenker, V. S. Barlier, S. W. Chin, M. T. Whited, R. E. McAnally, S. R. Forrest,M. E. Thompson, *Chem. Mat.,* **2011,** *23*, 4132.
[92] Z. Hong, R. Lessmann, B. Maennig, Q. Huang, K. Harada, M. Riede,K. Leo, *J. Appl. Phys.,* **2009,** *106*, 064511.
[93] M. Ichikawa, E. Suto, H. G. Jeon,Y. Taniguchi, *Org. Electron.,* **2010,** *11*, 700.
[94] O. L. Griffith,S. R. Forrest, *Nano Lett.,* **2014,** *14*, 2353.
[95] K. Cnops, B. P. Rand, D. Cheyns, B. Verreet, M. A. Empl,P. Heremans, *Nature communications,* **2014,** *5*, 3406.
[96] F. C. Krebs, *Stability and degradation of organic and polymer solar cells*: Wiley Online Library, 2012.
[97] K. Kawano, R. Pacios, D. Poplavskyy, J. Nelson, D. D. C. Bradley,J. R. Durrant, *Sol. Energy Mater. Sol. Cells,* **2006,** *90*, 3520.
[98] K. Norrman,F. C. Krebs, *Sol. Energy Mater. Sol. Cells,* **2006,** *90*, 213.
[99] S. A. Gevorgyan, M. V. Madsen, H. F. Dam, M. Jørgensen, C. J. Fell, K. F. Anderson, B. C. Duck, A. Mescheloff, E. A. Katz,A. Elschner, *Sol. Energy Mater. Sol. Cells,* **2013,** *116*, 187.
[100] H. Klumbies, M. Karl, M. Hermenau, R. Rösch, M. Seeland, H. Hoppe, L. Müller-Meskamp,K. Leo, *Sol. Energy Mater. Sol. Cells,* **2014,** *120*, 685.
[101] M. Jørgensen, K. Norrman, S. A. Gevorgyan, T. Tromholt, B. Andreasen,F. C. Krebs, *Adv. Mater.,* **2012,** *24*, 580.
[102] A. Turak, *RSC Advances,* **2013,** *3*, 6188.
[103] B. Andreasen, D. M. Tanenbaum, M. Hermenau, E. Voroshazi, M. T. Lloyd, Y. Galagan, B. Zimmernann, S. Kudret, W. Maes,L. Lutsen, *Physical Chemistry Chemical Physics,* **2012,** *14*, 11780.
[104] R. Rösch, D. M. Tanenbaum, M. Jørgensen, M. Seeland, M. Bärenklau, M. Hermenau, E. Voroshazi, M. T. Lloyd, Y. Galagan,B. Zimmermann, *Energy & Environmental Science,* **2012,** *5*, 6521.
[105] D. M. Tanenbaum, M. Hermenau, E. Voroshazi, M. T. Lloyd, Y. Galagan, B. Zimmermann, M. Hösel, H. F. Dam, M. Jørgensen,S. A. Gevorgyan, *RSC Advances,* **2012,** *2*, 882.
[106] G. Teran-Escobar, D. Tanenbaum, E. Voroshazid, M. Hermenau, K. Norrman, M. T. Lloyd, Y. Galagan, B. Zimmermann, M. Hösel,H. F. Dam, *Physical Chemistry Chemical Physics,* **2012,** *14*, 11824.
[107] A. Rivaton, S. Chambon, M. Manceau, J.-L. Gardette, N. Lemaître,S. Guillerez, *Polymer Degradation and Stability,* **2010,** *95*, 278.

[108] V. Turkovic, S. Engmann, D. A. Egbe, M. Himmerlich, S. Krischok, G. Gobsch,H. Hoppe, *Sol. Energy Mater. Sol. Cells,* **2014,** *120*, 654.
[109] G. Williams,H. Aziz, *Org. Electron.,* **2013,** *15*, 47.
[110] H. Aziz, Z. Popovic, C. P. Tripp, N. X. Hu, A. M. Hor,G. Xu, *Appl. Phys. Lett.,* **1998,** *72*, 2642.
[111] H. Aziz, Z. Popovic, S. Xie, A. M. Hor, N. X. Hu, C. Tripp,G. Xu, *Appl. Phys. Lett.,* **1998,** *72*, 756.
[112] F. C. Krebs, J. E. Carle, N. Cruys-Bagger, M. Andersen, M. R. Lilliedal, M. A. Hammond,S. Hvidt, *Sol. Energy Mater. Sol. Cells,* **2005,** *86*, 499.
[113] F. Zhang, X. Xu, W. Tang, J. Zhang, Z. Zhuo, J. Wang, Z. Xu,Y. Wang, *Sol. Energy Mater. Sol. Cells,* **2011,** *95*, 1785.
[114] S. K. Hau, H. L. Yip, N. S. Baek, J. Zou, K. OMalley,A. K. Y. Jen, *Appl. Phys. Lett.,* **2008,** *92*, 253301.
[115] C. Y. Li, T. C. Wen, T. H. Lee, T. F. Guo, Y. C. Lin,Y. J. Hsu, *J. Mater. Chem.,* **2009,** *19*, 1643.
[116] M. T. Greiner,Z.-H. Lu, *NPG Asia Materials,* **2013,** *5*, e55.
[117] H.-L. Yip,A. K.-Y. Jen, *Energy & Environmental Science,* **2012,** *5*, 5994.
[118] J. H. Park, T. W. Lee, B. D. Chin, D. H. Wang,O. O. Park, *Macromol. Rapid Commun.,* **2010,** *31*, 2095.
[119] R. Steim, F. R. Kogler,C. J. Brabec, *J. Mater. Chem.,* **2010,** *20*, 2499.
[120] C. Cabanetos, A. El Labban, J. A. Bartelt, J. D. Douglas, W. R. Mateker, J. M. J. Fréchet, M. D. McGehee,P. M. Beaujuge, *J. Am. Chem. Soc.,* **2013,** *135*, 4656.
[121] K. Li, Z. Li, K. Feng, X. Xu, L. Wang,Q. Peng, *J. Am. Chem. Soc.,* **2013,** *135*, 13549.
[122] T. L. Nguyen, H. Choi, S.-J. Ko, M. A. Uddin, B. Walker, S. Yum, J.-E. Jeong, M. H. Yun, T. Shin, S. Hwang, J. Y. Kim,H. Y. Woo, *Energy & Environmental Science,* **2014,** *7*, 3040.
[123] S.-H. Liao, H.-J. Jhuo, P.-N. Yeh, Y.-S. Cheng, Y.-L. Li, Y.-H. Lee, S. Sharma,S.-A. Chen, *Sci. Rep.,* **2014,** *4*.
[124] C. Liu, C. Yi, K. Wang, Y. Yang, R. S. Bhatta, M. Tsige, S. Xiao,X. Gong, *ACS Appl. Mater. Interfaces,* **2015**.
[125] Y. Lin, Y. Li,X. Zhan, *Chemical Society Reviews,* **2012,** *41*, 4245.
[126] J. E. Coughlin, Z. B. Henson, G. C. Welch,G. C. Bazan, *Accounts of chemical research,* **2013,** *47*, 257.
[127] Y. J. Cheng, S. H. Yang,C. S. Hsu, *Chemical reviews,* **2009,** *109*, 5868.
[128] S. Günes, H. Neugebauer,N. Sariciftci, *Chem. Rev,* **2007,** *107*, 1324.
[129] B. Walker, A. B. Tomayo, X. D. Dang, P. Zalar, J. H. Seo, A. Garcia, M. Tantiwiwat,T. Q. Nguyen, *Adv. Funct. Mater.,* **2009,** *19*, 3063.
[130] Y. Sun, G. C. Welch, W. L. Leong, C. J. Takacs, G. C. Bazan,A. J. Heeger, *Nat. Mater.,* **2011,** *11*, 44.
[131] Y.-H. Chen, L.-Y. Lin, C.-W. Lu, F. Lin, Z.-Y. Huang, H.-W. Lin, P.-H. Wang, Y.-H. Liu, K.-T. Wong,J. Wen, *J. Am. Chem. Soc.,* **2012,** *134*, 13616.
[132] Z. Wang, D. Yokoyama, X.-F. Wang, Z. Hong, Y. Yang,J. Kido, *Energy & Environmental Science,* **2013,** *6*, 249.
[133] R. Pandey, Y. L. Zou,R. J. Holmes, *Appl. Phys. Lett.,* **2012,** *101*, 033308.

[134] L. Derue, O. Dautel, A. Tournebize, M. Drees, H. Pan, S. Berthumeyrie, B. Pavageau, E. Cloutet, S. Chambon, L. Hirsch, A. Rivaton, P. Hudhomme, A. Facchetti,G. Wantz, *Adv. Mater.,* **2014,** *26*, 5831.
[135] L. Chen, X. Li,Y. Chen, *Polymer Chemistry,* **2013,** *4*, 5637.
[136] H. Waters, J. Kettle, S.-W. Chang, C.-J. Su, W.-R. Wu, U.-S. Jeng, Y.-C. Tsai,M. Horie, *Journal of Materials Chemistry A,* **2013,** *1*, 7370.
[137] K. Yuan, F. Li, L. Chen,Y. Chen, *Thin Solid Films,* **2012,** *520*, 6299.
[138] L. Y. Lin, Y. H. Chen, Z. Y. Huang, H. W. Lin, S. H. Chou, F. Lin, C. W. Chen, Y. H. Liu,K. T. Wong, *J. Am. Chem. Soc.,* **2011,** *133*, 15822.
[139] R. R. Søndergaard, N. Espinosa, M. Jørgensen,F. C. Krebs, *Energy & Environmental Science,* **2014,** *7*, 1006.
[140] F. C. Krebs, N. Espinosa, M. Hösel, R. R. Søndergaard,M. Jørgensen, *Adv. Mater.,* **2014,** *26*, 29.
[141] N. L. Beaumont, J. S. Castrucci, P. Sullivan, G. E. Morse, A. S. Paton, Z.-H. Lu, T. P. Bender,T. S. Jones, *The Journal of Physical Chemistry C,* **2014,** *118*, 14813.
[142] W. Li, W. Roelofs, M. Turbiez, M. M. Wienk,R. A. Janssen, *Adv. Mater.,* **2014,** *26*, 3304.
[143] D. Mori, H. Benten, I. Okada, H. Ohkita,S. Ito, *Energy & Environmental Science,* **2014,** *7*, 2939.
[144] B. Verreet, K. Cnops, D. Cheyns, P. Heremans, A. Stesmans, G. Zango, C. G. Claessens, T. Torres,B. P. Rand, *Adv. Energy Mater.,* **2014,** *4*, 1301413.
[145] P. Maillard, S. Gaspard, P. Krausz,C. Giannotti, *Journal of Organometallic Chemistry,* **1981,** *212*, 185.
[146] T. Ohno, S. Kato,N. N. Lichtin, *Bulletin of the Chemical Society of Japan,* **1982,** *55*, 2753.
[147] H. Ohtani, T. Kobayashi, T. Ohno, S. Kato, T. Tanno,A. Yamada, *The Journal of Physical Chemistry,* **1984,** *88*, 4431.
[148] J. Morenzin, C. Schlebusch, B. Kessler,W. Eberhardt, *Phys. Chem. Chem. Phys.,* **1999,** *1*, 1765.
[149] M. E. El-Khouly, O. Ito, P. M. Smith,F. D'Souza, *Journal of Photochemistry and Photobiology C: Photochemistry Reviews,* **2004,** *5*, 79.
[150] S. Uchida, J. G. Xue, B. P. Rand,S. R. Forrest, *Appl. Phys. Lett.,* **2004,** *84*, 4218.
[151] J. G. Xue, B. P. Rand, S. Uchida,S. R. Forrest, *Adv. Mater.,* **2005,** *17*, 66.
[152] D. Gebeyehu, B. Maennig, J. Drechsel, K. Leo,M. Pfeiffer, *Sol. Energy Mater. Sol. Cells,* **2003,** *79*, 81.
[153] J. Drechsel, B. Mannig, D. Gebeyehu, M. Pfeiffer, K. Leo,H. Hoppe, *Org. Electron.,* **2004,** *5*, 175.
[154] J. Drechsel, B. Mannig, F. Kozlowski, M. Pfeiffer, K. Leo,H. Hoppe, *Appl. Phys. Lett.,* **2005,** *86*, 244102.
[155] R. Pandey, A. A. Gunawan, K. A. Mkhoyan,R. J. Holmes, *Adv. Funct. Mater.,* **2012,** *22*, 617.
[156] R. F. Bailey-Salzman, B. P. Rand,S. R. Forrest, *Appl. Phys. Lett.,* **2007,** *91*, 013508.
[157] R. R. Lunt,V. Bulovic, *Appl. Phys. Lett.,* **2011,** *98*, 113305.
[158] D. Y. Kim, F. So,Y. Gao, *Sol. Energy Mater. Sol. Cells,* **2009,** *93*, 1688.
[159] B. Verreet, R. Müller, B. P. Rand, K. Vasseur,P. Heremans, *Org. Electron.,* **2011,** *12*, 2131.

[160] S. Sutty, G. Williams,H. Aziz, "New insights into charge extraction and formation of the band-bending region in Schottky junction organic solar cells," in *SPIE Organic Photovoltaics XIV*, 2013, p. 88300.
[161] A. P. Yuen, S. M. Jovanovic, A. M. Hor, R. A. Klenkler, G. A. Devenyi, R. O. Loutfy,J. S. Preston, *Solar Energy,* **2012,** *86*, 1683.
[162] B. Yang, F. Guo, Y. Yuan, Z. Xiao, Y. Lu, Q. Dong,J. Huang, *Adv. Mater.,* **2012,** *25*, 572.
[163] G. Williams,H. Aziz, "Insights into electron and hole extraction layers for upright and inverted vacuum-deposited small molecule organic solar cells," in *SPIE Organic Photovoltaics XIV*, 2013, p. 88301.
[164] G. Chen, H. Sasabe, Z. Wang, X. Wang, Z. Hong, J. Kido,Y. Yang, *Physical Chemistry Chemical Physics,* **2012,** *14*, 14661.
[165] Y.-q. Zheng, W. J. Potscavage Jr, T. Komino,C. Adachi, *Appl. Phys. Lett.,* **2013,** *102*, 153302.
[166] D. S. Weiss, *Organic photoreceptors for xerography* vol. 59: CRC Press, 1998.
[167] S. Shaheen, G. Jabbour, M. Morrell, Y. Kawabe, B. Kippelen, N. Peyghambarian, M.-F. Nabor, R. Schlaf, E. Mash,N. Armstrong, *J. Appl. Phys.,* **1998,** *84*, 2324.
[168] Z. Wu, H. Yang, Y. Duan, W. Xie, S. Liu,Y. Zhao, *Semicond. Sci. Technol.,* **2003,** *18*, 49.
[169] K. L. Mutolo, E. I. Mayo, B. P. Rand, S. R. Forrest,M. E. Thompson, *J. Am. Chem. Soc.,* **2006,** *128*, 8108.
[170] T. Heidel, D. Hochbaum, J. Sussman, V. Singh, M. Bahlke, I. Hiromi, J. Lee,M. Baldo, *J. Appl. Phys.,* **2011,** *109*, 104502.
[171] W. Wang, D. Placencia,N. R. Armstrong, *Org. Electron.,* **2011,** *12*, 383.
[172] M. Islam, M. Fukugauchi, N. Morii, H. Uegaito, S. Nishigaki,M. Takeuchi, "Improvement of photovoltaic properties in inorganic organic pigment particle heterojunction solar cell," in *2nd International Conference on the Developments in Renewable Energy Technology (ICDRET)*, 2012, pp. 1.
[173] D. R. Kearns,M. Calvin, *The Journal of Chemical Physics,* **1961,** *34*, 2026.
[174] M. Pope, *The Journal of Chemical Physics,* **1962,** *36*, 2810.
[175] W. D. Cheng, D. S. Wu, H. Zhang,J. T. Chen, *Physical Review B,* **2001,** *64*, 125109.
[176] M.-S. Liao,S. Scheiner, *The Journal of Chemical Physics,* **2001,** *114*, 9780.
[177] M.-S. Liao,S. Scheiner, *Journal of Computational Chemistry,* **2002,** *23*, 1391.
[178] C. C. Chen, L. Dou, R. Zhu, C. H. Chung, T. B. Song, Y. B. Zheng, S. Hawks, G. Li, P. S. Weiss,Y. Yang, *ACS Nano,* **2012,** *6*, 7185.
[179] N. C. Nicolaidis, B. S. Routley, J. L. Holdsworth, W. J. Belcher, X. Zhou,P. C. Dastoor, *The Journal of Physical Chemistry C,* **2011,** *115*, 7801.
[180] M. M. Wienk, J. M. Kroon, W. J. H. Verhees, J. Knol, J. C. Hummelen, P. A. van Hal,R. A. J. Janssen, *Angewandte Chemie International Edition,* **2003,** *42*, 3371.
[181] A. A. Bakulin, J. C. Hummelen, M. S. Pshenichnikov,P. H. Van Loosdrecht, *Adv. Funct. Mater.,* **2010,** *20*, 1653.
[182] M. Scharber, D. Mühlbacher, M. Koppe, P. Denk, C. Waldauf, A. Heeger,C. Brabec, *Adv. Mater.,* **2006,** *18*, 789.
[183] A. Wilke, J. Endres, U. Hormann, J. Niederhausen, R. Schlesinger, J. Frisch, P. Amsalem, J. Wagner, M. Gruber,A. Opitz, *Appl. Phys. Lett.,* **2012,** *101*, 233301.
[184] B. P. Rand, J. Xue, S. Uchida,S. R. Forrest, *J. Appl. Phys.,* **2005,** *98*, 124902.

[185] J. Gantz, D. Placencia, A. Giordano, S. R. Marder,N. R. Armstrong, *The Journal of Physical Chemistry C,* **2013,** *117*, 1205.
[186] R. Po, C. Carbonera, A. Bernardi,N. Camaioni, *Energy Environ. Sci.,* **2010,** *4*, 285.
[187] C. J. Brabec, S. E. Shaheen, C. Winder, N. S. Sariciftci,P. Denk, *Appl. Phys. Lett.,* **2002,** *80*, 1288.
[188] E. Voroshazi, B. Verreet, A. Buri, R. Müller, D. Di Nuzzo,P. Heremans, *Org. Electron.,* **2011,** *12*, 736.
[189] Q. Wang,H. Aziz, *Org. Electron.,* **2011,** *12*, 1571.
[190] Q. Wang,H. Aziz, *Org. Electron.,* **2013,** *14*, 3030.
[191] G. Williams,H. Aziz, *Sol. Energy Mater. Sol. Cells,* **2014,** *128*, 320.
[192] J. Huang, J. Yu, H. Lin,Y. Jiang, *J. Appl. Phys.,* **2009,** *105*, 073105.
[193] F. C. Chen,S. C. Chien, *J. Mater. Chem.,* **2009,** *19*, 6865.
[194] Z. R. Hong, Z. H. Huang,X. T. Zeng, *Chem. Phys. Lett.,* **2006,** *425*, 62.
[195] V. Tripathi, D. Datta, G. S. Samal, A. Awasthi,S. Kumar, *J. Non-Cryst. Solids,* **2008,** *354*, 2901.
[196] N. Wang, J. Yu, Y. Zang, J. Huang,Y. Jiang, *Sol. Energy Mater. Sol. Cells,* **2010,** *94*, 263.
[197] J. Yu, N. Wang, Y. Zang,Y. Jiang, *Sol. Energy Mater. Sol. Cells,* **2011,** *95*, 664.
[198] Y. Li, M. K. Fung, Z. Xie, S. T. Lee, L. S. Hung,J. Shi, *Adv. Mater.,* **2002,** *14*, 1317.
[199] S.-W. Liu,J.-K. Wang, "Charge mobility of mixed organic semiconductors: a NPB-AlQ3 study," in *SPIE Organic Light Emitting Materials and Devices X*, 2006, p. 63331R.
[200] C.-C. Lee, W.-C. Su, J.-C. Huang, C.-F. Lin,S.-W. Liu, *Journal of Photonics for Energy,* **2011,** *1*, 011108.
[201] Q. Song, F. Li, H. Yang, H. Wu, X. Wang, W. Zhou, J. Zhao, X. Ding, C. Huang,X. Hou, *Chem. Phys. Lett.,* **2005,** *416*, 42.
[202] J. Liu, S. Shao, G. Fang, B. Meng, Z. Xie,L. Wang, *Adv. Mater.,* **2012,** *24*, 2774.
[203] C. Wang, I. Irfan, X. Liu,Y. Gao, *Journal of Vacuum Science &Technology B,* **2014,** *32*, 040801.
[204] I. Irfan, A. J. Turinske, Z. Bao,Y. Gao, *Appl. Phys. Lett.,* **2012,** *101*, 093305.
[205] J. J. Jasieniak, J. Seifter, J. Jo, T. Mates,A. J. Heeger, *Adv. Funct. Mater.,* **2012,** *22*, 2594.
[206] B. J. Tremolet de Villers, R. C. MacKenzie, J. J. Jasieniak, N. D. Treat,M. L. Chabinyc, *Adv. Energy Mater.,* **2013,** *4*, 1.
[207] K. Zilberberg, H. Gharbi, A. Behrendt, S. Trost,T. Riedl, *ACS Appl. Mater. Interfaces,* **2012,** *4*, 1164.
[208] C. Girotto, E. Voroshazi, D. Cheyns, P. Heremans,B. P. Rand, *ACS Appl. Mater. Interfaces,* **2011,** *3*, 3244.
[209] G. Williams, S. Sutty, R. Klenkler,H. Aziz, *Sol. Energy Mater. Sol. Cells,* **2014,** *124*, 217.
[210] G. Williams, S. Sutty,H. Aziz, *Physical Chemistry Chemical Physics,* **2014,** *16*, 11398.
[211] S. Braun, W. R. Salaneck,M. Fahlman, *Adv. Mater.,* **2009,** *21*, 1450.
[212] M. Anwar, C. Hogarth,R. Bulpett, *J. Mater. Sci.,* **1989,** *24*, 3087.
[213] J. G. Xue, S. Uchida, B. P. Rand,S. R. Forrest, *Appl. Phys. Lett.,* **2004,** *85*, 5757.
[214] Y. Lin, L. Ma, Y. Li, Y. Liu, D. Zhu,X. Zhan, *Adv. Energy Mater.,* **2014,** *4*, 1300626.
[215] W. Tress, S. Corvers, K. Leo,M. Riede, *Adv. Energy Mater.,* **2013,** *3*, 873.
[216] Z. Li, F. Gao, N. C. Greenham,C. R. McNeill, *Adv. Funct. Mater.,* **2011,** *21*, 1419.
[217] P. Chen, J. Huang, Z. Xiong,F. Li, *Org. Electron.,* **2012,** *14*, 621.

[218] M. Riede, T. Mueller, W. Tress, R. Schueppel,K. Leo, *Nanotechnology,* **2008,** *19*, 424001.
[219] J. Halls, C. Walsh, N. Greenham, E. Marseglia, R. Friend, S. Moratti,A. Holmes, *Nature,* **1995,** *376*, 498.
[220] G. Yu,A. Heeger, *J. Appl. Phys.,* **1995,** *78*, 4510.
[221] G. Yu, J. Gao, J. Hummelen, F. Wudl,A. Heeger, *Science,* **1995,** *270*, 1789.
[222] R. M. Pinto, *The Journal of Physical Chemistry C,* **2014,** *118*, 2287.
[223] R. Lessmann, Z. Hong, S. Scholz, B. Maennig, M. Riede,K. Leo, *Org. Electron.,* **2010,** *11*, 539.
[224] Y. Zang, J. Yu, J. Huang, R. Jiang,G. Huang, *Journal of Physics D: Applied Physics,* **2012,** *45*, 175101.
[225] S. Kazaoui, R. Ross,N. Minami, *Physical Review B,* **1995,** *52*, R11665.
[226] A. Sanchez-Diaz, L. Burtone, M. Riede,E. Palomares, *J. Phys. Chem. C,* **2012,** *116*, 16384.
[227] R. Pandey,R. J. Holmes, *Adv. Mater.,* **2010,** *22*, 5301.
[228] S. Pfuetzner, J. Meiss, A. Petrich, M. Riede,K. Leo, *Appl. Phys. Lett.,* **2009,** *94*, 223307.
[229] Y. Yao, C. Shi, G. Li, V. Shrotriya, Q. Pei,Y. Yang, *Appl. Phys. Lett.,* **2006,** *89*, 153507.
[230] N. Beaumont, S. W. Cho, P. Sullivan, D. Newby, K. E. Smith,T. Jones, *Adv. Funct. Mater.,* **2012,** *22*, 561.
[231] R. Singh, E. Aulicio-Sarduy, Z. Kan, T. Ye, R. C. I. MacKenzie,P. E. Keivanidis, *Journal of Materials Chemistry A,* **2014,** *2*, 14348.
[232] D. Mori, H. Benten, I. Okada, H. Ohkita,S. Ito, *Adv. Energy Mater.,* **2014,** *4*, 1301006.
[233] Heliatek Press. (January 16, 2013, Accessed: December 17, 2014). *Heliatek consolidates its technology leadership by establishing a new world record for organic solar technology with a cell efficiency of 12%*. Available: http://www.heliatek.com/newscenter/latest_news/neuer-weltrekord-fur-organische-solarzellen-heliatek-behauptet-sich-mit-12-zelleffizienz-als-technologiefuhrer/?lang=en
[234] M. A. Green, K. Emery, Y. Hishikawa, W. Warta,E. D. Dunlop, *Progress in Photovoltaics: Research and Applications,* **2013,** *21*, 12.
[235] C.-C. Chen, W.-H. Chang, K. Yoshimura, K. Ohya, J. You, J. Gao, Z. Hong,Y. Yang, *Adv. Mater.,* **2014,** *26*, 5670.
[236] T. Ameri, P. Khoram, J. Min,C. J. Brabec, *Adv. Mater.,* **2013,** *25*, 4245.
[237] J. H. Huang, M. Velusamy, K. C. Ho, J. T. Lin,C. W. Chu, *J. Mater. Chem.,* **2010,** *20*, 2820.
[238] M. A. Ruderer, M. Hinterstocker,P. Muller-Buschbaum, *Synth. Met.,* **2011,** *161*, 2001.
[239] J. Lee, M. H. Yun, J. Kim, J. Y. Kim,C. Yang, *Macromol. Rapid Commun.,* **2012,** *33*, 140.
[240] I. Hwang, C. R. McNeill,N. C. Greenham, *Synth. Met.,* **2014,** *189*, 63.
[241] G. Chen, H. Sasabe, X.-F. Wang, Z. Hong,J. Kido, *Synth. Met.,* **2014,** *192*, 10.
[242] P. P. Khlyabich, A. E. Rudenko, R. A. Street,B. C. Thompson, *ACS Appl. Mater. Interfaces,* **2014,** *6*, 9913.
[243] P. Cheng, Y. Li,X. Zhan, *Energy & Environmental Science,* **2014,** *7*, 2005.
[244] X.-Y. Jiang, Z.-L. Zhang, W.-Q. Zhu,S.-H. Xu, *Displays,* **2006,** *27*, 161.
[245] Q. Wang, J. Ding, D. Ma, Y. Cheng, L. Wang, X. Jing,F. Wang, *Adv. Funct. Mater.,* **2009,** *19*, 84.
[246] U. Vongsaysy, B. Pavageau, G. Wantz, D. M. Bassani, L. Servant,H. Aziz, *Adv. Energy Mater.,* **2013,** *4*, 1300752.

[247] T. Salim, L. H. Wong, B. Bräuer, R. Kukreja, Y. L. Foo, Z. Bao,Y. M. Lam, *J. Mater. Chem.,* **2011,** *21*, 242.
[248] J. K. Lee, W. L. Ma, C. J. Brabec, J. Yuen, J. S. Moon, J. Y. Kim, K. Lee, G. C. Bazan,A. J. Heeger, *J. Am. Chem. Soc.,* **2008,** *130*, 3619.
[249] P. Peumans, S. Uchida,S. R. Forrest, *Nature,* **2003,** *425*, 158.
[250] P. Sullivan, S. Heutz, S. M. Schultes,T. S. Jones, *Appl. Phys. Lett.,* **2004,** *84*, 1210.
[251] H. Gommans, D. Cheyns, T. Aernouts, C. Girotto, J. Poortmans,P. Heremans, *Adv. Funct. Mater.,* **2007,** *17*, 2653.
[252] L. Zuo, J. Yao, H. Li,H. Chen, *Sol. Energy Mater. Sol. Cells,* **2014,** *122*, 88.
[253] H.-W. Lin, Y.-H. Chen, Z.-Y. Huang, C.-W. Chen, L.-Y. Lin, F. Lin,K.-T. Wong, *Org. Electron.,* **2012,** *13*, 1722.
[254] K. Cnops, B. P. Rand, D. Cheyns,P. Heremans, *Appl. Phys. Lett.,* **2012,** *101*, 143301.
[255] M. Ichikawa, D. Takekawa, H.-G. Jeon,G. D. Banoukepa, *Org. Electron.,* **2013,** *14*, 814.
[256] Z. K. Tan, K. Johnson, Y. Vaynzof, A. A. Bakulin, L. L. Chua, P. K. Ho,R. H. Friend, *Adv. Mater.,* **2013,** *25*, 4131.
[257] S. C. Chien, F. C. Chen, M. K. Chung,C. S. Hsu, *The Journal of Physical Chemistry C,* **2011,** *116*, 1354.
[258] B. Paci, A. Generosi, V. R. Albertini, P. Perfetti, R. de Bettignies, J. Leroy, M. Firon,C. Sentein, *Appl. Phys. Lett.,* **2006,** *89*, 043507.
[259] S. Schäfer, A. Petersen, T. A. Wagner, R. Kniprath, D. Lingenfelser, A. Zen, T. Kirchartz, B. Zimmermann, U. Würfel,X. Feng, *Physical Review B,* **2011,** *83*, 165311.
[260] Y. Kim, S. A. Choulis, J. Nelson, D. D. C. Bradley, S. Cook,J. R. Durrant, *Appl. Phys. Lett.,* **2005,** *86*, 063502
[261] G. Li, V. Shrotriya, Y. Yao,Y. Yang, *J. Appl. Phys.,* **2005,** *98*, 043704
[262] H. Kim, W. W. So,S. J. Moon, *Sol. Energy Mater. Sol. Cells,* **2007,** *91*, 581.
[263] K. Norrman, S. A. Gevorgyan,F. C. Krebs, *ACS Appl. Mater. Interfaces,* **2009,** *1*, 102.
[264] J. Kim, N. H. Kim, H. Kim, D. Jung,H. Chae, *J. Nanosci. Nanotechnol.,* **2011,** *11*, 6490.
[265] P. Dannetun, M. Boman, S. Stafström, W. Salaneck, R. Lazzaroni, C. Fredriksson, J. Brédas, R. Zamboni,C. Taliani, *The Journal of Chemical Physics,* **1993,** *99*, 664.
[266] R. Lazzaroni, J. L. Bredas, P. Dannetun, M. Logdlund, K. Uvdal,W. R. Salaneck, *Synth. Met.,* **1991,** *43*, 3323.
[267] M. G. Mason, C. W. Tang, L. S. Hung, P. Raychaudhuri, J. Madathil, D. J. Giesen, L. Yan, Q. T. Le, Y. Gao, S. T. Lee, L. S. Liao, L. F. Cheng, W. R. Salaneck, D. A. dos Santos,J. L. Bredas, *J. Appl. Phys.,* **2001,** *89*, 2756.
[268] Z. Xu, L. M. Chen, G. Yang, C. H. Huang, J. Hou, Y. Wu, G. Li, C. S. Hsu,Y. Yang, *Adv. Funct. Mater.,* **2009,** *19*, 1227.
[269] D. Y. Kondakov, J. R. Sandifer, C. W. Tang,R. H. Young, *J. Appl. Phys.,* **2003,** *93*, 1108.
[270] J. You, L. Dou, K. Yoshimura, T. Kato, K. Ohya, T. Moriarty, K. Emery, C.-C. Chen, J. Gao, G. Li,Y. Yang, *Nature communications,* **2013,** *4*, 1446.
[271] Y. Hashimoto,M. Hamagaki, *Electrical Engineering in Japan,* **2006,** *154*, 1.
[272] D. M. Han, J. H. Lee, K. H. Jeong,J. G. Lee, *Met. Mater.-Int.,* **2010,** *16*, 627.
[273] A. K. K. Kyaw, X. W. Sun, C. Y. Jiang, G. Q. Lo, D. W. Zhao,D. L. Kwong, *Appl. Phys. Lett.,* **2008,** *93*, 221107.
[274] V. Shrotriya, G. Li, Y. Yao, C. W. Chu,Y. Yang, *Appl. Phys. Lett.,* **2006,** *88*, 073508.

[275] N. M. Bamsey, A. P. Yuen, A. M. Hor, R. Klenkler, J. S. Preston,R. O. Loutfy, *Sol. Energy Mater. Sol. Cells,* **2011,** *95*, 2937.
[276] H. Ishii, K. Sugiyama, E. Ito,K. Seki, *Adv. Mater.,* **1999,** *11*, 605.
[277] E. L. Ratcliff, A. Garcia, S. A. Paniagua, S. R. Cowan, A. J. Giordano, D. S. Ginley, S. R. Marder, J. J. Berry,D. C. Olson, *Adv. Energy Mater.,* **2013,** *3*, 647.
[278] T. Xiao, F. Fungura, M. Cai, J. W. Anderegg, J. Shinar,R. Shinar, *Org. Electron.,* **2013,** *14*, 2555.
[279] K. Sugiyama, H. Ishii, Y. Ouchi,K. Seki, *J. Appl. Phys.,* **2000,** *87*, 295.
[280] Y.-q. Zheng, W. J. Potscavage Jr, Q.-s. Zhang, T. Komino, M. Taneda,C. Adachi, *Org. Electron.,* **2014,** *15*, 878.
[281] B. Dasgupta, W. P. Goh, Z. E. Ooi, L. M. Wong, C. Y. Jiang, Y. Ren, E. S. Tok, J. Pan, J. Zhang,S. Y. Chiam, *The Journal of Physical Chemistry C,* **2013,** *117*, 9206.
[282] K. H. Wong, K. Ananthanarayanan, J. Luther,P. Balaya, *The Journal of Physical Chemistry C,* **2012,** *116*, 16346.
[283] X. Tong, N. Wang, M. Slootsky, J. Yu,S. R. Forrest, *Sol. Energy Mater. Sol. Cells,* **2013,** *118*, 116.
[284] N. Wang, X. Tong, Q. Burlingame, J. Yu,S. R. Forrest, *Sol. Energy Mater. Sol. Cells,* **2014,** *125*, 170.
[285] R. Taylor, M. P. Barrow,T. Drewello, *Chem. Commun.,* **1998,** *22*, 2497.
[286] M. O. Reese, A. M. Nardes, B. L. Rupert, R. E. Larsen, D. C. Olson, M. T. Lloyd, S. E. Shaheen, D. S. Ginley, G. Rumbles,N. Kopidakis, *Adv. Funct. Mater.,* **2010,** *20*, 3476.
[287] T. M. Clarke, C. Lungenschmied, J. Peet, N. Drolet, K. Sunahara, A. Furube,A. J. Mozer, *Adv. Energy Mater.,* **2013,** *3*, 1473.
[288] S. M. Schultes, P. Sullivan, S. Heutz, B. M. Sanderson,T. S. Jones, *Materials Science and Engineering: C,* **2005,** *25*, 858.
[289] S. Yoo, W. J. Potscavage Jr, B. Domercq, S.-H. Han, T.-D. Li, S. C. Jones, R. Szoszkiewicz, D. Levi, E. Riedo, S. R. Marder,B. Kippelen, *Solid-State Electronics,* **2007,** *51*, 1367.
[290] H. Zhang, A. Borgschulte, F. A. Castro, R. Crockett, A. C. Gerecke, O. Deniz, J. Heier, S. Jenatsch, F. Nüesch, C. Sanchez-Sanchez, A. Zoladek-Lemanczyk,R. Hany, *Adv. Energy Mater.,* **2014**, 1400734.
[291] D. A. Chen, A. Nakahara, D. G. Wei, D. Nordlund,T. P. Russell, *Nano Lett.,* **2011,** *11*, 561.
[292] M. Campoy-Quiles, T. Ferenczi, T. Agostinelli, P. G. Etchegoin, Y. Kim, T. D. Anthopoulos, P. N. Stavrinou, D. D. C. Bradley,J. Nelson, *Nat. Mater.,* **2008,** *7*, 158.
[293] M. Seeland, R. Rosch,H. Hoppe, *J. Appl. Phys.,* **2011,** *109*, 064513.
[294] F. Shirland, *Advanced Energy Conversion,* **1966,** *6*, 201.
[295] Z. Ouennoughi,M. Chegaar, *Solid-State Electronics,* **1999,** *43*, 1985.
[296] N. Nehaoua, Y. Chergui,D. Mekki, *Vacuum,* **2009,** *84*, 326.
[297] M. Chegaar, G. Azzouzi,P. Mialhe, *Solid-State Electronics,* **2006,** *50*, 1234.
[298] K. Bouzidi, M. Chegaar,A. Bouhemadou, *Sol. Energy Mater. Sol. Cells,* **2007,** *91*, 1647.
[299] A. Jain,A. Kapoor, *Sol. Energy Mater. Sol. Cells,* **2005,** *85*, 391.
[300] A. Jain,A. Kapoor, *Sol. Energy Mater. Sol. Cells,* **2005,** *86*, 197.
[301] A. Kaminski, J. Marchand,A. Laugier, *Sol. Energy Mater. Sol. Cells,* **1998,** *51*, 221.
[302] P. Schilinsky, C. Waldauf, J. Hauch,C. J. Brabec, *J. Appl. Phys.,* **2004,** *95*, 2816.
[303] Z. Liu, C. Kwong, C. Cheung, A. Djurišić, Y. Chan,P. Chui, *Synth. Met.,* **2005,** *150*, 159.

[304] A. Djurisic, C. Kwong, T. Lau, W. Guo, E. Li, Z. Liu, H. Kwok, L. Lam,W. Chan, *Optics communications,* **2002,** *205*, 155.
[305] H. Hoppe, N. S. Sariciftci,D. Meissner, *Molecular Crystals and Liquid Crystals,* **2002,** *385*, 113.
[306] G. Dennler, K. Forberich, M. C. Scharber, C. J. Brabec, I. Tomis, K. Hingerl,T. Fromherz, *J. Appl. Phys.,* **2007,** *102*, 054516.
[307] Z. Liu, H. S. Kwok,A. Djurišić, *Journal of Physics D: Applied Physics,* **2004,** *37*, 678.

Appendices

Appendix 1:

Chapter-Specific Supplemental Information

1.1. Supplemental Information for Chapter Four: Renewed Interest for Metal Phthalocyanine Donors in Small Molecule Organic Solar Cells

In the main body of this chapter, EQE data for OSCs with four different m-Pc donors were provided, as these donors provided the most critical and pertinent information. Here the EQE data for all of the examined m-Pc donors are presented, including: H_2Pc (monovalent), CuPc (divalent), ZnPc (divalent), ClInPc (trivalent), ClAlPc (trivalent), ClGaPc (trivalent), TiOPc (tetravalent) and SubPc.

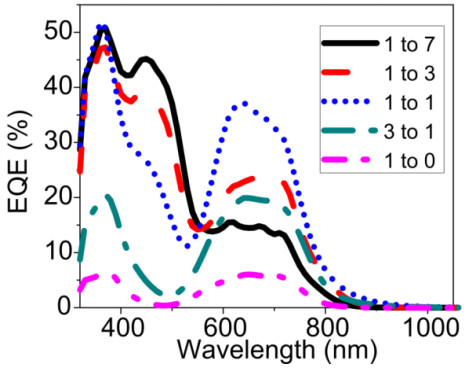

Supplemental Figure 1.1.1 - EQE curves for $H_2Pc:C_{60}$ OSCs at varying mixing ratios.

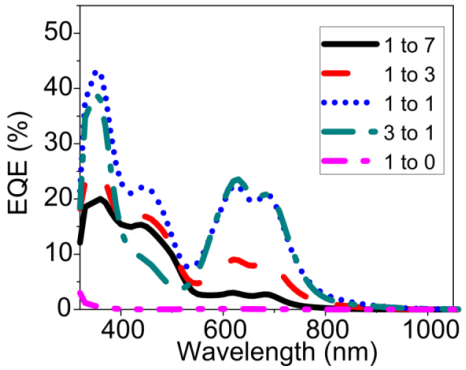

Supplemental Figure 1.1.2 - EQE curves for $CuPc:C_{60}$ OSCs at varying mixing ratios.

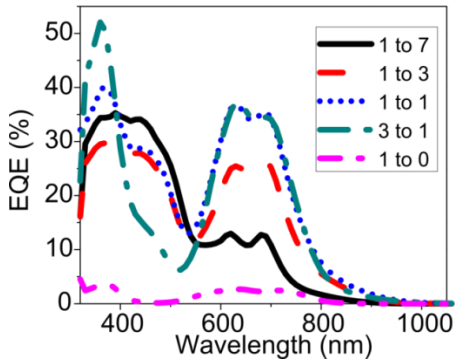

Supplemental Figure 1.1.3 - EQE Curves for ZnPc:C_{60} OSCs at varying mixing ratios.

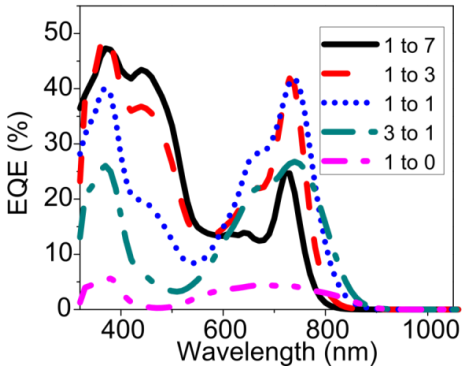

Supplemental Figure 1.1.4 - EQE Curves for ClInPc:C_{60} OSCs at varying mixing ratios.

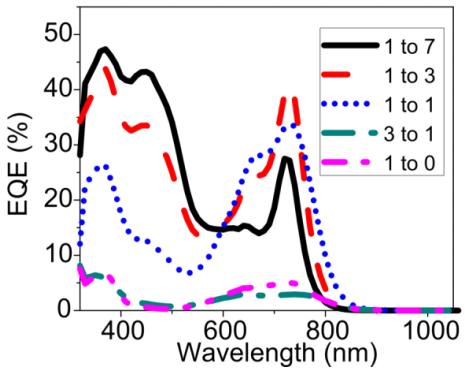

Supplemental Figure 1.1.5 - EQE Curves for ClAlPc:C_{60} OSCs at varying mixing ratios.

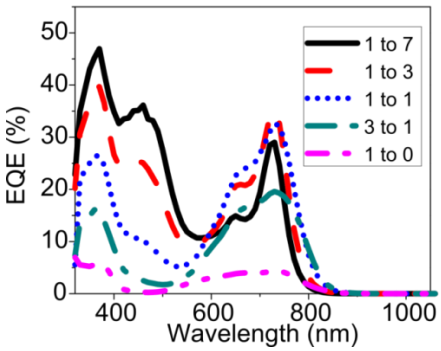

Supplemental Figure 1.1.6 - EQE Curves for ClGaPc:C_{60} OSCs at varying mixing ratios.

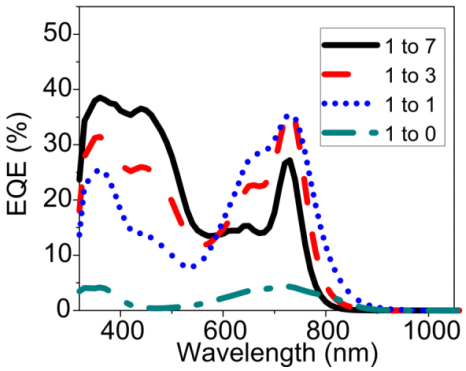

Supplemental Figure 1.1.7 - EQE Curves for TiOPc:C_{60} OSCs at varying mixing ratios.

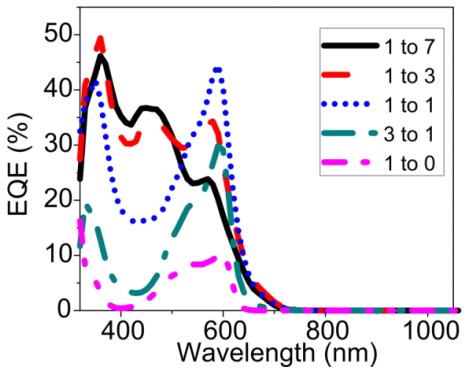

Supplemental Figure 1.1.8 - EQE Curves for SubPc:C_{60} OSCs at varying mixing ratios.

1.2. Supplemental Information for Chapter Six: Interplay between Efficiency and Device Architecture for Small Molecule Organic Solar Cells

Further Information on the EQE of PHJ OSCs with Increasing C_{60} Content

In the PHJ device architecture, increasing the C_{60} layer thickness (and thus decreasing the ClGaPc thickness) is accompanied by a broad increase in EQE from 530 nm to 720 nm. While this increase appears as a hypsochromatic shift of the 750-nm ClGaPc absorption, it is initially unclear how decreasing the ClGaPc content would result in such a drastic shift in peak absorption – such changes are not observed in the UV/Vis absorbance of neat films of ClGaPc. Instead, it is worthwhile to look toward the increasing C_{60} layer thickness. To this end, it has been established that the Frenkel exciton bandgap in fullerenes can be quite low in energy – on the order of 1.7 eV to 2.3 eV.[225] These low energy Frenkel excitons can be efficiently harvested when paired with a donor material at low donor concentrations.[162]

To study this effect in the present devices, it is necessary to decouple the EQE contributions from ClGaPc and C_{60}. Therefore, as a rough approach to visualize the low energy C_{60} Frenkel excitons, the 750 nm/664 nm ClGaPc peak/shoulder contributions were removed from the EQE spectra (using the ClGaPc absorption curve). Specifically, the UV/Vis absorption data were used to first identify the ClGaPc curve shape, which was normalized to the EQE values using its peak intensity. The curve was then subtracted directly from the EQE plot. The modified EQE spectra are shown in Supplemental Figure 1.2.1. These data show that the apparent shift in peak EQE is due to tail-end photocurrent contributions from C_{60} from low-energy Frenkel excitons. Consequently, the apparent shift in peak EQE is more substantial with increasing C_{60} layer thickness.

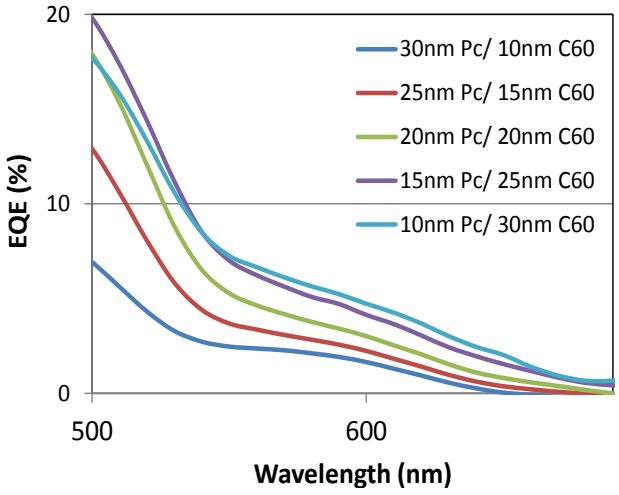

Supplemental Figure 1.2.1 - Modified EQE spectra of the PHJ ClGaPc/C_{60} OSC with varying layer thicknesses. m-Pc contributions have been subtracted using normalized UV/Vis data.

Further Information on Negative Photocurrent Transients in donor/BHJ/acceptor OSCs

A single exponential fit was performed on the negative photocurrent transient recoveries (using a bright blue LED pulse) for the donor/BHJ/acceptor devices, as per equation (6.1). The τ values extracted from this analysis are shown in Supplemental Figure 1.2.2 under the label 'SE – τ, bright,' where SE refers to a single exponential fit. This negative transient recovery occurs over a much longer timescale (hundreds of μs) than the simple transient photocurrent decay observed with dim white light (tens of μs). This is due to the slow injection of carriers from the electrodes to compensate for the accumulated charges within the device, especially compared to the fast sweep-out of free carriers in the donor/BHJ/acceptor under dim white light where space charge effects are not as severe.

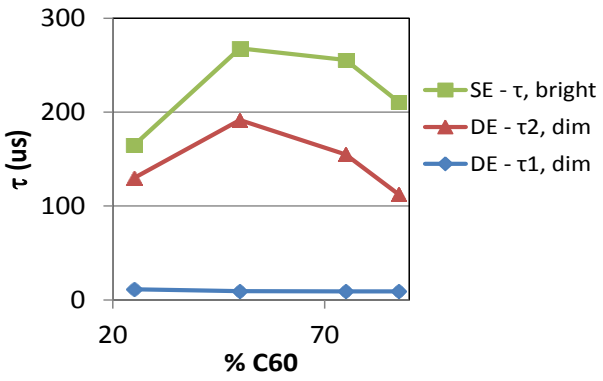

Supplemental Figure 1.2.2 - Single exponential fit (SE) and double exponential fit (DE) τ values for the transient photocurrent decays of donor/BHJ/acceptor ClGaPc:C_{60} OSCs.

Biexponential fits, as per equation (A1.2-1), on the basic photocurrent transient decay curves were also conducted (for the same devices illuminated with a dim white LED light pulse, i.e. those curves fitted previously with a single exponential term).

$$I = C_1 \cdot \exp(-C_2 t) + C_3 \cdot \exp(-C_4 t), \qquad C_2 = 1/\tau_1 \; ; \; C_4 = 1/\tau_2 \tag{A1.2-1}$$

In this case, the biexponential fit provides slightly better R2 values (generally >0.999 versus >0.9), indicating that the added exponential term allows for a more accurate representation of the data. The biexponential fitted τ_1 and τ_2 values for the donor/BHJ/acceptor devices with varying mixing concentrations are also shown in Supplemental Figure 1.2.2. The fast τ_1 component of the biexponential fit is relatively constant at ~10μs for all mixing concentrations. More significantly, from Supplemental Figure 1.2.2, the slow τ_2 component of the fit is found to have the same variations with mixing concentration and a similar timing as the τ values extracted for the negative transient recovery (when illuminated with the bright blue LED pulse). It is thus strongly implied that the slow component of the biexponential fit is related to a weak space charge effect, which is present even under dim white light. One may then conclude that, even with low light intensity, the donor/BHJ/acceptor structure is susceptible to charge accumulation and associated space charge effects. These space charge effects

become dominant with more intense light and, correspondingly, a higher exciton generation rate that leads to a larger number of charges within the photo-active layers. When the space charge effects become dominant and the photo-generated charges do not rapidly recombine, a negative photocurrent transient is observed.

Interestingly, while structures C and D (BHJ/acceptor and donor/BHJ respectively) did not show the negative photocurrent transients with bright red/blue LED pulses, their transient photocurrent decays were also successfully fit with a biexponential model (for dim white LED pulses). To this end, these structures' photocurrent decays showed slightly improved R2 values with biexponential fits, had non-zero pre-exponents (C_1 and C_3 in equation (A1.2-1)) and exhibited realistic τ_1 and τ_2 values (with a fast τ_1 and a slow τ_2 for each fit). However, when the biexponential fit was applied to the photocurrent decays of structures A and B (the PHJ and simple BHJ respectively), the second pre-exponential term always converged to zero, indicating that the single exponential model already adequately described the data. Having established the slow τ_2 value in the biexponential fit to be potentially related to space charge effects, it follows that structures C, D and E may all suffer from weak space charge effects. The commonality in these structures is the combination of a BHJ layer with a neat donor and/or acceptor layer, which is believed to be a contributor to these space charge effects, as discussed in the results and discussion of this chapter.

Additional Figures (JV Characteristics)

Representative JV curves for the different architecture OSCs (with varying C60 content), as described in the results and discussion of the chapter, are provided below. For the PHJ structure, C_{60} content is defined by the ratio of C_{60} layer thickness to total active layer thickness. For all other device structures, C_{60} content is defined as the amount of C_{60} within the mixed layer.

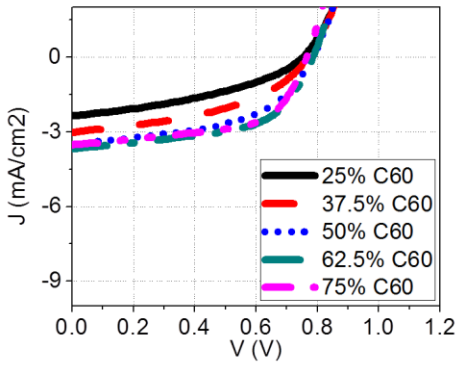

Supplemental Figure 1.2.3 - JV characteristics for ClGaPc/C_{60} PHJ OSCs (structure A) with varying C_{60} content.

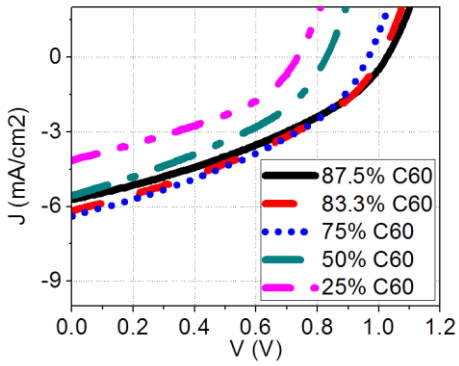

Supplemental Figure 1.2.4 - JV characteristics for ClGaPc:C_{60} BHJ OSCs (structure B) with varying C_{60} content.

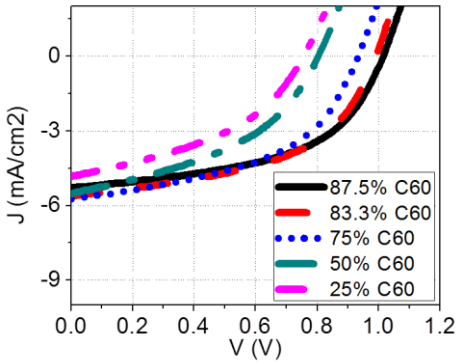

Supplemental Figure 1.2.5 - JV characteristics for BHJ/a ClGaPc:C_{60} OSCs (structure C) with varying C_{60} content.

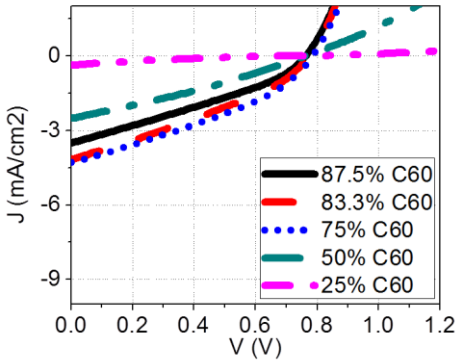

Supplemental Figure 1.2.6 - JV characteristics for d/BHJ ClGaPc:C_{60} OSCs (structure D) with varying C_{60} content.

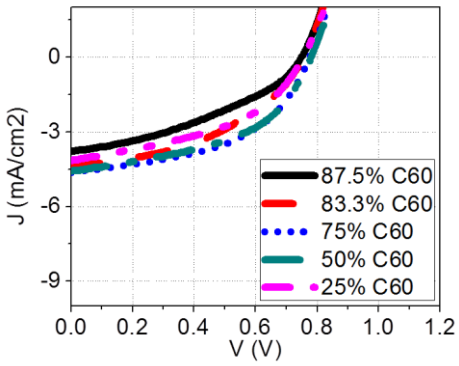

Supplemental Figure 1.2.7 - JV characteristics for d/BHJ/a ClGaPc:C_{60} OSCs (structure E) with varying C_{60} content.

1.3. Supplemental Information for Chapter Seven: Vacuum-Deposited Ternary Mixture Organic Solar Cells

In the body of this chapter, EQE mappings for ClInPc:SubPc:C_{60} ternary OSCs at the ClInPc Q band, the SubPc Q band and the C_{60} aggregate peak were provided. An additional peak in the UV, which comprises contributions from C_{60}, the ClInPc B band and the SubPc B band, can also be identified. The EQE mappings for this UV peak are shown in Supplementary Figure 1.3.1 below.

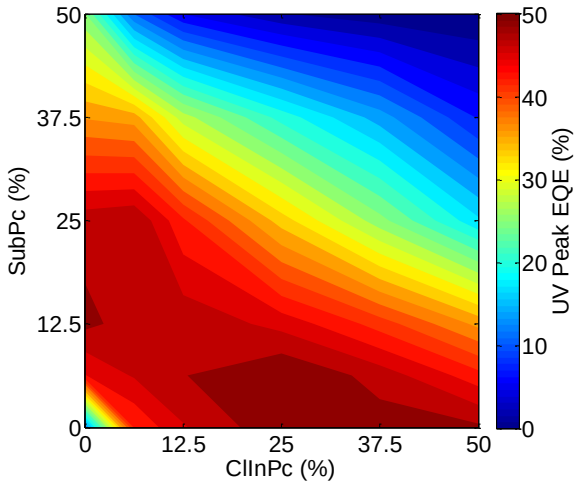

Supplementary Figure 1.3.1 – UV peak EQE spectra mapping of ternary ClInPc:SubPc:C_{60} OSCs (composition shown by x/y-axes, balance is C_{60}).

While discussing multiple donor PHJ OSCs, it was noted that ClInPc/SubPc/C_{60} OSCs show no contributions to photocurrent from ClInPc due to the wider bandgap of SubPc. This is clearly demonstrated in the EQE of these OSCs, as shown in Supplementary Figure 1.3.2 below.

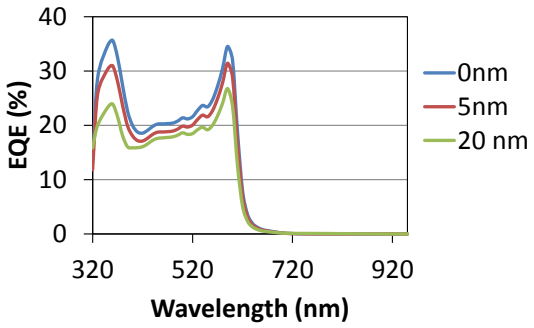

Supplementary Figure 1.3.2 - EQE spectra of ClInPc/SubPc/C_{60} OSCs with varying thickness ClInPc.

In the results and discussion section of this chapter, DTDCTB was mixed with ClInPc because of its similar HOMO energy level. The two materials were also noted for their overlapping absorption properties. The latter point is shown in Supplementary Figure 1.3.3 below.

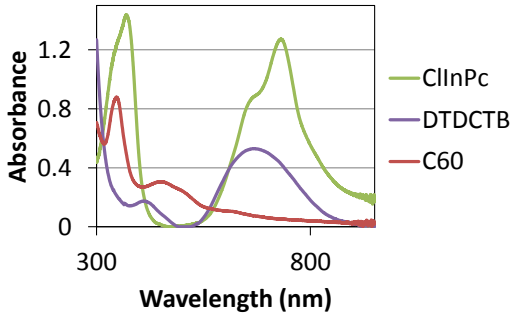

Supplementary Figure 1.3.3 - UV/Vis absorbance of 50 nm thin films of ClInPc, DTDCTB and C_{60}.

The full set of photovoltaic parameters for the relevant OSCs in the discussion of the ClInPc:DTDCTB:C_{60} ternary OSCs are provided below in Supplemental Tables 1.3.1 to 1.3.3.

Supplemental Table 1.3.1 - Photovoltaic parameters for binary ClInPc:C_{60} OSCs at various donor to acceptor mixing ratios.

[Donor] [%]	Jsc [mA/cm2]	Voc [mV]	FF [%]	Eta [%]	Rshunt [Ohm.cm2]	Rseries [Ohm.cm2]
12.5%	6.22	1011	40	2.50	1962	26
50%	6.31	825	41	2.11	1529	21

Supplemental Table 1.3.2 - Photovoltaic parameters for ternary ClInPc:SubPc:C_{60} OSCs at various donor to acceptor mixing ratios (with [ClInPc]=[SubPc]).

[Donor]	Jsc	Voc	FF	Eta	Rshunt	Rseries
[%]	[mA/cm2]	[mV]	[%]	[%]	[Ohm.cm2]	[Ohm.cm2]
12.5%	5.64	1048	35	2.08	1847	43
50%	3.98	835	34	1.12	1552	39

Supplemental Table 1.3.3 - Photovoltaic parameters for ternary ClInPc:DTDCTB:C_{60} OSCs at various donor to acceptor mixing ratios (with [ClInPc]=[DTDCTB])

[Donor]	Jsc	Voc	FF	Eta	Rshunt	Rseries
[%]	[mA/cm2]	[mV]	[%]	[%]	[Ohm.cm2]	[Ohm.cm2]
12.5%	5.99	895	42	2.23	1926	24
50%	5.99	775	43	1.99	1590	21

For all ternary OSCs, the J_{sc} values were also calculated from the EQE and are tabulated below.

Supplementary Table 4 - Summary of J_{sc} values for ClInPc:SubPc:C_{60} ternary OSCs (measured vs. calculated by EQE)

ClInPc (%)	SubPc (%)	C60 (%)	Jsc (mA/cm^2)	J_{sc} by EQE (mA/cm^2)
6.25	0	93.75	5.09	5.15
12.5	0	87.5	6.22	6.04
25	0	75	6.93	6.79
50	0	50	6.31	6.50
75	0	25	4.12	5.06
0	6.25	93.75	5.06	4.95
0	12.5	87.5	6.35	6.25
0	25	75	7.13	7.23
0	50	50	4.57	5.04
0	75	25	0.85	1.40
6.25	6.25	87.5	5.30	5.27
12.5	6.25	81.25	5.83	5.65
25	6.25	68.75	6.19	6.07
37.5	6.25	56.25	5.83	5.93
50	6.25	43.75	5.23	5.54
6.25	12.5	81.25	5.97	5.82
12.5	12.5	75	6.19	6.04
25	12.5	62.5	5.83	5.84
37.5	12.5	50	5.14	5.39
50	12.5	37.5	4.24	4.46
6.25	25	68.75	5.80	5.67
12.5	25	62.5	5.45	5.36
25	25	50	4.15	4.27
37.5	25	37.5	3.10	3.31
50	25	25	2.05	2.25
6.25	37.5	56.25	5.50	6.07
12.5	37.5	50	4.61	5.11
25	37.5	37.5	3.20	3.59
37.5	37.5	25	1.96	2.41
50	37.5	12.5	0.92	1.24
6.25	50	43.75	4.05	4.51
12.5	50	37.5	2.81	3.07
25	50	25	1.36	1.63
37.5	50	12.5	0.57	0.69
50	50	0	0.10	0.10
0	0	100	1.10	0.73

1.4. Supplemental Information for Chapter Eight: The Photo-stability of Polymer Solar Cells: Contact Photo-degradation and the Benefits of Interfacial Layers

R_s and R_{sh} values were also measured throughout the duration of the experiments described in the body of this chapter, as shown in Supplemental Figure 1.4.1.

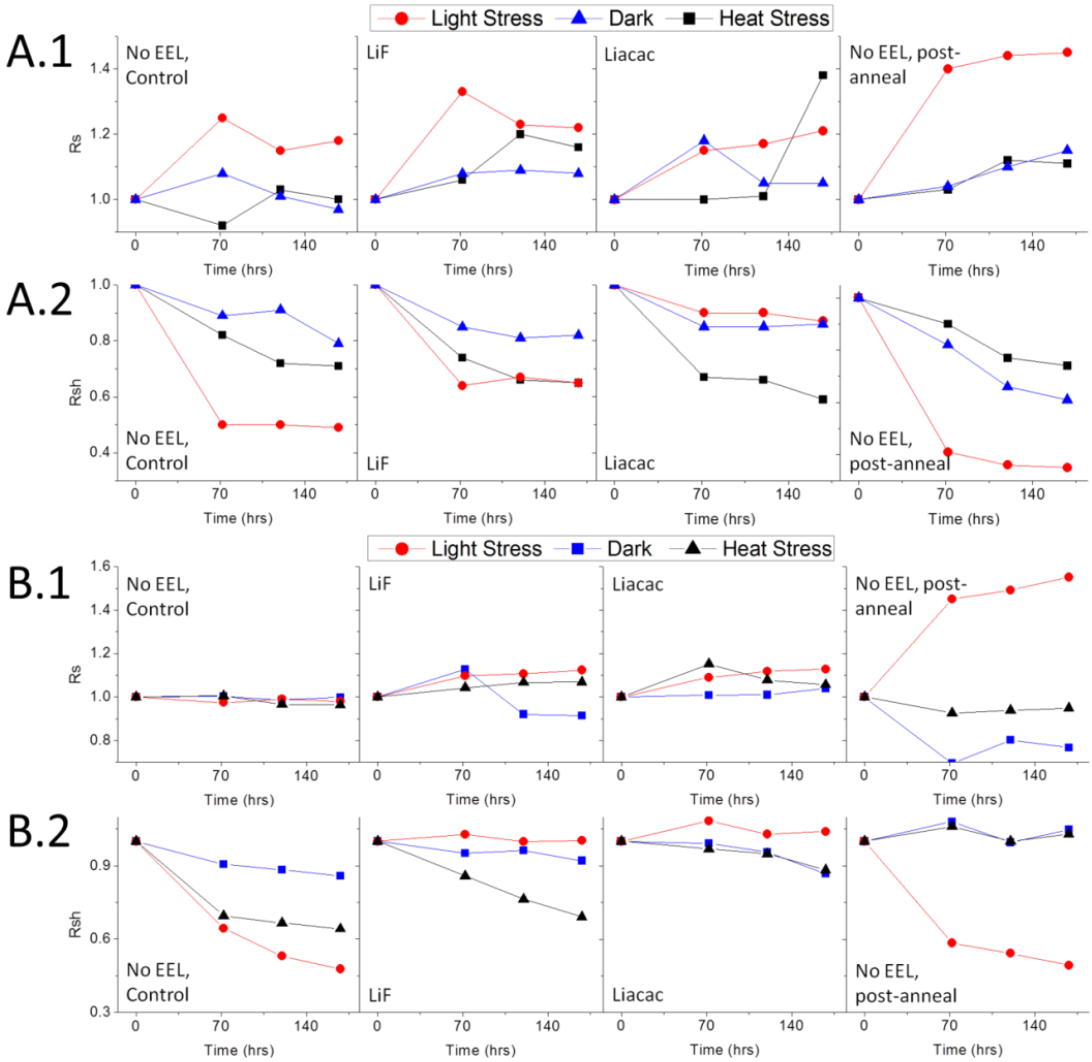

Figure 1.4.1 - Normalized 1) R_s and 2) R_{sh} values for A) ITO/PEDOT:PSS /P3HT:PCBM/x/Al and B) ITO/MoO3 /P3HT:PCBM/x/Al OSCs during 168-hour aging studies. x=LiF, Liacac or nothing. (Note: All points are taken as averages from 4-6 devices).

As noted in the body of the work, the data presented comprise only a small sub-set of a larger body of data collected over a period of 18 months and obtained from tests on twelve to fifteen solar cell samples from each group. This specific sub-set of data was obtained from samples fabricated and tested over a shorter period of time (6 months) to minimize experimental variation. Statistical averages from the larger body of data (i.e. 12-15 samples for each group) are shown in Supplemental Figures 1.4.2 and 1.4.3 below. From these data, as compared to that shown in the body of this work, it is clear that there are no substantial deviations in the results. Note: A common measurement timing for all experiments was 168 hours. As such, the data shown in Supplemental Figures 2 and 3 give a snapshot of 'before' and 'after' states of the OSCs.

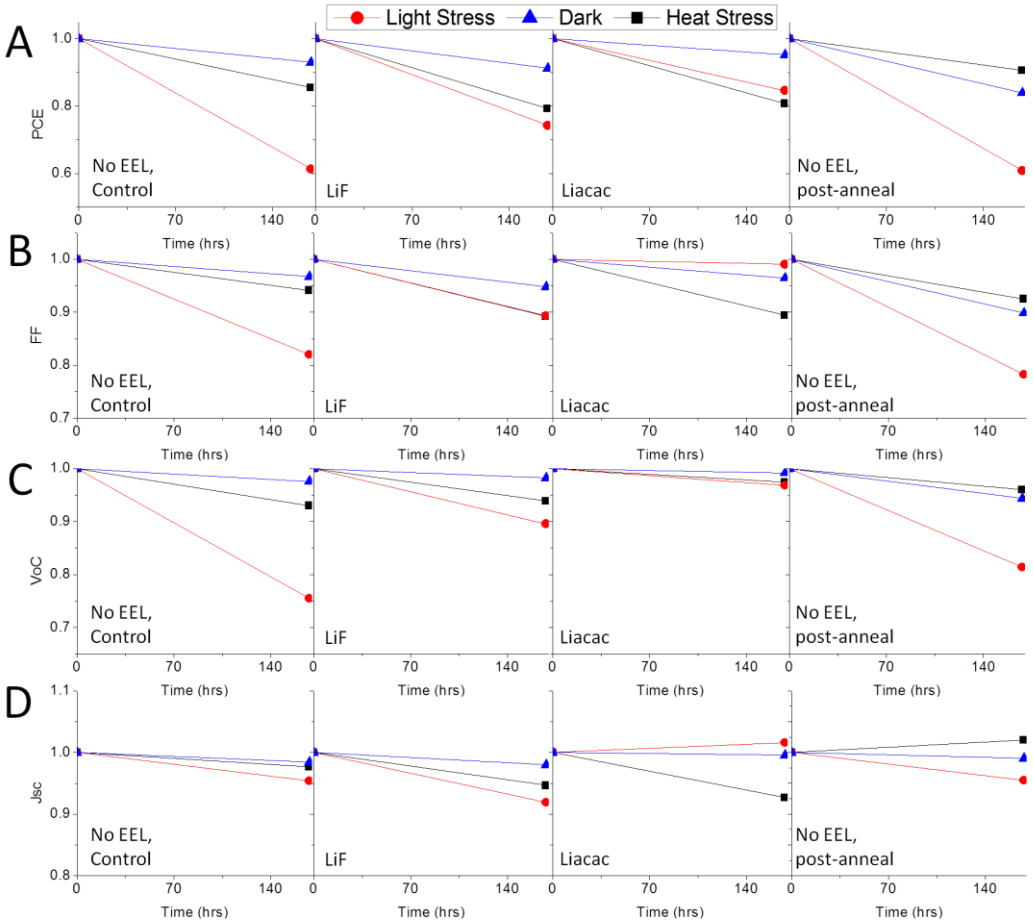

Figure 1.4.2 - Grand average normalized PCE (A), FF (B), V_{oc} (C) and J_{sc} (D) values of ITO/PEDOT:PSS/P3HT:PCBM/x/Al OSCs during 168-hour Aging Studies. x=LiF, Liacac or nothing.

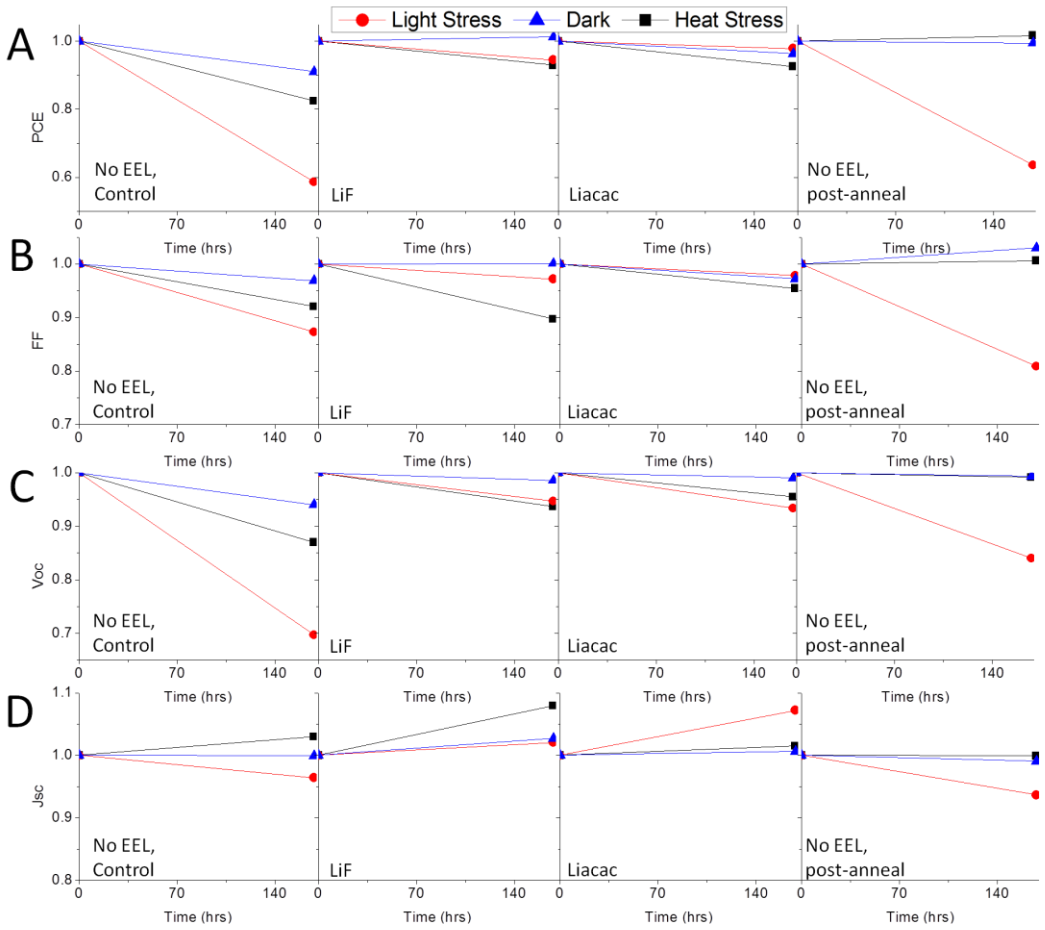

Figure 1.4.3 - Grand average normalized PCE (A), FF (B), V_{oc} (C) and J_{sc} (D) values of ITO/MoO_3/P3HT:PCBM/x/Al OSCs during 168-hour aging studies. x=LiF, Liacac or nothing.

The original photovoltaic results from the devices in the first two figures of this chapter (i.e. not normalized) are provided below. Note that the y-axis varies from figure to figure.

PEDOT:PSS HEL + No EEL/Control

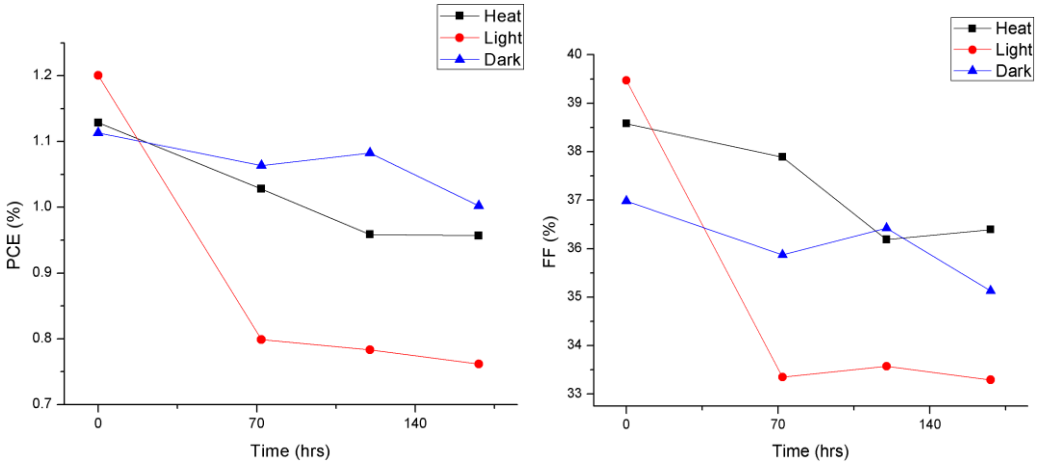

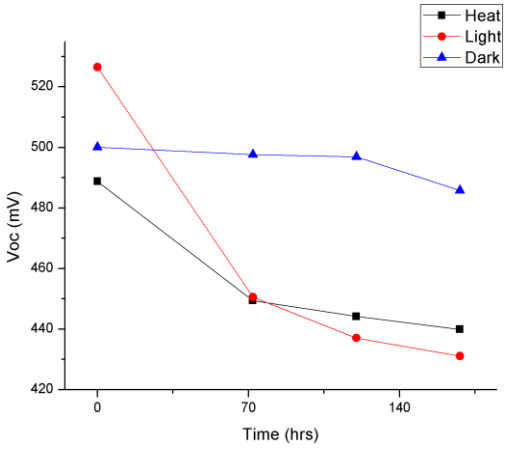

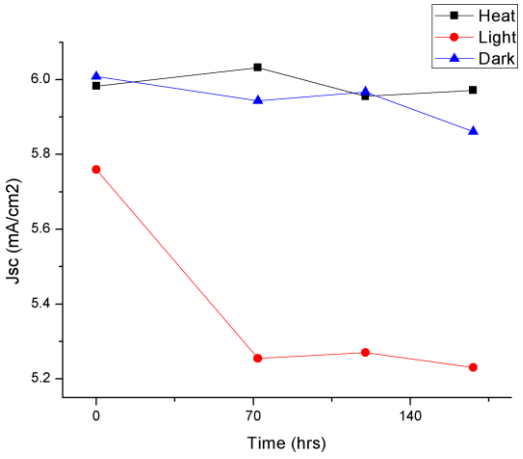

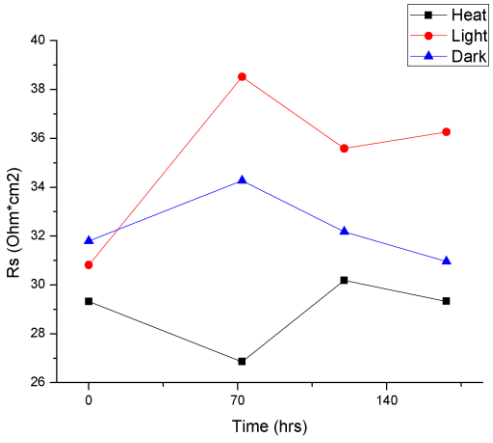

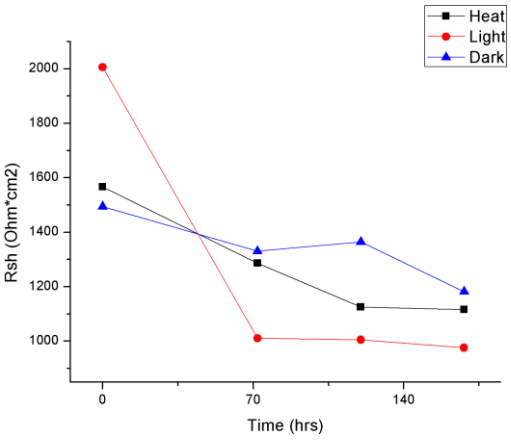

PEDOT:PSS HEL + LiF EEL

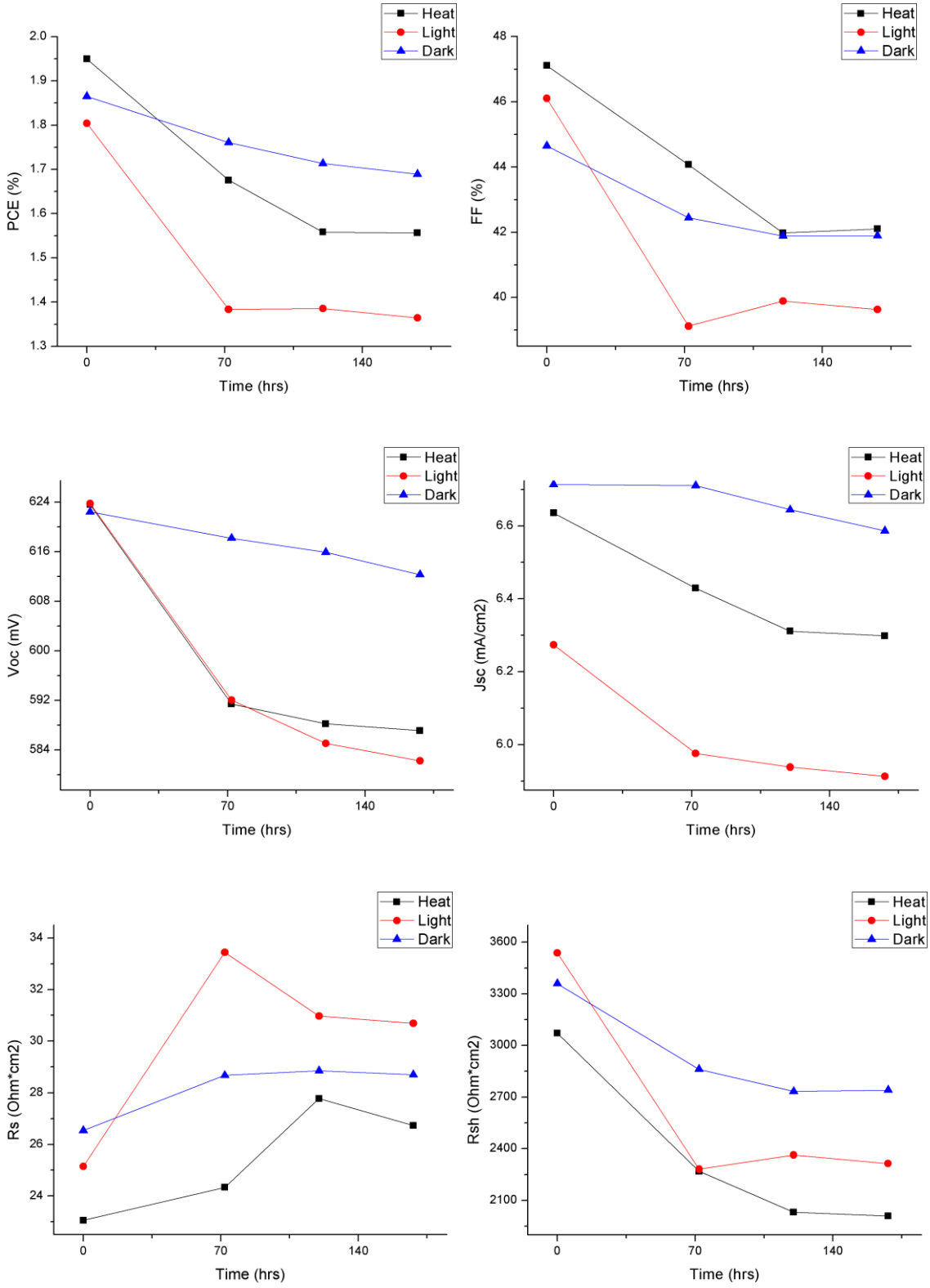

PEDOT:PSS HEL + Liacac EEL

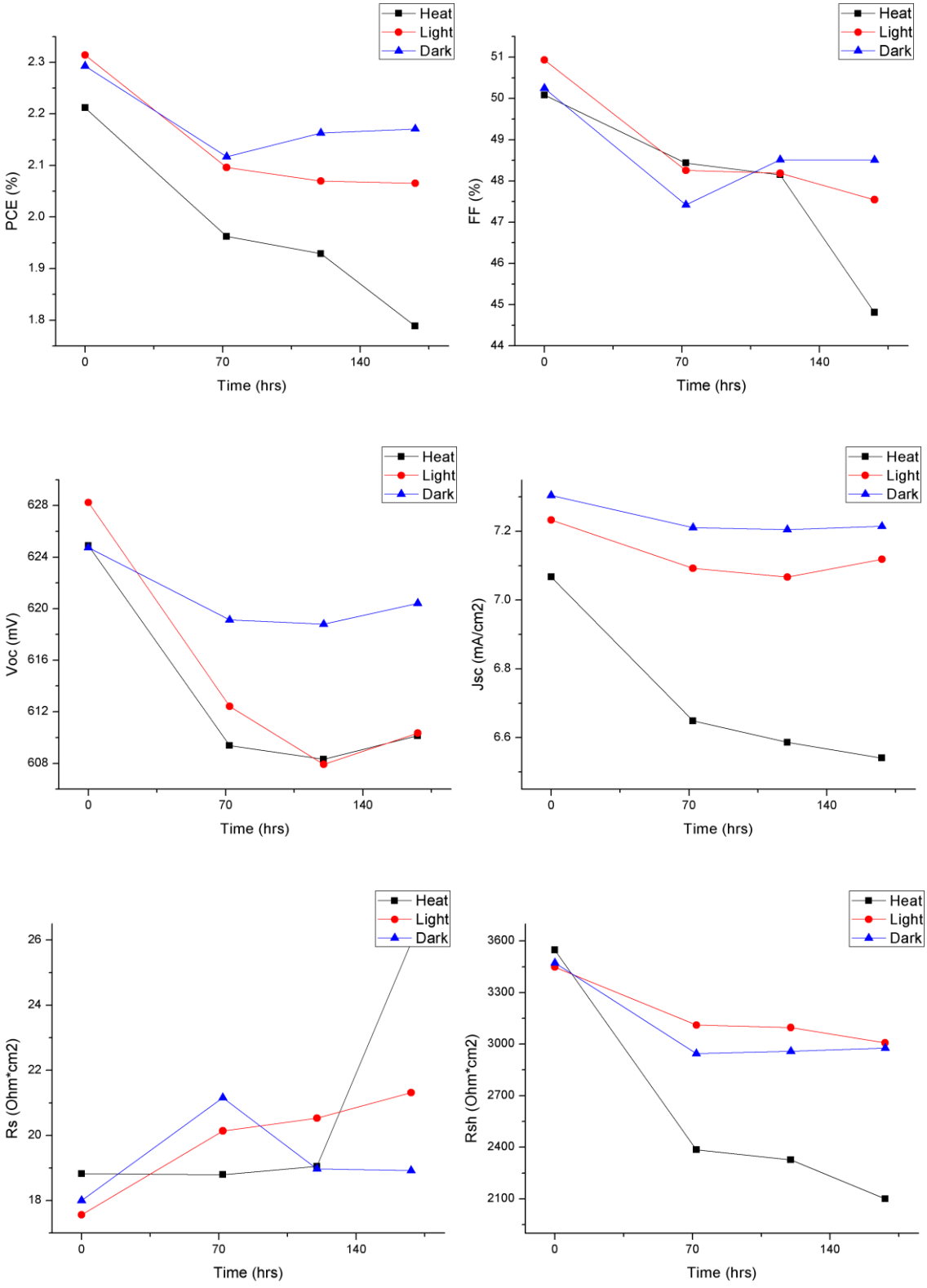

PEDOT:PSS HEL + No EEL/Post-Anneal

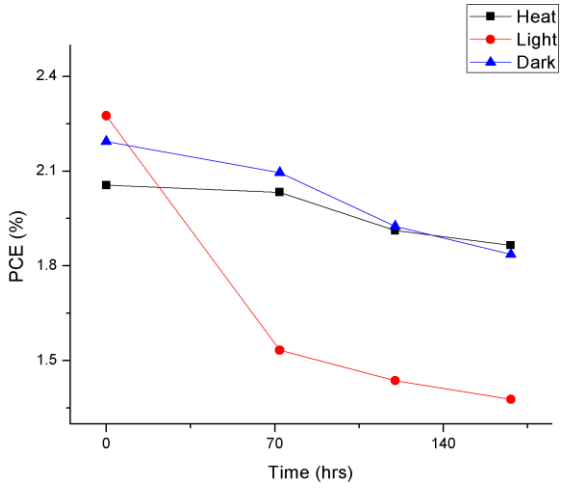

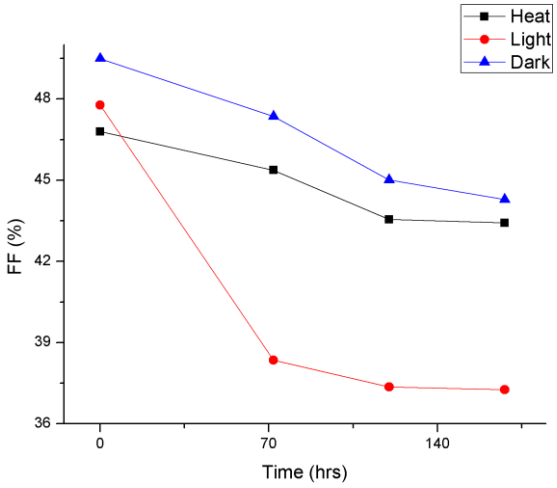

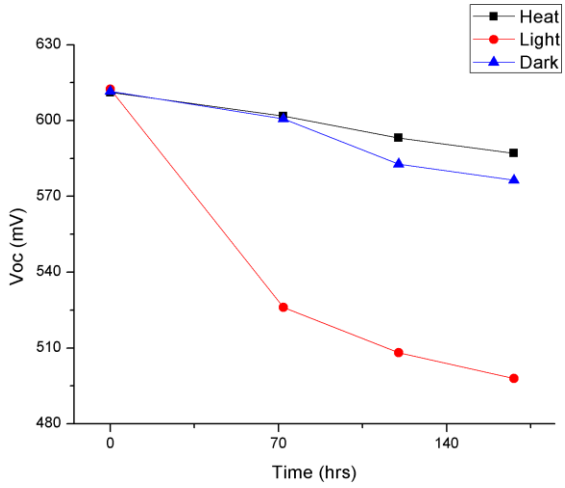

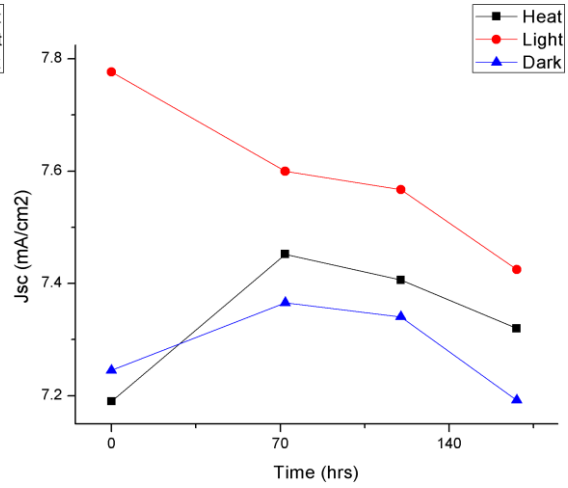

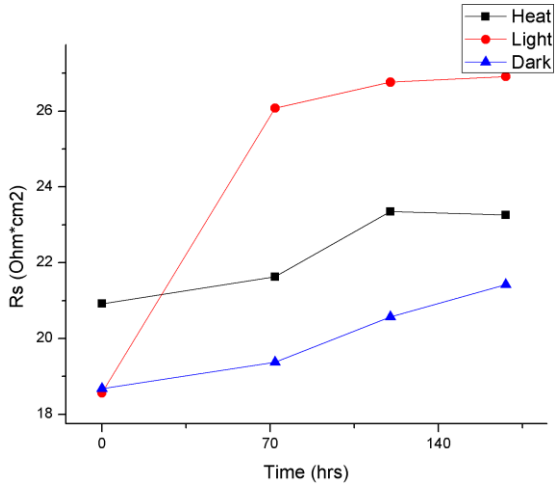

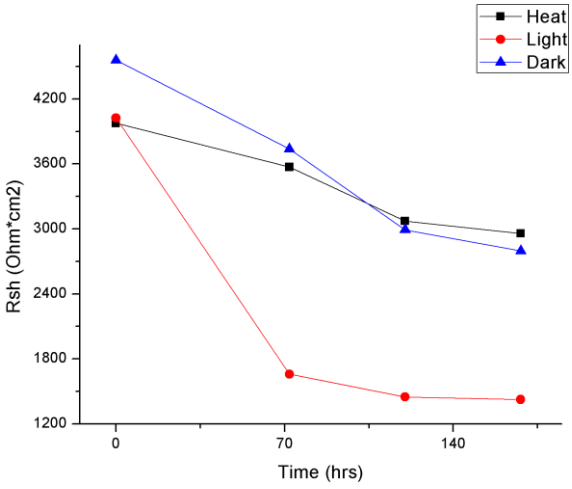

MoO_3 HEL + No EEL/Control

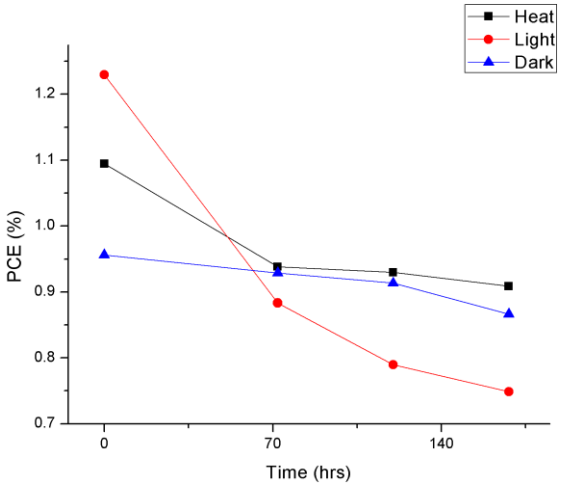

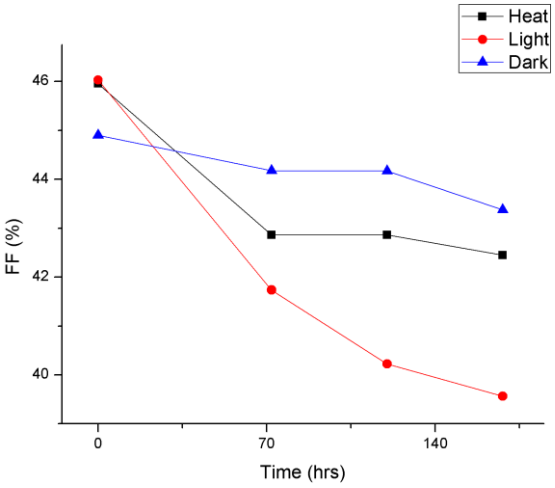

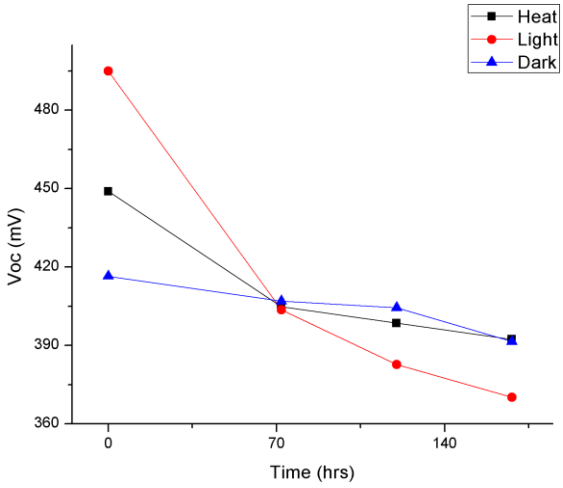

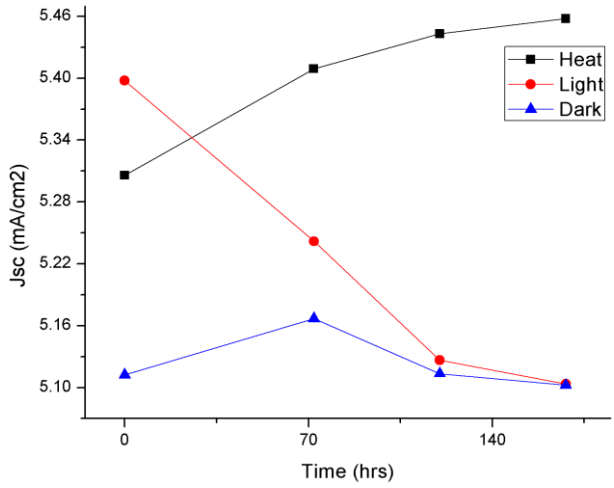

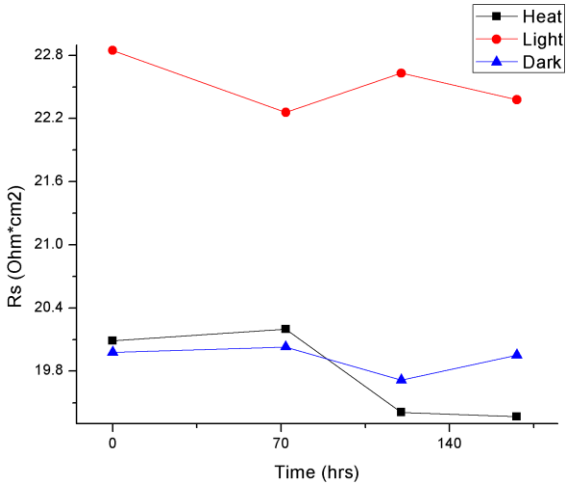

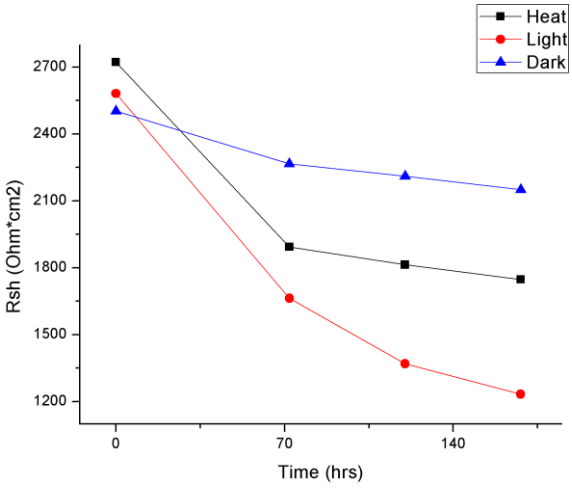

MoO_3 HEL + LiF EEL

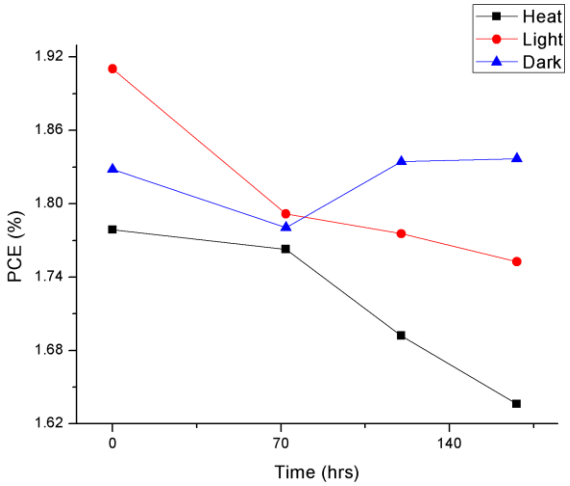

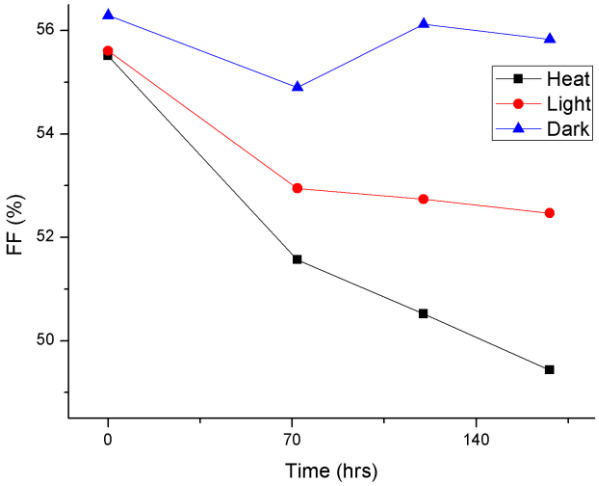

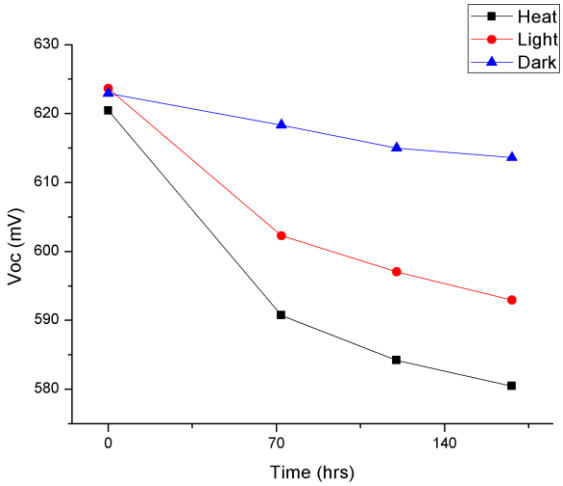

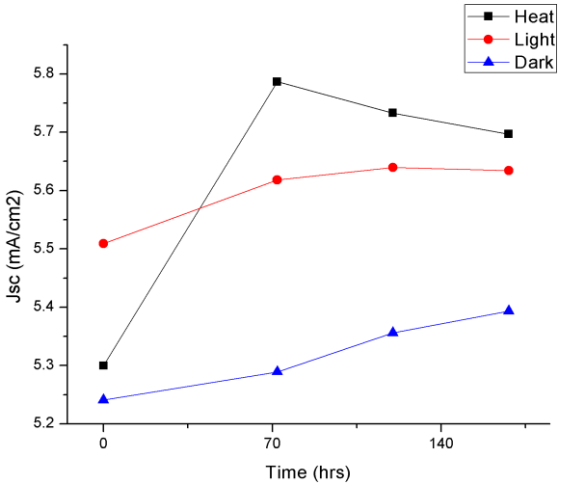

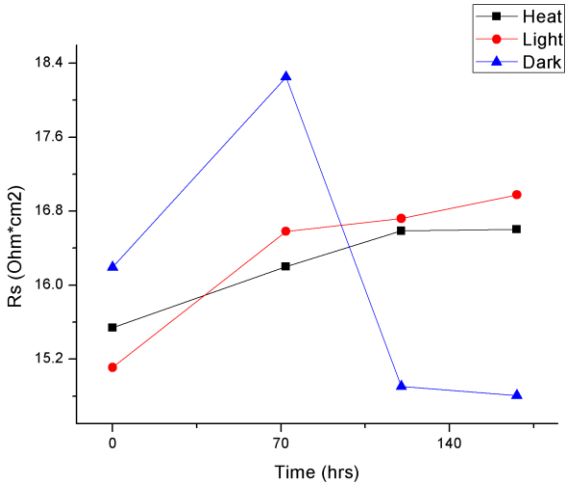

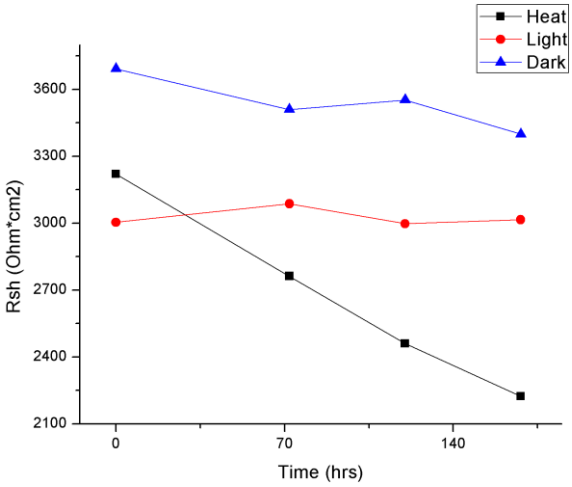

MoO_3 HEL + Liacac EEL

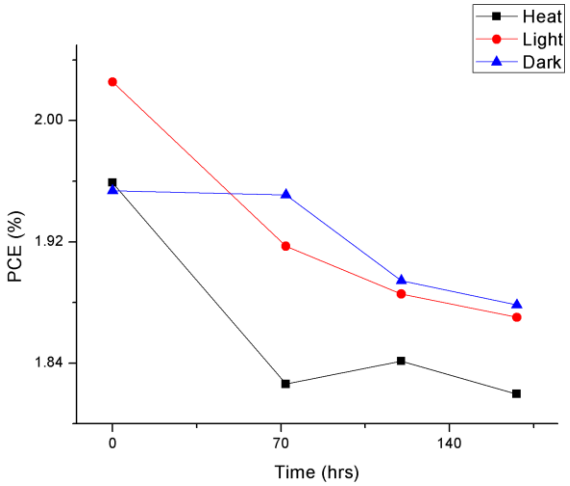

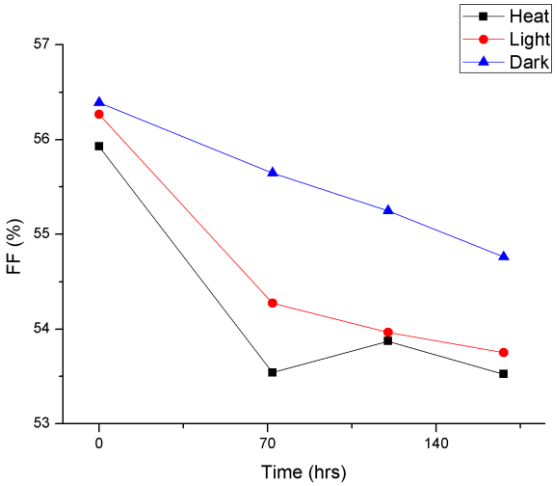

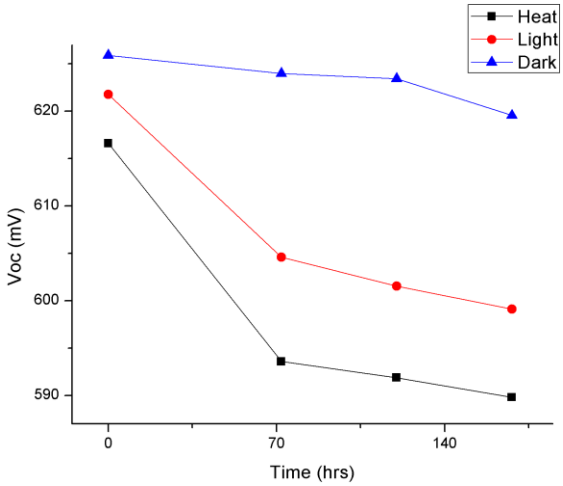

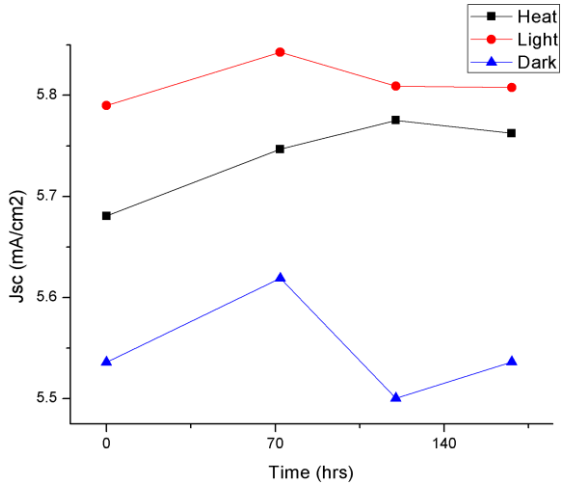

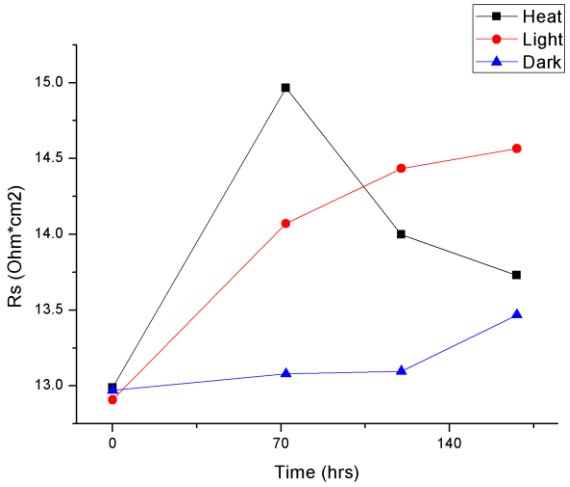

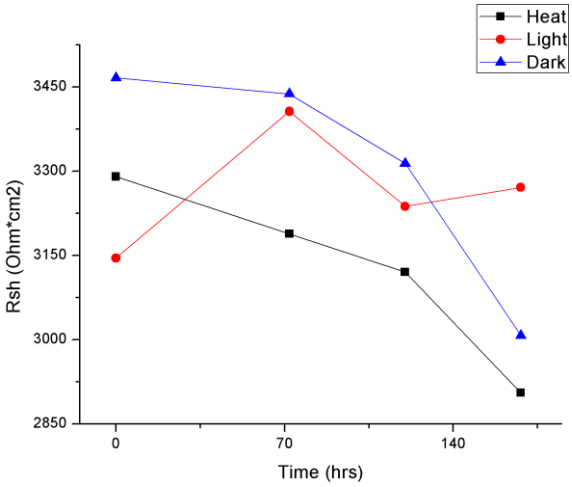

MoO_3 HEL + No EEL/Post-Anneal

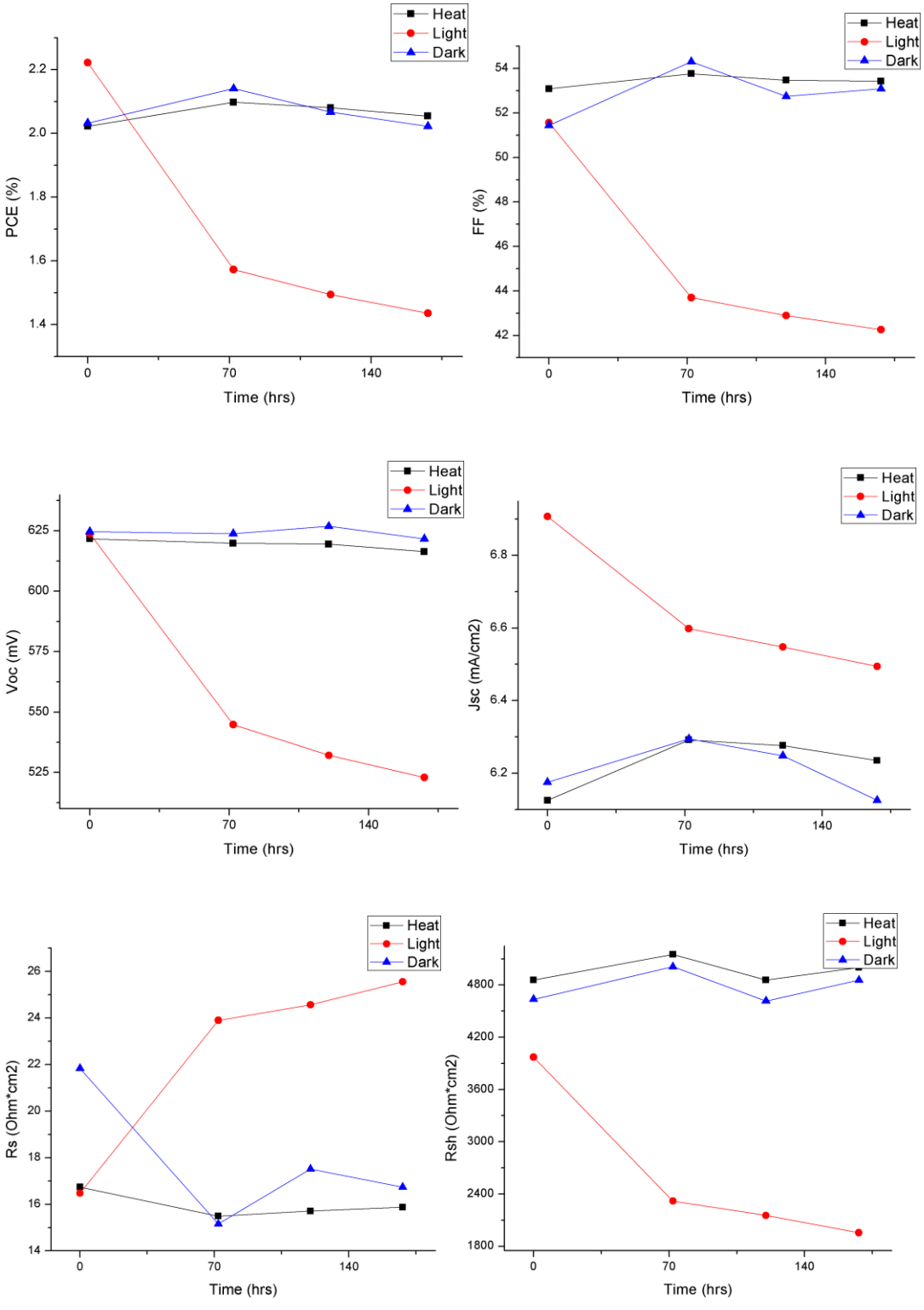

1.5. Supplemental Information for Chapter Nine: The Effect of Charge Extraction Layers on the Photo-Stability of Vacuum-Deposited versus Solution-Coated Organic Solar Cells

The body of this chapter includes normalized figures of photovoltaic output parameters to better observe trends in OSC stability and degradation. The original, non-normalized photovoltaic parameter data are provided on the following pages. 'Dark' samples are those that were kept in the dark. 'Light' samples are those that were illuminated.

ClInPc:C_{60} (vacuum-deposited) SM-OSCs

CF_4 HEL: ITO/CF_4/CLInPc:C_{60}/C_{60}/Variable EEL/Al

Dark

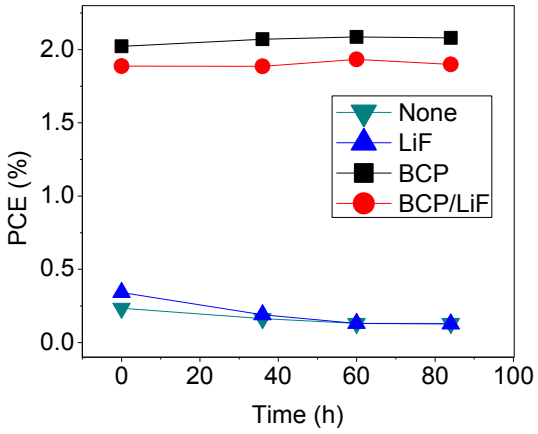

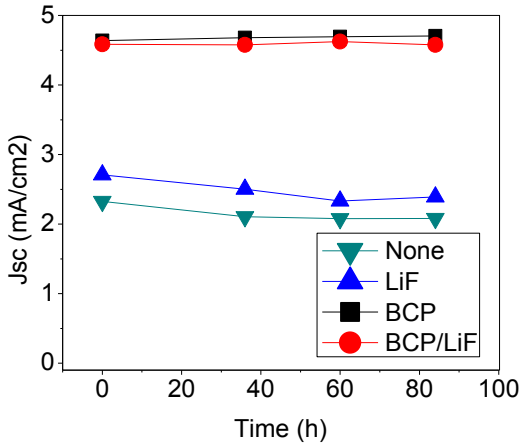

Light

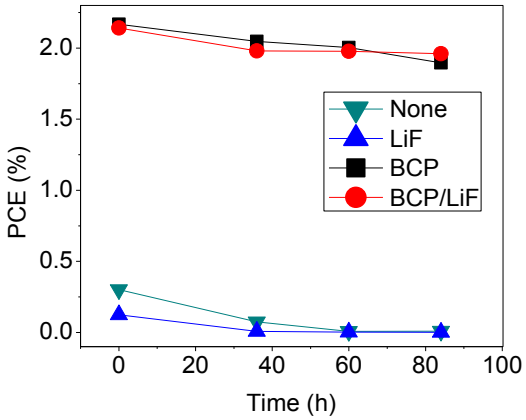

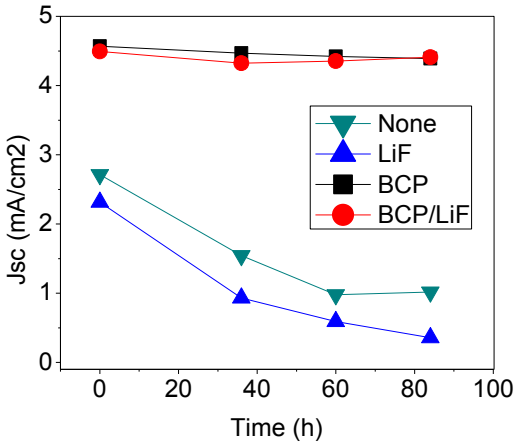

ClInPc:C_{60} SM-OSC, CF_4 HEL, cont'd

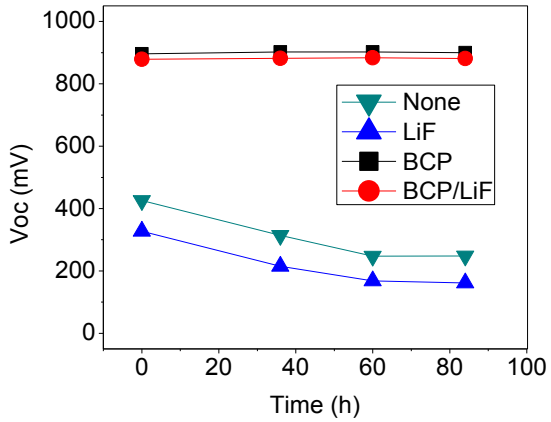

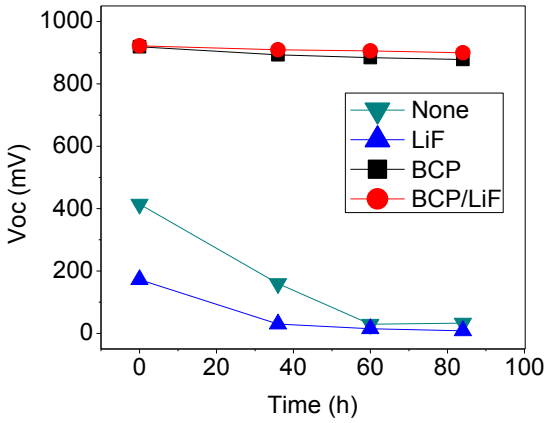

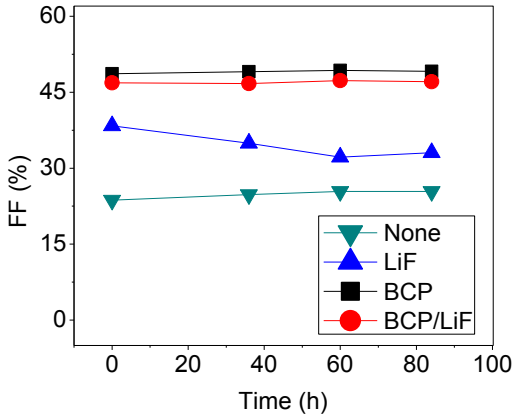

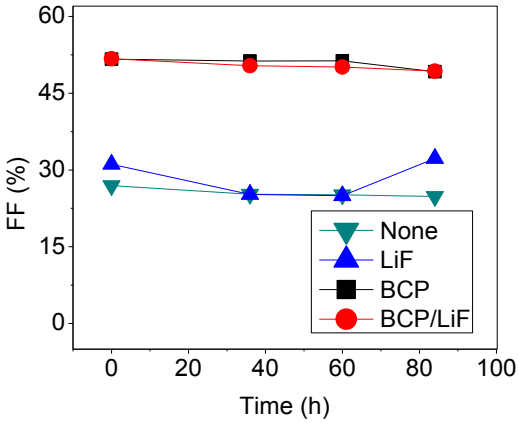

MoO_3 HEL: ITO/MoO_3/ClInPc:C_{60}/C_{60}/Variable EEL/Al

Dark

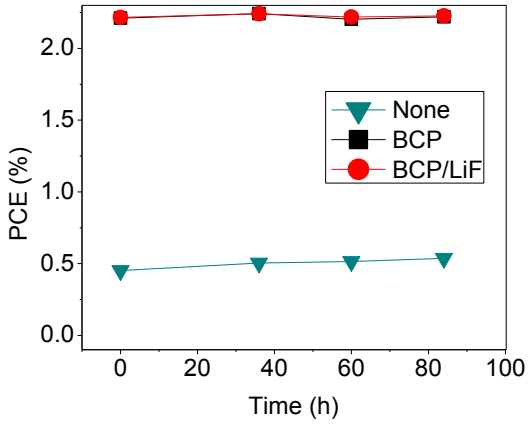

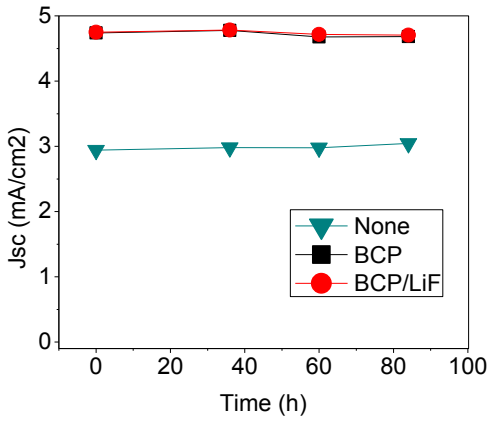

Light

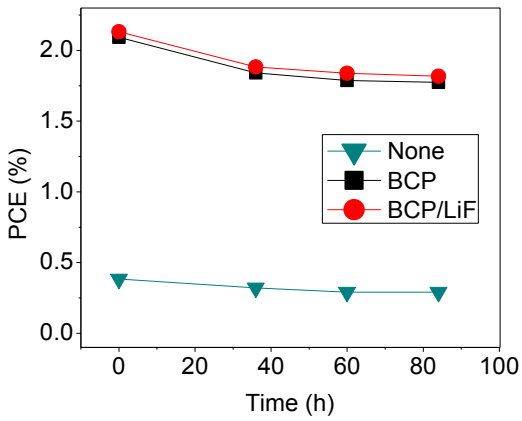

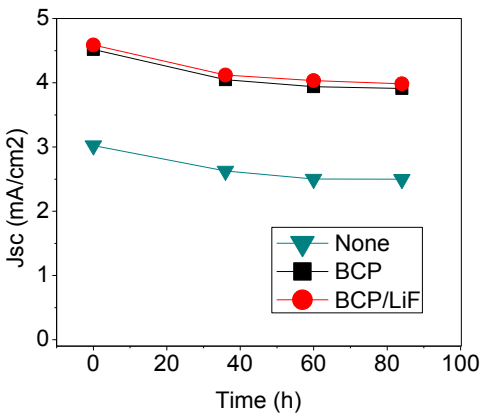

ClInPc:C_{60} SM-OSC, MoO_3 HEL, cont'd

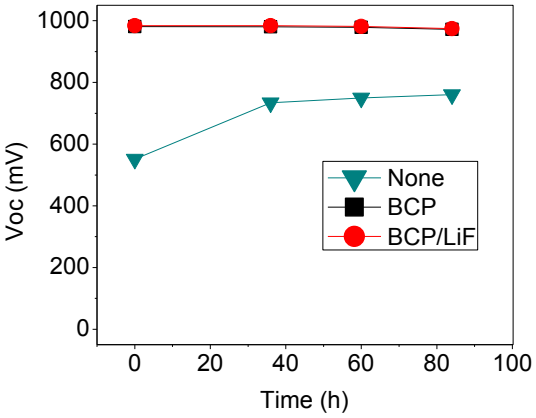

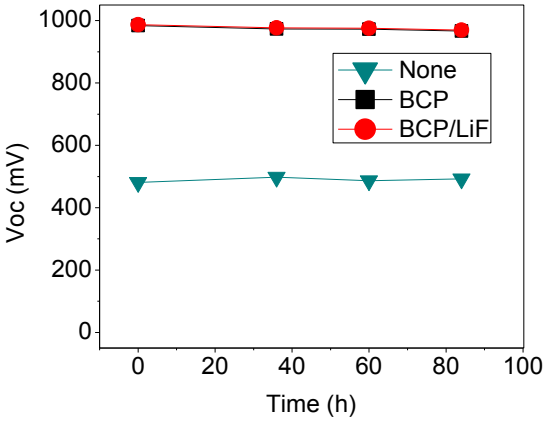

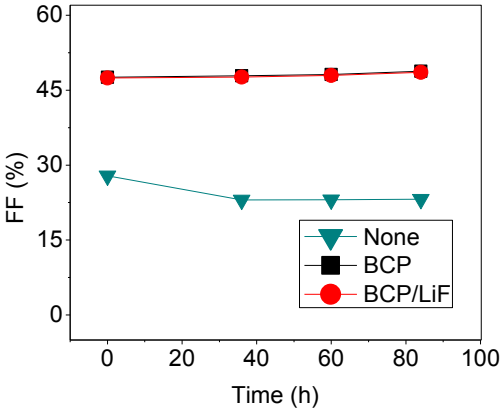

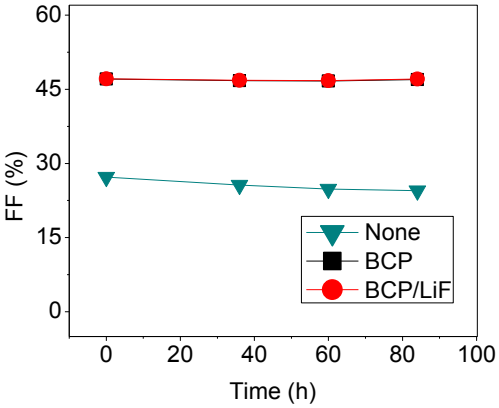

No HEL: ITO/ClInPc:C_{60}/C_{60}/Variable EEL/Al

Dark

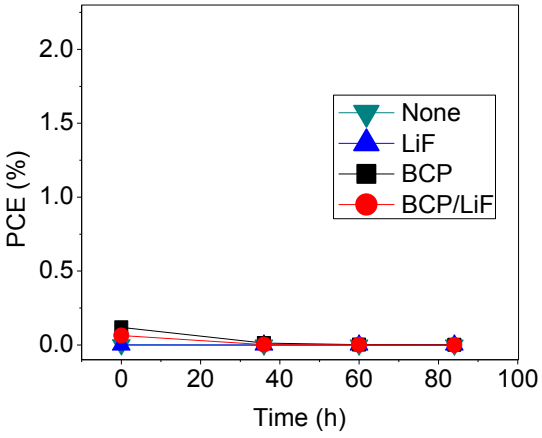

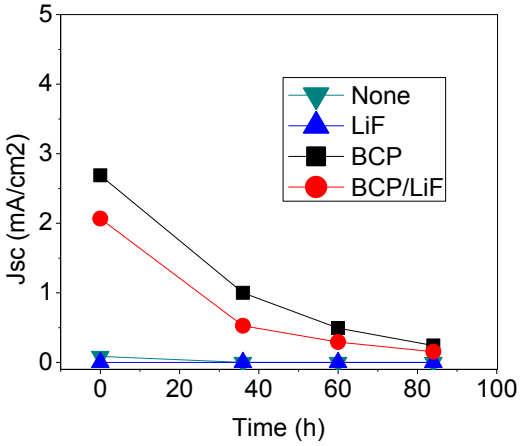

Light

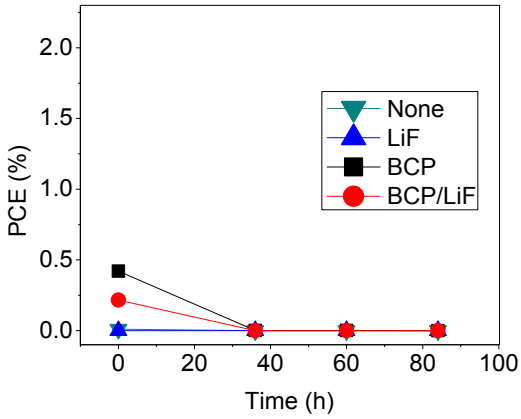

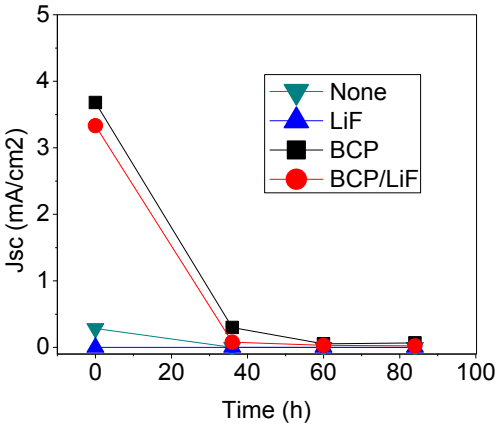

ClInPc:C_{60} SM-OSC, No HEL, cont'd

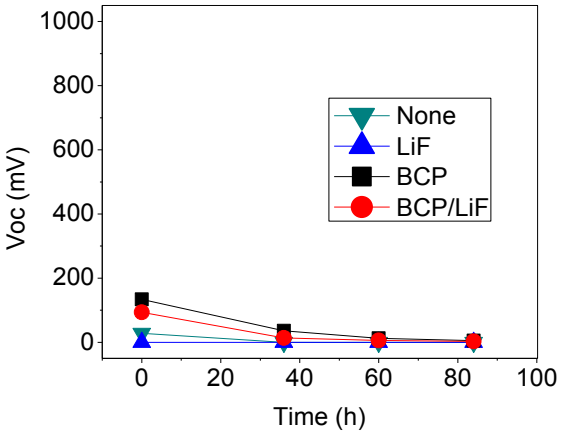

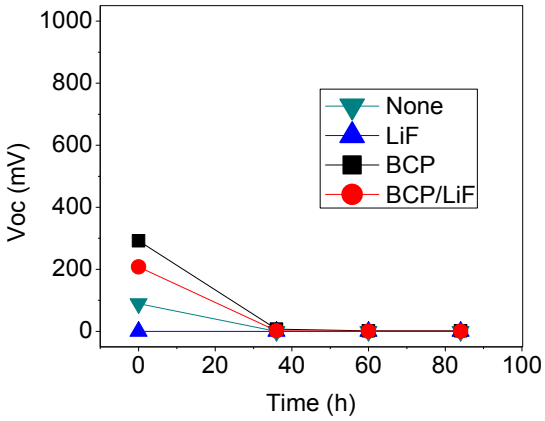

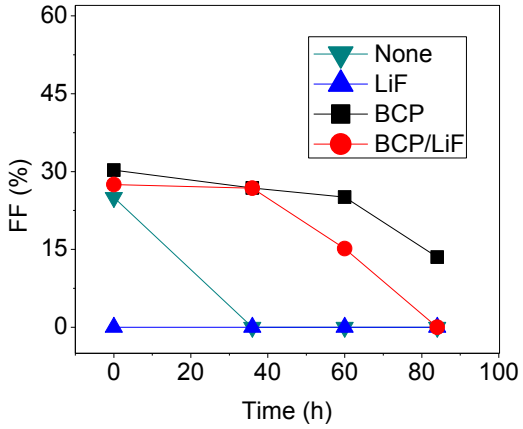

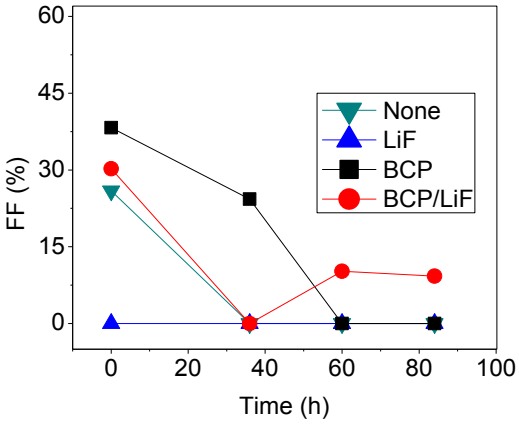

PEDOT:PSS: ITO/PEDOT:PSS/ClInPc:C_{60}/C_{60}/Variable EEL/Al

Dark

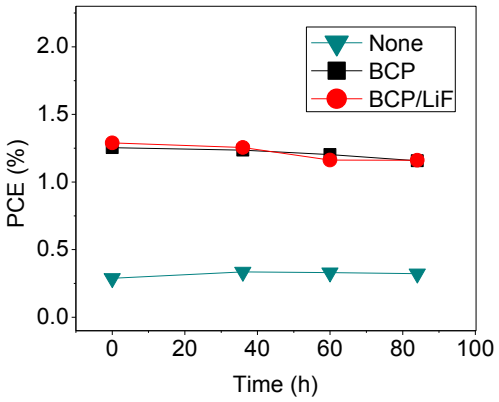

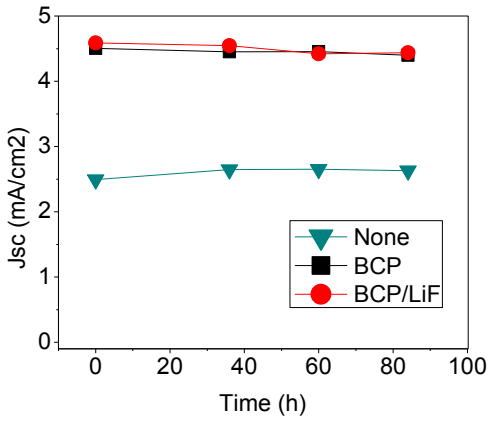

Light

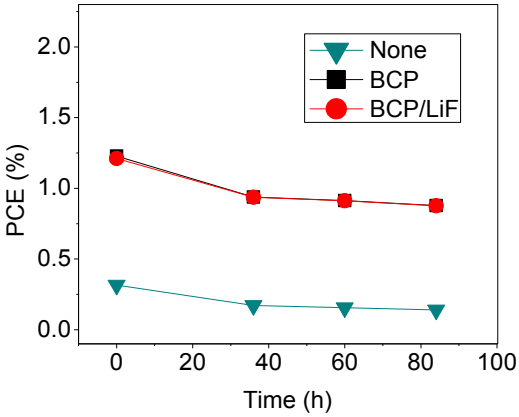

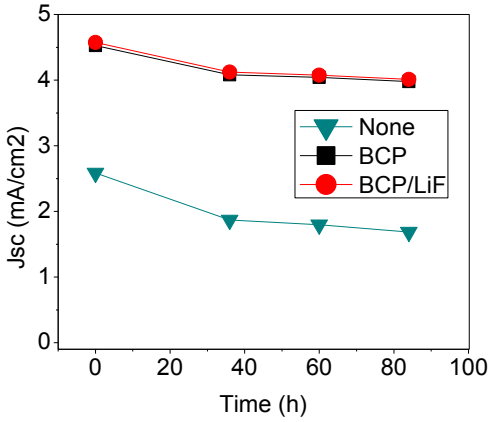

ClInPc:C_{60} SM-OSC, PEDOT:PSS HEL, cont'd

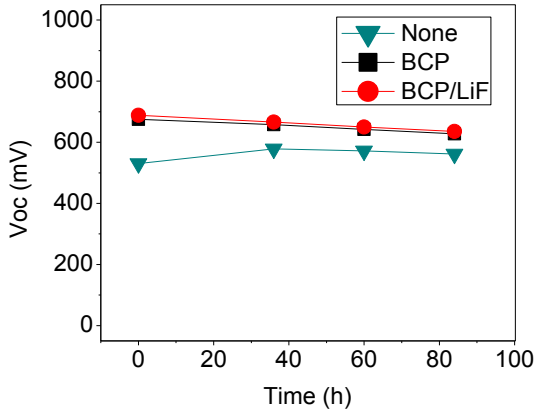

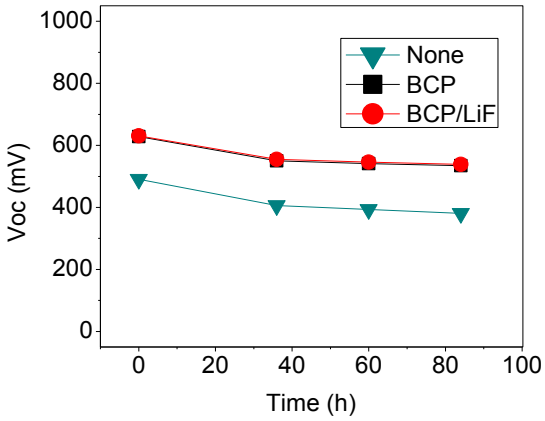

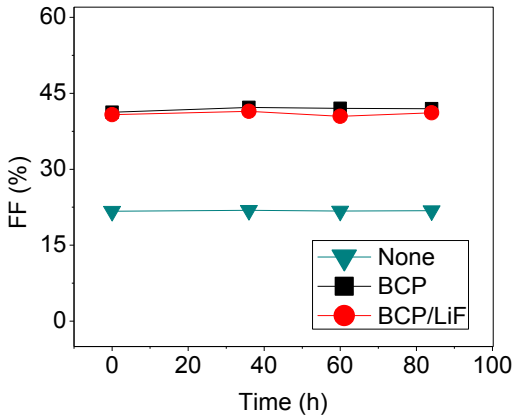

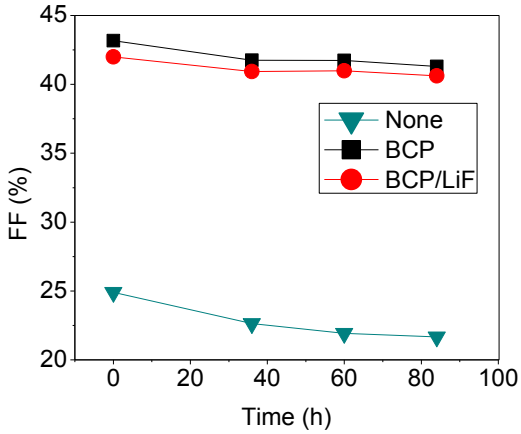

P3HT:PCBM (solution-coated) P-OSCs

CF_4 HEL: ITO/CF_4/P3HT:PCBM/Variable EEL/Al

Dark

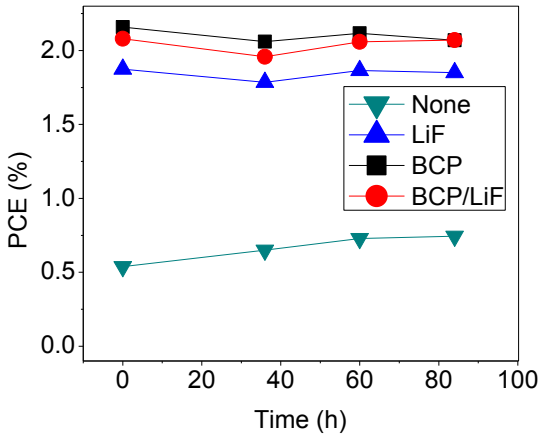

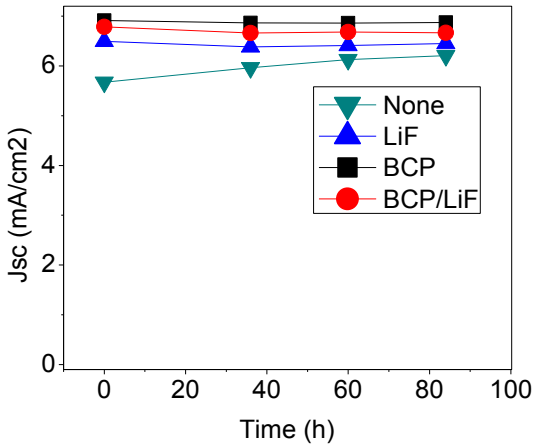

Light

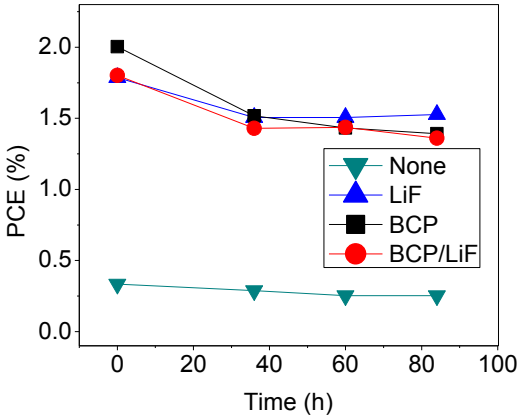

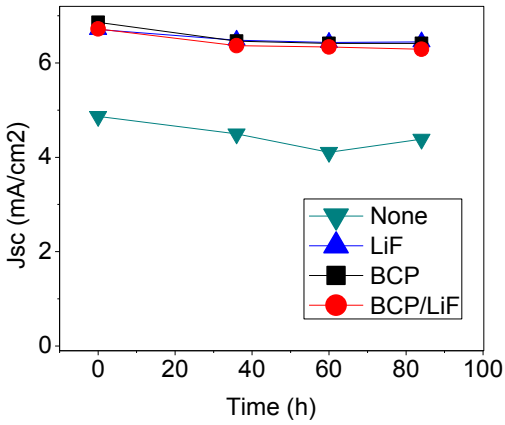

P3HT:PCBM P-OSC, CF_4 HEL, cont'd

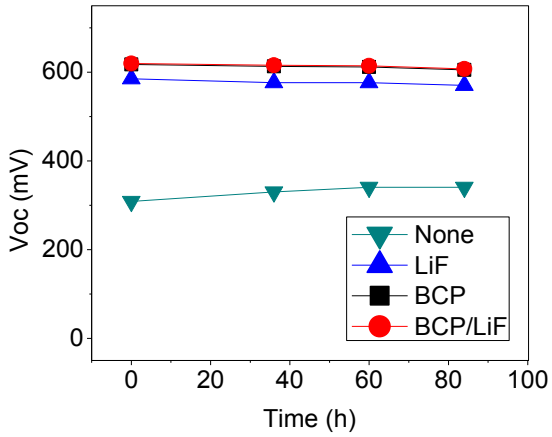

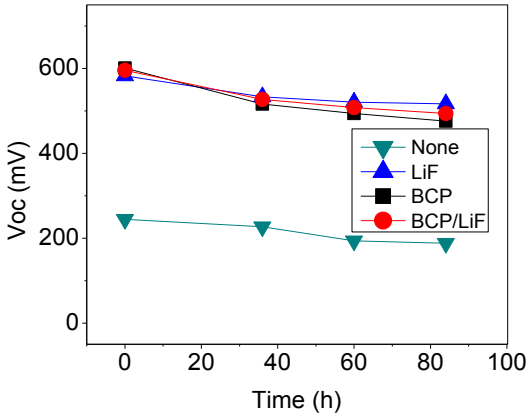

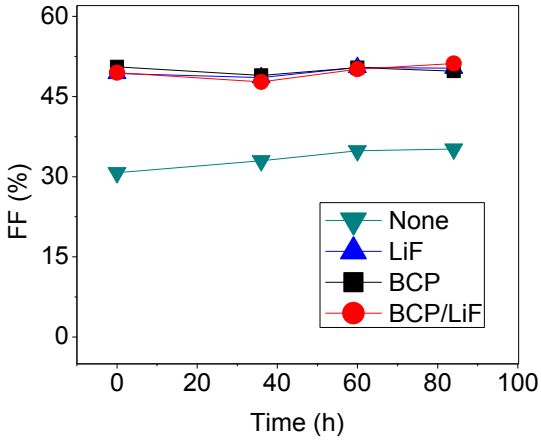

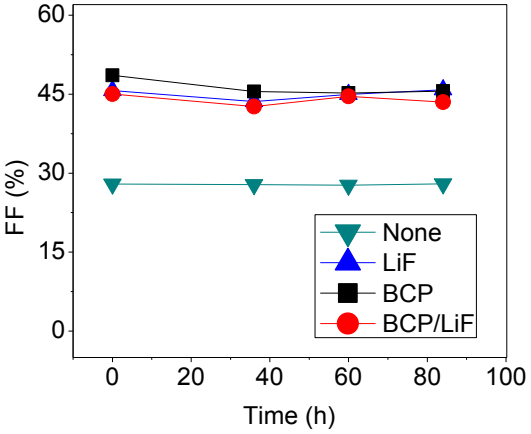

MoO_3 HEL: ITO/MoO_3/P3HT:PCBM/Variable EEL/Al

Dark

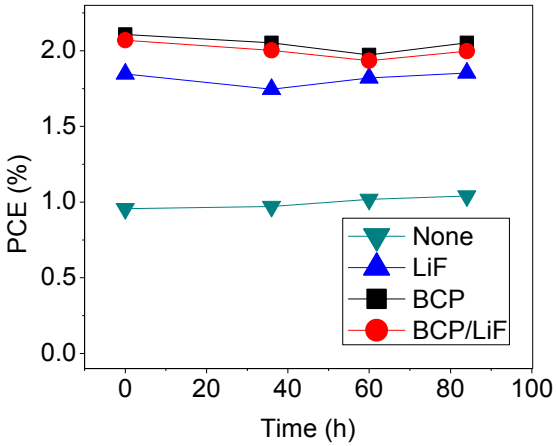

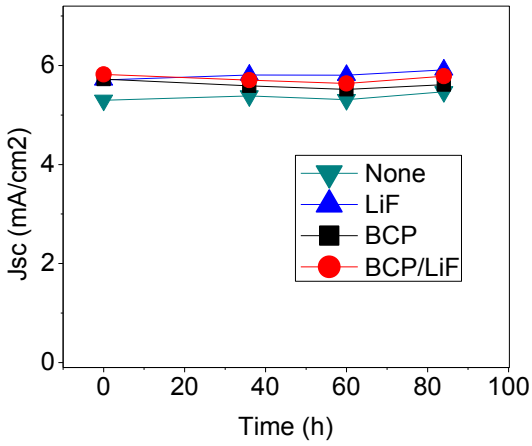

Light

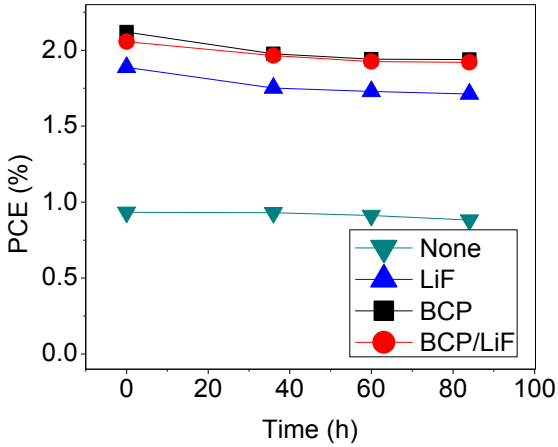

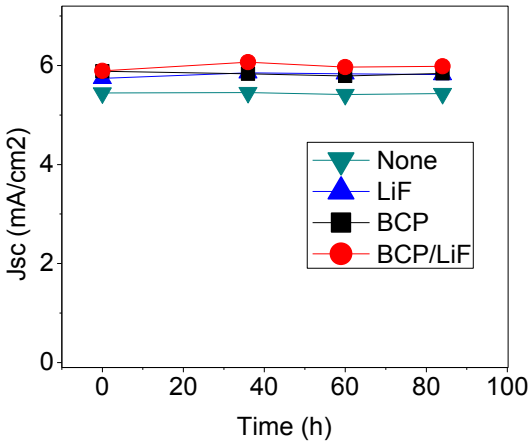

P3HT:PCBM P-OSC, MoO_3 HEL, cont'd

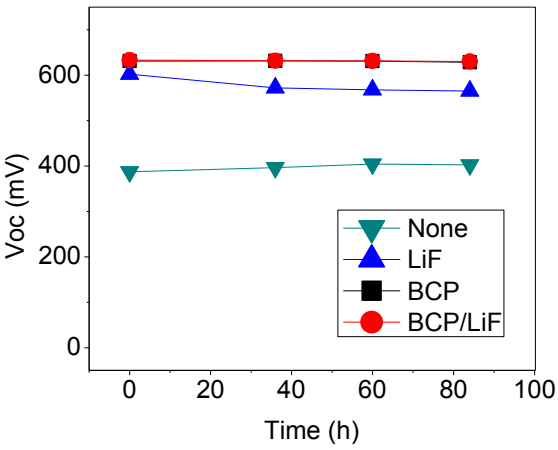

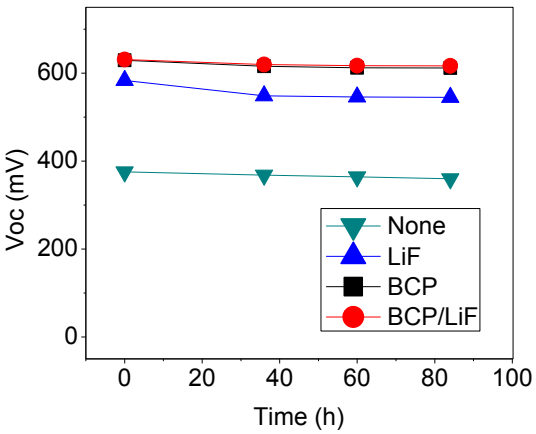

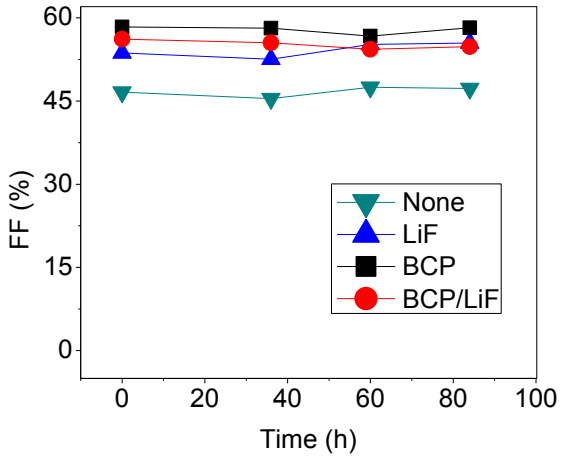

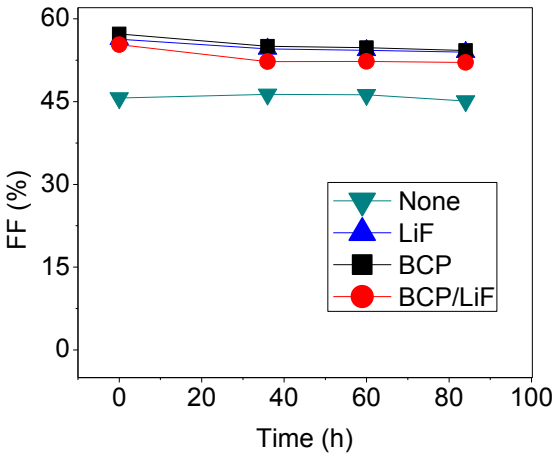

No HEL: ITO/P3HT:PCBM/Variable EEL/Al

Dark

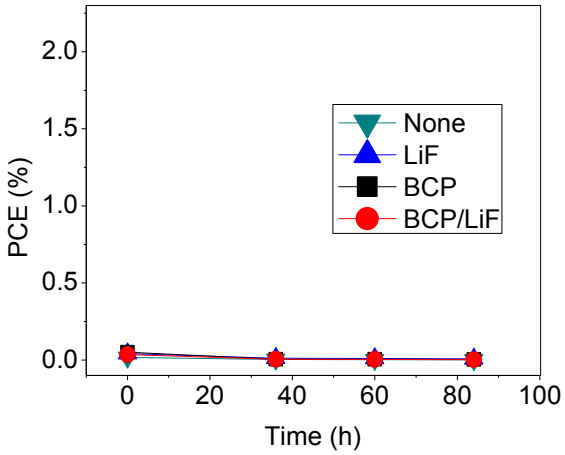

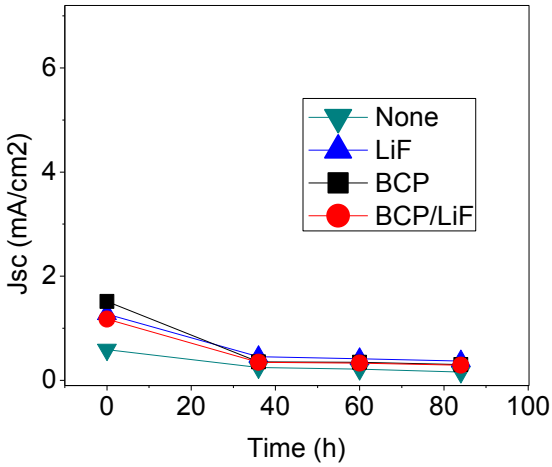

Light

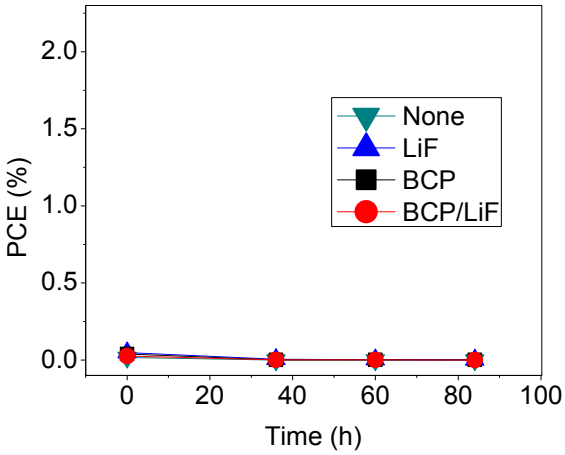

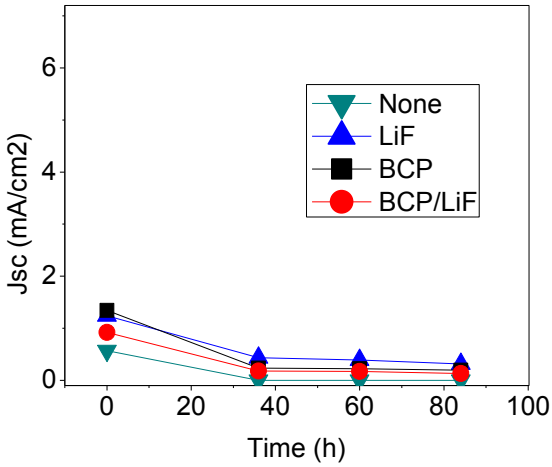

P3HT:PCBM P-OSC, No HEL, cont'd

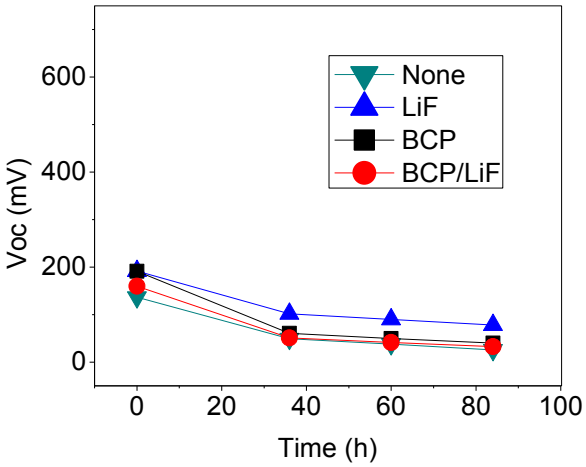

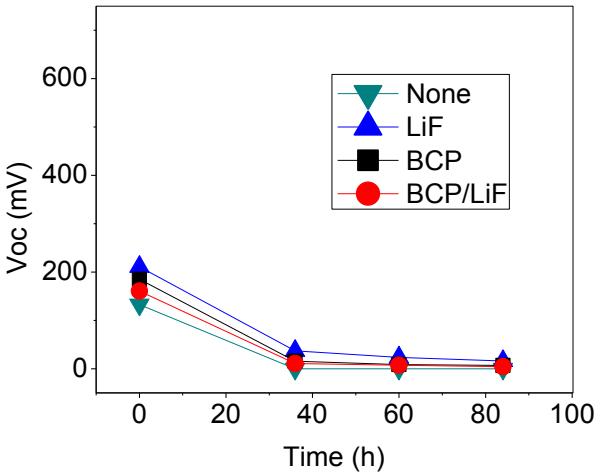

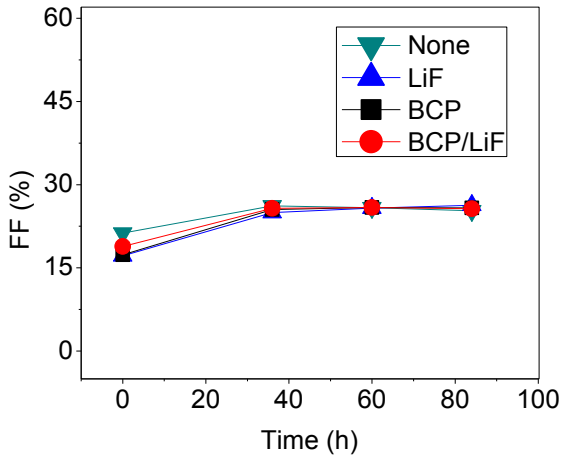

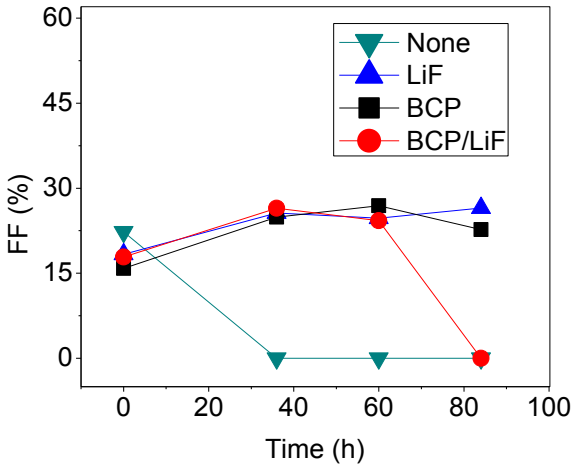

PEDOT:PSS HEL: ITO/ PEDOT:PSS/P3HT:PCBM/Variable EEL/Al

Dark

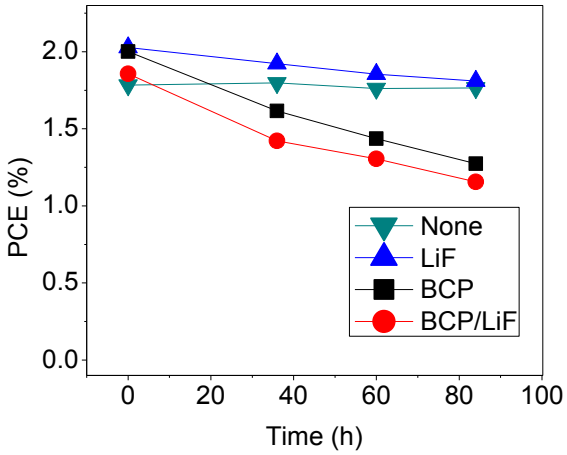

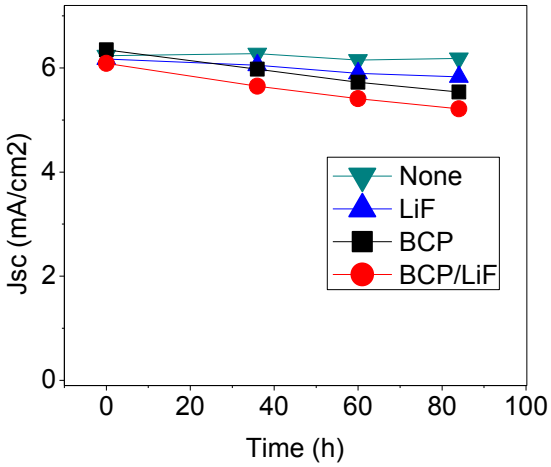

Light

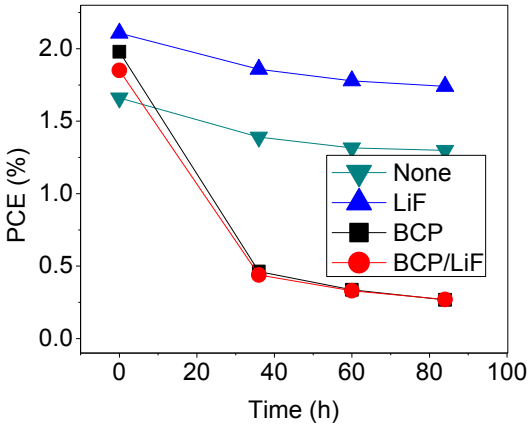

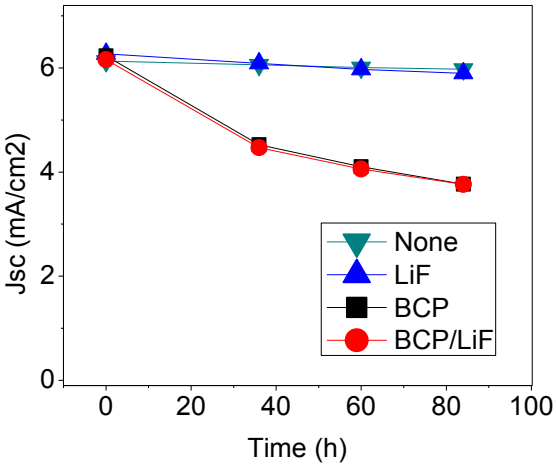

P3HT:PCBM P-OSC, PEDOT:PSS HEL, cont'd

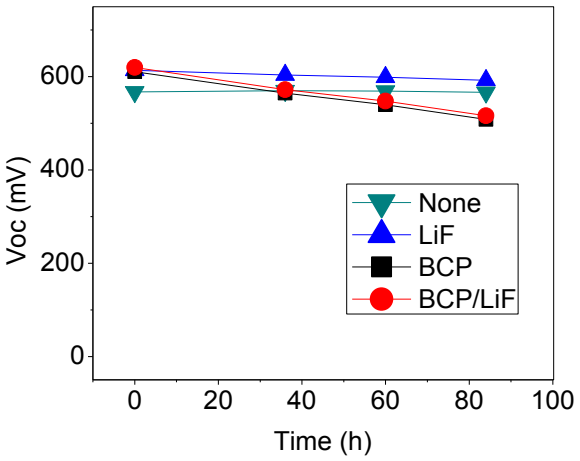

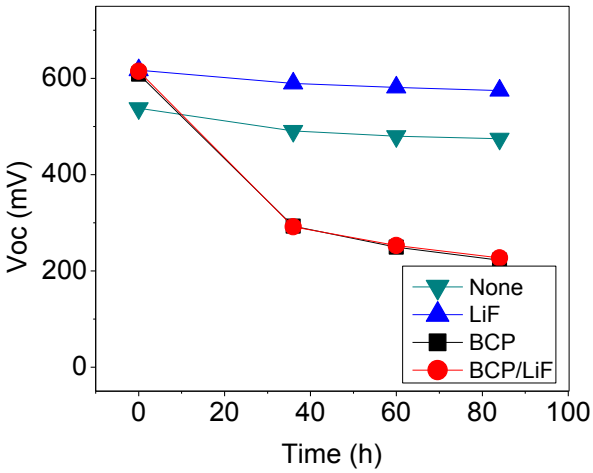

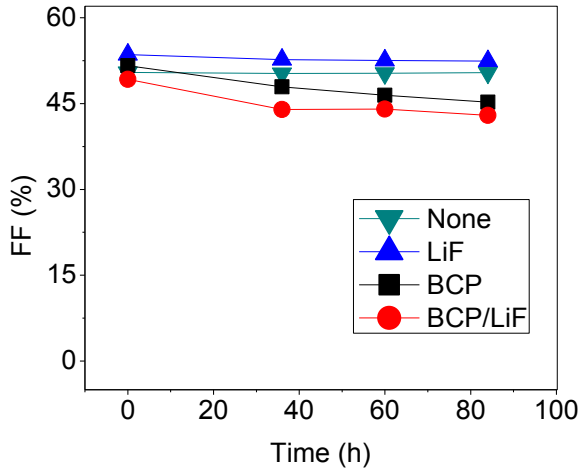

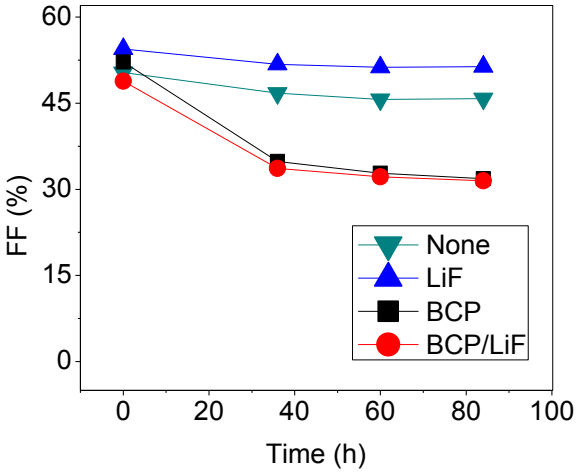

1.6. Supplemental Information for Chapter Ten: Implications of the Device Structure on the Photo-Stability of Organic Solar Cells

In this chapter, the stability of ClInPc:C_{60} OSCs at different mixing ratios and under different stresses (dark, heat and light). For meaningful analysis, the photovoltaic parameters are normalized to the dark-aged data (removing any variations simply due to storage of the devices). The raw data of each stress scenario are provided in Supplemental Figures 1.6.1 to 1.6.3 below.

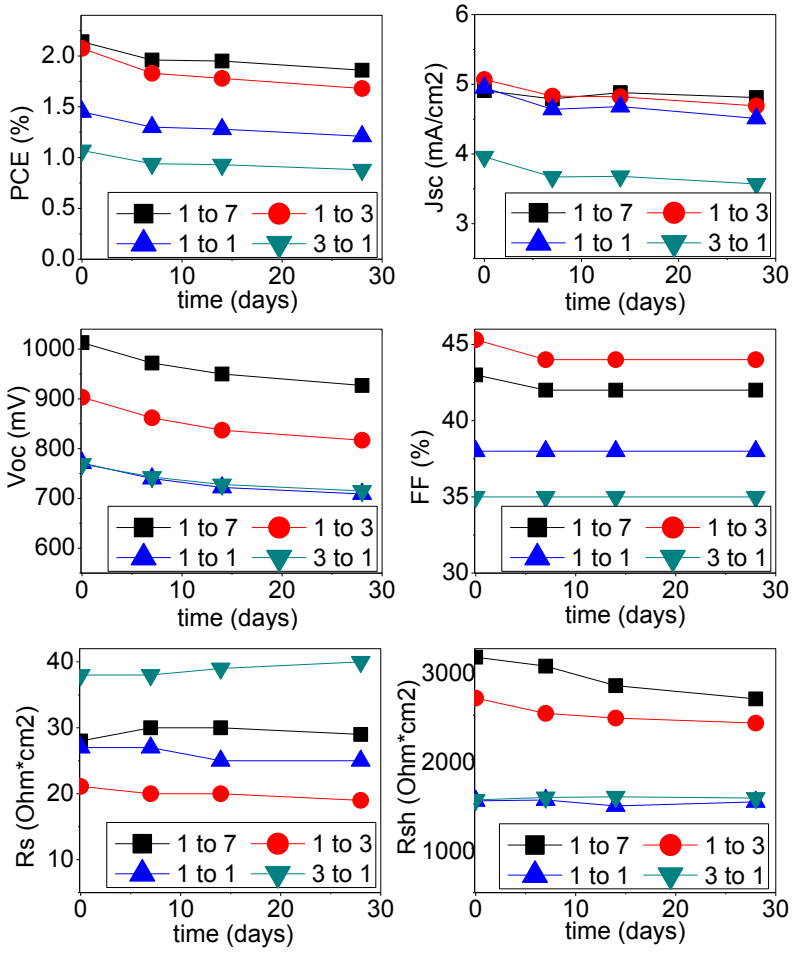

Supplemental Figure 1.6.1 - Raw photovoltaic output parameters for ClInPc:C_{60} OSCs at varying mixing ratios, as they are kept in a N_2 environment and exposed to 1-sun intensity light over the course of 28 days.

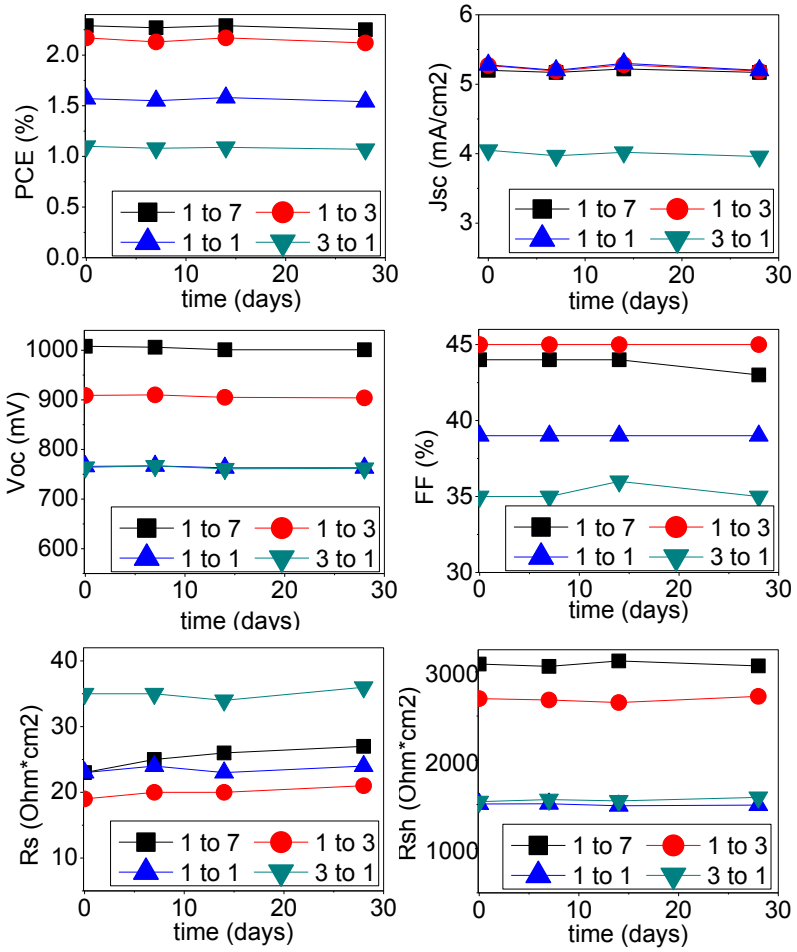

Supplemental Figure 1.6.2 - Raw photovoltaic output parameters for ClInPc:C_{60} OSCs at varying mixing ratios, as they are kept in a dark N_2 environment and heated at 40 ^{o}C over the course of 28 days.

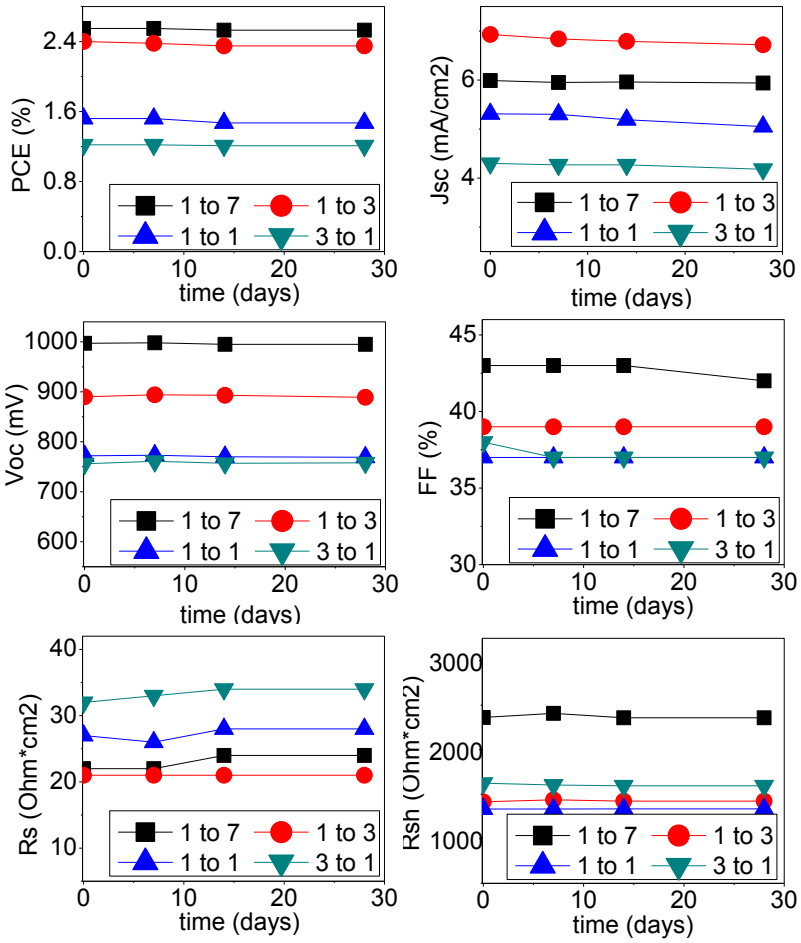

Supplemental Figure 1.6.3 - Raw photovoltaic output parameters for ClInPc:C_{60} OSCs at varying mixing ratios, as they are kept in a dark N_2 environment over the course of 28 days.

The results and discussion section for this chapter includes analysis of the EQE spectra for select mixing ratios of ClInPc:C_{60} OSCs. The full set of EQE spectra are provided below in Supplemental Figures 1.6.4 to 1.6.6 below.

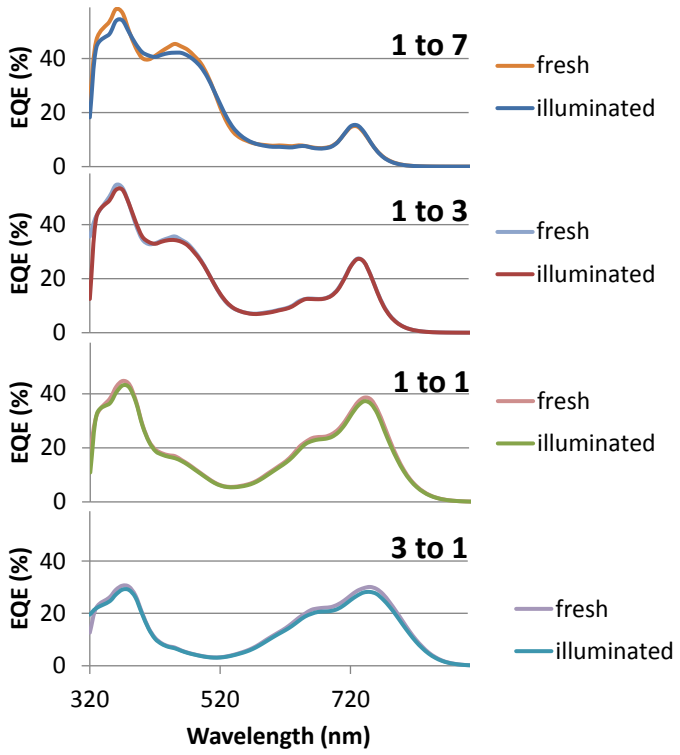

Supplemental Figure 1.6.4 - EQE spectra of ClInPc:C_{60} OSCs at varying mixing ratios pre- and post-illumination (1-sun intensity light for 28 days in N_2).

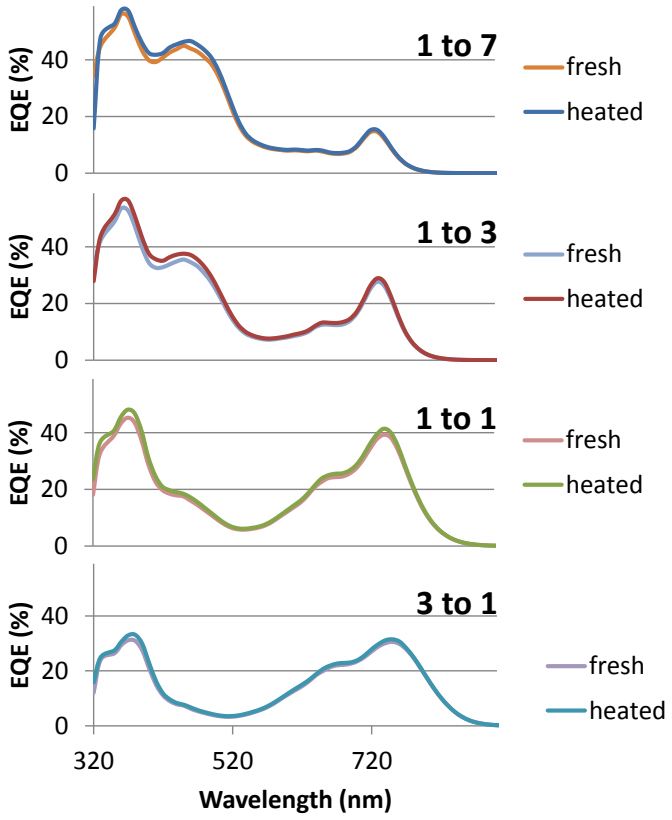

Supplemental Figure 1.6.5 - EQE spectra of ClInPc:C_{60} OSCs at varying mixing ratios pre- and post-heat treatment (40 $^{\circ}$C for 28 days in the dark in N_2).

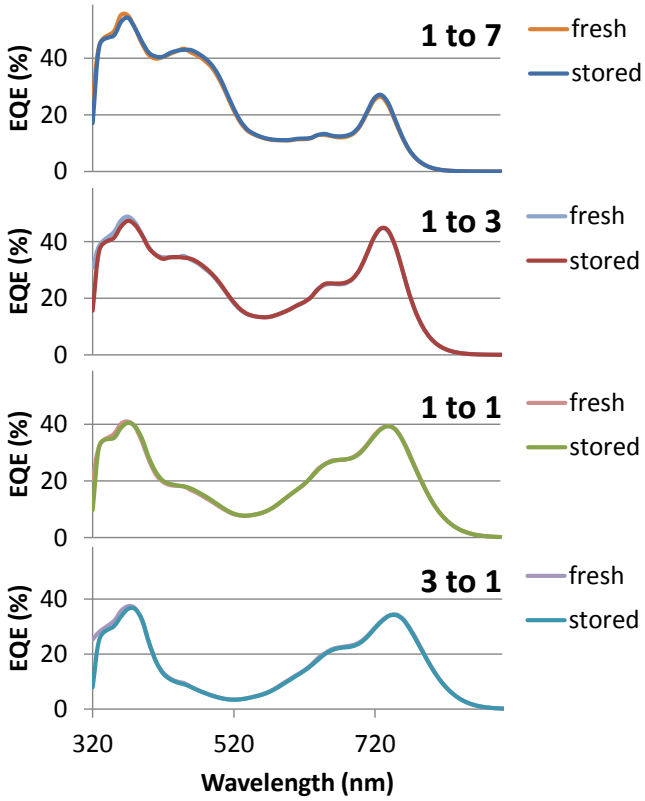

Supplemental Figure 1.6.6 - EQE spectra of ClInPc:C_{60} OSCs at varying mixing ratios pre- and post-storage for 28 days in the dark in N_2.

In the results and discussion section of this chapter, it is noted that no significant changes in the UV-Vis spectra of the ClInPc:C_{60} OSCs were observed after 28 days of either storage of the devices (in dark, in N_2) or exposure to light (1-sun intensity, in N_2). To this end, the UV/Vis absorption spectra show a perfect overlap, as shown in Supplemental Figures 1.6.7 and 1.6.8.

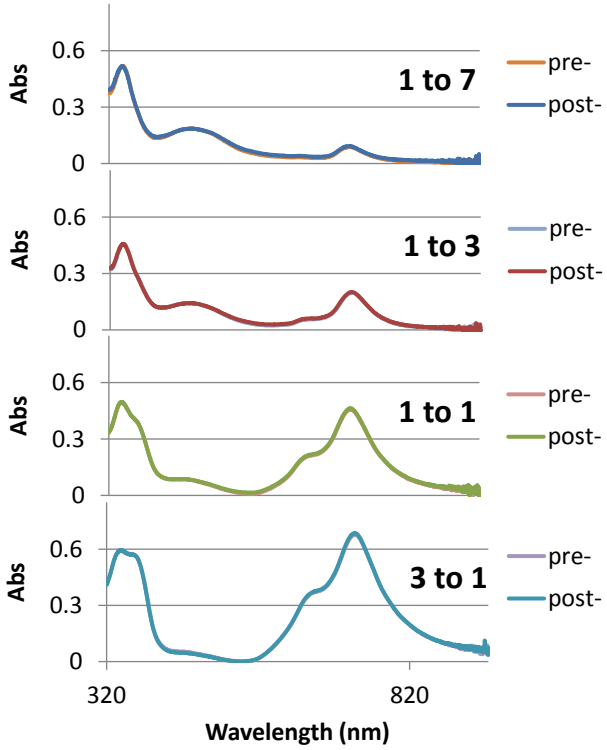

Supplemental Figure 1.6.7 - UV/Vis absorption spectra of ClInPc:C_{60} OSCs at varying mixing ratios pre- and post-illumination (1-sun intensity light for 28 days in N_2).

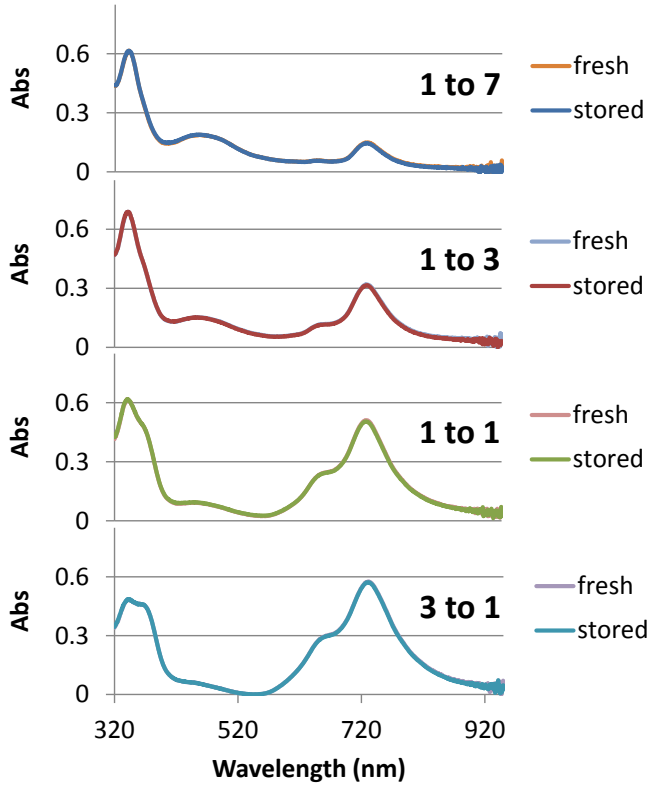

Supplemental Figure 1.6.8 - UV/Vis absorption spectra of ClInPc:C_{60} OSCs at varying mixing ratios pre- and post-storage for 28 days in the dark in N_2.

In the results and discussion section of this chapter, AFM measurements of ITO/MoO_3/ClInPc:C_{60}/BCP and ITO/MoO_3/ClInPc:C_{60} films after various different stress regimes are presented and discussed. Select figures are shown to illustrate trends as they relate to OSC stability. The full set of AFM measurements are provided in Supplemental Figures 1.6.9 and 1.6.10 below.

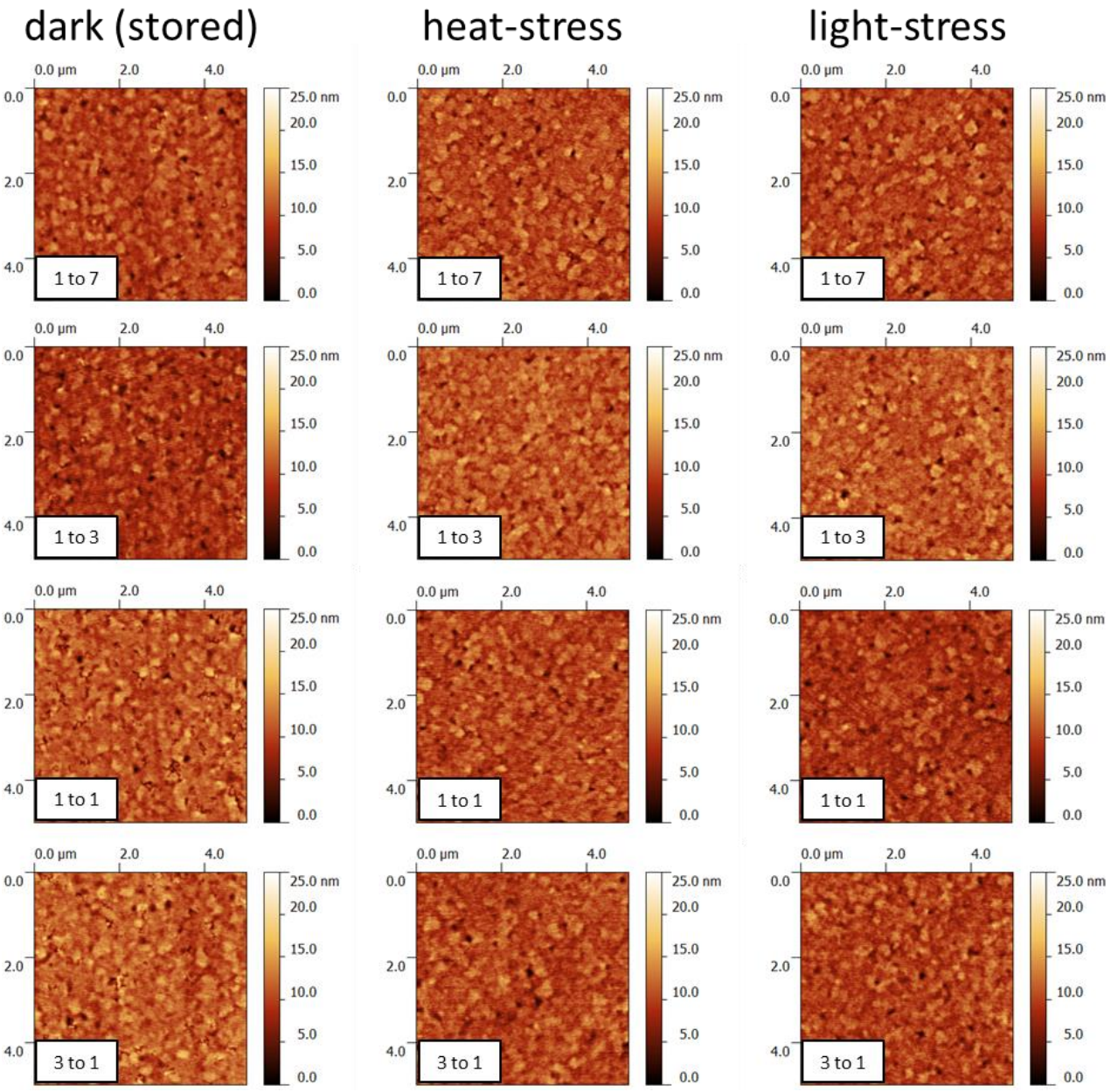

Supplemental Figure 1.6.9 - AFM measurements of ITO/MoO_3/ClInPc:C_{60}/BCP films at varying mixing ratios and under different stresses (dark/stored, heated at 40 ^{o}C and illuminated with 100 mW/cm^2 light).

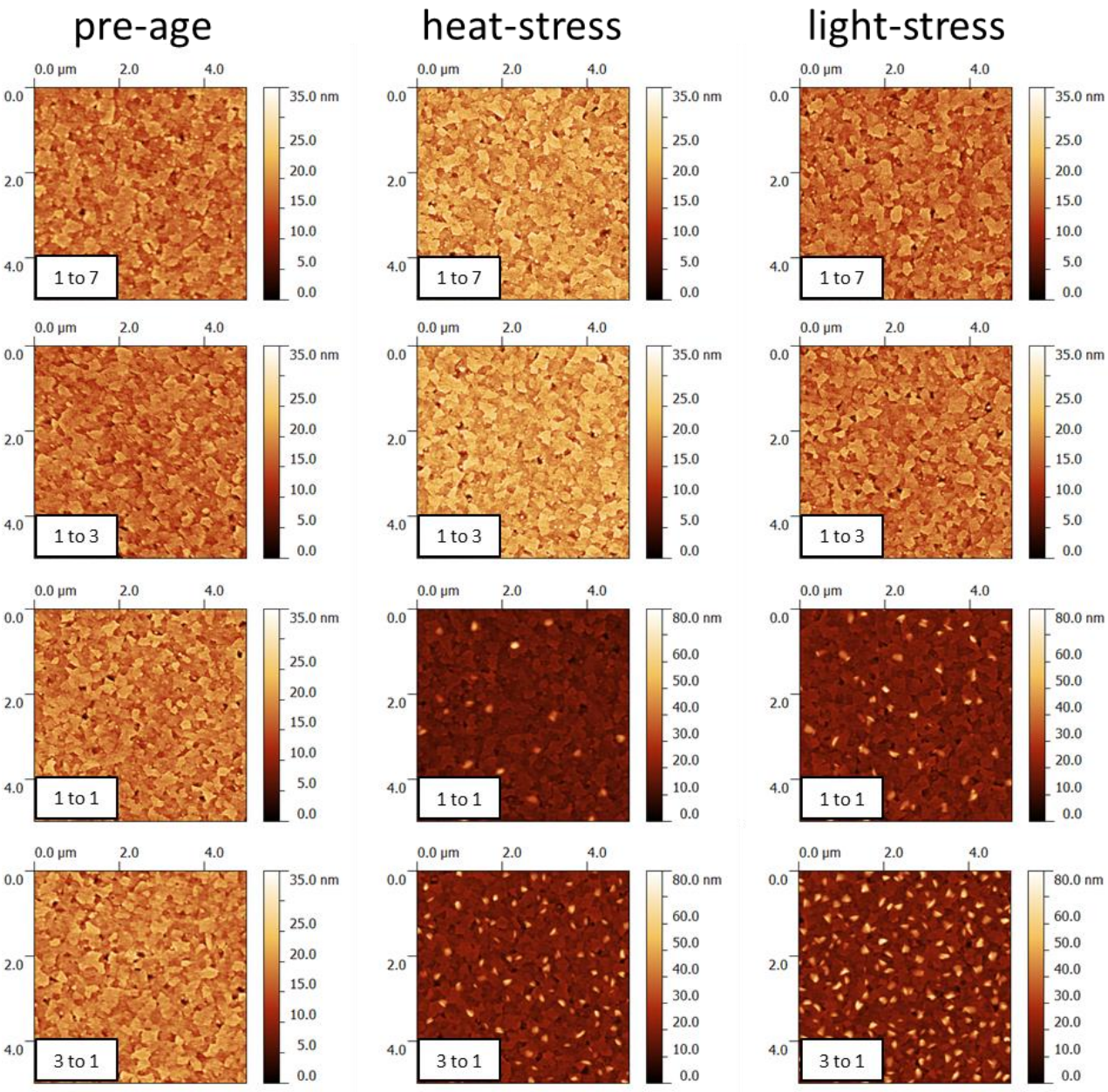

Supplemental Figure 1.6.10 - AFM measurements of ITO/MoO_3/ClInPc:C_{60} films at varying mixing ratios and under different stresses (pre-aged, heated at 40 ^{o}C and illuminated with 100 mW/cm^2 light).

Appendix 2:

Supplemental Characterization Tools, Software and Techniques

2.1. Imaging Organic Solar Cell Morphology with Organic Light Emitting Diode-Organic Solar Cell Devices[1]

P-OSCs have enjoyed a great deal of intense research, largely owing to their rapid improvements in PCE values. The morphology of these P-OSCs, both during fabrication and throughout their lifetime, has remained a critical area of study, and has been tied closely to PCE. This is perhaps most true for the widely studied P3HT: PCBM OSCs, which have exhibited significant morphological variations due to annealing, as well as due to a myriad of experimental conditions. The manner in which this active layer morphology has been probed is vast, with a most recent comprehensive study including high resolution transmission electron microscopy (HRTEM), small angle neutron scattering (SANS), dynamic secondary ion mass spectroscopy (DSIMS) and grazing incidence x-ray diffraction (GIXD).[291] Others have pursued an understanding of the visible (micro/macroscopic) morphology of P3HT:PCBM layers by optical microscopy.[292] More recently, researchers have examined electroluminescence and PL of the P3HT material itself, with the aid of a green-emitting laser and a highly sensitive Si-charge-coupled device (CCD).[293] In the present work, the visible morphology of P3HT:PCBM active layers is examined through electroluminescence of OSC-OLED composite structures.

The OSC-OLED structure is illustrated in Supplemental Figure 2.1.1.A) below. In its simplest operation as a light emitter, the OSC-OLED composite operates by injecting electrons from the Mg:Ag contact into Alq_3 and injecting holes from the ITO contact into PEDOT:PSS. The electrons traverse the Alq_3 layer until they reach the NPB/Alq_3 interface. The holes, however, must traverse the PEDOT:PSS layer, the P3HT:PCBM BHJ and the NPB layer to the NPB/Alq_3 interface. Once both species have arrived at the NPB/Alq_3 interface, they form an exciton, recombine and emit green light. This process is shown

[1] Including content from: G. Williams,H. Aziz, *SPIE Organic Photovoltaics XIII*, 2012, pp. 84770G1.

in Supplemental Figure 2.1.1.B. From Supplemental Figure 2.1.1.B, the holes will almost exclusively traverse the P3HT in the P3HT:PCBM BHJ due to the large energy barrier at P3HT/PCBM interfaces.

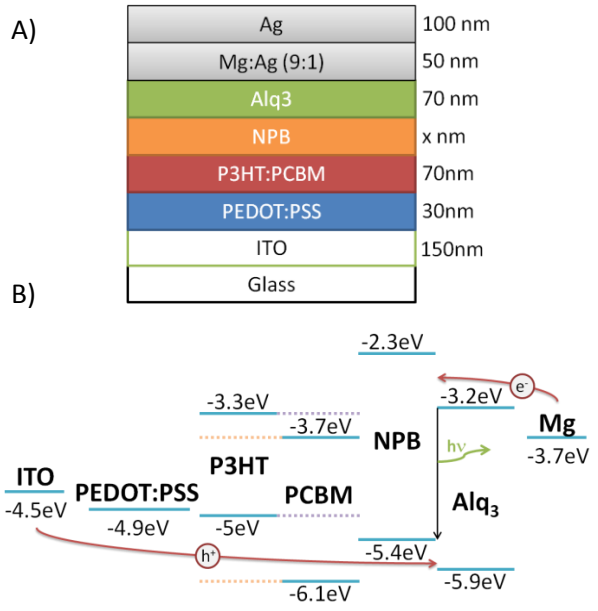

Supplemental Figure 2.1.1 - Illustration of the OSC-OLED composite structure used in this appendix. The hole-transport layer (NPB) thickness (x) is varied from 0 nm to 80 nm. B) Energy levels and work functions for the OSC-OLED composite structure.

The inherent difficulty with this device structure is the long trek that holes must make prior to reaching the NPB/Alq_3 interface. A vital caveat to high efficiency OLEDs is the balance of electron and hole current in the device to avoid unnecessary leakage and recombination current. For this particular device, if the NPB layer is too thick, the hole current will be much less than the electron current. However, NPB also serves the role of blocking electrons. Hence if the NPB layer is too thin or if no NPB is present at all, electrons will freely transfer into PCBM and there will be no exciton formation. It is thus logical to vary the hole transport layer (i.e. NPB) thickness to minimize leakage and recombination current and to maximize the OSC-OLED brightness.

The emission output parameters for OSC-OLED devices at NPB thicknesses of 0 nm to 80 nm are shown in Supplemental Table 2.1.1 below. In spite of the PEDOT:PSS and P3HT:PCBM layers present in the device structure, the driving voltages are reasonable, varying from 7.3 V to 11.9 V with an applied current of 12.5 mA/cm^2. For NPB thicknesses from 80 nm to 30 nm, the brightness remains relatively

constant at ~150 cd/m^2. 20 nm-NBP-thick devices were identified as ideal, providing a brightness of 175 cd/m^2 at a driving voltage of 8.5 V. The associated JVL characteristic for a representative 20 nm-NPB sample is shown in Supplemental Figure 2.1.2.

Supplemental Table 2.1.1 - OSC-OLED emission parameters for varying NPB thicknesses.

NPB Thickness (nm)	Current Density (mA/cm^2)	Driving Voltage (V)	Brightness (cd/m^2)	CIE Coordinates
80	12.5	11.9	147.8	0.367,0.527
50	12.5	9.3	147.8	0.337,0.544
30	12.5	8.8	148	0.319,0.531
20	12.5	8.5	175	0.316,0.515
10	12.5	7.3	40.2	0.323,0.506
0	12.5	10.5	1.2	0.459,0.437

With further reduction in the NPB thickness to 10 nm, the brightness drops sharply. Factoring in the roughness of P3HT:PCBM films after annealing, it is likely that NPB does not form a fully coherent film below 20 nm. In this case, it is energetically favorable for electrons to transfer directly to the PCBM acceptor and electroluminescence is quenched. It follows that in the case of the 0 nm-NPB-thick device the electroluminescence is virtually non-existent.

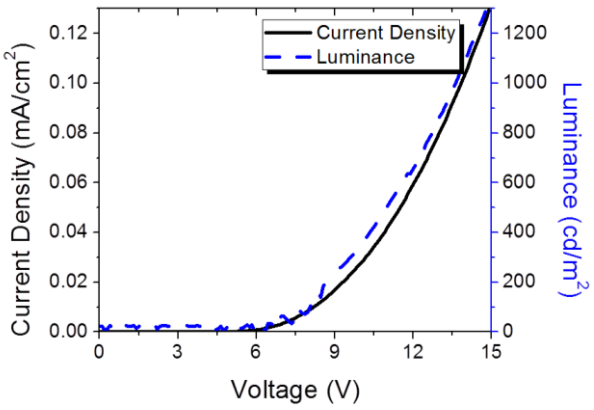

Supplemental Figure 2.1.2 – JV/Luminance (JVL) characteristic of a 20 nm-thick NPB OSC-OLED device.

Given the sensitivity of the emission brightness to the NPB thickness (and the likelihood for complete quenching of light with thin NPB), subsequent devices were fabricated with an NPB thickness of 30 nm, which operate with slightly lower luminance values and slightly higher driving voltages. A

digital image of the emission from a standard-fabrication device of device area 0.5 cm by 0.4 cm is shown in Supplemental Figure 2.1.3.A. This device was stored in the dark in an N_2 environment prior to and during imaging.

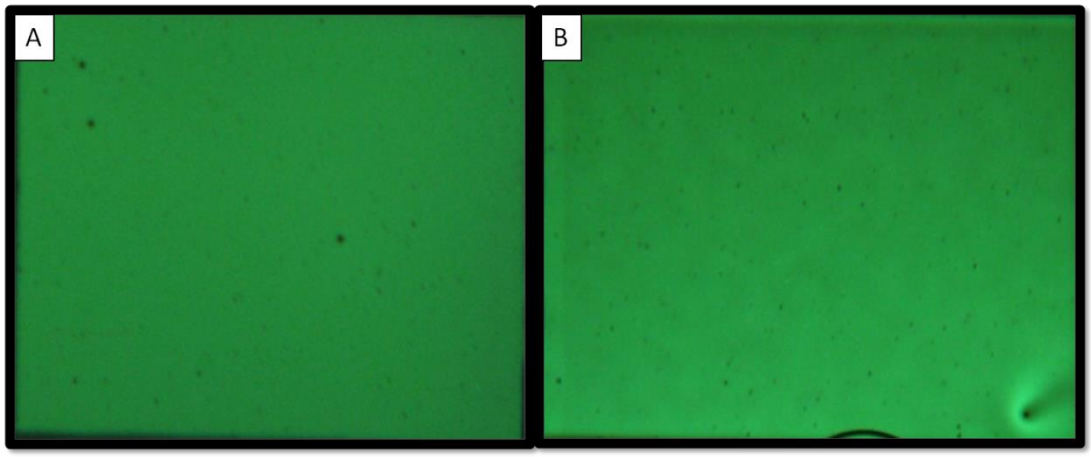

Supplemental Figure 2.1.3 - A) Image of the full emission area from a 0.4 cm by 0.5 cm OSC-OLED device. B) Image of the full emission area for an OSC-OLED device that has skipped the OSC annealing steps.

Of immediate interest are the dark spots present throughout the device area, which correspond to non-emissive areas. They are comprised of impurities, large aggregates that were unable to dissolve during solution preparation or large aggregates that formed during the thermal annealing step. However, as a point of interest, these dark spots were not visible as any form of defect or aggregate to the naked eye for the freshly spincoated or the thermally annealed P3HT:PCBM film (prior to the OLED deposition). Since these areas are non-emissive, it follows that they are not sufficiently conductive to carry current. In terms of the corresponding solar cell for this device, these areas would ultimately yield zero photocurrent. A polymer formulation that results in significant dark spot formation in an OSC-OLED device will logically have low performance (poor photovoltaic output parameters).

In order to probe the effect of annealing on the emission of the OSC-OLED device, an OSC-OLED was fabricated without any OSC annealing. A digital image of the emission from this device is shown in Supplemental Figure 2.1.3.B. The comet-tail defect in the bottom-right of this image formed due to the movement of a larger aggregate or impurity during spincoating, and has resulted in a streak of non-

emissive area. Following the above argument, a polymer formulation that yields significant *visible* particulate matter will obviously yield lower photocurrent and thus result in poorer OSC performance. The un-annealed OSC-OLED (Supplemental Figure 2.1.3.B) exhibits an underlying 'cloudiness' compared to the rather coherent and constant green texture of the annealed OSC-OLED (Supplemental Figure 2.1.3.A)). The cloudiness implies a change in morphology underneath the emissive areas of the OLED (i.e. beneath NPB and Alq_3). The origin of the cloudiness for the un-annealed sample is currently unclear. It is feasible that during the annealing step, the vertical segregation of PCBM results in a rougher P3HT:PCBM/air surface, as discussed in literature,[292] which leads to the incoherent and random scattering of light at the P3HT:PCBM/NPB interface. Without this annealing step, significantly more P3HT would be present at this interface and its natural phase separation could yield a more coherent reflection of light, resulting in the cloudy appearance.

As an additional point of note, this OSC-OLED device structure may prove to have some applications to help further characterize electrical properties of OSC layers as well as OSC aging mechanisms. For example, one may consider using such devices to test the photoconductivity of the BHJ layer. By altering the configuration of the device, inverting either the OSC or OLED portion, one could feasibly make use of the OSC photocurrent to amplify any variations in photoconductivity. Coupling this technique with a fine-point emission source, either with lasers or optical fibres, could grant 2-D mapping of photoconductivity and photocurrent. One may also consider recent data comparing PEDOT:PSS HELs to MoO_3 HELs, which have suggested cathode sensitivity to the residual moisture present in PEDOT:PSS films.[11]. The NPB/Alq_3 OLED is incredibly sensitive to ambient (H_2O- and O_2-related) degradation,[111] especially at the Mg:Ag cathode.[110] As such, the OSC-OLED device is uniquely situated to verify these stipulations, and it serves as a useful technique in testing the effects of residual solvent for numerous other OSC systems and polymer formulations.

2.2. Solar Cell Parameter Extraction by MATLAB

In all OSC research, it is assumed that researchers use similar methods to obtain relevant solar cell parameters from the solar cell output IV characteristics. The equivalent circuit for a generic solar cell has the following current-voltage relationship:

$$I_{total} = I = -I_{photocurrent} + I_{diode} + I_{shunt} \quad \text{(A2.2-1)}$$

$$I = -I_{ph} + I_0\left(\exp\left[\frac{V+IR_s}{nV_{th}}\right] - 1\right) + G_{sh}(V + IR_s) \quad \text{(A2.2-2)}$$

, where I_0 is the reverse saturation current, n is the diode ideality factor, $V_{th}=k_BT/q$ is the thermal voltage, R_s is the series resistance and G_{sh} is the shunt conductance ($G_{sh}=1/R_{sh}$).

It is important to note that the diode parameters in the equation above do not have the same explicit meanings as they do for single crystal p-n junction or Schottky junction diodes. However, these values are inherently related to equivalent processes that produce similar device behaviour in the organic devices. For example, since the diode ideality factor is strongly related to recombination in silicon p-n junctions, either by space charge recombination or high level injection, it is expected that this parameter is similarly related to recombination mechanisms in OSCs. As such, comparison of these parameters across different experimental OSCs can still yield important information regarding device operation.

The most frequently reported solar cell parameters are the V_{oc}, J_{sc}, FF and PCE. These values are straightforward to calculate from solar cell output characteristics. However, the R_{sh} and R_s values, which are arguably the next most useful parameters for OSCs, are not as simple to ascertain. In recent studies on OSCs, researchers used the slope of the output curve under dark conditions at V=0 V and V=2 V to find the R_{sh} and R_s values respectively.[29] This very simple approach was described many years earlier

for CdS thin film solar cells, [294] and involves the assumption that R_s is small and R_{sh} is large. This approach generally provides reasonable values for the R_{sh} based on the logic shown below:

- R_{shunt}: I_{ph}~=0 (dark output), so $I = I_0\left(\exp\left[\frac{V+IR_s}{nV_{th}}\right]-1\right)+G_{sh}(V+IR_s)$
  At the current axis V=0 V, I is small and if R_s is small, $\exp\left[\frac{V+IR_s}{nV_{th}}\right] \cong \exp[0] = 1$.

  Further, G_{sh} is generally small because R_{sh} is ideally large, so $G_{sh}IR_s$ must be very small. Thus,

$$I \cong I_0(1-1) + G_{sh}V + G_{sh}IR_s \cong G_{sh}V$$

$$I \cong G_{sh}V \; or \; \frac{dI}{dV} \cong G_{sh} \quad \therefore \frac{dV}{dI}(V=0V) \cong R_{sh}$$

However, as noted above, this method is only valid under the condition that the solar cell has reasonably good properties with a high R_{sh} and low R_s. Furthermore, the calculation for R_s is only valid if a 'good' voltage point is chosen for the slope calculation. In the study of OSCs, especially with new materials and varying device architectures, the assumptions of low R_s and high R_{sh} are not strictly valid. In order to obtain more accurate values for both the R_s and R_{sh} as well as the diode parameters of the solar cell, one must fit the solar cell parameters to the current equation shown in (A2.2-2) above.

There are numerous methods described in literature to extract the relevant diode parameters.[295-299] In this appendix, three of these methods are examined for their relative success in analyzing sample IV output data representative of an illuminated organic solar cell. A summative comparison of the extracted parameters using several different methods is provided in Supplemental Table 2.2.1. The MATLAB code for all methods examined is provided below.

The simplest manner to extract the solar cell parameters is through the use of a nonlinear least squared error fit where equation (A2.2-2) is used to calculate current directly. Unfortunately, since equation (A2.2-2) is a transcendental equation, it is difficult to solve for explicit current values. In order

to circumvent this problem, it is convenient to use the Lambert W function, as described in greater detail in [299, 300]. After some algebra, equation (A2.2-2) may be rearranged into the form:

$$I = -\frac{V}{R_s+R_{sh}} - \frac{nV_{th}}{R_s} \cdot LambertW\left[\frac{R_s I_0 R_{sh} e^{\left[\frac{R_{sh}\left(V+R_s I_0+R_s I_{ph}\right)}{nV_{th}\left(R_s+R_{sh}\right)}\right]}}{nV_{th}(R_s+R_{sh})}\right] + \frac{R_{sh}\left(I_0+I_{ph}\right)}{R_s+R_{sh}} \qquad \text{(A2.2-3)}$$

, where LambertW is the Lambert W function and I_{ph} is assumed to be approximately equal to the I_{sc}.[299] The results for this method are detailed under the heading 'Method 1' in Supplemental Table 2.2.1 and Supplemental Figure 2.2.1 below. Unfortunately, this method is computationally intensive and susceptible to divergence problems as well as local minima convergence issues. Furthermore, the requirement of initial guesses infers that the researcher has some knowledge regarding the device characteristics prior to analysis, which may not always be true.

As an alternative approach for efficient parameter extraction, Chegaar and coworkers developed a very simple, robust method for solving the solar cell parameters using only the illuminated-device IV characteristics of a solar cell.[298] This method is particularly appropriate for organic solar cells because it makes minimal assumptions regarding the device structure. This method also requires no prior knowledge regarding the solar cell parameters. Furthermore, it has been shown to work reasonably well with IV characteristics that contain a significant amount of noise.

In brief, Chegaar and coworkers modified equation (A2.2-2) to collect the non-exponential current terms and then performed a shunt current correction to obtain I_c. The authors then re-wrote the current-voltage equation with the voltage as the dependent term and the current as the independent term, as shown below:

$$I_c = I_{pA} - I_0\left[exp\left(\frac{\beta}{n}(V+IR_s)\right)\right] \;\Rightarrow\; V = \frac{n}{\beta} ln\frac{I_{pA}}{I_0} + \frac{n}{\beta} ln\left(1-\frac{I_c}{I_{pA}}\right) - R_s I \qquad \text{(A2.2-4)}$$

Since the right side of (7) is of the form $f(I) = C_0 + C_1 I + C_2 \ln(1 - \frac{I_c}{I_{pA}})$, it is simple to perform a simple least squares method to determine the relevant solar cell parameters. In this particular study, the least squares approach is accomplished through the solution of a system of equations. This method, denoted 'Method 2,' proved to be very quick and yielded experimentally accurate and relevant data, as shown in Supplemental Table 2.2.1 and Supplemental Figure 2.2.1.

The final method examined in this review is based off of recent work by Nehaoua et. al. that was aimed to help with parameter determination for organic solar cells.[296] This method uses a very unique approach to solve for the series resistance and diode ideality factor, which involves linear regression on a set of data derived from subsets of the initial IV output data. The reader is encouraged to examine references [296, 301] for a more detailed explanation of this process. Unfortunately, this method proved to be rather unstable for the sample data. The extracted diode parameters were found to vary strongly depending on the amount and range of input IV data passed to the MATLAB function. The results are also presented as 'Method 3' in Supplemental Table 2.2.1 and Supplemental Figure 2.2.1.

Supplemental Table 2.2.1 - Summary of Extracted Diode Parameters for Different Methods of Analysis on Sample Illuminated IV Organic Solar Cell Data

	I_{SC} (A)	V_{OC} (V)	FF	R_{sh} (Ω)	R_s (Ω)	n	I_0 (A)
Method 1[299]	0.0064	0.6	0.4902	3.64E+04	38.2436	1.0688	2.21E-12
Method 2[298]	0.0064	0.6	0.4902	3.63E+04	35.4685	1.3637	2.63E-10
Method 3[296]	0.0064	0.6	0.4902	3.62E+04	107.4207	3.0274	2.00E-08*

**Method 3 does not output a reverse saturation current. This value was determined graphically by attempting to best fit the model to the input data. It is noted that this simple approach to finding I_0 is the likely cause for error with the present implementation of this method.*

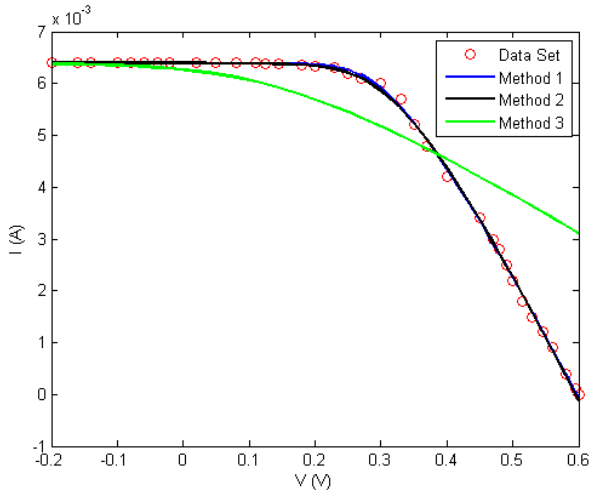

Supplemental Figure 2.2.1 - Experimental and modelled solar cell IV output for various methods of parameter extraction.

The methods detailed by Jain and Kapoor in 2005[299] and by Bouzidi et. al. in 2007[298] have shown to provide very close fits to the illuminated IV data. From the tabulated data in Supplemental Table 2.2.1, it is clear that variations between the R_s and R_{sh} values from both methods 1 and 2 are relatively small, indicating that cross comparisons between data using either method are valid. However, one should take precaution when cross-comparing diode ideality factors and reverse saturation current values, as they are shown to vary by up to ~1.3-times and 2 orders of magnitude respectively between the two methods for the same data set.

As an additional note, Schilinsky et. al. have examined a modified single-diode model where the photocurrent, I_{ph}, varies as a function of the applied voltage, such that the model can account for the field dependence of the photocurrent.[302] The authors note that a similar approach has been previously successful in the study of amorphous silicon diodes and solar cells. In typical models, the photocurrent is generally assumed to be equal to the I_{sc}. In contrast, this model defines the photocurrent as shown below, which allows for accurate measurements over a wider range of illumination intensities.

$$I_{ph} = \begin{cases} -|I_{sc}| & \text{if } \mu\tau(-V + V_{bi})/L > L \\ |I_{sc}| & \text{if } \mu\tau(V - V_{bi})/L > L \\ |I_{sc}|\mu\tau(-V + V_{bi})/L^2 & else \end{cases}$$

This variation introduces the free carrier mobility, μ, the free carrier lifetime, τ, and the built in voltage of the junction as additional fitting parameters. While these fitting parameters should only be taken as estimates of their true values, they may provide crucial information in the study and comparison of organic solar cells among different research groups.

The MATLAB code used in the solar cell parameter extraction is provided below.

Method 1

Jain2005.m

```
function [  ] = Jain2005(IVData)
%This function calculates all of the relevant solar cell parameters given
%an input matrix IVData containing data in the form [Voltage Current]

%This script uses a very simple sum of squared approach to converge toward
%the ideal fitting parameters.  This script requires initial guess values.

%Constants
q = 1.602*10^-19;
k = 1.38*10^-23;
T = 298;
beta = q./(k.*T);
Vth = 1./beta;

global I V Isc Rsh

%-------------------------------------------------------------------------
%Breaking apart input matrix
V=IVData(:,1);
I=IVData(:,2);

%Finding the Isc (foo is a dummy variable)
[foo, SCindex] = min(abs(V));
Isc = I(SCindex);

%Finding the Voc
[foo, OCindex] = min(abs(I));
Voc = V(OCindex);

%Selecting the region of interest for the input data
V=IVData(SCindex+6:OCindex-1,1);
I=IVData(SCindex+6:OCindex-1,2);

%Using the slope at V=0V as Rsh (otherwise the function is under-defined and
%diverges)
Vlin=IVData(1:SCindex+1,1);
Ilin=IVData(1:SCindex+1,2);
[f,err] = polyfit(Vlin, Ilin,1);
Gsh = -f(1); %Defining the shunt resistance as the slope
Rsh = 1./Gsh;

%Initial guess values
Rs = 10;
```

```
n = 2;
I0 = 1*10^-10;

a= [Rs; n; I0];

%Calculating the modelling variables by minimizing SSE (using a
%user-defined function that takes the input data + initial guesses and
%outputs the sum of squared error)
solved = fminsearch(@diode_minerr, a);

%----------------------------------
%Fill factor and power calculations
V=IVData(:,1);
I=IVData(:,2);
Vmod = V(SCindex:OCindex);
Imod = I(SCindex:OCindex);

P = Vmod.*Imod;
[Pmax,Pmaxpt] = max(abs(P));
Vprime = Vmod(Pmaxpt);
Iprime = Imod(Pmaxpt);

FF = (Iprime.*Vprime)./(Voc.*Isc);
%----------------------------------

%Outputting relevant data
Isc
Voc
FF
Rsh
Rs = solved(1)
n = solved(2)
I0 = solved(3)
```

diode_minerr.m

```
function SSE = diode_minerr(a)
%This function requires the (global) data from the IV characteristics and
%the initial guesses for the fitting parameters.  It calculates the
%error between the diode-Rs-Rsh model and the experimental IV values.

%The rearranged, explicitly solved current equation (making use of the
%Lambert W function) was taken from Jain & Kapoor, 2005, "A new method to
%determine the diode ideality factor of real solar cell using Lambert
%W-function"

%Variables
q = 1.602*10^-19;
k = 1.38*10^-23;
T = 298;
beta = q./(k.*T);
Vth = 1./beta;

global I V Isc Rsh

%Exploding the a variable
Rs = a(1);
n = a(2);
I0 = a(3);

%Prediction of the current using the Lambert W function
```

```
Ipred = -V./(Rs+Rsh)-
lambertw(((Rs.*I0.*Rsh).*exp((Rsh.*(Rs.*Isc+Rs.*I0+V))./(n.*Vth.*(Rs+Rsh)))).*(Rs.*n.*
Vth+Rsh.*n.*Vth)).*(n.*Vth)./Rs + Rsh.*(I0+Isc)./(Rs+Rsh);

%Calculating sum of square errors
SSE = sum((Ipred-I).^2);
```

Method 2

Chegaar2007.m

```
function [  ] = Chegaar2007( IVData )
%This function calculates all of the relevant solar cell parameters given
%an input matrix IVData containing data in the form [Voltage Current]

%The methods of this script are based on the paper 'Ouennoughi and
%Chegaar,' 1999 - "A simpler method for extracting solar cell parameters
%using the conductance method"

%Variables
q = 1.602*10^-19;
k = 1.38*10^-23;
T = 298;
beta = q./(k.*T);

%-------------------------------------------------------------------------
%Breaking apart input matrix
V=IVData(:,1);
I=IVData(:,2);

%Finding the Isc (foo is a dummy variable)
[foo, SCindex] = min(abs(V));
Isc = I(SCindex);

%Finding the Voc
[foo, OCindex] = min(abs(I));
Voc = V(OCindex);

%Selecting the region of interest for the input data
V=IVData(SCindex+6:OCindex-1,1);
I=IVData(SCindex+6:OCindex-1,2);

%Calculating low bias correction values
Vlin=IVData(1:SCindex+1,1);
Ilin=IVData(1:SCindex+1,2);

%Computing the linear fit
[f,err] = polyfit(Vlin, Ilin,1);
%Defining the modified shunt resistance as the slope
Ga = -f(1);
Ipa = f(2);

%Calculating the corrected current
Ic = I - Ga.*V;

%-----
%Defining the variables of the least squares matrix
ls1 = sum(I.^2);

ls2 = 0;
for i = 1:length(I)
```

```
    ls2 = ls2 + I(i).*log(1-Ic(i)./Ipa);
end

ls3 = sum(I);

ls4 = sum(I);

ls5 = 0;
for i = 1:length(I)
    ls5 = ls5 + log(1-Ic(i)./Ipa);
end

ls6 = length(I);

ls7 = 0;
for i = 1:length(I)
    ls7 = ls7 + I(i).*log(1-Ic(i)./Ipa);
end

ls8 = 0;
for i = 1:length(I)
    ls8 = ls8 + (log(1-Ic(i)./Ipa)).^2;
end


ls9 = 0;
for i = 1:length(I)
    ls9 = ls9 + log(1-Ic(i)./Ipa);
end

lsmatrix = [ls1 ls2 ls3; ls4 ls5 ls6; ls7 ls8 ls9];
%------

a1 = sum(I.*V);

a2 = sum(V);

a3 = 0;
for i = 1:length(I)
    a3 = a3 + V(i).*log(1-Ic(i)./Ipa);
end

amatrix = [a1; a2; a3];

%Solving for the variables of the least squares matrix
C = linsolve(lsmatrix,amatrix);

%Solving for various parameters
Rs = -C(1);  %series resistance
n = beta.*C(2);  %diode ideality coefficient
I0 = Ipa.*exp(-C(3)./C(2));  %I0

foo = 1 - Ga.*Rs;  %dummy variable

Gsh = Ga./foo;  %shunt conductance
Rsh = 1./Gsh; %shunt resistance
Iph = Ipa./foo;   %photocurrent
Is = I0./foo;  %saturation current

%---------------------------------
%Fill factor and power calculations
V=IVData(:,1);
I=IVData(:,2);
```

```
Vmod = V(SCindex:OCindex);
Imod = I(SCindex:OCindex);

P = Vmod.*Imod;
[Pmax,Pmaxpt] = max(abs(P));
Vprime = Vmod(Pmaxpt);
Iprime = Imod(Pmaxpt);

FF = (Iprime.*Vprime)./(Voc.*Isc);
%----------------------------------

%Outputting relevant data
Isc
Voc
FF
Rsh
Rs
n
I0
```

Method 3

Nehaoua2010.m

```
function [  ] = Nehaoua2010( IVData )
%This function calculates Rs, Rsh and n given an input matrix IVData
%containing data in the form [Voltage Current]

%The method for parameter extraction is based on Nehaoua et. al. in
%'Determination of organic solar cell parameters based on single or
%multiple pin structures,' Vacuum, 2010.

%Reverse saturation current is not calculated in this particular method as
%the authors calculate I0 separately

%Variables
q = 1.602*10^-19;
k = 1.38*10^-23;
T = 298;
beta = q./(k.*T);

%--------------------------------------------------------------------------
%Breaking apart input matrix
V = IVData(:,1);
I = -IVData(:,2);

%Finding the location of Isc/Voc (foo is a dummy variable)
[foo, SCindex] = min(abs(V)); %min(abs(V))=y-axis intercept
Isc = I(SCindex);
[foo, OCindex] = min(abs(I)); %min(abs(I))=x-axis intercept
Voc = V(OCindex);

%Calculating the shunt conductance/resistance
Vlin = IVData(1:SCindex+6,1);
Ilin = -IVData(1:SCindex+6,2);
[f,err]=polyfit(Vlin, Ilin,1);
Gshunt=f(1); %This sets the conductance as the slope
Rsh = 1./Gshunt;

%Calculating shunt current
Ip = Gshunt.*V;
%Calculating the true current across the solar cell
```

```
I = I+Ip;

%Finding the new Isc & Voc taking shunt current into consideration
[foo, SCindex] = min(abs(V));
Isc = I(SCindex);
[foo, OCindex] = min(abs(I));
Voc = V(OCindex);

%Fill factor and power calculations
Vmod = V(SCindex:OCindex);
Imod = I(SCindex:OCindex);

P = Vmod.*Imod;
[Pmax,Pmaxpt] = max(abs(P));

Vprime = Vmod(Pmaxpt);
Iprime = Imod(Pmaxpt);

FF = (Iprime.*Vprime)./(Voc.*Isc);

%----------------------------------
%Rshunt, Rseries and n
%Redefining the range of data - only focusing on the region of 'diode'
%behaviour
V = IVData(1:OCindex-1,1);
I = -IVData(1:OCindex-1,2);
%Calculating shunt current
Ip = Gshunt.*V;
%Calculating the current across the solar cell
I = I+Ip;

%Solving for the linear regression parameters
X = [];
Y = [];
Iph = Isc; %Ishort circuit approximately equals photocurrent

for i = 1:(length(V)-1)
    for j = (i+1):length(V)
        if abs(Iph) > abs(I(j))  %Protection from noise, which can cause |I| > |Isc|
            if abs(Iph) > abs(I(i))  %Same as above
                X = [X; (V(j)-V(i))./(I(j)-I(i))];
                Y = [Y; (1./(I(j)-I(i))).*log((Iph-I(j))./(Iph-I(i)))];
            end
        end
    end
end

%Computing the linear fit
[f,err] = polyfit(X,Y,1);

%Solving for pertinent data
slope = f(1);
yint = f(2);
nval = beta./slope;
Rs = nval.*yint./beta;

%Outputting the relevant data
Isc
Voc
FF
Rsh
Rs
nval
```

Plotting Function

Plotting.m

```
function [  ] = Plotting( IVData, SolvedParam )

%Variables
q = 1.602*10^-19;
k = 1.38*10^-23;
T = 298;
beta = q./(k.*T);
Vth = 1./beta;

%Breaking apart input matrix
V=IVData(:,1);
I=IVData(:,2);

%Generic Solved Data
Isc = SolvedParam(1,1);
Voc = SolvedParam(1,2);
FF = SolvedParam(1,3);

%Method-specific Data
%Method 1
m1_Rsh = SolvedParam(1,4);
m1_Rs = SolvedParam(1,5);
m1_n = SolvedParam(1,6);
m1_I0 = SolvedParam(1,7);

%Method 2
m2_Rsh = SolvedParam(2,4);
m2_Rs = SolvedParam(2,5);
m2_n = SolvedParam(2,6);
m2_I0 = SolvedParam(2,7);

%Method 3
m3_Rsh = SolvedParam(3,4);
m3_Rs = SolvedParam(3,5);
m3_n = SolvedParam(3,6);
m3_I0 = SolvedParam(3,7);

%Creating a separate folder in which to save the figures
mkdir('DataFigures');
figsavepath = ['DataFigures\'];

%Model 1
Rsh = m1_Rsh;
Rs = m1_Rs;
n = m1_n;
I0 = m1_I0;
%Generating the model data
Ipred1 = -V./(Rs+Rsh)-
lambertw(((Rs.*I0.*Rsh).*exp((Rsh.*(Rs.*Isc+Rs.*I0+V))./(n.*Vth.*(Rs+Rsh)))).*(Rs.*n.*
Vth+Rsh.*n.*Vth)).*(n.*Vth)./Rs + Rsh.*(I0+Isc)./(Rs+Rsh);

%Model 2
Rsh = m2_Rsh;
Rs = m2_Rs;
n = m2_n;
I0 = m2_I0;
```

```
%Generating the model data
Ipred2 = -V./(Rs+Rsh)-
lambertw(((Rs.*I0.*Rsh).*exp((Rsh.*(Rs.*Isc+Rs.*I0+V))./(n.*Vth.*(Rs+Rsh)))).*(Rs.*n.*
Vth+Rsh.*n.*Vth)).*(n.*Vth)./Rs + Rsh.*(I0+Isc)./(Rs+Rsh);

%Model 3
Rsh = m3_Rsh;
Rs = m3_Rs;
n = m3_n;
I0 = m3_I0;
%Generating the model data
Ipred3 = -V./(Rs+Rsh)-
lambertw(((Rs.*I0.*Rsh).*exp((Rsh.*(Rs.*Isc+Rs.*I0+V))./(n.*Vth.*(Rs+Rsh)))).*(Rs.*n.*
Vth+Rsh.*n.*Vth)).*(n.*Vth)./Rs + Rsh.*(I0+Isc)./(Rs+Rsh);

%Creating a filename
figname = [figsavepath 'PlotComparison' '.png'];

figsave = figure;
p = plot(V,I,'o'); %Plotting experimental data
set(p,'Color','red')
hold on
q = plot(V,Ipred1,'-'); %Plotting Method 1
set(q,'Color','blue','LineWidth',2)
r = plot(V,Ipred2,'-'); %Plotting Method 2
set(r,'Color','black','LineWidth',2)
s = plot(V,Ipred3,'-'); %Plotting Method 3
set(s,'Color','green','LineWidth',2)
xlabel('V (V)');
ylabel('I (A)');
legend('Data Set', 'Method 1', 'Method 2', 'Method 3');
print(figsave, figname, '-dpng');

end
```

2.3. Transfer Matrix Formalism for Calculation of Optical Field Distribution in Organic Solar Cells

Modelling of the electric field within the OSC can be used to accurately determine the layer thicknesses required to obtain maximum OSC efficiency. This approach relies on the notion that the generation rate of excitons is proportional to the intensity of the optical field within the cell. The electric field throughout the device is dependent on the reflection and absorption of light due to variations in the complex refractive indices of the various OSC layers. The transmittance and reflectance of light can thus be modelled by Fresnel equations. The electric field can be further plotted by transfer matrix formalism, as has been shown by Pettersson et al. and Sievers et al.[44, 45]

2.3.1. Modelling Theory

It is first useful to consider a plane wave of light incident on a superstrate OSC. The behaviour of the light at any interface can be described by Fresnel coefficients, which can be organized in an interference matrix for an arbitrary interface of material j and material k:

$$I_{jk} = \begin{bmatrix} \frac{1}{t_{jk}} & \frac{r_{jk}}{t_{jk}} \\ \frac{r_{jk}}{t_{jk}} & \frac{1}{t_{jk}} \end{bmatrix} \quad \text{(A2.3-1)}$$

, where t_{jk} and r_{jk} are the complex transmission and reflection coefficients:

$$t_{jk} = \frac{2\boldsymbol{n_j}}{\boldsymbol{n_j}+\boldsymbol{n_k}} \quad \text{(A2.3-2)}$$

$$r_{jk} = \frac{\boldsymbol{n_j}-\boldsymbol{n_k}}{\boldsymbol{n_j}+\boldsymbol{n_k}} \quad \text{(A2.3-3)}$$

, where $\mathbf{n_j}$ and $\mathbf{n_k}$ are the complex indices of refraction for materials j and k respectively – for example, $\mathbf{n_j}$=n+i*κ, where n is the real part and κ is the imaginary part of the refractive index.

The interference matrix can then be rewritten as:

$$\boldsymbol{I_{jk}} = \begin{bmatrix} \frac{\boldsymbol{n_j}+\boldsymbol{n_k}}{2\boldsymbol{n_j}} & \frac{\boldsymbol{n_j}-\boldsymbol{n_k}}{2\boldsymbol{n_j}} \\ \frac{\boldsymbol{n_j}-\boldsymbol{n_k}}{2\boldsymbol{n_j}} & \frac{\boldsymbol{n_j}+\boldsymbol{n_k}}{2\boldsymbol{n_j}} \end{bmatrix} \quad \text{(A2.3-4)}$$

The propagation of light through a given layer j may similarly be described by a 2x2 matrix:

$$L_j = \begin{bmatrix} e^{-i\xi_j d_j} & 0 \\ 0 & e^{-i\xi_j d_j} \end{bmatrix} \quad \text{(A2.3-5)}$$

, where $\xi_j = \frac{2\pi}{\lambda}\boldsymbol{n_j}$, λ is the wavelength of light and d_j is the thickness of the layer.

It is now necessary to consider both the forward and backward propagating complex quantities of electric field along an axis 'x', denoted as $E^+(x)$ and $E^-(x)$. The electric field of light as it interacts with a series of 'm' layers (i.e. as light passes through the OSC) can be described by the total system transfer matrix, also known as the scattering matrix (**S**):

$$\begin{bmatrix} \boldsymbol{E_0^+} \\ \boldsymbol{E_0^-} \end{bmatrix} = \boldsymbol{S}\begin{bmatrix} \boldsymbol{E_{m+1}^+} \\ \boldsymbol{E_{m+1}^-} \end{bmatrix} \quad \text{(A2.3-6)}$$

, where E_0 refers to the electric field of light just as it approaches the front side of the solar cell, and E_{m+1} refers to the electric field of light just as it exits the back side. Further, S can be written as the product of all interference and propagation matrices:

$$\boldsymbol{S} = \begin{bmatrix} S_{11} & S_{12} \\ S_{21} & S_{22} \end{bmatrix} = \left(\prod_{\nu=1}^{m} \boldsymbol{I}_{(\nu-1)\nu}\boldsymbol{L}_\nu\right) \cdot \boldsymbol{I}_{m(m+1)} \quad \text{(A2.3-7)}$$

The reflection and transmission coefficients of the m-layer stack may be written as:

$$r = \frac{S_{21}}{S_{11}} \quad \text{(A2.3-8)}$$

$$t = \frac{1}{S_{11}} \quad \text{(A2.3-9)}$$

Since the glass substrate is generally quite thick, it is cumbersome and impractical to include it in the transfer-matrix calculation. Following the approach by [45], the intensity of the light after it has passed through the substrate can instead be calculated as:

$$I_s = I_0 \cdot \frac{T_S e^{-\alpha_S d_S}}{1 - R R_s e^{-2\alpha_S d_S}} = I_0 \cdot T_{int} \quad \text{(A2.3-10)}$$

, where I_0 is the intensity of the incident plane wave, T_s is the transmittance of the substrate, R_s is the reflectance of the substrate, α_s is the absorption coefficient of the substrate, d_s is the thickness of the substrate and R is the reflectance of the remaining layers of the OSC.

The reflectance of the remaining layers of the OSC can be found as:

$$R = |r^2| \quad \text{(A2.3-11)}$$

The intensity of the input light varies with wavelength and is defined by the AM1.5 1-sun solar spectrum.

Using I_s, the incident electric field, after passage through the substrate, can be found as:

$$E_S = \sqrt{\frac{2I_S}{c n_S \epsilon_0}} \quad \text{(A2.3-12)}$$

For the purposes of this model, E_S effectively refers to E_0^+ in **equation (6)** above.

In order to calculate the electric field at a specific distance x within layer j, it is necessary to break apart the total system transfer matrix into partial transfer matrices. One may define $\mathbf{S=S_j'L_jS_j''}$, where $\mathbf{S_j'}$ is the partial transfer matrix prior to layer j, $\mathbf{S_j''}$ is the partial transfer matrix after layer j, and $\mathbf{L_j}$ is the propagation matrix for layer j, as defined in **equation (5)** above. $\mathbf{S_j'}$ and $\mathbf{S_j''}$ may be written as:

$$\mathbf{S_j'} = \begin{bmatrix} S'_{j11} & S'_{j12} \\ S'_{j21} & S'_{j22} \end{bmatrix} = \left(\prod_{v=1}^{j-1} \boldsymbol{I}_{(v-1)v} \boldsymbol{L}_v\right) \cdot \boldsymbol{I}_{(j-1)j} \quad \text{(A2.3-13)}$$

$$\mathbf{S_j''} = \begin{bmatrix} S_{j11}'' & S_{j12}'' \\ S_{j21}'' & S_{j22}'' \end{bmatrix} = \left(\prod_{\nu=j+1}^{m} \boldsymbol{I}_{(\nu-1)\nu}\boldsymbol{L}_{\nu}\right) \cdot \boldsymbol{I}_{m(m+1)} \qquad \text{(A2.3-14)}$$

The complex reflection and transmission coefficients may then be written as $r'_j = \frac{S'_{j21}}{S'_{j11}}$, $t'_j = \frac{1}{S'_{j11}}$, $r''_j = \frac{S''_{j21}}{S''_{j11}}$ and $t''_j = \frac{1}{S''_{j11}}$.

Further, the internal transmission coefficient relating to the propagation of light in the forward direction can be found as:

$$t_j^+ = \frac{1}{S'_{j11} + S'_{j12} r''_j e^{2i\xi_j d_j}}$$

Finally, the total electric field in layer j at a distance x from its interface with layer (j-1) can be written as:

$$\boldsymbol{E_j}(x) = t_j^+ \left[e^{i\xi_j x} + r''_j e^{i\xi_j (2d_j - x)}\right] \boldsymbol{E_0^+} \qquad \text{(A2.3-15)}$$

Since the input intensity and the complex indices of refraction are a function of wavelength, the electric field is necessarily a function of wavelength. The square of the absolute value of the electric field at each point x can be integrated across the wavelengths of the input light to provide an approximate understanding of the total electric field as it varies in the OSC.

2.3.2. Input Data for Models

For simplicity, the range of wavelengths considered is 300 nm to 800 nm. The 1-sun, AM1.5 input spectrum was obtained from the National Renewable Energy Laboratory (NREL) and is available at http://rredc.nrel.gov/solar/spectra/am1.5/. Complex indices of refraction were obtained by digitizing graphs found in literature. The data were interpolated and smoothed to generate 1 nm spacing between points in the range of interest. The following sources were used to obtain the data:

- BCP: [303]
- CuPc: [304]
- C_{60}: [44]
- glass: [305]
- ITO: [305]
- PEDOT:PSS: [305]
- P3HT:PCBM (1:1) BHJ: [306]
- ZnPc: [307]
- ZnPc:C_{60} (1:1) BHJ: [25]

Metal complex indices of refraction were obtained from http://refractiveindex.info/. Printouts of the complex indices of refraction are available upon request.

2.3.3. MATLAB Implementation and Model Output

In order to demonstrate the basic implementation of this model, the following P3HT:PCBM BHJ device is modelled:

- Layer 0: Glass, thickness = 0.7 mm
- Layer 1: ITO, thickness = 100 nm
- Layer 2: PEDOT:PSS, thickness = 30 nm
- Layer 3: P3HT:PCBM (1:1), thickness = 70 nm & 200 nm
- Layer 4: Aluminum, thickness = 100 nm
- Layer 5: Air

All thicknesses are representative of a realistic device structure capable of producing 2-3% PCE in a laboratory device. 70 nm P3HT:PCBM would be fabricated by spincoating from a chlorobenzene solvent. 200 nm P3HT:PCBM would be fabricated by spinning at a higher weight percent from a dichlorobenzene solvent. The code used for this model is available at the end of this document. The output figures are shown below in Supplemental Figure 2.3.1 with the various layers labelled.

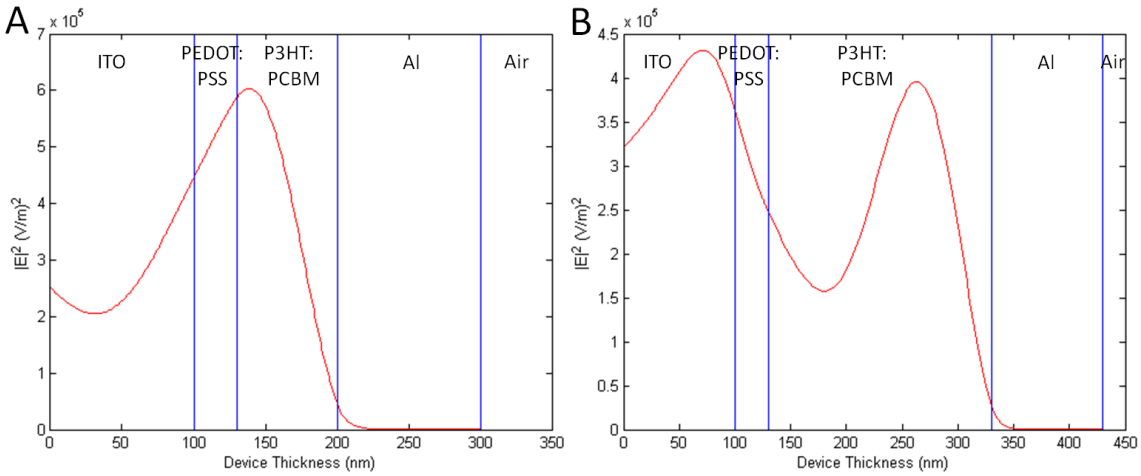

Supplemental Figure 2.3.1 - Distribution of the squared absolute electric field in a P3HT:PCBM BHJ OSC with A. 70 nm P3HT:PCBM and B. 200 nm P3HT:PCBM.

From Supplemental Figure 2.3.1, it is clear that a large portion of the electric field falls in the PEDOT:PSS and ITO regions. Since these regions are non-absorbing and they do not contribute to photocurrent, a significant portion of the incident light is effectively wasted. Increasing the P3HT:PCBM layer thickness to 200 nm (Supplemental Figure 2.3.1.B) helps to isolate the original peak within the active layer; however, a secondary peak arises in the ITO/PEDOT:PSS region.

In order to better isolate the optical field within the active region, a final P3HT:PCBM thickness of 130 nm is chosen. The results are shown below in Supplemental Figure 2.3.2.

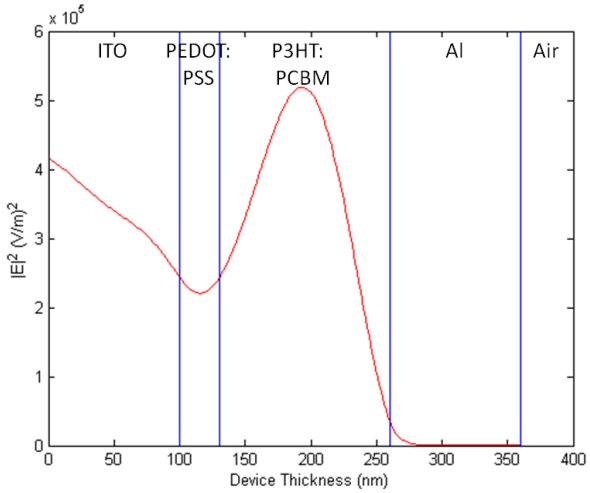

Supplemental Figure 2.3.2 - Distribution of the squared absolute electric field in a 130 nm P3HT:PCBM OSC.

This device is shown to have a significantly improved electric field distribution, with the maximum electric field centered within the active region of the device.

In order to further verify the power of this technique, the following device configurations are also examined:

i. A simple PHJ device with ZnPc donor and C_{60} acceptor
   glass(0.7 mm)/ITO(100 nm)/ZnPc(30 nm)/C_{60}(30 nm)/BCP(5 nm)/Al(100 nm)
ii. A PM-HJ device with ZnPc donor and C_{60} acceptor
   glass(0.7 mm)/ITO(100 nm)/ZnPc(30 nm)/ZnPc:C_{60}(20 nm)/C_{60}(30 nm)/BCP(5 nm)/Al(100 nm)
iii. A PM-HJ device in tandem configuration with ZnPc donor and C_{60} acceptor
   glass(0.7 mm)/ITO(100 nm)/ZnPc(30 nm)/ZnPc:C_{60}(20 nm)/C_{60}(10 nm)/Au(0.5 nm)/ZnPc(10 nm)/ZnPc:C_{60}(20 nm)/C_{60}(30 nm)/BCP(5 nm)/Al(100 nm)

For these devices, the MATLAB code was modified to include additional layers as required. This additional MATLAB code is available upon request. The squared electric field distributions for devices i and ii are shown in Supplemental Figure 2.3.3. The electric field distribution is quite poor for the simple PHJ, with very little possibility for light absorption by C_{60} and a large portion of the electric field in the ITO region. Incorporation of these materials into a PM-HJ device (Supplemental Figure 2.3.2.B), however, improves the positioning of the electric field, shifting its peak to the ZnPc:C_{60} BHJ.

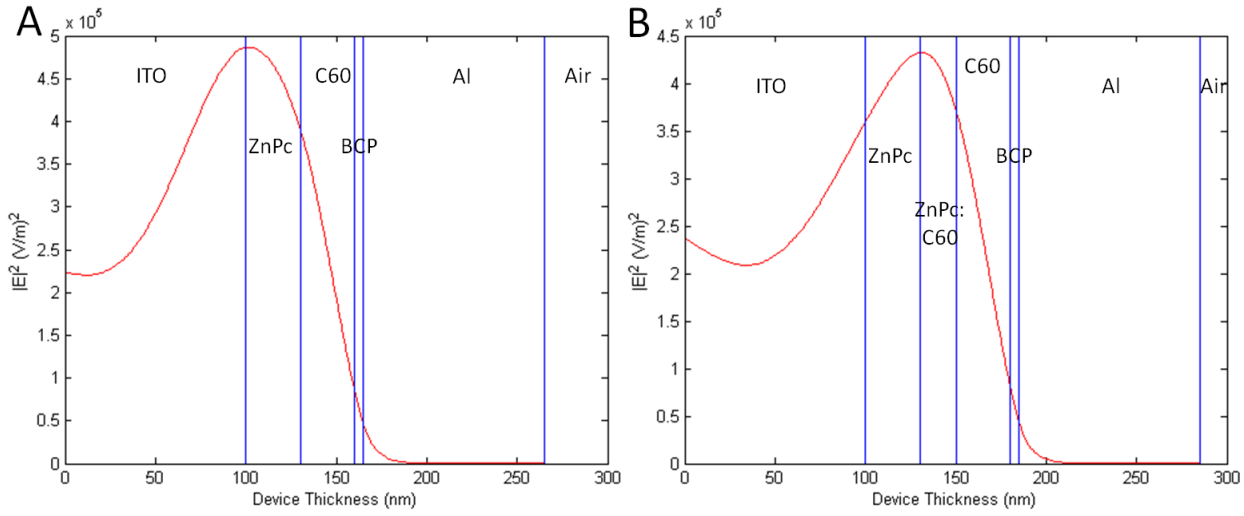

Supplemental Figure 2.3.3 - Distribution of the squared absolute electric field in a A. ZnPc/C_{60} PHJ and B. ZnPc:C_{60} PM-HJ OSC.

The electric field distribution is further complicated by the implementation of the tandem device, as shown in Supplemental Figure 2.3.4. The ideal electric field would have two peaks, centered at each of the ZnPc:C_{60} BHJs. However, as shown in Supplemental Figure 2.3.4.A, which is the device based off of iii above, the peak electric field occurs almost nearly at the Au metal cluster interface between the two sub-cells. This is non-ideal, as photogenerated excitons will recombine directly in this region before splitting into their constituent electrons and holes.

In order to better align the electric field, a 130 nm p-doped ZnPc optical spacer can be added and the thickness of the BHJ layer closer to the Al electrode can be increased to 30 nm, as shown in Supplemental Figure 2.3.4.B. In this case, the original local maximum shifts directly into the ZnPc:C_{60} BHJ. The minimum occurs within the optical spacer as desired, and the second BHJ occurs within a plateau of the electric field. Unfortunately the absolute maximum electric field occurs within the ITO layer, which is non-absorbing and does not contribute to device photocurrent. This stresses the strong sensitivity of the system to any changes in the layer thicknesses. To this end, further optimization is required to achieve the optimal optical field distribution.

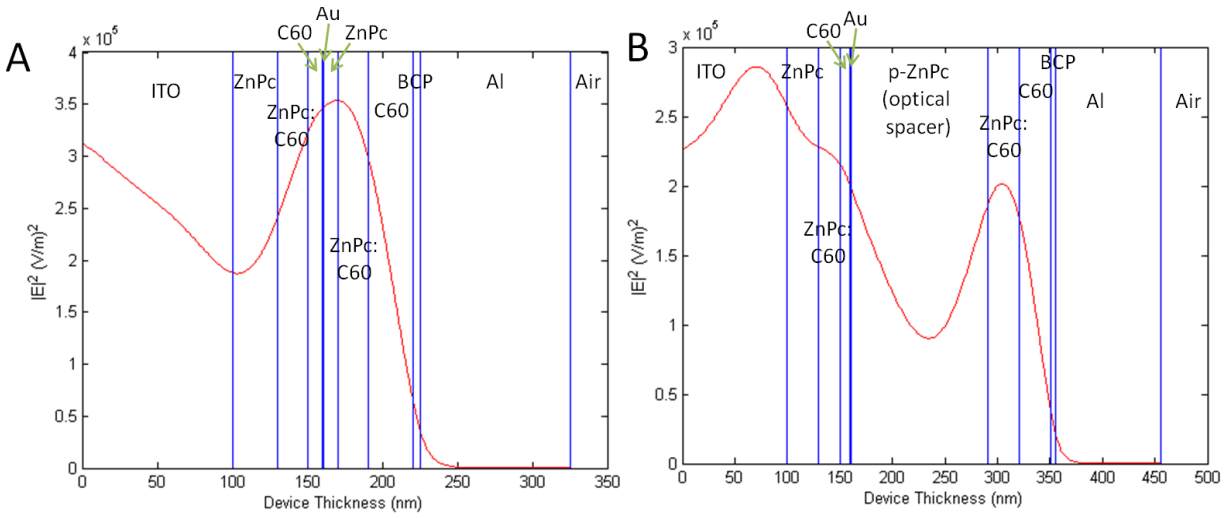

Supplemental Figure 2.3.4 - Distribution of the squared absolute electric field in a ZnPc:C_{60} PM-HJ tandem OSC A. without an optical spacer and B. with an optical spacer.

```
%*****************************************************
%Electric Field Calculation by Transfer Matrix Formalism
%*****************************************************

%Author:  Graeme Williams
%Contact:  g3willia@uwaterloo.ca

%Description:  This function maps the square of the absolute value of the
%electric field within a stack of m layers with known complex indices of
%refraction.
%Devices are considered to be fabricated superstrate, such that the light
%first passes through a substrate of a given thickness.

%All input complex index of refraction matrices are defined as:
    %| WAVELENGTH | Re(n) | Im(n) |
    %|    300     |  x0   |  y0   |
    %|    ...     |  ..   |  ..   |
    %|    800     | x500  | y500  |

%Variables
c = 299792458; %speed of light, m/s
eps_0 =  8.854187817620*10^-12; %vacuum permittivity, F/m


%---------------------------------------------------------------------------
%INPUT DATA
%Spread of wavelengths
lamset = [300:1:800]'*(10^-9); %300 nm to 800 nm

%Number of data points along the x-dimension per layer
x_pts = 100; %in reality, will actually be x_pts + 1

%Input Light Intensity
%Listed by NREL, available:  http://rredc.nrel.gov/solar/spectra/am1.5/
I0 = AM1p5(:,2);

%Note:  Due to its thickness, the glass substrate will be excluded from the
%transfer matrix methods.  Intensity of light through the glass will be
%calculated separately
d_glass = 0.7*10^-3; %m
R_glass = [n_glass(:,1), ((1 - n_glass(:,2))./(1 + n_glass(:,2))).^2];
T_glass = [R_glass(:,1), (1 - R_glass(:,2))];
alpha_glass = 30; %m^-1, roughly
k_glass = lamset*(alpha_glass)/(4*pi);

%Layered Structure
%n0 - Air to Glass
n_0 = n_glass(:,2) + i*k_glass(3);
T_s = T_glass(:,2);
R_s = R_glass(:,2);
alpha_s = alpha_glass;
d_s = d_glass;

%1 - ITO
n_1 = n_ITO(:,2) + i*n_ITO(:,3);
xi_1 = (2*pi*n_1)./lamset;
```

```
alpha_1 = n_ITO(:,3)*(4*pi)./lamset;
d_1 = 100*10^-9; %100nm, in m
%2 - PEDOT:PSS
n_2 = n_pedot(:,2) + i*n_pedot(:,3);
xi_2 = (2*pi*n_2)./lamset;
alpha_2 = n_pedot(:,3)*(4*pi)./lamset;
d_2 = 30*10^-9; %30nm, in m
%3 - P3HT:PCBM
n_3 = n_p3pc(:,2) + i*n_p3pc(:,3);
xi_3 = (2*pi*n_3)./lamset;
alpha_3 = n_p3pc(:,3)*(4*pi)./lamset;
d_3 = 70*10^-9; %70nm, in m
%4 - Al
n_4 = n_Al(:,2) + i*n_Al(:,3);
xi_4 = (2*pi*n_4)./lamset;
alpha_4 = n_Al(:,3)*(4*pi)./lamset;
d_4 = 100*10^-9; %100nm, in m
%5 - Air (assume vacuum for simplicity)
n_5 = zeros(501,1);
%--------------------------------------------------------------------------

%--------------------------------------------------------------------------
%Calculation of overall reflection and transmission coefficients
%& Definition of parameters for subsequent analysis

%Initializing variables for later use
R = [];
T = [];
t1_plus = [];
r1_pp = [];
t2_plus = [];
r2_pp = [];
t3_plus = [];
r3_pp = [];
t4_plus = [];
r4_pp = [];

%Looping through the wavelengths 300nm to 800nm
for j=1:501
    %*** Across n0 to n1
        %Interface Matrix
        I_01 = [ ( (n_0(j) + n_1(j))/(2*n_0(j)) ), ( (n_0(j) - ...
            n_1(j))/(2*n_0(j)) ); ( (n_0(j) - n_1(j))/(2*n_0(j)) ), ...
            ( (n_0(j) + n_1(j))/(2*n_0(j)) )];

    %*** Through n1
        %Layer Matrix
        L_1 = [exp(-i*(xi_1(j)*d_1)), 0; 0, exp(i*(xi_1(j)*d_1))];

    %*** Across n1 to n2
        %Interface Matrix
        I_12 = [ ( (n_1(j) + n_2(j))/(2*n_1(j)) ), ( (n_1(j) - ...
            n_2(j))/(2*n_1(j)) ); ( (n_1(j) - n_2(j))/(2*n_1(j)) ), ...
            ( (n_1(j) + n_2(j))/(2*n_1(j)) )];

    %*** Through n2
```

```
    %Layer Matrix
    L_2 = [exp(-i*(xi_2(j)*d_2)), 0; 0, exp(i*(xi_2(j)*d_2))];

%*** Across n2 to n3
    %Interface Matrix
    I_23 = [ ( (n_2(j) + n_3(j))/(2*n_2(j)) ), ( (n_2(j) - ...
        n_3(j))/(2*n_2(j)) ); ( (n_2(j) - n_3(j))/(2*n_2(j)) ), ...
        ( (n_2(j) + n_3(j))/(2*n_2(j)) )];

%*** Through n3
    %Layer Matrix
    L_3 = [exp(-i*(xi_3(j)*d_3)), 0; 0, exp(i*(xi_3(j)*d_3))];

%*** Across n3 to n4
    %Interface Matrix
    I_34 = [ ( (n_3(j) + n_4(j))/(2*n_3(j)) ), ( (n_3(j) - ...
        n_4(j))/(2*n_3(j)) ); ( (n_3(j) - n_4(j))/(2*n_3(j)) ), ...
        ( (n_3(j) + n_4(j))/(2*n_3(j)) )];

%Through n4
    %Layer Matrix
    L_4 = [exp(-i*(xi_4(j)*d_4)), 0; 0, exp(i*(xi_4(j)*d_4))];

%*** Across n4 to n5
    %Interface Matrix
    I_45 = [ ( (n_4(j) + n_5(j))/(2*n_4(j)) ), ( (n_4(j) - ...
        n_5(j))/(2*n_4(j)) ); ( (n_4(j) - n_5(j))/(2*n_4(j)) ), ...
        ( (n_4(j) + n_5(j))/(2*n_4(j)) )];

%Calculating the total transfer matrix for this lambda
S = I_01*L_1*I_12*L_2*I_23*L_3*I_34*L_4*I_45;

%Calculating the total reflectance and transmittance parameters
r = S(2,1)/S(1,1);
t = 1/S(1,1);

%Calculating the parameters wrt power/intensity
R = [R; abs(r^2)];

%**************************************************************************
%Calculating partial transfer matrices (for position-dependent
%intensity calculations - see below)
S1_p = I_01;
S1_pp = I_12*L_2*I_23*L_3*I_34*L_4*I_45;
S2_p = I_01*L_1*I_12;
S2_pp = I_23*L_3*I_34*L_4*I_45;
S3_p = I_01*L_1*I_12*L_2*I_23;
S3_pp = I_34*L_4*I_45;
S4_p = I_01*L_1*I_12*L_2*I_23*L_3*I_34;
S4_pp = I_45;

%Calculating relevant transmission and reflection parameters
r1_pp = [r1_pp; S1_pp(2,1)/S1_pp(1,1)];
r2_pp = [r2_pp; S2_pp(2,1)/S2_pp(1,1)];
r3_pp = [r3_pp; S3_pp(2,1)/S3_pp(1,1)];
r4_pp = [r4_pp; S4_pp(2,1)/S4_pp(1,1)];
```

```
    t1_plus = [t1_plus; (S1_p(1,1) + S1_p(1,2)*r1_pp(j)*...
        exp(2*i*xi_1(j)*d_1))^(-1)];
    t2_plus = [t2_plus; (S2_p(1,1) + S2_p(1,2)*r2_pp(j)*...
        exp(2*i*xi_2(j)*d_2))^(-1)];
    t3_plus = [t3_plus; (S3_p(1,1) + S3_p(1,2)*r3_pp(j)*...
        exp(2*i*xi_3(j)*d_3))^(-1)];
    t4_plus = [t4_plus; (S4_p(1,1) + S4_p(1,2)*r4_pp(j)*...
        exp(2*i*xi_4(j)*d_4))^(-1)];

end
%-------------------------------------------------------------------------

%-------------------------------------------------------------------------
%Calculation of the internal transmittance through the glass substrate
T_int = (T_s.*exp(-alpha_s.*d_s))./(1-(R.*R_s.*exp(-2.*alpha_s.*d_s)));
%-------------------------------------------------------------------------

%-------------------------------------------------------------------------
%Calculation of position-dependent reflection and transmission coefficients

%Defining the inital electric field intensity based on:
%I=(c*n*eps0/2)*abs(E)^2
E0 = sqrt(2*(I0.*T_int)./(c*n_glass(:,2)*eps_0));

%Initializing variables for later use
E1 = [];
E2 = [];
E3 = [];

%Layer 0 (substrate)
Is = I0.*T_int;

%Layer 1-3
    %Splitting layers into finite segments
    %Layer 1
    delta_d1 = d_1 / x_pts;
    d1_pts = [0:delta_d1:d_1];
    %Layer 2
    delta_d2 = d_2 / x_pts;
    d2_pts = [0:delta_d2:d_2];
    %Layer 3
    delta_d3 = d_3 / x_pts;
    d3_pts = [0:delta_d3:d_3];
    %Layer 4
    delta_d4 = d_4 / x_pts;
    d4_pts = [0:delta_d4:d_4];


    %Looping through the wavelengths
    for j=1:501
        for k=1:(x_pts+1)
            E1(j,k) = E0(j) * t1_plus(j)*(exp(i*xi_1(j)*d1_pts(k)) + ...
                r1_pp(j)*exp(i*xi_1(j)*(2*d_1-d1_pts(k))));
            E2(j,k) = E0(j) * t2_plus(j)*(exp(i*xi_2(j)*d2_pts(k)) + ...
                r2_pp(j)*exp(i*xi_2(j)*(2*d_2-d2_pts(k))));
```

```
            E3(j,k) = E0(j) * t3_plus(j)*(exp(i*xi_3(j)*d3_pts(k)) + ...
                r3_pp(j)*exp(i*xi_3(j)*(2*d_3-d3_pts(k))));
            E4(j,k) = E0(j) * t4_plus(j)*(exp(i*xi_4(j)*d4_pts(k)) + ...
                r4_pp(j)*exp(i*xi_4(j)*(2*d_4-d4_pts(k))));
        end
    end


%Integrating intensity across the visible spectrum
Esq1 = abs(E1).^2;
Esq2 = abs(E2).^2;
Esq3 = abs(E3).^2;
Esq4 = abs(E4).^2;

xvals = AM1p5(:,1);
Esq1sum = [];
Esq2sum = [];
Esq3sum = [];
Esq4sum = [];

for k=1:(x_pts+1)
    y1vals = Esq1(:,k);
    y2vals = Esq2(:,k);
    y3vals = Esq3(:,k);
    y4vals = Esq4(:,k);

    Esq1sum = [Esq1sum, trapz(xvals,y1vals)];
    Esq2sum = [Esq2sum, trapz(xvals,y2vals)];
    Esq3sum = [Esq3sum, trapz(xvals,y3vals)];
    Esq4sum = [Esq4sum, trapz(xvals,y4vals)];
end

%Plotting the output data
total_y = [Esq1sum Esq2sum Esq3sum Esq4sum];
x1max = max(d1_pts);
x2max = max(d2_pts) + x1max;
x3max = max(d3_pts) + x2max;
x4max = max(d4_pts) + x3max;
total_x = [d1_pts (x1max + d2_pts) (x2max + d3_pts) (x3max + d4_pts)];
p1 = plot(total_x,total_y, 'red');
p1_axis = axis;

%Drawing vertical lines to visually separate layers
hold on
line([x1max x1max], [0 p1_axis(4)])
line([x2max x2max], [0 p1_axis(4)])
line([x3max x3max], [0 p1_axis(4)])
line([x4max x4max], [0 p1_axis(4)])
```